

Large-eddy simulation of confined transitional plumes

Citation for published version (APA):

Bastiaans, R. J. M. (1997). *Large-eddy simulation of confined transitional plumes*. [Phd Thesis 1 (Research TU/e / Graduation TU/e), Mechanical Engineering]. Technische Universiteit Eindhoven.
<https://doi.org/10.6100/IR474556>

DOI:

[10.6100/IR474556](https://doi.org/10.6100/IR474556)

Document status and date:

Published: 01/01/1997

Document Version:

Publisher's PDF, also known as Version of Record (includes final page, issue and volume numbers)

Please check the document version of this publication:

- A submitted manuscript is the version of the article upon submission and before peer-review. There can be important differences between the submitted version and the official published version of record. People interested in the research are advised to contact the author for the final version of the publication, or visit the DOI to the publisher's website.
- The final author version and the galley proof are versions of the publication after peer review.
- The final published version features the final layout of the paper including the volume, issue and page numbers.

[Link to publication](#)

General rights

Copyright and moral rights for the publications made accessible in the public portal are retained by the authors and/or other copyright owners and it is a condition of accessing publications that users recognise and abide by the legal requirements associated with these rights.

- Users may download and print one copy of any publication from the public portal for the purpose of private study or research.
- You may not further distribute the material or use it for any profit-making activity or commercial gain
- You may freely distribute the URL identifying the publication in the public portal.

If the publication is distributed under the terms of Article 25fa of the Dutch Copyright Act, indicated by the "Taverne" license above, please follow below link for the End User Agreement:

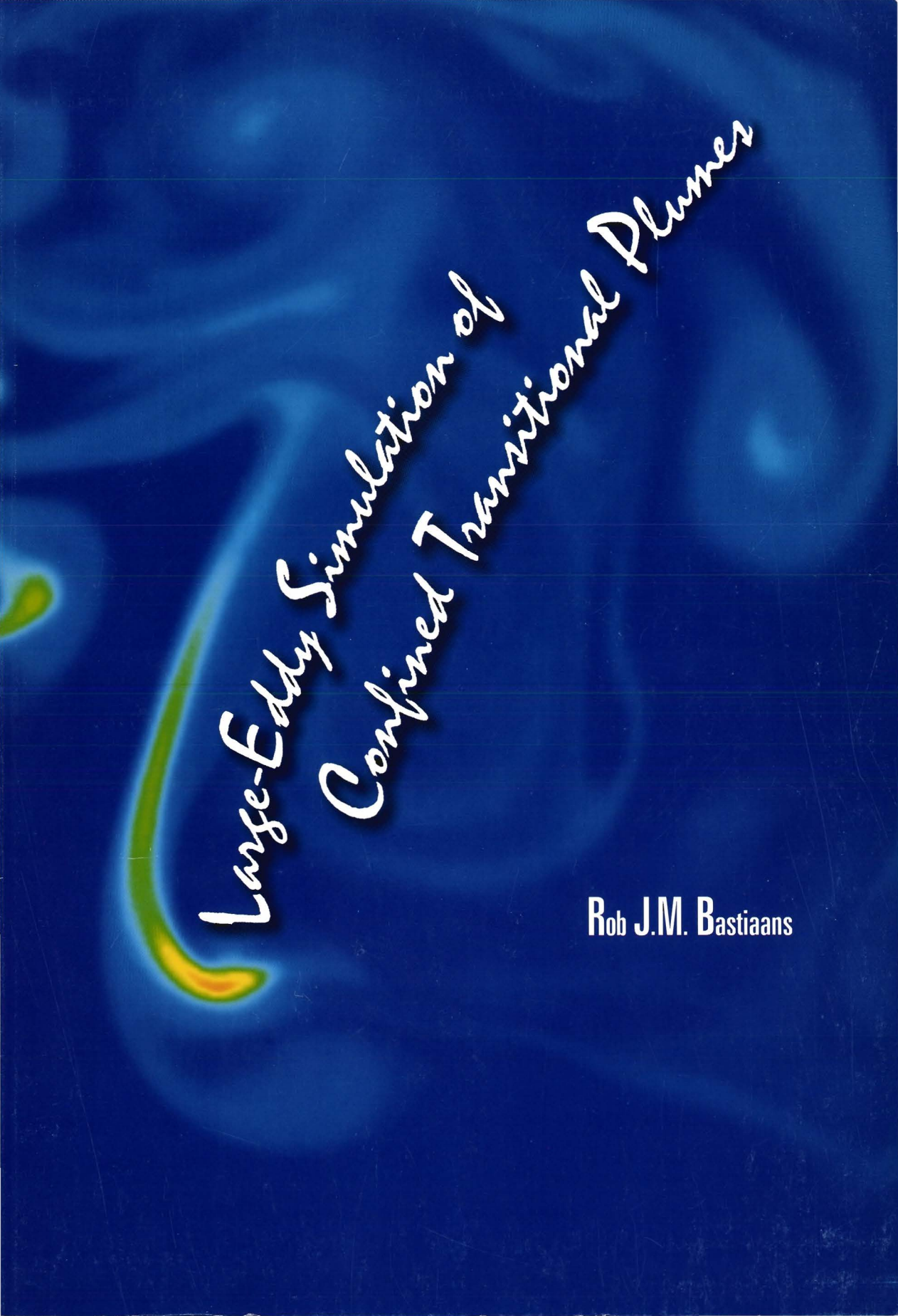
www.tue.nl/taverne

Take down policy

If you believe that this document breaches copyright please contact us at:

openaccess@tue.nl

providing details and we will investigate your claim.



*Large-Eddy Simulation of
Confined Transitional Plumes*

Rob J.M. Bastiaans

Large-Eddy Simulation of Confined Transitional Plumes

PROEFSCHRIFT

ter verkrijging van de graad van doctor aan de
Technische Universiteit Eindhoven, op gezag van
de Rector Magnificus, prof.dr. M. Rem,
voor een commissie aangewezen door het College
van Dekanen in het openbaar te verdedigen op
woensdag 22 januari 1997 om 16.00 uur

door

Robert Johan Maria Bastiaans

geboren te Mill.

Dit proefschrift is goedgekeurd door de promotoren:

prof.dr.ir. A.A. van Steenhoven
prof.dr.ir. F.T.M. Nieuwstadt

Copromotor:

dr.ir. C.C.M. Rindt

CIP-DATA KONINKLIJKE BIBLIOTHEEK, DEN HAAG

Bastiaans, Rob J.M.

Large-Eddy Simulation of Confined Transitional Plumes

Rob J.M. Bastiaans. - Eindhoven: Eindhoven University Press. -

Thesis Eindhoven University of Technology, 1996. -

With ref. - With summary in Dutch.

ISBN 90-386-0259-6

Eindhoven University Press, the Netherlands.

Copyright ©1996 by R.J.M. Bastiaans

All rights reserved.

No part of the material protected by this copyright notice may be reproduced or utilized in any form or by any means, electronic or mechanical, including photocopying, recording or by any information storage and retrieval system, without permission from the publisher.

This work was sponsored by the Stichting Nationale Computerfaciliteiten (NCF) for the use of supercomputer facilities, with financial support from the Nederlandse Organisatie voor Wetenschappelijk Onderzoek (NWO).

Contents

1	Introduction	1
1.1	Background	1
1.1.1	General framework	1
1.1.2	Engineering flows	2
1.2	Transitional Fluid Flow	3
1.3	Fluid flow simulations	4
1.4	Objectives	5
1.5	Thesis synopsis	6
2	Governing equations and analysis	9
2.1	Governing equations	9
2.1.1	Navier-Stokes equations	9
2.1.2	The Boussinesq approximation	10
2.1.3	The non-dimensional formulation	11
2.2	Routes to chaos and turbulence	13
2.3	Turbulence: length and time scales	15
2.4	Analytical results and literature	19
2.4.1	Similarity equations for the laminar boundary layer	19
2.4.2	Solutions for the laminar boundary layer equations	20
2.4.3	Stability of laminar plumes	23
2.4.4	Turbulent plume: an integral model	24
2.4.5	Turbulent plume measurements	26
3	Direct and large-eddy numerical simulation	29
3.1	Direct numerical simulation	29
3.2	Large-Eddy simulation	30
3.2.1	Introduction	30
3.2.2	The filtering procedure	30
3.2.3	Subgrid-scale stresses and fluxes	32
3.2.4	Kinetic energy transfer	34
3.3	Subgrid-scale models	36
3.3.1	Introduction	36

3.3.2	Smagorinsky model	37
3.3.3	Structure-function model	39
3.3.4	Kolmogorov-Prandtl model	40
3.3.5	Germano's dynamic model	42
3.3.6	Recent developments	45
4	Numerical method and performance in plume flows	47
4.1	Numerical method	47
4.1.1	Time integration	47
4.1.2	Spatial discretization	49
4.1.3	Boundary conditions	51
4.2	Performance test	52
4.2.1	Test problem description	52
4.2.2	Present calculations	54
4.2.3	Stationary case	55
4.2.4	Oscillating plumes	58
4.2.5	Conclusions	60
4.2.6	Epilogue	61
5	Laboratory measurements	63
5.1	Introduction	63
5.2	Experimental setup	64
5.2.1	Construction	64
5.2.2	Constraints	67
5.2.3	Flow regime adjustment	68
5.3	Measurement techniques	70
5.3.1	Thermocouples	70
5.3.2	Particle tracking velocimetry	75
6	Results for water plumes: Experiment versus LES	83
6.1	Introduction	83
6.2	Results from particle tracking experiments	84
6.2.1	Experimental conditions	84
6.2.2	Mean flow	85
6.2.3	Flow fluctuations	88
6.2.4	Subgrid stresses	91
6.2.5	Energy transfer	93
6.2.6	<i>A priori</i> testing	94
6.3	LES results: <i>a posteriori</i> testing	98
6.3.1	General remarks	98
6.3.2	Velocity information	99
6.3.3	The initially rising dipole	105
6.3.4	Local temperatures: measurements versus LES	107

6.4	Conclusions	109
7	Results for air plumes: DNS versus LES	111
7.1	Introduction	111
7.2	Results of two-dimensional simulations	113
7.2.1	Convergence of two-dimensional flow	113
7.2.2	The predictability horizon in $2D$ flow	116
7.2.3	Turbulence statistics of $2D$ flow	118
7.2.4	Results of $2D$ LES	119
7.3	Results of direct numerical simulation	121
7.3.1	The transient	121
7.3.2	Flow statistics	123
7.4	Large-Eddy simulations	128
7.5	Conclusions	131
8	Concluding discussion and final remarks	133
	References	138
A	Convergence of similarity solutions	143
B	Discretization of non-linear advection	145
C	The "ULTIMATE"-van Leer scheme	149
D	PTV cost minimization algorithm	153
E	Experimental stresses and <i>a priori</i> test	155
F	Development of a $2D$ plume in air	161
G	Development of a $3D$ plume in air	165
	Frequently used nomenclature	169
	Summary	171
	Samenvatting	172
	Nawoord	173
	Curriculum vitae	174

Chapter 1

Introduction

1.1 Background

1.1.1 General framework

The scarcity of employable energy is considered widespread to be a major problem. Power supply still depends heavily on the use of fossile energy sources. Related to this, the harm of the associated emissions to the ecological environment are recognized. Depletion of conventional energy sources to an increasing extent together with the increase in energy demand are the main causes. This situation impels a frugal use of these traditional sources and a competitive management of alternative, more sustainable energy sources. One of the important themes in energy technology research is heat transfer control.

External heat transfer from located sources in a quiescent (fluid) ambient, is accompanied by the formation of plumes. Fluid flow in a plume originates from the buoyancy force, the apparent gravity differences experienced as a result of spatial density variations. The source of these differential dilatations is the fact that temperature and density are related. The intensity of the flow depends on the rate at which the heat is supplied.

Plumes are manifestations of continuous and local heating of a fluid. Familiar examples are a cigarette plume and the flow originating from a chimney or a fire. These plumes can be observed easily due to the presence of a visible tracer agent, like smoke or water vapour. Often they are not visible like the plumes above radiators, in our central heating system. Plumes do also appear on a larger scale in geophysical systems like in the atmosphere, oceans and in the interior of the earth. At relatively high heating rates or if the heating is not constant, blobs of rising fluid may appear, known as thermals.

1.1.2 Engineering flows

The present research originates from an interest in heat transfer management from an engineering point of view. An example is the process of natural convection in heat storage vessels. These are used, for instance, in solar domestic hot water systems. Heat has to be stored because supply and demand are not in phase. The quality of the stored heat depends on the temperature. Heat stored at high temperature contains more available energy than heat stored at low temperatures. Therefore it is advantageous to keep the temperature differences as large as possible. Generally this results in a stratified situation. Water of high temperature is therefore stored on top of cold water. This favourable configuration may be destroyed by fluid flow. The accompanying mixing creates enhanced diffusion of heat, decreasing the temperature differences. On top of the inevitable molecular diffusion, this decreases the storage quality.

A heat storage vessel contains a heat exchanger consisting of a spiral tube. At the charging state hot fluid flows through the coil exchanging its heat to the cold ambient fluid in the vessel. A plume of relatively hot fluid is released. This may cause undesirable mixing. In this case the quality of the stored heat is strongly dependent on the action of convection and diffusion. This is of major importance on the economical operation of systems that use water heated by sustainable energy resources, like solar energy. At the moment solar domestic hot water systems can almost compete with conventional heating systems at moderate latitudes. An optimization of the presently available systems could make the difference.

A second example is the formation of plumes induced by hot electronic components in all kind of configurations and housings. Especially in increasing the performance of computers the cooling management, in addition to the minimization of heat production, is the key element.

In most cases the design of these systems with respect to the desired heat exchange is based on empirical data and analytical solutions of strongly simplified problems. The reason for the application of these simplified kinds of treatments is because of the complexity of both the geometries considered (3D-effects) and the resulting flow phenomena. Often the flows involved are even turbulent. Therefore in a large amount of circumstances the solution of simplified problems is only able to display a very limited validity. More detailed theories of describing these complex flows are much less well developed. However for engineering purposes, in the recent past, there were no alternatives (*Turner [1973], Gebhart et al. [1988]*).

With the increase of computer capacity, i.e. a combination of speed and storage capacity, numerical simulations of time dependent fluid flow at sufficient resolution come into play in the near future. In this perspective, one of the things that are required in the designing process is the development of a physically correct numerical code in order to simulate the flow and heat exchange in complicated flow configurations.

1.2 Transitional Fluid Flow

Two main categories of fluid flows are those generated by external forcing and fluid flows created by temperature differences. In the latter case the buoyancy force is responsible for the flow, which is referred to as "natural convection". The externally forced flow is called "forced convection" and the general case is "mixed convection", in which both types of forcing are present.

Fluid flow can also be categorized by the flow regime. With increased forcing the flow first is laminar. The laminar flow regime is characterized by being stationary, i.e. there is a stable and therefore steady shear flow. However, with an increase of the forcing the flow structure may change to another pattern. At a high forcing rate, flows consist of many whirls or vortical structures, continuously moving with time. This was demonstrated about a century ago by *Reynolds* [1883], who enunciated also the criterion for the prediction of the flow regime, whether it will be laminar or in a turbulent state. It is based on the ratio of destabilizing forces to stabilizing forces, and the measure is now called the Reynolds number, Re .

In the so-called turbulent flows there is a very large difference between the length scales of individual whirls. The equilibrium of kinetic energy transfer in turbulent flow was the key to find the distribution of scales by *Kolmogorov* [1941], which was a very important break-through.

Between the two regimes of laminar and turbulent flow there is transition. The flow changes from unsteady purely and/or quasi-periodic flows to chaotic flows. In the latter regime all independent flow features stay on a geometrical figure called "attractor" (*Lorenz* [1963]). This became clear with the first numerical simulations of idealized dynamical systems. Later it was confirmed by detailed experimental data as well. An important feature of chaotic and turbulent motion is the exponential increase in distance of initially very close particles. Turbulent flows are chaotic, though very commonly chaos is associated with low dimensional systems.

Within the context of natural convection flows, transition was first studied successfully by *Rayleigh* [1916], who determined the onset of flow between differentially heated horizontal planes with the higher temperature on the lower side. The Rayleigh number, Ra , a measure of the forcing rate in natural convection flows, was named after him. This was the beginning of the research of more and more complex natural convection flows.

Transition between flow regimes can occur with change of forcing, as mentioned above, change of time, generally called transients, and change of position. This thesis is about natural convection flows, induced by a relatively small heated element, with a spatial transition from laminar to turbulent flow. In everyday life these flows are called "plumes" and a striking example is the plume of a cigarette. Smoke of a burning cigarette in quiescent air shows a straight upstream part, some oscillations downstream developing into a turbulent plume. The position of the

transitional oscillatory part is very sensitive to slight disturbances.

1.3 Fluid flow simulations

With the introduction of the digital computer, approximately halfway this century, it became possible to perform numerical simulations of fluid flows. A set of "governing equations" appropriate for the considered problem is approximated in a discrete sense. First the memory size and processing speed allowed only simulation of simple flow configurations and regimes. At the moment it is possible to perform time dependent three-dimensional simulations for turbulent flows, although only at rather low forcing rates.

With Direct Numerical Simulation (DNS) the governing equations are solved on a grid that is sufficiently fine to resolve the flow up to the smallest detail. As a consequence of this, a very large computer capacity has to be claimed because the turbulent part of the flow consists of many different scales of motion. Also, turbulence is essential three-dimensional. The large scales of motion are related to the geometry of the flow, whereas the small scales of motion are determined by molecular processes such as viscosity. The ratio of the macroscopic scales to the microscopic scales depends on the rate of forcing of the flow. The higher the forcing rate (expressed by a dimensionless number such as the Reynolds number, in case of forced convection, or the Rayleigh number, in case of natural convection, which is considered here) the wider the kinetic energy spectrum. Furthermore, in the transition region the balance between buoyant, viscous, inertial and pressure forces is very subtle.

In the future it will be possible to simulate turbulent flows at increasing forcing rates, requiring a finer and finer discretization. To be able to use the increasing computing power in designing processes and research, the main items will be the necessity of real-time simulation, visualization and parameter and design variation. Not only the forcing rate but also the sizes of the systems to be simulated will increase. This results in an ever lasting state of computer capacity, that is the state of being too small.

In order to overcome this problem, at least partially, a reduction in the required resolution is always desirable. The classical method for this used to be the so-called Reynolds averaging. It consists of averaging the governing equations in time, resulting in the appearance of new unknown terms representing the fluctuations, called the Reynolds stresses. By using this method no detailed, time dependent, information can be obtained. The effect of the model in the case of large instationary scales, that are always present, can be considerable.

Since the early 70's a new simulation technique called Large-Eddy Simulation (LES) has become available. The first LES was reported by *Deardorff* [1970], dealing with channel flow at infinite Reynolds number. The basic idea of this method is to filter the governing equations using a spatial low-pass filter, remov-

ing the small scale structure of the flow. By doing this unresolved terms appear in the equations. These terms have to be expressed in terms of resolved quantities with a so-called SubGrid-scale Model (SGM). These models account for the influence of small whirls, that are not resolved, on the dynamics of the larger whirls. This leads to a large reduction of computer capacity because the flow is only discretized and resolved up to the cut-off wave number determined by the grid size. Because of the fact that the smallest eddies are more isotropic and homogeneously distributed than the large eddies it is expected that simulations based on subgrid modelling are more accurate than in the case of time filtering. Therefore the models, that are in general quite simple, are believed to be more universally applicable.

1.4 Objectives

Although Large-Eddy simulations have been performed successfully for all kinds of flows in the past twentyfive years, there are no standard SGMs yet that can predict the transition. Only recently there have been some proposals for SGMs that resolve the transitional features quite well.

All present SGMs are models derived in principle from the theory of homogeneous isotropic turbulence, a turbulent flow that can only exist in a theoretically unbounded space in which the fluid is randomly perturbed initially. In the very first large eddy simulations *Deardorff* [1970] used the Smagorinsky model, (after *Smagorinsky* [1963]) based on an equilibrium state of turbulent production and dissipation. This model gave good results for "fully turbulent" flows and became very popular. Later on there were some modifications and extensions of the model, including the one as used by *Nieuwstadt* [1990] in which the transport of subgrid kinetic energy was solved with an additional convection-diffusion equation. It became clear that the standard Smagorinsky model gave the best results in forced convection flows and that the subgrid kinetic energy model performed best in the case of natural convection flows.

More recently *Métais and Lesieur* [1992] proposed their structure-function model, a localization in physical space from homogeneous isotropic turbulence theory in wave-number space. It was found that the model gave good results, also in wall-bounded and separating flows like the flow over a backward-facing step simulated by *Silveira Neto et al.* [1991].

A subgrid-scale model to simulate intermittent and non-homogeneous flows as in the transitional case was developed by *Germano et al.* [1991]. In this so-called dynamical model a Smagorinsky closure was proposed in which the model coefficient has to be calculated dynamically. It is based on the assumption that the Smagorinsky model is valid at two filtering levels: the gridfilter and a testfilter. The resolved stress between the two filters is then used to determine the constant. The obtained subgrid-scale stresses vanish in laminar flow and at

solid boundaries where a correct asymptotic behaviour of the turbulent boundary layer was predicted. *Lilly* [1992] optimized the formulation for more general use. A revolutionary feature of the method is the possible appearance of negative eddy viscosities. However, this can lead to numerical instabilities if no precaution is applied.

Finally, *Ducros et al.* [1994] propose a SGM on the basis of the structure-function model giving nearly zero eddy viscosity during the laminar and transitional stages of the flow, a property which they refer to as "selectivity". This property is needed because the first instability effectively decreases the Reynolds number in the original model and relaminarizes the flow. They conclude that for the transitional boundary layer near a flat surface their filtered structure-function model gives the best results compared to the structure-function model, the Smagorinsky model and the dynamic model.

The objective of this research is to find a subgrid scale model that gives good results in a large region of forcing of the flow, or turbulent intensities. Furthermore, the model must be able to display transition. Therefore the influence of the model must be negligible in laminar regions but it must possess the potential to drain enough kinetic energy in isotropic homogeneous turbulence. Also the properties of non-homogeneity and non-isotropy as occurring in the transitional region of a 'plane buoyant plume' may not be affected too much.

In order to determine which model performs best, two forms of reference data will be used. The first one is a direct numerical simulation, providing detailed time dependent three dimensional information that can be compared with the Large-Eddy simulations. Here the medium properties of air are used. Secondly, an experiment is performed for a plume in a water container in which the velocity is measured in a two-dimensional plane using particle tracking velocimetry. Additional thermocouple measurements were used together with shadowgraphy in order to obtain information about the temperature distribution.

1.5 Thesis synopsis

This thesis starts with a description of the governing equations in chapter 2, together with considerations about the transition and length and time scales that will appear. Also a summary is given of results obtained by analytical treatment of approximations of the equations for the plane buoyant plumes in a laminar state as well as in a fully developed turbulent regime. Furthermore, results as obtained by experiments and analyses found in the literature will be discussed. In this part of the thesis the flow configuration under consideration is as given in figure 1.1. In the figure a length scale is given in which all distances are measured. As indicated in the figure, two sets of notations are used. The first one is generally applied, whereas the second one is used whenever more appropriate.

In chapters 3 and 4 the applied numerical simulation techniques will be dis-

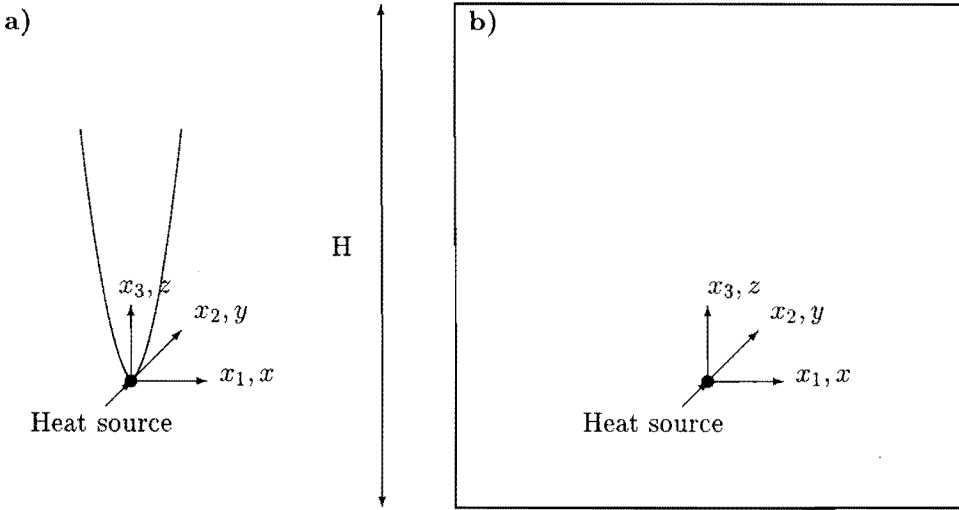


Figure 1.1: Plume in a) an infinite medium and b) a confined enclosure

cussed. It is started with Direct Numerical Simulation (DNS), followed by Large-Eddy Simulation (LES) and finally, a description of the applied subgrid-scale models (SGMs). The latter chapter deals with the discrete approximation technique that is used. Also a test is presented to validate the numerical code for a two-dimensional plume in a confined geometry as given in figure 1.1. The experimental set-up will be discussed in chapter 5, together with the applied measurement techniques: particle tracking velocimetry with additional thermocouple measurements and liquid crystal thermography. The experimental data acquisition and processing will be described in detail. The geometry considered in the experiment is basically displayed in figure 1.2 and it has a front and back wall at a mutual distance equal to the cavity height.

The results will be discussed in chapters 6 and 7 for the water and air configurations respectively. First the results of a direct numerical simulation will be described. The geometry in this case is configured as displayed in figure 1.1. It concerns a two-dimensional as well as a three-dimensional turbulent air plume. In the case of the three-dimensional simulations, the front and back boundaries are separated one enclosure height from each other and the boundary conditions are taken to be periodic. Then the results of three-dimensional Large-Eddy simulations will be presented and compared. The thesis will be continued with a chapter containing the experimental results of the water plume in the configuration as given schematically in figure 1.2. For this situation the results of Large-Eddy simulations will be given and compared to the experimental data. The forcing rate in this case is higher than for the air plume. Furthermore, experiments and simulations will be compared with analytical results and experimental values as

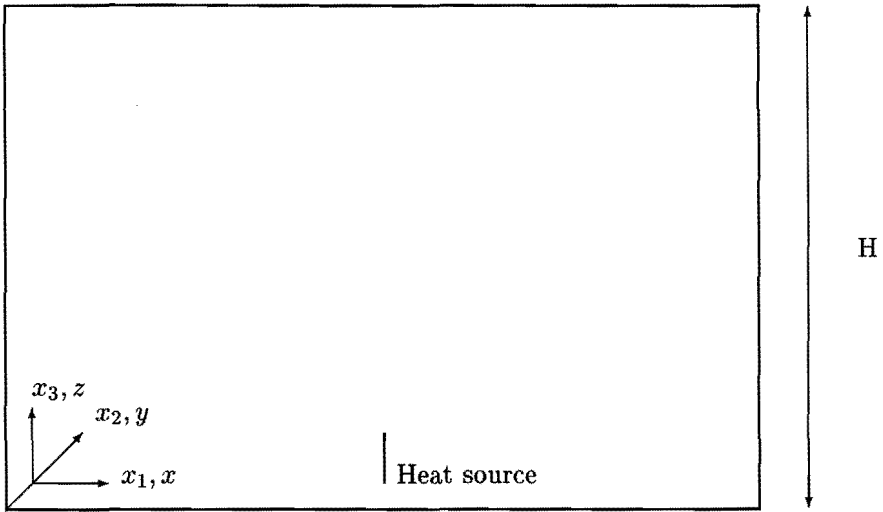


Figure 1.2: Experimental flow configuration

presented in the literature and discussed in chapter 2

Finally, some conclusions and recommendations will be given in chapter 8.

Chapter 2

Governing equations and analysis

2.1 Governing equations

2.1.1 Navier-Stokes equations

The equations, commonly used to describe the flow variables in a continuum, consist of a set of conservation laws. It contains a continuity equation wherein the conservation of mass is described. Additionally it includes Newton's second law for the conservation of momentum in the fluid. The resulting equation is the Navier-Stokes equation. It is assumed that the density and viscosity are invariant in space and time. The internal friction of the fluid is supposed to be Newtonian. This means that the shear stresses are linearly proportional to the strain. For many ordinary fluids like air and water this is a good approximation. The system of equations, written in an Eulerian frame, in Cartesian coordinates and in tensorial notation, reads:

$$\frac{\partial u_i}{\partial x_i} = 0; \quad (2.1)$$

$$\frac{\partial u_i}{\partial t} + \frac{\partial}{\partial x_j} (u_i u_j) = -\frac{1}{\rho} \frac{\partial p}{\partial x_i} + \nu \frac{\partial^2 u_i}{\partial x_j \partial x_j} + f_i. \quad (2.2)$$

Repetition of an index in a term means summing over the index under consideration. The velocity is denoted by u_i , ρ is the density, p the pressure, ν the kinematic viscosity and f_i is an additional body force. These equations, together with appropriate boundary and initial conditions, describe the flow for all later times. This does not mean that it is always possible to predict exactly the solution at all times, as pointed out by *Lighthill* [1986]. A closer look at this point will be given in section 2.2.

2.1.2 The Boussinesq approximation

Considering plume flow, the body force contains a term accounting for buoyancy effects. In the previous section effects accompanying the presence of density variations are neglected. Here, density differences as far as responsible for buoyancy effects will be taken into account, as a first approximation. In all other terms the variation of the density is neglected. The buoyancy term then, can be written as

$$f_i = \frac{\rho}{\rho_0} g_i. \quad (2.3)$$

The gravitational acceleration g_i only has a non-zero value $-g$ in the vertical direction. The density ρ_0 is defined at some reference temperature. Defining a hydrostatic case, the fluid being at rest and with constant density $\rho = \rho_0$, a hydrostatic pressure can be obtained. Employing the momentum equation for this situation, the hydrostatic pressure p_h may be calculated, according to

$$-\frac{1}{\rho_0} \frac{\partial p}{\partial x_i} + g_i = 0. \quad (2.4)$$

Integration with respect to x_3 , also denoted as z , yields $p_h = p_0 - \rho_0 g z$. If the hydrostatic part (2.4) is subtracted from the full momentum equation (2.2) a modified pressure and body force appears. If the density varies, the local difference in weight gives rise to a net forcing so that the gravitational force becomes apparent. In fact this is what is called buoyancy. Now the modified body force can be written as

$$f_i = \frac{\rho}{\rho_0} g_i - g_i = \frac{(\rho - \rho_0)}{\rho_0} g_i. \quad (2.5)$$

A further simplification is the linearization of the temperature dependency of the density, by expanding it into a Taylor series around the reference temperature T_0 (at which $\rho(T_0) = \rho_0$) and truncating after the second term. This yields

$$\rho = \rho_0 + (T - T_0) \left. \frac{\partial \rho}{\partial T} \right|_{T=T_0}. \quad (2.6)$$

By defining a coefficient of thermal expansion $\beta_0 = \beta(T_0)$ at constant pressure according to

$$\beta_0 = -\frac{1}{\rho_0} \left. \frac{\partial \rho}{\partial T} \right|_{T=T_0} \quad (2.7)$$

and substitution into the momentum equation the number of unknowns is extended to include the temperature as a new variable. An additional equation for the temperature is thus required to close the system. The set of assumptions to account for the variable density so far is often referred to as the "Boussinesq approximation", after *Boussinesq* [1903], although they were first used by *Oberbeck* [1879].

To determine the temperature as function of space and time the first law of thermodynamics is used. Denoting the conservation of energy e and neglecting viscous dissipation it reads

$$\frac{\partial e}{\partial t} + \frac{\partial}{\partial x_j} (u_j e) = -\frac{1}{\rho_0} \frac{\partial q_j''}{\partial x_j} + \frac{q'''}{\rho_0}, \quad (2.8)$$

with q_j'' the heat flux density vector and q''' a volume source. Fourier's constitutive law is used to relate the temperature gradient to the heat flux density by means of the thermal conductivity λ

$$q_j'' = -\lambda \frac{\partial T}{\partial x_j}. \quad (2.9)$$

Internal energy is defined as a function of basic thermodynamical quantities, $e = e(T, \rho, p)$, which remains constant in an isolated system. With the assumption of incompressibility it is a function of temperature only, as given by $\delta e = c_p \delta T$ (Batchelor [1967]), so that only an arbitrary reference level has to be chosen. The heat capacity at constant pressure is denoted by c_p .

Now the system of governing equations, i.e. the Navier-Stokes equations in Boussinesq form extended with the energy equation, becomes

$$\frac{\partial u_i}{\partial x_i} = 0; \quad (2.10)$$

$$\frac{\partial u_i}{\partial t} + \frac{\partial}{\partial x_j} (u_j u_i) = -\frac{1}{\rho_0} \frac{\partial p}{\partial x_i} + \nu_0 \frac{\partial^2 u_i}{\partial x_j \partial x_j} + \beta_0 (T - T_0) g \delta_{i3}; \quad (2.11)$$

$$\frac{\partial T}{\partial t} + \frac{\partial}{\partial x_j} (u_j T) = \kappa_0 \frac{\partial^2 T}{\partial x_j \partial x_j} + \frac{q'''}{\rho_0 c_{p0}}, \quad (2.12)$$

where $\kappa = \lambda/(\rho c_p)$ is the thermal diffusivity and δ is the Kronecker delta. The subscript $_0$ for fluid properties at the reference temperature shall be omitted in the rest of this thesis. For a more extended discussion of the Boussinesq approximation and an analysis of its validity the reader is referred to the literature e.g. Gray and Giorgini [1976] and Tritton [1988].

2.1.3 The non-dimensional formulation

With the aid of characteristic scales in the problem definition, it is possible to non-dimensionalize the governing equations. This is a favourable way of dealing with the problem because of the dynamic similarity, allowing us to scale the problem to any size. The length scale which is taken, is a characteristic length H of the geometry under consideration. Since all problems dealt with in this thesis

have in common that only volume heat sources are applied with one homogeneous direction, a heating rate per unit length is defined according to

$$q' = \iint q''' dA, \quad (2.13)$$

where the area A is defined as the total area perpendicular to the homogeneous direction. Now a characteristic temperature scale can be taken to be equal to q'/λ . Since the present work deals with natural convection only, there is no prescribed characteristic velocity scale in the problem. However, from balancing convection and diffusion in the energy equation a velocity scale can be derived to be $U = \kappa/H$. This is one of the possibilities to derive a velocity scale without *a priori* knowledge of it. Another possible way is balancing convection and diffusion of the momentum equations, but since $Pr = \mathcal{O}(1)$ this makes no real difference. Another frequently used velocity scale is obtained by balancing convection and buoyancy in the momentum equation, resulting in the Brunt-Väisälä velocity: $U = \sqrt{g\beta\Delta T H}$. Employing $U = \kappa/H$ it is possible to write the non-dimensional equations

$$\frac{\partial u_i^*}{\partial x_i^*} = 0; \quad (2.14)$$

$$\frac{\partial u_i^*}{\partial t^*} + \frac{\partial}{\partial x_j^*} (u_i^* u_j^*) = -\frac{\partial p^*}{\partial x_i^*} + Pr \frac{\partial^2 u_i^*}{\partial x_j^{*2}} + Ra Pr T^* \delta_{i3}; \quad (2.15)$$

$$\frac{\partial T^*}{\partial t^*} + \frac{\partial}{\partial x_j^*} (u_j^* T^*) = \frac{\partial^2 T^*}{\partial x_j^{*2}} + q''', \quad (2.16)$$

in which two dimensionless quantities Ra and Pr appear. The Rayleigh number is defined as

$$Ra = \frac{g\beta q' H^3}{\lambda \nu \kappa} \quad (2.17)$$

and the Prandtl number is given by

$$Pr = \frac{\nu}{\kappa}. \quad (2.18)$$

The Prandtl number, the ratio of viscosity to thermal diffusivity, is a property of the fluid. It can be seen easily that the combination $Ra Pr$ is a measure of the ratio of buoyancy forces and inertia forces. So when dealing with a fluid with given Prandtl number the Rayleigh number is a measure of the buoyant forcing of the flow.

The variables are scaled (non-dimensionalized) according to

$$x = Hx^*; u = \frac{\kappa}{H}u^*; t = \frac{H^2}{\kappa}t^*; p = \frac{\rho\kappa^2}{H^2}p^*; T = \frac{q'}{\lambda}T^*; q''' = \frac{q'}{H^2}q'''. \quad (2.19)$$

Note that with definition (2.13), and the scaling for the area, $A = H^2 A^*$, the dimensionless heating rate per unit length equals unity:

$$q^{l*} = \iint q^{l**} dA^* = \frac{\iint q^{l**} dA^*}{\iint q^{l**} dA^*} H^2 = \frac{\iint q^{l**} dA^*}{\iint q^{l**} dA^*} \frac{A^*}{A} H^2 = 1. \quad (2.20)$$

In the remaining part of this thesis the superscripts * will be omitted.

2.2 Routes to chaos and turbulence

As stated in the introduction (chapter 1), fluid flow can be characterized by its flow regime. The flow may be either laminar, turbulent or somewhere in between. The transition of one flow regime to another is called a bifurcation. The spectrum of flow regimes is distributed from laminar flow at low Reynolds or in this case Rayleigh number, up to fully developed almost homogeneous and isotropic turbulence at high forcing rates. In between there is a transition from laminar to time-dependent motion, and then in some complex way to turbulence. In the latter regime large, apparently irregular, fluctuations are present in both space and time. It is generally believed that all regimes are solutions of the Navier-Stokes equations and at the moment there is also numerical evidence for low forcing rates.

Strongly connected to the irregular motion in turbulent flow is its sensitivity to perturbations of the initial condition. This was first found by meteorologists, who noticed exponentially diverging numerical predictions, compared to observations. This phenomenon was already observed by *Poincaré* [1892] in his studies of the dynamics of celestial bodies. In these Hamiltonian systems there are no dissipative effects as is the case in Navier-Stokes dynamics. In the first half of this century the main effort was put into the development of statistical theories of homogeneous isotropic turbulent flow and the stability of laminar flows. To extend the insight in dynamical systems later on, the study of Hamiltonian systems got renewed attention. Especially the KAM theorem (after Kolmogorov, Arnol'd and Moser) gave insight in the conditions whether the motion is quasi-periodic or chaotic, see *Ottino* [1990].

In real hydrodynamics it was *Landau* [1944] who suggested to study the initiation of turbulent flow. He proposed a mechanism consisting of a sequence of bifurcations in which each time a discrete frequency is added. In general the ratio of separate frequencies is not integer and a quasi-periodic motion occurs. This leads to a turbulent flow with a broad band spectrum, consisting of an infinite number of discrete frequencies. In the phase space, i.e. the space of all independent variables ϕ , this corresponds to a torus of dimension equal to the number of frequencies.

If the Rayleigh number is below some critical value, Ra_{cr} , the motion is steady and stable, corresponding to a single point in phase space. Since the flow is stable

this point attracts all other points, initially deviating from the stable situation. Therefore this point in phase space is called an attractor. Above the critical Rayleigh number the flow becomes instationary, corresponding to an attracting closed orbit or a limit cycle. The limit cycle is purely periodic. This is called a Hopf bifurcation (*Hopf* [1942]). A Hopf bifurcation can be either supercritical or subcritical. The amplitude of the oscillations in case of a supercritical bifurcation satisfies the relation

$$\phi_{max} - \phi_{min} \propto \sqrt{Ra - Ra_{cr}} \quad (2.21)$$

(\propto means proportional to). In the case of a subcritical bifurcation the same behaviour is present only when the disturbances are large enough. There is an hysteresis effect: decreasing the Rayleigh number results in a behaviour as given by (2.21), but increasing Ra results in a behaviour like

$$\phi_{max} - \phi_{min} \propto \sqrt{Ra - Ra_{cr}} \cdot \mathbf{H}(Ra - Ra_p), \quad (2.22)$$

where \mathbf{H} denotes a Heavyside function and $Ra_p > Ra_{cr}$, its exact value depending on the disturbances present.

It was supposed that at a second critical Rayleigh number the limit cycle loses stability in the same way, leading to a second Hopf bifurcation. The attractor would now be a closed tube or a 2-torus. If the two frequencies have an integer ratio, the torus forms only a tangent plane to the orbit. Otherwise the frequencies are incommensurate and the flow is called to be quasi-periodic and fills the surface of the torus. Landau allowed an infinite number of subsequent Hopf bifurcations. Therefore this scenario is called the Landau-Hopf route to turbulence.

With the advent of the digital computer it became possible to do numerical simulations of the transition. One of the first simulations, that later received a wide attention, was the numerical simulation of transitional two-dimensional Rayleigh-Bénard convection, by *Lorenz* [1963]. He tackled the problem by using a streamfunction formulation, eliminating the continuity equation and the pressure from the momentum equation. Furthermore he used a highly truncated Fourier modes representation, reducing phase space to only three variables. Exceeding some critical Rayleigh number led to a strange pattern in phase space, that became known as Lorenz's butterfly. It consists of two foci. The orbit spirals outwards around a focus up to a certain moment at which it is more attracted to the other focus. The system is very sensitive to initial conditions. Hence it is impossible to predict at what instant the trajectory changes to another focus without knowing the equations and initial conditions. No limit cycles were found, causing the question of physical significance of the truncation. However, as described by *Miles* [1984], it can be proved that the equations used by Lorenz have a direct correspondence to a laboratory reproducible fluid system called the Howard-Malkus-Welander convection loop. It consists of natural convection of a fluid in a vertically oriented toroidal tube.

The study of Lorenz was a starting point of a large amount of research in the past decades, in the area of "chaos theory". Here chaos relates to non-periodic motion in time evolution, whereas turbulence could be defined as "spatio-temporal chaos". It is important to recognize the feature of sensitivity to initial conditions and the loss of predictability beyond a certain definite time horizon, as summarized very lucidly by *Lighthill* [1986].

In numerical or laboratory experiments the Landau-Hopf route was never found, after two or three independent frequencies the spectrum always shows broadband noise. Incommensurable frequencies do interact with each other, excluding the possibility of filling the spectrum without interaction. *Ruelle and Takens* [1971] showed that long before the appearance of infinite incommensurate frequencies the flow may be chaotic. They show that quasi-periodic flow on a 4-torus is not stable anymore and the phase space will consist of what they call a "strange attractor", some low-dimensional manifold in phase space, corresponding to turbulent motion. This means that after the fourth consecutive Hopf bifurcation the flow is turbulent and in the route to turbulence there may appear not more than three incommensurate frequencies.

In the experiments of *Gollub and Benson* [1980], for Rayleigh-Bénard convection in a confined flow domain, it has been observed that the Ruelle-Takens route to chaos (in the sense that there are only a small number of time dependent instabilities needed) is generally consistent with the observations. Furthermore they conclude that a diversity of processes is involved in transition to turbulent convection, but that relative simple mechanisms prevail (period doubling bifurcations, quasi-periodic motion and phase locking).

Two other routes are important to mention, for they both have also been measured. The first one is the period-doubling route of *Feigenbaum* [1978]. Here the first step is a Hopf bifurcation, succeeded by a period doubling bifurcation sequence. This scenario is followed by a spherical pendulum, also observed in the fluid experiments of *Gollub and Benson* [1980]. The second one is the intermittent scenario of *Pomeau and Manneville* [1980]. In this case the solution may alternate between a periodic limit cycle and a strange attractor. Intermittency is frequently observed in natural convection flows.

For more detailed information about chaos the reader is referred to the articles of *Lighthill* [1986] and *Miles* [1984] and to the book of *Bai-Lin* [1984], which contains a compilation of articles in the field.

2.3 Turbulence: length and time scales

With respect to the performance of physical and numerical experiments it is important to have some estimate of the relevant scales involved in the problem of interest. Especially resolution requirements are essential in order to determine the sampling rates and the size of the domain, both in space and time, in advance.

First it is necessary to have some characteristic velocity scale and a characteristic temperature scale. The mean velocity, in a spatial sense, for the flow configuration under consideration is zero, $U = 0$. Therefore it is necessary to have some information about the distribution in space as well as the fluctuations in time that are coupled through some advection velocity. Due to the nonlinearity in the momentum equation, kinetic energy is transferred from the large-scale velocity field to smaller scales down to some smallest viscous scale. A characteristic velocity and temperature scale may be obtained by a balance of the convection and source terms in both the momentum and energy equation, as given by

$$\left| \frac{\partial}{\partial x_j} (u_i u_j) \right| \sim |RaPrT|, \quad (2.23)$$

$$\left| \frac{\partial}{\partial x_j} (u_j T) \right| \sim |q'''|. \quad (2.24)$$

The dimensionless height and the integral of the heat flux over a plane perpendicular to the heat source direction are both taken equal to one. Then the characteristic velocity and temperature scales become

$$U' \sim (RaPr)^{1/3}, \quad (2.25)$$

$$T' \sim (RaPr)^{-1/3}. \quad (2.26)$$

With the macroscopic length scale $H = 1$, the macroscopic time scale for the velocity fluctuations becomes

$$\tau_B \sim H/U' = (RaPr)^{-1/3}. \quad (2.27)$$

To get some insight in the distribution of scales we may follow *Kolmogorov* [1941]. His approach consisted of a combination of the ideas of statistical physics, with the concept of dimensional analysis. First it is assumed that the turbulent fluid flow is in a state of statistical equilibrium. Furthermore Kolmogorov made the hypothesis that the small-scale motion is independent from the large scale motion. This means that the large scales and small scales are uncorrelated and this assumption can only be made if the Reynolds or Rayleigh number is high enough. In this case the statistics of the small scale motions of the turbulent fluid flow is independent of the large scales and therefore they are universal. An important statistical quantity of the small scale motions is the standard deviation or the mean square of the velocity differences in neighbouring points with mutual distance l , as given by $\langle \delta u(l)^2 \rangle$. Here the angular brackets denote a mean with respect to time.

The ideas of Kolmogorov were probably very much influenced by the picture of fluid turbulence as described already by *Richardson* [1922] in the form of a poem¹. The very extended footnote in *Kolmogorov* [1941] describes the same picture of the turbulent energy "cascade".

The idea of an equilibrium state is only meaningful if the statistical dynamics of the turbulence is governed by forcing at large scales and viscosity at small scales. Thus it is independent of the exact governing equations and the initial conditions. In order to determine the statistical state of fully developed turbulence *Kolmogorov* [1941] introduced the average rate of kinetic energy transfer, ϵ , between large scale motions and small scale motions in the inertial subrange, i.e. at wavenumbers where viscous dissipation is not yet effective. This amount of energy is transferred to smaller scales of motion, where at a certain range of wavenumbers the energy has to be dissipated. So the mean transfer of kinetic energy is equal to the mean dissipation of energy due to viscous stresses at the smallest scales of motion. Therefore the kinetic energy transfer, ϵ , and the diffusivity of momentum, Pr , are the characteristic quantities to describe the cascade down to the smallest dimensionless length scales, which are $(Pr^3/\epsilon)^{1/4}$ on average.

The main result is obtained for the mentioned mean square velocity fluctuations between points separated a distance l from each other, in the inertial subrange, also called the "structure function":

$$\langle \delta u(l)^2 \rangle \sim (\epsilon l)^{2/3}. \quad (2.28)$$

Following *Obukhov* [1941] this expression can also be written in the form of a power spectrum for the turbulent energy $E(k)$ as function of the wavenumber k , using the Wiener-Khintchine relation between correlations and power spectra. This yields

$$E(k) = C_k \epsilon^{2/3} k^{-5/3}, \quad (2.29)$$

where C_k is the Kolmogorov constant. The value of C_k was estimated to be $C_k \sim 1.5$ first by Kolmogorov himself, by using grid turbulence measurements. This value was confirmed by most later measurements although *Yaglom* [1985] suggests a value of $C_k \sim 2$, according to new available data, with an error not larger than 10-15%.

The mean kinetic energy transfer can be estimated using the characteristic buoyant velocity scale U' and the accompanying eddy-turnover time $l/U' \sim 1/U'$.

1

*Big whirls have little whirls,
That feed on their velocity;
And little whirls have smaller whirls
And so on to viscosity*

This results in a non-dimensional kinetic energy transfer with characteristic magnitude:

$$\epsilon \sim U'^3 \sim Ra Pr. \quad (2.30)$$

Now the relations for the small-scale length and time scales, also referred to as the Kolmogorov scales, become respectively

$$\eta \sim (Pr^2/Ra)^{1/4}, \quad (2.31)$$

and

$$\tau \sim Ra^{-1/2}. \quad (2.32)$$

With these relations of large and small scales, an estimation of the wavenumber and frequency range yields

$$\frac{H}{\eta} = \frac{1}{\eta} \sim (Ra/Pr^2)^{1/4}, \quad (2.33)$$

$$\frac{H/U'}{\tau} = \frac{1}{U'\tau} \sim (Ra/Pr^2)^{1/6}. \quad (2.34)$$

On the other hand, the exact dissipation of kinetic energy is defined by

$$\epsilon \equiv 2Pr \langle s_{ij} s_{ij} \rangle, \quad (2.35)$$

with

$$s_{ij} = \frac{1}{2} \left(\frac{\partial u'_i}{\partial x_j} + \frac{\partial u'_j}{\partial x_i} \right), \quad (2.36)$$

in which the fluctuating parts of the velocity components have to be used, and an overbar is used for denoting the mean in time. In the case that the turbulence is statistically isotropic, i.e. that the fluctuations have the same intensities in all directions, and with the use of the spatial correlation function, the Taylor microscale may be denoted as

$$\lambda = U' \left(\frac{15Pr}{\epsilon} \right)^{1/2} = \sqrt{15} \left(\frac{Pr^2}{Ra} \right)^{1/6}. \quad (2.37)$$

The Taylor microscale is mostly used by experimentalists. It was originally meant to give an estimation about the smallest eddies present, the length scale at which the dissipation takes place. However, it is just an average eddy size. Frequently the Reynolds number is based on the Taylor microscale

$$Re_\lambda = \frac{U'\lambda}{Pr} \sim \sqrt{15} \left(\frac{Ra}{Pr^2} \right)^{1/6}. \quad (2.38)$$

An extensive description of Kolmogorov theory, together with modern insights can be found in *Frisch* [1995].

2.4 Analytical results and literature

2.4.1 Similarity equations for the laminar boundary layer

In this section the idealized problem of a laminar flow generated by a horizontal line heat source in an infinite medium is discussed. In practice this flow would be approached by the flow arising from thin wires and long tubes that are heated. Here the derivation of *Gebhart et al.* [1988] will be followed. A numerical solution of the highly non-linear equations is obtained.

The governing non-dimensional continuity, momentum and energy equations are simplified by the boundary layer assumptions to yield the boundary layer approximation,

$$\frac{\partial w}{\partial z} + \frac{\partial u}{\partial x} = 0; \quad (2.39)$$

$$w \frac{\partial w}{\partial z} + u \frac{\partial w}{\partial x} = RaPrT + Pr \frac{\partial^2 w}{\partial x^2}; \quad (2.40)$$

$$w \frac{\partial T}{\partial z} + u \frac{\partial T}{\partial x} = \frac{\partial^2 T}{\partial x^2}. \quad (2.41)$$

These equations are solved by using a similarity variable $\eta(z, x)$, a streamfunction $\psi(z, x)$ (for which $w = \partial\psi/\partial x$ and $u = -\partial\psi/\partial z$) and a temperature corrected with the background as follows:

$$\begin{aligned} \eta(z, x) &= b(z)x; \\ \psi(z, x) &= c(z)f(\eta); \\ T(z, x) - T_\infty &= d(z)\phi(\eta), \end{aligned} \quad (2.42)$$

with f the similarity streamfunction and ϕ the similarity temperature. This leads to the set of equations given by

$$\begin{aligned} Pr f''' + \frac{c_z}{b} f f'' - \left(\frac{c}{b^2} b_z + \frac{c_z}{b} \right) f'^2 + RaPr \frac{d}{b^3 c} \phi &= 0; \\ \phi'' - \frac{cd_z}{bd} f' \phi + \frac{c_z}{b} f \phi' &= 0. \end{aligned} \quad (2.43)$$

The primes denote differentiation with respect to η and the subscript z denotes partial differentiation with respect to the vertical direction z .

The existence of a similarity solution now requires that the coefficients in the given set of equations are not z -dependent. This results in the solution

$$\begin{aligned} b(z) &= \frac{1}{z} \left(\frac{1}{4} RaPr d(z) z^3 \right)^{1/4}; \\ c(z) &= 4b(z)z; \\ d(z) &= Nz^n. \end{aligned} \quad (2.44)$$

Now the set of governing boundary layer equations can be written as

$$\begin{aligned} Pr f''' + (n+3)ff'' - (2n+2)f'^2 + \phi &= 0; \\ \phi'' - 4nf'\phi + (n+3)f\phi' &= 0. \end{aligned} \quad (2.45)$$

An additional requirement is given by the fact that the downstream buoyancy flux is equal to the heat input. The latter was scaled to unity, leading to

$$\int_{-\infty}^{+\infty} w(T - T_{\infty})dx = 1. \quad (2.46)$$

Thus, the downstream buoyancy flux does not depend on z . This leads respectively to

$$n = -\frac{3}{5}; \quad (2.47)$$

$$N = (4^3 I^4 Ra Pr)^{-1/5}. \quad (2.48)$$

The integral I has to be evaluated from the boundary layer solution, according to

$$I = \int_{-\infty}^{+\infty} f'(\eta)\phi(\eta)d\eta. \quad (2.49)$$

Using appropriate boundary conditions the boundary layer equations can now be solved. These conditions are given by the symmetry around $x = 0$, the definition of ϕ and the vanishing of w or T at $\eta \rightarrow \infty$ (since these are not independent), resulting in

$$f(0) = f''(0) = f'(\infty) = \phi'(0) = \phi(0) - 1 = 0. \quad (2.50)$$

The two-dimensional plume flow is specified and by numerical integration solutions can be obtained for $\phi(\eta)$, $f(\eta)$ and $f'(\eta)$ as function of Pr .

2.4.2 Solutions for the laminar boundary layer equations

The system of differential equations (2.45) together with the boundary conditions (2.50) were solved numerically by discretizing them on a finite difference grid. Central differences were used to obtain a second order spatial discretization. The highly non-linear system is linearized by Picard-linearization, i.e. discretizing the highest derivative at the previous iteration level. At each iteration level the system was solved using Gauss-Jordan elimination (*Press et al.* [1992]) for both the momentum and energy equations. The coupling terms, i.e. the dimensionless temperature in the momentum equation and the dimensionless streamfunction in the energy equation, were decoupled by taking them from the previous iteration level. The maximum difference between the solution at two subsequent iteration levels was used as a convergence criterion, both for the streamfunction f and

the temperature ϕ . Fastest convergence was found using an underrelaxation factor of 0.3. The convergence criterion was set to 10^{-6} and calculations were performed for $Pr = 0.71$ and 1.0 on the domain $\eta = [0, 10]$, and for $Pr = 5.0$ and 7.0 on $\eta = [0, 15]$ using 200 elements. In fact the number of elements and the domain was varied, leading to a verified accurate solution for the given values. Convergence tables are given in appendix A. Results for the streamfunction $f(\eta)$, the distribution of the vertical velocity component $f'(\eta)$ and the distribution of the temperature $\phi(\eta)$ are given in figures 2.1 and 2.2.

Indications of the thickness of the temperature and velocity boundary regions can be obtained by considering $\phi(\eta) = 0.05$ and $w/w_{max} = f'(\eta)/f'(0) = 0.05$. Numerical values of these quantities are given in table 2.1. For increasing Prandtl number the velocity layer becomes thicker. This may be expected because of the fact that Pr appears in front of the diffusive term in the momentum equation. On the contrary, the thermal boundary layer appears to be almost constant for all Prandtl numbers. In the case of air ($Pr = 0.71$) both boundary layers are of nearly the same thickness. In the full dimensional form as used by *Gebhart et al.* [1970] the Prandtl number appears in front of the nonlinear terms in the energy equation. In this case the velocity boundary layers have almost the same thickness and the temperature boundary layer becomes thinner with increasing Prandtl number. With the present scaling the quantity I is for all cases very near to unity.

Pr	$f'(0)$	$\eta_{\phi=0.05}$	$\eta_{f'/f'(0)=0.05}$	I	J
0.71	0.660	2.39	2.54	1.014	1.562
1.0	0.626	2.38	2.81	1.022	1.654
5.0	0.474	2.46	6.23	1.008	2.518
7.0	0.444	2.51	7.55	0.992	2.796

Table 2.1: Calculated similarity parameters

Now it is possible to calculate the relevant variables u , w and T with

$$\begin{aligned}
 u &= \frac{2}{5} (2I^{-1} Ra Pr)^{2/5} x z^{-4/5} f'(\eta) - \frac{3}{5} (4^3 I^{-1} Ra Pr)^{1/5} z^{-2/5} f(\eta); \\
 w &= (2I^{-1} Ra Pr)^{2/5} z^{1/5} f'(\eta); \\
 T - T_{\infty} &= (4^3 I^4 Ra Pr)^{-1/5} z^{-3/5} \phi(\eta).
 \end{aligned} \tag{2.51}$$

By defining

$$J = \int_{-\infty}^{+\infty} f' d\eta, \tag{2.52}$$

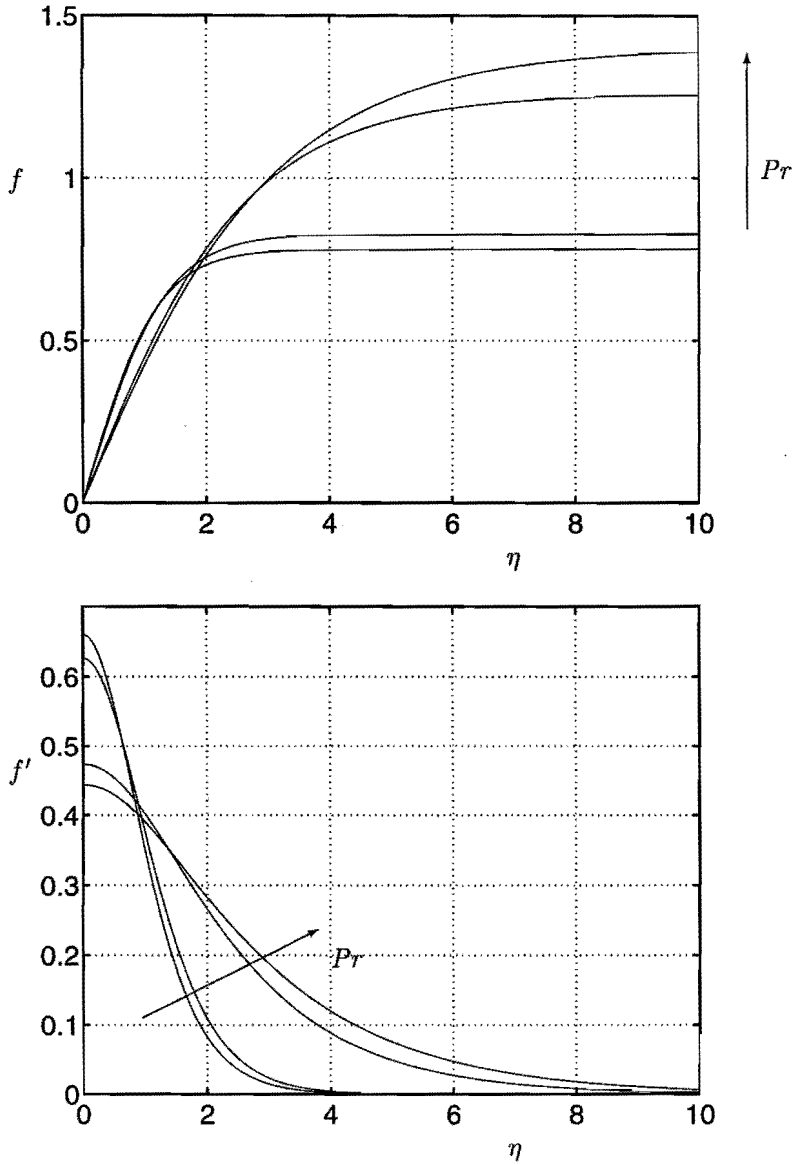


Figure 2.1: Calculated similarity streamfunction (top) and velocity profiles (bottom)

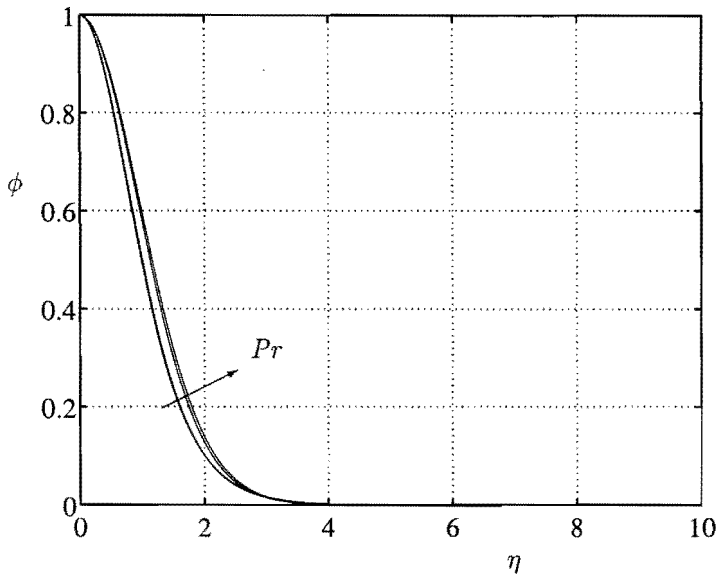


Figure 2.2: Calculated similarity temperature profiles

of which the value is given in table 2.1, the flow rate in the plume can be determined.

Experimental studies reviewed by *Jaluria* [1985] were compared with the solution as obtained by *Gebhart* using the full dimensional boundary layer equations. They show a maximum temperature of 15-20 percent lower than the theoretically predicted centreline temperature. It is suggested that the difference is due to scattering of data caused by a slightly swaying motion of the plume. Of course, the laminar downstream part of the plume will always be influenced by the turbulent upstream part. The influence may be either direct or due to the confinement of the flow. The latter leads to an interaction with the not yet fully died out turbulence that is advected to the heat source.

Another point is the theoretically considered region $z \geq 0$ which implies no entrainment from below the source. If a horizontal plate is placed to obstruct entrainment from below, the centreline temperature has been observed to rise. A complication that arises here however is the introduction of a no-slip condition at the plate surface.

2.4.3 Stability of laminar plumes

The hydrodynamic stability of the laminar plume induced by a horizontal line source of heat was investigated by *Pera and Gebhart* [1971]. Since two-dimensional disturbances are the least stable they considered only two-dimensional distur-

bances for the temperature distribution and the streamfunction superimposed upon the parallel base flow.

From the inviscid solution it was found that the flow was much less stable for asymmetric disturbances than it was for symmetric ones. Low frequency disturbances were found to yield an unstable flow. These disturbances are strongly amplified downstream. At sufficiently high frequency ($f > 15$ Hz for $Pr=0.7$) disturbances are always damped. In experiments, also performed by *Pera and Gebhart* [1971], it was found that disturbances with frequencies higher than about 12 Hz were not detected downstream, disturbances of lower frequencies gave amplification. Total disruption of the flow happened at a shorter distance of the source with decreasing disturbance frequency.

In experiments without artificially imposed disturbances *Bill Jr. and Gebhart* [1975] found that the end of the transitional region is positioned at a height $z = (3 \cdot 10^8)^{5/12} 4^{-5/4} I^{-5/3} Ra^{-1/3} Pr^{1/2}$. The transition was defined by a criterion based on visual inspection of the flow (interferometry) along with the maximum instantaneous mid-plane temperature. Such a criterion was found to be necessary due to the fact that not all observed flow fluctuations may be associated with turbulence. The beginning of the transition could not be determined that accurately due to the intermittency, together with an insufficient control of boundary conditions.

2.4.4 Turbulent plume: an integral model

In an integral model the momentum and buoyancy equations are averaged over the plume cross section. Furthermore an entrainment assumption is used as described by *Turner* [1986]. Additionally a hypothetical profile is taken for vertical velocity and temperature. Then, in the two-dimensional case, the vertical momentum equation for the time-mean components can be written as

$$\frac{\partial}{\partial x}(uw) + \frac{\partial}{\partial z}w^2 = RaPrT. \quad (2.53)$$

By integration over a horizontal plane $z = C$ the first term vanishes because of symmetry, leading to

$$\frac{\partial}{\partial z} \int_{-\infty}^{+\infty} w^2 dx = RaPr \int_{-\infty}^{+\infty} T dx. \quad (2.54)$$

In the same way the energy equation becomes

$$\frac{\partial}{\partial z} \int_{-\infty}^{+\infty} wT dx = 0. \quad (2.55)$$

Integrating the continuity equation over the same plane relates the vertical plume velocity w to the entrainment velocity u_∞ :

$$\int_{-\infty}^{+\infty} \frac{\partial u}{\partial x} dx + \int_{-\infty}^{+\infty} \frac{\partial w}{\partial z} dx = u|_{-\infty}^{+\infty} + \frac{\partial}{\partial z} \int_{-\infty}^{+\infty} w dx, \quad (2.56)$$

resulting in

$$\frac{\partial}{\partial z} \int_{-\infty}^{+\infty} w dx = 2u_\infty. \quad (2.57)$$

If it is assumed that the distributions of velocity and temperature have a Gaussian distribution with different widths, according to

$$w = w_c e^{-x^2/b^2}; \quad T = T_c e^{-\beta_T x^2/b^2}, \quad (2.58)$$

the plane integrated quantities become

$$\begin{aligned} \int_{-\infty}^{+\infty} w^2 dx &= \sqrt{\frac{\pi}{2}} w_c^2 b; \\ \int_{-\infty}^{+\infty} w T dx &= \sqrt{\frac{\pi}{\beta_T + 1}} w_c T_c b; \\ \int_{-\infty}^{+\infty} w dx &= \sqrt{\pi} w_c b; \\ \int_{-\infty}^{+\infty} T dx &= \sqrt{\frac{\pi}{\beta_T}} T_c b. \end{aligned} \quad (2.59)$$

To close the equations an entrainment hypothesis may be used that prescribes the inflow in the plume. In turbulent conditions a linear spread of the plume width with height is commonly observed. Thus it follows that a suitable entrainment hypothesis is given by a constant ratio α of time mean entrainment velocity to vertical velocity at the core

$$u_\infty = \alpha w_c. \quad (2.60)$$

The set of equations now becomes

$$\begin{aligned} \frac{\partial}{\partial z} (\sqrt{\pi} w_c b) &= 2\alpha w_c; \\ \frac{\partial}{\partial z} \left(\sqrt{\frac{\pi}{2}} w_c^2 b \right) &= Ra Pr \sqrt{\frac{\pi}{\beta_T}} T_c b; \\ \frac{\partial}{\partial z} \left(\sqrt{\frac{\pi}{\beta_T + 1}} T_c w_c b \right) &= 0. \end{aligned} \quad (2.61)$$

Incorporation of the conservation of mass of the above set of equations into the momentum equation yields an equation relating w_c to T_c . This can be solved by using the buoyancy flux, leading to a second equation for w_c and T_c ,

$$\int_{-\infty}^{+\infty} wT dx = \sqrt{\frac{\pi}{\beta_T + 1}} w_c T_c b = 1. \quad (2.62)$$

The solution for w_c becomes

$$w_c = \frac{1}{2} \sqrt{2} \alpha^{-1/3} \left(\frac{\beta_T + 1}{\beta_T} \right)^{1/6} (RaPr)^{1/3}, \quad (2.63)$$

so that

$$\frac{\partial w_c}{\partial z} = 0. \quad (2.64)$$

This leads to the solution of the Gaussian integral entrainment model for a plane turbulent plume,

$$\begin{aligned} b &= \frac{2\alpha}{\sqrt{\pi}} z; \\ w &= \frac{1}{2} \sqrt{2} \alpha^{-1/3} \left(\frac{\beta_T + 1}{\beta_T} \right)^{1/6} (RaPr)^{1/3} e^{-(x/b)^2}; \\ T &= \frac{1}{2} \sqrt{2} \alpha^{-2/3} \beta_T^{1/6} (\beta_T + 1)^{1/3} (RaPr)^{-1/3} z^{-1} e^{-\beta_T(x/b)^2}. \end{aligned} \quad (2.65)$$

2.4.5 Turbulent plume measurements

From experimental observations, as found in the literature, α and β_T can be estimated. In full dimensions the specific buoyancy flux is the relevant scaling factor. It is defined by

$$B = \frac{g\beta q'}{\rho c_p} = RaPr \left(\frac{\kappa}{H} \right)^3. \quad (2.66)$$

The first important measurements were performed by *Rouse et al.* [1952]. These experiments were conducted in air, using gas burners as a heat source ("yielding low, blue flames"). The experimental results were obtained using a vane anemometer for determination of the velocity and copper-constantan thermocouples for the temperature. They found for the dimensional time mean velocity and temperature profiles the following relations

$$\begin{aligned} w &= k_w B^{1/3} e^{-32(x/b)^2}; \\ T &= k_T B^{-1/3} z^{-1} e^{-41(x/b)^2}, \end{aligned} \quad (2.67)$$

with $k_w = 1.80$ and $k_T = 2.60$. Combination of these results with those obtained by the entrainment model does not lead to a consistent set of α and β_T values.

Deriving them on the basis of the exponents, values of 0.157 and 1.281 are obtained, respectively. Using these values to calculate k_w and k_T yields $k_w = 1.44$ and $k_T = 3.34$. Both the model and the measurements are expected to suffer from inaccuracies, resulting in the discrepancy.

Kotsovinos [1975] determined the mean midplane velocities for turbulent plane buoyant water plumes, using laser doppler anemometry. In his measurement the plume flow was created by releasing low density water from a slit in an environment at reference density. A value of $k_w = 1.66$ was obtained. Later on *Kotsovinos and List* [1977] measured k_T to be equal to 2.4.

It can be concluded that with the data of the cited measurements a consistent determination of the values of α and β_T is not possible yet. Furthermore the domains in which the values of k_w and k_T are located are rather large, covering the range $k_w = 1.4 - 1.8$ and $k_T = 2.4 - 3.3$.

Furthermore *Kotsovinos* found for the fluctuations both for the temperature and vertical velocity, $\sqrt{T'^2}/\bar{T}$ and $\sqrt{w'^2}/\bar{w}$, a maximum value of 0.4 in the central region of the plume.

Reviews of turbulent jets and plumes can be found in *List* [1982] and *Rodi* [1982]. More recent research advances are published in *Davies and Valente Neves* [1994].

Chapter 3

Direct and large-eddy numerical simulation

3.1 Direct numerical simulation

With an increase of the forcing of the flow the kinetic energy spectrum broadens. This means that kinetic energy is cascaded to smaller and smaller eddies. The computational grid must be refined enough to resolve the smallest occurring spatial modes. Using a kinetic energy conserving scheme on a grid that is too coarse for this would introduce so-called aliasing errors. It leads to an accumulation of kinetic energy at wavenumbers corresponding to the mesh size. Hence, for high forcing rates the flow cannot be resolved anymore on a given computational grid, within an acceptable computational storage or computing time.

The computational grid must be refined in order to capture even the smallest length scales with sufficient accuracy. With the wavenumber also the sampling frequency increases. At the same time, both from a physical and a numerical point of view, the time-step has to be decreased.

The ranges in physical length and time scales have been estimated in equations (2.33) and (2.34). For a three-dimensional computation this leaves us with a core storage in words that is proportional to

$$M \propto (Ra/Pr^2)^{3/4}. \quad (3.1)$$

The total amount of computational work to obtain a physical description of the turbulence is proportional to

$$W \propto (Ra/Pr^2)^{11/12}. \quad (3.2)$$

For natural convective flows, the computational work does not increase as fast as in the case of forced convection where it is given by $W_f \propto Re^{11/4}$. However, in terms of power-supply the scaling is similar. The velocity, as used in the definition

of the Reynolds number, scales with the cubic root of the power supplied in the turbulent case as given for example by 2.65. Thus both relations show an identical behaviour.

From a phenomenological point of view there are some differences between forced convection and natural convective flows. Natural convection tends to fill its available space on every scale. All sizes of eddies tend to be uniformly distributed, whereas in forced convective flows regions of increasing shear and vorticity are distributed more and more sparse.

As will be outlined in the discretization section of this chapter the temporal numerical sampling rate is higher than the largest physical frequencies. This is necessary in order to maintain a numerically stable integration process.

3.2 Large-Eddy simulation

3.2.1 Introduction

In large-eddy simulation subgrid advection is lumped into nonlinear grid scale diffusion by a model. In this way the spatial resolution is decreased and with it also the temporal resolution. This leads to a substantial decrease in both computational storage and work.

To cut off the highest wavenumbers (and thus frequencies) the governing equations have to be filtered with a spatial filter to obtain a set of equations for the grid scale variables, that can reasonably be discretized. By performing the filtering operation extra terms appear, accounting for the subgrid contributions. The subgrid contributions are unknown in principle and therefore they have to be modelled. The model should be denoted in terms of known, grid scale variables to close the system of equations. It should mimic the kinetic energy drain from grid scale to subgrid scale wavenumbers in a satisfying way. There should be no excessive accumulation or drain of kinetic energy at the end of the resolved spectrum. Furthermore the physical cascading process should be approximated as close as possible.

3.2.2 The filtering procedure

The basis of the theory of large-eddy simulation consists of the application of a spatial convolution filter to the governing equations. This procedure splits a generic turbulent variable f into a large scale, or grid scale component \bar{f} that can be resolved, and a small scale or subgrid component f' . The subgrid component is a spatial fluctuation around the spatially varying grid scale component. The decomposition and the convolution of f with a filter function g over the flow domain Ω are given by

$$f(x_i, t) = \bar{f}(x_i, t) + f'(x_i, t) \quad (3.3)$$

and

$$\bar{f}(x_i, t) = \int_{\Omega} g(x_i - x'_i) f(x'_i, t) dx'_i, \quad (3.4)$$

or in spectral space (in which a function denoted by a capital is the Fourier transform of the lower case denoted function) $\bar{F}(k_i, t) = G(k_i)F(k_i, t)$. The filter function g has to satisfy the normalization condition, so that the filtered variable is not amplified or damped, $\int_{\Omega} g(x_i - x'_i) dx'_i = 1$.

It is also possible to average a quantity over a fixed volume cell. In contrast to the use of the convolution filter procedure the quantity will be piecewise constant within each grid cell. This method was used by *Deardorff* [1970] and *Schumann* [1975] and may have some advantages as will be explained further on. The method will be referred to as the "volume balance method", as it was called by Schumann.

Leonard [1974] gives some examples of the most important filters. The filters with characteristic widths Δ are the top-hat filter or (continuous) volume average filter,

$$g(x_i - x'_i) = \begin{cases} 1/\Delta & \text{if } |x_i - x'_i| < \Delta/2; \\ 0 & \text{otherwise} \end{cases}, \quad (3.5)$$

the Gaussian filter,

$$g(x_i - x'_i) = \sqrt{\frac{6}{\pi\Delta^2}} e^{-6(x_i - x'_i)^2/\Delta^2} \quad (3.6)$$

and the sharp Fourier cut-off filter,

$$g(x_i - x'_i) = \frac{2 \sin(\pi(x_i - x'_i)/\Delta)}{\pi(x_i - x'_i)}. \quad (3.7)$$

The Fourier cut-off filter is a top-hat filter in wavenumber space, that is why the attributive "sharp" is frequently used. This filter thus filters out the high wavenumbers abruptly from a certain cut-off wavenumber without disturbing the low wavenumber contents. The Fourier transform of a Gaussian filter is also a Gaussian, whereas the transformed top-hat filter has the form of the Fourier filter in the physical domain. Because of the fact that the kernels of the Gaussian filter and especially the Fourier filter are not limited, application of these filters in physical space is very time consuming. In spectral space the Fourier filter has a discretely limited kernel and is easy to adopt.

The top-hat filter is implicitly applied by finite difference operators as in the present work. *Rogallo and Moin* [1984] show that the derivative of a continuous function, $f(x)$, evaluated with standard second order finite differences is equal to the derivative of this function filtered with a top-hat kernel, according to

$$\frac{\partial \bar{f}}{\partial x} = \frac{\partial}{\partial x} \left\{ \frac{1}{\Delta} \int_{x-\frac{1}{2}\Delta}^{x+\frac{1}{2}\Delta} f(x') dx' \right\} = \frac{f(x + \frac{1}{2}\Delta) - f(x - \frac{1}{2}\Delta)}{\Delta}. \quad (3.8)$$

This means that small scale variations f' , as defined by top-hat filtering, are implicitly filtered out by the finite difference operator.

If the filter is symmetric and if it possesses the property of having a constant filter width, it can be shown that the commutative property of the filtering process with respect to space and time holds, i.e.

$$\overline{\frac{\partial f}{\partial x_i}} = \frac{\partial \bar{f}}{\partial x_i}; \quad \overline{\frac{\partial f}{\partial t}} = \frac{\partial \bar{f}}{\partial t}. \quad (3.9)$$

The filtering operation is linear, i.e. $\overline{f_1 + f_2} = \bar{f}_1 + \bar{f}_2$ and $\overline{\alpha f} = \alpha \bar{f}$. For the top-hat filter the inequalities

$$\overline{\bar{f}} \neq \bar{f}; \quad \overline{f'} \neq 0 \quad (3.10)$$

hold, the second derived from the first with the aid of (3.3). In the case of adoption of a sharp cut-off filter, or a volume balance method these inequalities turn into equalities, which may be regarded as advantageous. This will be shown in the next section. Application of the filtering operation (3.4) to the governing equations and assuming that both the large scale and filtered subgrid scale contributions of the continuity equation are solenoidal, yields for the evolution of the large scales

$$\frac{\partial \bar{u}_i}{\partial x_i} = 0; \quad (3.11)$$

$$\frac{\partial \bar{u}_i}{\partial t} + \frac{\partial}{\partial x_j} (\overline{u_i u_j}) = -\frac{\partial \bar{p}}{\partial x_i} + Pr \frac{\partial^2 \bar{u}_i}{\partial x_j^2} + Ra Pr \bar{T} \delta_{i3}; \quad (3.12)$$

$$\frac{\partial \bar{T}}{\partial t} + \frac{\partial}{\partial x_j} (\overline{u_j T}) = \frac{\partial^2 \bar{T}}{\partial x_j^2} + q'''. \quad (3.13)$$

3.2.3 Subgrid-scale stresses and fluxes

Definition of subgrid stresses and fluxes

A discrete approximation of the equations for the large scale motion may be adopted to simulate the flow. Yet, the terms $\overline{u_i u_j}$ and $\overline{u_j T}$ can not be evaluated directly. These terms can be unraveled to yield

$$\overline{u_i u_j} = \bar{u}_i \bar{u}_j + (\overline{u_i u_j} - \bar{u}_i \bar{u}_j); \quad (3.14)$$

$$\overline{u_j T} = \bar{u}_j \bar{T} + (\overline{u_j T} - \bar{u}_j \bar{T}). \quad (3.15)$$

Now the first term on the right hand side is the new resolved non-linear term. The second terms are the subgrid stresses and fluxes, respectively. They are unknown and will be subjected to parameterization to close the system of equations.

First the subgrid stresses will be discussed as given by

$$\tau_{ij} = \overline{u_i u_j} - \bar{u}_i \bar{u}_j. \quad (3.16)$$

By virtue of the decomposition 3.3 these stresses can be recast in the form

$$\tau_{ij} = \overline{u_i u_j} - \bar{u}_i \bar{u}_j = L_{ij} + C_{ij} + R_{ij}, \quad (3.17)$$

with the Leonard stresses (L_{ij}), which consist of fully resolved quantities, the cross stresses (C_{ij}) and the Reynolds subgrid scale stresses (R_{ij}), which are defined by

$$L_{ij} = \overline{\bar{u}_i \bar{u}_j} - \bar{u}_i \bar{u}_j; \quad (3.18)$$

$$C_{ij} = \overline{\bar{u}_i u'_j} + \overline{u'_i \bar{u}_j} \quad (3.19)$$

and

$$R_{ij} = \overline{u'_i u'_j}. \quad (3.20)$$

The subgrid fluxes are defined by

$$h_j = \overline{u_j T} - \bar{u}_j \bar{T}. \quad (3.21)$$

This expression can also be split into resolved, cross and Reynolds fluxes, respectively.

With the definitions of τ_{ij} and h_j the governing equations for the large scale motion become

$$\frac{\partial \bar{u}_i}{\partial x_i} = 0; \quad (3.22)$$

$$\frac{\partial \bar{u}_i}{\partial t} + \frac{\partial}{\partial x_j} (\bar{u}_i \bar{u}_j) = -\frac{\partial \bar{p}}{\partial x_i} + Pr \frac{\partial^2 \bar{u}_i}{\partial x_j^2} + Ra Pr \bar{T} \delta_{i3} - \frac{\partial \tau_{ij}}{\partial x_j}; \quad (3.23)$$

$$\frac{\partial \bar{T}}{\partial t} + \frac{\partial}{\partial x_j} (\bar{u}_j \bar{T}) = \frac{\partial^2 \bar{T}}{\partial x_j^2} + \bar{q}''' - \frac{\partial h_j}{\partial x_j}. \quad (3.24)$$

Interpretation and modelling consequences

If a sharp Fourier cut-off filter is applied, or in a volume balance method, the relation $\overline{\bar{f}} = \bar{f}$ holds. Substitution of this expression in the filtered decomposition (3.3) would yield $\bar{f}' = 0$. Thus both the Leonard stresses and the cross stresses would be equal to zero. However, the filtering operation is applied implicitly. The contribution of subgrid stresses that have to be modelled depends on a hypothetical filter definition.

As can be observed from (3.18), in principal the Leonard stresses have nothing to do with "subgrid" contributions. With the aid of the theory of homogeneous isotropic turbulence *Leonard* [1974] estimated its value by assuming that a non-sharp convolution filter is employed (i.e. the top-hat or Gaussian filter). The result is given by $L_{ij} \sim \frac{\Delta^2}{24} \frac{\partial^2}{\partial x_j^2} \bar{u}_i \bar{u}_j + \mathcal{O}(\Delta^4)$. Then a tentative lower bound for the additional accompanying energy drain was estimated to be about $30 \pm 10\%$ of the total kinetic energy dissipation. Because of the second order behaviour of

the Leonard term it is expected to be of equal magnitude as the truncation error, $\mathcal{O}(\Delta^2)$ in a second order discretization.

On the one hand this conclusion pleads for an explicit evaluation of the Leonard stresses. On the other hand *Speziale* [1985] has shown that the Leonard stresses and cross stresses are not Galilean invariant. This is contradicting the basics of turbulence theory in which the description of the fluctuations is independent of any reference frame of linear uniform motion.

The effects of inclusion of the Leonard term were studied by *Antonopoulos-Domis* [1981], using a staggered grid as employed in the present thesis. He found that instead of draining kinetic energy from the largest resolved scales, the effect of the Leonard term was a backscatter from the high resolved wave numbers to smaller ones. This was also found to be true for scalar variance.

In the present work the total of the composing stresses of τ_{ij} will be subjected to parametrization, omitting the explicit effect of the Leonard terms, as is usually the case. From now on τ_{ij} and h_j will simply be called subgrid stresses and fluxes. The closures used to model the contributions of the subgrid stresses and fluxes in terms of the resolved quantities are formulated in the next sections. Recent investigations concerning the filtering approach and the handling of subgrid stresses are presented in *Germano* [1990] and *Germano* [1992].

3.2.4 Kinetic energy transfer

In this section a closer look is taken at the kinetic energy of the flow in order to study the energy drain. An equation for the transport of kinetic energy of the resolved scales,

$$\bar{e} = \frac{1}{2} \bar{u}_i \bar{u}_i, \quad (3.25)$$

can be obtained from multiplication of the momentum equation (3.23) by the resolved velocity \bar{u}_i . With the identity $\tau_{ij} = \tau_{ji}$ and the deformation rate tensor of the resolved scales (which is also symmetrical),

$$\bar{S}_{ij} = \frac{1}{2} \left(\frac{\partial \bar{u}_i}{\partial x_j} + \frac{\partial \bar{u}_j}{\partial x_i} \right), \quad (3.26)$$

the subgrid scale contribution to the large scale motion can be written as

$$-\bar{u}_i \frac{\partial \tau_{ij}}{\partial x_j} = -\frac{\partial}{\partial x_j} (\bar{u}_i \tau_{ij}) + \tau_{ij} \bar{S}_{ij}. \quad (3.27)$$

This yields for the kinetic energy of the resolved scales:

$$\begin{aligned} \frac{\partial \bar{e}}{\partial t} + \frac{\partial}{\partial x_j} (\bar{u}_j \bar{e}) &= -\frac{\partial \bar{u}_i \bar{p}}{\partial x_i} + Pr \frac{\partial^2 \bar{e}}{\partial x_j^2} - Pr \left(\frac{\partial \bar{u}_i}{\partial x_j} \right)^2 \\ &\quad + Ra Pr \bar{u}_i \bar{T} \delta_{i3} - \frac{\partial}{\partial x_j} (\bar{u}_i \tau_{ij}) + \tau_{ij} \bar{S}_{ij}. \end{aligned} \quad (3.28)$$

The first term on the right-hand side of (3.27) redistributes kinetic energy. Therefore the second term has to account for the kinetic energy transfer over the cut-off, i.e. the subgrid scale dissipation $-\epsilon(k_c) = \tau_{ij}\bar{S}_{ij}$. The mean interscale kinetic energy transfer over the cut-off is from small to large wavenumbers. Locally, both in space and time, there may be a transfer of kinetic energy from the small scales to the large scales. This phenomenon is called "backscatter". Especially in two-dimensional flows the transfer of kinetic energy is towards the large scales of motion, resulting in a so-called inverse energy cascade, see *Kraichnan* [1976].

In plume flows this phenomenon might also be important. In a plume the vertical component of the velocity is the largest and attains a local maximum. This holds both for a laminar and for a turbulent time mean plume flow. Furthermore, in a laminar plume the flow accelerates downstream. This will also be the case in a fluctuating turbulent plume at a significant number of locations, as the mean upward turbulent plume flow is constant. Recognizing that the main contribution to the subgrid scale dissipation in the plume is provided by the vertical component reveals the importance of backscatter in this situation. It is given by

$$\tau_{33}\bar{S}_{33} = \left(\overline{u_3^2} - \bar{u}_3^2\right) \frac{\partial \bar{u}_3}{\partial x_3}, \quad (3.29)$$

with both $\overline{u_3^2} > \bar{u}_3^2$, and $\partial \bar{u}_3 / \partial x_3 > 0$. Thus for these locations a positive source term for the resolved kinetic energy is provided.

An equation similar to (3.28) can be derived for the transport of filtered subgrid scale energy, $e_{sgs} = \frac{1}{2}\overline{u'_i u'_i}$. Subtracting the resolved momentum equation from the full momentum equation and multiplying it by u'_i gives

$$\begin{aligned} \frac{\partial e_{sgs}}{\partial t} + \frac{\partial}{\partial x_j} (\bar{u}_j e_{sgs}) &= -\frac{\partial \overline{u'_i p'}}{\partial x_i} + Pr \frac{\partial^2 e_{sgs}}{\partial x_j^2} - Pr \overline{\left(\frac{\partial u'_i}{\partial x_j}\right)^2} \\ &\quad + Ra Pr \overline{u'_i T'} \delta_{i3} - \frac{\partial}{\partial x_j} \left(\frac{1}{2} \overline{u'_i u'_i u'_j}\right) - \tau_{ij} \bar{S}_{ij}. \end{aligned} \quad (3.30)$$

Most terms in this equation are again of a redistributing kind. Here the subgrid scale dissipation appears with opposite sign in comparison with the same term in the equation for resolved kinetic energy. In this equation it is a production term fed by the large scales motion. The third term on the right hand side is responsible for the viscous dissipation of kinetic energy.

Several researchers investigated the value of the subgrid scale dissipation $\epsilon(k_c)$ as obtained by direct numerical simulations. Amongst them *Piomelli et al.* [1991] found that the energy transfer upscale and downscale have almost the same values. They also found that these values were large compared to the viscous dissipation. Recently *Domaradzki et al.* [1994] studied the energy transfer between wavenumbers in turbulent channel flow. They found that the main energy transfer is between successive octave bands, i.e. between $\frac{1}{2}k_c < k < k_c$ and $k_c < k < 2k_c$.

Additionally it is well known that kinetic energy transfer can have very large spatial variations. Another fact is that the viscous energy drain occurs in very localized vortical regions as already remarked by *Taylor* [1935].

3.3 Subgrid-scale models

3.3.1 Introduction

Most subgrid scale models have been developed from the viewpoint of forced, fully developed, turbulent convection. The parametrization of the subgrid scale stresses is usually based on the Kolmogorov spectrum. The main assumptions for the parametrization as used in the present work are summarized here.

First the subgrid scale stresses are decomposed into an isotropic and a deviatoric part, resulting for the deviatoric part in

$$\tau_{ij}^d = \tau_{ij} - \tau_{ij}^i = \tau_{ij} - \frac{1}{3}\tau_{kk}\delta_{ij}. \quad (3.31)$$

The isotropic part does not give rise to any deformation. So the subgrid isotropic stress leads to a grid scale pressure rise that is recombined with the resolved specific pressure. The parametrization is applied to the deviatoric part of the subgrid scale stress tensor. The notation for the modification of the pressure and stresses will be omitted.

As a first step to model the subgrid scale stresses a gradient diffusion form hypothesis will be exploited. In this way an eddy viscosity model arises, similar to the Newtonian molecular diffusion:

$$\tau_{ij} = -2K_m \bar{S}_{ij}, \quad (3.32)$$

with K_m the eddy viscosity. Subgrid convection is lumped to grid scale dissipation. The parametrization is shifted from the stresses to the eddy viscosity. Here it can directly be observed that a positive definite K_m yields a positive definite kinetic energy transfer to the subgrid scales. Thus, it always removes kinetic energy from the resolved scales to account for the hypothesized dissipation. In a similar way an eddy diffusivity K_h is defined (analogous to Fourier's law) as

$$h_j = -K_h \frac{\partial \bar{T}}{\partial x_j}. \quad (3.33)$$

It is assumed that the subgrid heat fluxes behave in a similar way as the stresses do. Subgrid advection is lumped to grid scale diffusion at a rate proportional to the dissipation. This requires the introduction of a turbulent Prandtl number Pr_t defined by

$$Pr_t = \frac{K_m}{K_h}. \quad (3.34)$$

In contrast to the molecular Prandtl number, which is a property of the fluid, the turbulent Prandtl number is a property of the flow. On the basis of several publications *Eidson* [1985] observed that the turbulent Prandtl number was mostly chosen in the range $\frac{1}{3} < Pr_t < \frac{1}{2}$. Most of these publications dealt with relative high Rayleigh numbers and it is not clear what the value should be at low turbulence intensities. From Reynolds-averaged $k - \epsilon$ turbulence modelling it is observed that $Pr_t \approx 0.9$, even for low Reynolds number models (see e.g. *Henkes* [1990]).

In the description of the Navier-Stokes equations in the previous chapter a Newtonian fluid with constant viscosity and diffusivity was assumed. With this assumption the diffusion parameters could be taken out of the differencing operation of the viscous stresses and conductive heat fluxes. Zero divergence then led to the form as presented in chapter 2. Now the coefficients are not constant any longer and we must use the original stress and heat flux formulation. Incorporation of the eddy viscosity and eddy diffusivity concept, yields for the diffusive terms in the momentum and energy equation respectively

$$Pr \frac{\partial^2 \bar{u}_i}{\partial x_j^2} - \frac{\partial \tau_{ij}}{\partial x_j} = 2 \frac{\partial}{\partial x_j} ((Pr + K_m) \bar{S}_{ij}); \quad (3.35)$$

$$\frac{\partial^2 \bar{T}}{\partial x_j^2} - \frac{\partial h_j}{\partial x_j} = \frac{\partial}{\partial x_j} \left(1 + \frac{K_m}{Pr_t} \right) \frac{\partial \bar{T}}{\partial x_j}. \quad (3.36)$$

Models for the parametrization of K_m as used in the present work are discussed in the next sections. Another point of view to be mentioned is the direct modelling of τ_{ij} by means of resolved stresses, at a slightly larger scale than the cut-off scale. The most important model in this class is the scale similarity model of *Bardina et al.* [1984].

3.3.2 Smagorinsky model

In statistical equilibrium the drain of kinetic energy over the cut-off wavenumber k_c is constant if k_c is in the inertial range. This kinetic energy transfer is given by

$$-\epsilon(k_c) = \tau_{ij} \bar{S}_{ij} = -2K_m \bar{S}_{ij} \bar{S}_{ij}. \quad (3.37)$$

On the basis of dimensional arguments the Smagorinsky model (*Smagorinsky* [1963]) can be derived. Assuming a fluctuating subgrid velocity scale u'_{sgs} and a subgrid mixing length l_{sgs} the viscous dissipation and eddy viscosity can be estimated with

$$\epsilon(k_c) \sim \frac{u'^3_{sgs}}{l_{sgs}}; \quad K_m \sim u'_{sgs} l_{sgs}. \quad (3.38)$$

Using (3.37) the subgrid velocity scale becomes

$$u'_{sgs} = l_{sgs} |\bar{S}|, \quad (3.39)$$

with the magnitude of the resolved rate of strain defined as

$$|\bar{S}| \equiv \sqrt{2\bar{S}_{ij}\bar{S}_{ij}}. \quad (3.40)$$

Relating the subgrid mixing length to the grid scale Δ , using the Smagorinsky constant of proportionality C_s , results in a model for the eddy viscosity, given by

$$K_m = (C_s\Delta)^2 |\bar{S}|. \quad (3.41)$$

Lilly [1967] adjusted the Smagorinsky constant in a fashion to be consistent with the Kolmogorov spectrum. To that end he approximated the energy transfer by

$$2K_m\bar{S}_{ij}\bar{S}_{ij} = \int_0^{k_c} 2K_m k^2 E(k) dk. \quad (3.42)$$

With the Kolmogorov spectrum for $E(k)$ a minimum estimate for $\epsilon(k_c)$ can be made:

$$2\bar{S}_{ij}\bar{S}_{ij} \leq \int_0^{k_c} 2C_k \epsilon(k_c)^{2/3} k^{1/3} dk = \frac{3}{2} C_k \epsilon(k_c)^{2/3} k_c^{4/3}. \quad (3.43)$$

It is a minimum estimate for the energy drain due to the fact that the inertial range is not extended up to $k = 0$, in the direction of decreasing wavenumbers. Substituting the obtained dissipation back into (3.37) yields a value for the eddy viscosity K_m ,

$$K_m \geq \left(\frac{2}{3C_k}\right)^{3/2} \frac{(2\bar{S}_{ij}\bar{S}_{ij})^{3/2}}{2\bar{S}_{ij}\bar{S}_{ij}} k_c^{-2}. \quad (3.44)$$

Substitution of the cut-off wavenumber for the top-hat filter $k_c = \pi/\Delta$ yields an eddy viscosity model, given by

$$K_m = \left(\frac{2}{3C_k}\right)^{3/2} \left(\frac{\Delta}{\pi}\right)^2 |\bar{S}|, \quad (3.45)$$

that can be written in the form (3.41), with

$$C_s = \frac{1}{\pi} \left(\frac{2}{3C_k}\right)^{3/4}. \quad (3.46)$$

For a common used value of the Kolmogorov constant $C_k = 1.5$ the Smagorinsky constant becomes $C_s = 0.173$. The values of C_s that are used in practical large eddy simulations vary in the range $C_s = 0.1 - 0.2$, see *Schmidt and Schumann* [1989]. *Nieuwstadt* [1990] reports high correlations of successful large eddy simulations of forced convection flows with small C_s and successful LES of free convection flows with large C_s , within the above given range.

3.3.3 Structure-function model

The structure-function model was developed by *Métais and Lesieur* [1992] on the basis of the spectral eddy viscosity concept as established by *Kraichnan* [1976]. This idea was generalized to physical space. The spectral eddy viscosity is based upon a kinetic energy spectrum local in space:

$$K_m = \frac{2}{3} C_k^{-3/2} \sqrt{\frac{E_{\mathbf{x}}(k_c)}{k_c}} \quad (3.47)$$

and the kinetic energy spectrum $E_{\mathbf{x}}(k_c)$ at \mathbf{x} is calculated with the aid of a local second-order velocity structure-function. In their study of homogeneous isotropic turbulence, where internal intermittency exists, *Métais and Lesieur* [1992] show that the structure-function model gives the best agreement with a Kolmogorov $k^{-5/3}$ spectrum if a Kolmogorov constant of $C_k = 1.4$ is used. The comparison was made between the structure-function model, spectral models and the Smagorinsky model. Therefore some improvement could be made with the structure-function model.

Like the Smagorinsky model the structure-function model can be written as a mixing length model, i.e. in terms of the second expression of (3.38), where u'_{sgs} denotes a characteristic velocity difference on the computational grid mesh with spacing $l_{sgs} = \Delta$. For the mixing length velocity u'_{sgs} the square root of the second order resolved velocity structure function is evaluated within a volume of characteristic length Δ . Over this volume, the second order velocity structure function is defined as

$$F_2(\mathbf{x}, \Delta, t) = \langle \|\mathbf{u}(\mathbf{x} + \mathbf{r}, t) - \mathbf{u}(\mathbf{x}, t)\|^2 \rangle_{\|\mathbf{r}\|=\Delta} \quad (3.48)$$

(where $\langle \cdot \rangle$ denotes the spatial average over the given volume). In *Batchelor* [1953] the relation between the second order structure function and the energy spectrum is given, assuming a Kolmogorov spectrum from $k = 0$ up to ∞ :

$$F_2(r = \|\mathbf{r}\| = \Delta) = \Gamma(1/3) C_k (\epsilon r)^{2/3}, \quad (3.49)$$

with $\Gamma(1/3) = 4.82$.

The local kinetic energy, needed to calculate (3.47), can be evaluated using the dissipation ϵ from the $-5/3$ law, substituted into (3.49), which results in

$$E(k_c = \pi/\Delta) = \frac{1}{4.82\pi^{5/3}} \Delta F_2(\Delta). \quad (3.50)$$

This yields for the eddy viscosity (3.47):

$$K_m = \frac{2}{3} C_k^{-3/2} \left(4.82\pi^{8/3} \right)^{-1/2} \Delta \sqrt{F_2}. \quad (3.51)$$

In their paper *Métais and Lesieur* [1992] deduce a relation between the structure function and the filtered structure function: $F_2 = 2.53\overline{F_2}$, so that the final model is given by

$$K_m = 0.105C_k^{-3/2}\Delta\sqrt{\overline{F_2}}. \quad (3.52)$$

The eddy viscosity model based on the structure function can be related to the Smagorinsky model. The spatial average of the structure function on a cubic equidistant grid is given by

$$\begin{aligned} \overline{F_2}(\mathbf{x}) = \frac{1}{6} & \left(\|\overline{\mathbf{u}}(\mathbf{x} + \Delta\mathbf{x}) - \overline{\mathbf{u}}(\mathbf{x})\|^2 + \|\overline{\mathbf{u}}(\mathbf{x} - \Delta\mathbf{x}) - \overline{\mathbf{u}}(\mathbf{x})\|^2 + \right. \\ & \|\overline{\mathbf{u}}(\mathbf{x} + \Delta\mathbf{y}) - \overline{\mathbf{u}}(\mathbf{x})\|^2 + \|\overline{\mathbf{u}}(\mathbf{x} - \Delta\mathbf{y}) - \overline{\mathbf{u}}(\mathbf{x})\|^2 + \\ & \left. \|\overline{\mathbf{u}}(\mathbf{x} + \Delta\mathbf{z}) - \overline{\mathbf{u}}(\mathbf{x})\|^2 + \|\overline{\mathbf{u}}(\mathbf{x} - \Delta\mathbf{z}) - \overline{\mathbf{u}}(\mathbf{x})\|^2 \right). \end{aligned} \quad (3.53)$$

The velocity in this expression may be expanded in a Taylor series, according to

$$\overline{\mathbf{u}}(\mathbf{x} + \Delta\mathbf{x}_i) - \overline{\mathbf{u}}(\mathbf{x}) = \Delta x_i \left(\frac{\partial \overline{\mathbf{u}}}{\partial x_i} \right)_{\mathbf{x}} + \mathcal{O}(\Delta x_i^2). \quad (3.54)$$

With $\Delta = \Delta x = \Delta y = \Delta z$ the structure function becomes

$$\overline{F_2} = \frac{\Delta^2}{6} (2\overline{S_{ij}S_{ij}} + \overline{\omega_i\omega_i}) + \mathcal{O}(\Delta^3), \quad (3.55)$$

with the vorticity defined as $\omega_i = \epsilon_{ijk}\partial u_k/\partial x_j$. Here ϵ_{ijk} is Levi-Civita's alternating tensor. This results in

$$\begin{aligned} K_m &= \frac{0.105}{\sqrt{6}}C_k^{-3/2}\Delta^2\sqrt{2\overline{S_{ij}S_{ij}} + \overline{\omega_i\omega_i}} \\ &= (0.882C_s\Delta)^2\sqrt{2\overline{S_{ij}S_{ij}} + \overline{\omega_i\omega_i}}. \end{aligned} \quad (3.56)$$

This is a mixture of the original and a variant of the Smagorinsky model as proposed by *Kwak et al.* [1975]. Instead of the resolved strain they used a formulation based on the resolved vorticity, as given by

$$K_m = (C_\omega\Delta)^2\sqrt{\overline{\omega_i\omega_i}}. \quad (3.57)$$

The constant of the form (3.56) is reduced to $0.882C_s$.

3.3.4 Kolmogorov-Prandtl model

A slightly more complicated model can be derived from the equation for the subgrid energy (3.30). Solving this equation yields a value for the resolved subgrid energy as function of space and time. This energy can be used as a subgrid

velocity scale for, again, a mixing length type of closure. The turbulent viscosity in terms of the subgrid energy is then defined as

$$K_m = C_\mu \Delta \sqrt{e_{sgs}}. \quad (3.58)$$

However, equation (3.30) can not be solved immediately. Some additional assumptions have to be made. The gradient diffusion hypothesis is used for subgrid stresses and fluxes. This is also used for the combination of transport terms of the correlation of subgrid velocity with subgrid energy ($e'_{sgs} = \frac{1}{2} u'_i u'_i$), and subgrid velocity with subgrid pressure, see e.g. *Speziale* [1991]:

$$-\overline{u'_j e'_{sgs}} - \overline{u'_j p'} = K_e \frac{\partial e_{sgs}}{\partial x_j} \quad (3.59)$$

and an assumption is needed for the value of K_e . In the present study K_e is taken to be equal to K_m , as discussed in the paper of *Speziale*.

The last unknown term is the dissipation,

$$Pr \overline{\left(\frac{\partial u'_i}{\partial x_j} \right)^2} = \epsilon_{k_c}. \quad (3.60)$$

By assuming a Kolmogorov spectrum from $k = k_c$ up to ∞ we can express ϵ in terms of e_{sgs} , according to

$$\epsilon_{k_c} = C_d \frac{e_{sgs}^{3/2}}{\Delta}; \quad C_d = \pi \left(\frac{2}{3C_k} \right)^{3/2}. \quad (3.61)$$

With the aid of the identity $\partial/\partial x_i(\overline{u'_i p'}) \equiv \partial/\partial x_j(\overline{u'_j p'})$, the additional equation that has to be solved finally reads:

$$\begin{aligned} \frac{\partial e_{sgs}}{\partial t} + \frac{\partial}{\partial x_j} (\overline{u'_j e_{sgs}}) &= 2K_m \overline{S_{ij} S_{ij}} - \frac{Ra Pr K_m}{Pr_t} \frac{\partial \overline{T}}{\partial x_i} \delta_{i3} + \\ &\frac{\partial}{\partial x_j} (K_e + Pr) \frac{\partial e_{sgs}}{\partial x_j} - C_d \frac{e_{sgs}^{3/2}}{\Delta}. \end{aligned} \quad (3.62)$$

A one-equation model like (3.62) is generally referred to as a Kolmogorov-Prandtl model. It provides the computation of the resolved turbulent kinetic subgrid scale energy and accounts for some limited nonlocal and history effects in the determination of the eddy viscosity. This type of model has been preferred by *Schumann* [1975], *Grötzbach and Schumann* [1979], *Deardorff* [1980] and *Moeng* [1984] for natural convection flows in buoyant channel flows and convection in the planetary boundary layer. *Korte et al.* [1992] used this type of model to study the decay of homogeneous isotropic turbulence.

By balancing production and dissipation in equation 3.62 and using 3.58 for the dissipation we obtain again a Smagorinsky type of model:

$$K_m = \sqrt{\frac{C_\mu^3}{C_d} \Delta^2} \sqrt{2\overline{S}_{ij}\overline{S}_{ij} - \frac{RaPr}{Pr_t} \frac{\partial \overline{T}}{\partial x_i} \delta_{i3}}. \quad (3.63)$$

This is an extended Smagorinsky model that also takes buoyancy effects into account. On the one hand, the influence of an unstable stratification, yielding an increased kinetic energy drain to the subgrid scales, is thus taken into account. On the other hand, the model accounts for the physical aspects accompanying stable stratification, in which case a decrease in energy transfer to small scale motion occurs. Note that the value of the eddy viscosity has to be confined to zero at the lower end. In fact this model was used by *Eidson* [1985] and preliminary tests in this study showed some improvement. Now also the value of C_μ can be determined, according to

$$C_\mu = \frac{1}{\pi} \left(\frac{2}{3C_k} \right)^{3/2}. \quad (3.64)$$

For a generally accepted Kolmogorov constant of $C_k = 1.5$ the value of the constant becomes $C_\mu = 0.094$. Using ϵ_{k_c} of 3.61 and a Smagorinsky closure, the resolved subgrid kinetic energy can be estimated by

$$e_{sgs} = \left(\frac{K_m}{\Delta C_\mu} \right)^2. \quad (3.65)$$

3.3.5 Germano's dynamic model

In the recent past *Germano et al.* [1991] proposed a new eddy viscosity model in which the model coefficient is calculated dynamically. It allows the coefficient to vary with the flow problem temporally as well as spatially. This may overcome the drawbacks of the traditional Smagorinsky model, especially in the context of transition from laminar to turbulent flow. No a priori knowledge of the model constant is needed and the subgrid scale stresses obtained with the model are claimed to vanish in laminar flows and at solid boundaries in a physically correct way.

The model is obtained by evaluating the subgrid scale stresses in a confined region at the underside of the cut-off wavenumber k_c . In this way large resolved wavenumbers do not affect the model. The subgrid scale stress tensor for the large-scale (grid) field reads

$$\tau_{ij} = (\overline{u_i u_j} - \overline{u_i} \overline{u_j}). \quad (3.66)$$

Application of a coarser spatial "test" filter with width $\widehat{\Delta} \sim \mathcal{O}(2\Delta)$ to the equations gives subtest-scale stresses, signified by a caret over the overbar:

$$T_{ij} = \left(\widehat{\overline{u_i u_j}} - \widehat{\overline{u_i}} \widehat{\overline{u_j}} \right). \quad (3.67)$$

Here, in actual computations, test-filtered quantities are obtained by convoluting the large-scale quantities with a filter of width $\widehat{\Delta}$.

In the initial formulation the Smagorinsky model was assumed to hold for both the isotropic parts of the subgrid and the subtest-scale stresses, i.e.:

$$\tau_{ij} = -2K_m \overline{S}_{ij}, \quad K_m = C \Delta^2 |\overline{S}|; \quad (3.68)$$

$$T_{ij} = -2K_m \widehat{S}_{ij}, \quad K_m = C \widehat{\Delta}^2 |\widehat{S}|. \quad (3.69)$$

Consistent Smagorinsky modelling of τ_{ij} and T_{ij} depends on a proper local choice of $C = C_s^2$. It can be directly observed that it is possible now to have a vanishing subgrid-scale contribution in the case of laminar flow. In that case the constant should also vanish. Even stronger, when there is an inverse energy cascade, as is the case for the hypothetical two-dimensional turbulence of *Kraichnan* [1967], the constant is able to obtain a negative value.

The main observation of *Germano et al.* [1991] is that the stresses at the two levels are related to each other by the algebraic identity

$$\mathcal{L}_{ij} = T_{ij} - \widehat{\tau}_{ij} = \widehat{u_i u_j} - \widehat{u_i} \widehat{u_j} = -2C \alpha_{ij} + 2\widehat{C} \beta_{ij}, \quad (3.70)$$

with

$$\alpha_{ij} = \widehat{\Delta}^2 |\widehat{S}| \widehat{S}_{ij} \quad \text{and} \quad \beta_{ij} = \Delta^2 |\overline{S}| \overline{S}_{ij}. \quad (3.71)$$

\mathcal{L}_{ij} is the resolved small-scale stress, i.e. the stresses in the test window between the test scale and the grid scale.

In the original formulation it was assumed that C is a slowly varying function of space. This was used as a justification for taking it out of the filtering operation. However, in generic cases, taking C out of the filtering operation is not consistent. The problem can be avoided by averaging C in one or more suitably chosen spatial directions. Subsequently, the filtering operation is applied only in this direction. This means that in the filter direction C does not vary anymore. In this case the constant may be taken out of the filtering operation. In order to obtain a physically meaningful solution the averaging direction must be a homogeneous direction. If there is no homogeneous direction present in the flow problem, a localization method must be used (see e.g. *Piomelli and Liu* [1995]). In the calculations as presented in this thesis the averaging strategy is applied. The averaging direction is taken parallel to the heat source. Thus the filtering plane is perpendicular to the heating element.

Equation (3.70) involves symmetric second-rank tensors giving (together with continuity) five independent equations for C . *Germano et al.* [1991] originally used an arbitrary contraction of 3.70 with \overline{S}_{ij} to make it unambiguous. *Lilly* [1992] suggested to apply a least-squares approach to minimize at each point the energy of the errors of the independent equations. Defining Q_{ij} as the residual of (3.70), i.e.

$$Q_{ij} = (\mathcal{L}_{ij} - 2CM_{ij}), \quad (3.72)$$

with

$$M_{ij} = \widehat{\beta}_{ij} - \alpha_{ij} \quad (3.73)$$

and by minimizing the square of the residual with respect to C , i.e. $\partial(Q_{ij}Q_{ij})/\partial C = 0$, the dynamic constant is obtained, yielding

$$C = \frac{1}{2} \frac{\mathcal{L}_{ij}M_{ij}}{M_{kl}M_{kl}}. \quad (3.74)$$

Computationally this formulation is more stable than the original contraction, in which the denominator could become very small. The denominator of Lilly's expression (3.74) vanishes only if all components of M_{ij} vanish separately, in which case the numerator also vanishes.

Application of the above outlined procedure to the energy equation, yields a dynamic evaluation of the turbulent Prandtl number,

$$\frac{1}{Pr_t} = \frac{1}{C} \frac{P_i R_i}{R_j R_j}, \quad (3.75)$$

with

$$P_i = \widehat{\overline{u_i T}} - \widehat{\overline{u_i}} \widehat{\overline{T}}, \quad R_i = \Delta^2 |\widehat{S}| \frac{\partial \overline{T}}{\partial x_i} - \widehat{\Delta^2} |\widehat{S}| \frac{\partial \widehat{T}}{\partial x_i}. \quad (3.76)$$

Now the constants are evaluated during the calculation and are a function of space and time. The only adjustable parameter is the ratio between the test and grid-scale filter widths. The results of *Germano et al.* [1991] suggest that the sensitivity associated with the ratio of grid widths is low. It was proposed to be in the order of $\widehat{\Delta}/\Delta = 2$. In principle this gridratio is taken in calculations as presented in this thesis. However the testfilter operation is performed on the gridfiltered variables. In the present work an explicit gridfiltering is needed to define grid scale stresses. This is due to the grid arrangement as will be outlined in chapter 4. Subsequent application of the gridfilter and the testfilter using a top-hat kernel then results in a trapezoidal filter shape with a somewhat broader effective width. To account for this in the evaluation of M_{ij} , *Vreman* [1995] derived an optimal value for the ratio to be equal to $\sqrt{5}$ instead of 2.

The value of C may become negative, thus allowing subgrid scale turbulence to "backscatter" kinetic energy to the grid scales, which is also found in direct numerical simulations. If the total viscosity becomes negative the calculations are no longer stable in a numerical sense. For a FTCS scheme over $2\Delta t$ (forward in time centred in space, see next section) applied to a diffusion problem, von Neumann stability analysis indicates that the maximum amplification factor is given by: $G_{max} = 1 - 8K\Delta t/\Delta x^2$. For a total viscosity or diffusivity K lower than zero there is amplification. Therefore measures have to be made to ensure a stable integration process. An option that is used in the present work, is to limit the value of the total viscosity or diffusivity at least with a lower bound, taken to be zero. This allows a limited negative value for C .

3.3.6 Recent developments

Moin and Jimenéz [1993] state that the scalar eddy viscosity approximation is a good model if the small scales being modelled are separated from the large scales in spectral space. They refer to meteorological situations, in which case an eddy viscosity should work quite well, the lateral dimensions being far more extended than the vertical dimension normal to the planetary surface. However, in Navier-Stokes flow kinetic energy can not be transferred from a discrete wavenumber to another. Furthermore, for engineering calculations a scale separation is generally not present. In addition three other drawbacks of the Smagorinsky model can be identified. First, there is the necessity of adjustment of the model constant in different types of flows and flow regimes, i.e. type and magnitude of the forcing. Secondly, there is an inadequate limiting behaviour in the presence of a wall. Another important drawback is the non-vanishing of the subgrid stresses in the case of laminar flows. The latter leads to inaccurate prediction of the laminar to turbulent transition, the phenomenon of our main interest. In the next few paragraphs some important and interesting developments are presented, although it is not supposed to be a complete review of the state of affairs.

In order to improve the model for "soft"-turbulence at low Rayleigh numbers, *Voke* [1994] modified the Smagorinsky model with the use of a dissipation range at high wavenumbers. Such a modification is also needed when the resolution approaches the one required for full resolution of the simulated turbulent flow. Still, the dynamics are assumed to be isotropic and homogeneous and an eddy viscosity assumption is adopted.

In making the structure function model more "selective", *Ducros et al.* [1994] developed the filtered structure function model. In this model, in evaluating the eddy viscosity, the velocity field is high-pass filtered in order to use only the information near to the cut-off wavenumber. This procedure gives a nearly zero eddy viscosity during the laminar and transitional stages of the flow. This property is referred to as "selectivity".

Generalisation to flow conditions in which also laminar flow may occur is provided both by the structure-function model (by its estimation of the local spectrum) and the dynamic model. According to *Moin and Jimenéz* [1993] the structure function model does not have the correct behaviour in the presence of a wall. On the other hand, the dynamic model, which satisfies adequately the wall behaviour, could be improved in several ways. *Zang et al.* [1993] used a dynamic mixed model in which the base model of the dynamic modelling is a combination of the Smagorinsky model and the scale similarity model of *Bardina et al.* [1984]. In this case the full subgrid scale stress tensor is predicted, in contrast to the application of an eddy viscosity model which requires an alignment of the principal axes of the subgrid scale stress tensor with the resolved strain rate tensor. They justify their way of modelling by the observation that the dynamic model accurately predicts the mean dissipation rate. An improved correlation

with DNS data is then obtained by the Smagorinsky model, estimating a better local dissipation rate. *Vreman et al.* [1994] modified the mixed model in order to make it more consistent. On the basis of a thorough investigation of experimental data obtained from two-dimensional particle displacement velocimetry in a jet *Liu et al.* [1994] conclude that a mixed formulation performs best.

As described in the previous section the dynamic model needs averaging of the constant in a homogeneous direction. This means that the constant is not fully local anymore. Furthermore the procedure can not be applied in cases where no homogeneous direction exists. *Piomelli and Liu* [1995] solved the problem by using extrapolation of the model constant with a Taylor series up to any desired order of accuracy in time. It was stated that the model coefficient vanishes in regions of quiescent flow, accurately reproducing the intermittent character of the flow.

Furthermore *Ghosal et al.* [1995] proposed a variational formulation of the dynamic model, removing the inconsistency encountered by just taking the constant out of the filter operation. They use a constant that minimizes the L_2 norm of the error Q_{ij} , resulting in a Fredholm integral equation of the second kind for C . In order to account for backscatter they used also an alternative formulation. A one-equation model was applied in which the resolved subgrid scale kinetic energy diminishes to zero in regions where C is negative, in which case the eddy viscosity vanishes.

In dynamic modelling *Moin and Jimenéz* [1993] suggest some other improvements. First they propose a model in which the constants at the test-filtered scale and the grid scale are not identical. From the five independent equations for the two unknowns they determine both constants. Furthermore they propose a tensor formulation for the model constant to remove the well-known criticism of the eddy viscosity. Additionally it is suggested to model the dissipation over the test-filter wave length by the Kolmogorov equilibrium hypothesis, i.e. the average rate of kinetic energy drain over the test filter scale is the same as that over the grid filter scale.

The research concerning the improvement of subgrid-scale models is carried out far most for forced convective flows. In thermal convection flows an important contribution is given by *Wong and Lilly* [1994]. They describe two additional methods for the determination of the dynamic parameters for the stresses and fluxes. In the first they propose a dynamic procedure for the buoyant Smagorinsky model. It involves an iterative scheme for solving C and Pr_t , which is quite expensive and may suffer from convergence problems. A second more successful method is presented which is based on a scale analysis. A dynamic parameter is introduced in which the total dissipation is incorporated. Thus the combination of the subgrid dissipation and the subgrid buoyant production term is left as an unknown, avoiding the coupling problems.

Chapter 4

Numerical method and performance in plume flows

4.1 Numerical method

4.1.1 Time integration

A major difficulty in discretizing the momentum and continuity equations is that they appear coupled. Continuity is a constraint in the treatment of the momentum equation in incompressible fluid flow. Therefore, so-called projection methods are used in a large number of time dependent numerical simulations. A projection method consists of determining an intermediate (generally non-solenoidal) velocity field, employing an approximate pressure gradient on the next time level. Frequently, in executing this step, the pressure gradient is estimated to be zero everywhere. Then, in completing the time-step, the intermediate velocity field is projected onto a solenoidal subspace. A comprehensive overview of this method is given in *Gresho* [1990].

The most convenient way to describe the method is using the momentum equation formulated as

$$\frac{\partial u_i}{\partial t} = -\frac{\partial p}{\partial x_i} + R_i, \quad (4.1)$$

in which R_i contains everything not explicitly written, i.e. advection, diffusion and body forces, according to

$$R_i = -\frac{\partial}{\partial x_j} (u_i u_j) + RaPrT\delta_{i3} + 2\frac{\partial}{\partial x_j} ((Pr + K_m) S_{ij}). \quad (4.2)$$

Here, any variable may be a DNS variable or a grid filtered LES variable, resulting in a general description for the numerical method (as also used by *Nieuwstadt* [1990]). Application of a leap-frog scheme to the advective term and an Euler

forward scheme to the diffusion and forcing yields

$$\frac{u_i^{n+1} - u_i^{n-1}}{2\Delta t} = -\frac{\partial p^{n+1}}{\partial x_i} + R_i^n, \quad (4.3)$$

with:

$$R_i^n = -\left[\frac{\partial}{\partial x_j}(u_i u_j)\right]^n + [RaPrT\delta_{i3}]^{n-1} + \left[2\frac{\partial}{\partial x_j}((Pr + K_m)S_{ij})\right]^{n-1}. \quad (4.4)$$

The buoyancy term is taken at the same instant in time, $(n-1)$, as the viscous diffusion term. It might be argued that it should be taken at the n level, though there were no differences observed in the present flow problems. Splitting equation (4.3) using an approximate velocity field u_i^* gives

$$\frac{u_i^* - u_i^{n-1}}{2\Delta t} = R_i^n; \quad (4.5)$$

$$\frac{u_i^{n+1} - u_i^*}{2\Delta t} = -\frac{\partial p^{n+1}}{\partial x_i}. \quad (4.6)$$

These steps are performed in the given order for determining u_i^* and u_i^{n+1} , respectively. The first step is called the prediction step and the second step is called the correction or projection.

The prediction step to determine u_i^* is straightforward once the spatial discretization is defined. The correction step is used to enforce continuity. To that end the discrete divergence of (4.6) is taken,

$$\frac{1}{2\Delta t} \left(\frac{\delta u_i^{n+1}}{\delta x_i} - \frac{\delta u_i^*}{\delta x_i} \right) = -\frac{\delta^2 p^{n+1}}{\delta x_i^2}. \quad (4.7)$$

Here δ is the discrete spatial difference operator. The spatial discretization is discussed in more detail in the next section. Enforcing discrete continuity at the present time level,

$$\frac{\delta u_i^{n+1}}{\delta x_i} = 0, \quad (4.8)$$

results in an explicit discrete Poisson equation for the pressure:

$$\frac{\delta^2 p^{n+1}}{\delta x_i^2} = \frac{1}{2\Delta t} \frac{\delta u_i^*}{\delta x_i}. \quad (4.9)$$

The new divergence-free velocity field u_i^{n+1} can now be calculated from (4.6). Before evaluating the pressure by (4.9), first the boundary conditions are imposed on u_i^* . Also when computing u_i^{n+1} from the projection (4.6), boundary conditions are needed for pressure points in volumes outside the calculation domain. The boundary conditions are discussed in more detail in section 4.1.3.

Finally a weak low pass time filter is used to prevent the solution from time splitting. This may occur due to the "leap-frogging", causing a decoupling of the odd and even time steps. A symmetrical discrete three-point filter is used as proposed by *Asselin* [1972]. The velocities at time-step n are replaced by

$$u_i^n := \gamma u_i^{n-1} + (1 - 2\gamma)u_i^n + \gamma u_i^{n+1}. \quad (4.10)$$

The value of γ determines the width of the filter and is usually taken in the range $\gamma = 0.05 - 0.1$. Since we have an explicit scheme the time-steps must be taken small in order to obtain computational stability. It was found that the frequency associated with the time-stepping is very much higher than the physical frequencies occurring in the problems to be computed. Therefore the Asselin filter has only a negligible effect on the results obtained.

The time-step criterion is determined by the temporal and the spatial discretization. For the present method it is given by *Pourquié* [1994] as

$$\Delta t \leq \left(\left\| \frac{u_i}{\Delta x_i} \right\| + \frac{4K}{\Delta x_i^2} \right)^{-1}, \quad (4.11)$$

in which K is the maximum diffusion coefficient, i.e. the maximum of the total viscosity and the total diffusivity of heat. The first part between the brackets in the right hand side of (4.11) is generally called the Courant-Friedrichs-Lax stability condition (CFL condition) for advection. The second term is a stability condition for the diffusive part. Actual simulations are performed by estimating a proper constant time-step in advance. For each discrete point in space it is checked whether this time-step exceeds 95 % of the right hand side of (4.11). If it does the calculation is stopped and may be restarted with a smaller time-step. In order to balance the claims on the time-step restriction of the diffusion and advection parts we have: $u_i \sim K/\Delta x_i$. In this sense the scaling of the problem, in the way as outlined in chapter 2, may be regarded as advantageous.

The diffusion terms are lagged in time because otherwise the scheme would be unconditionally unstable for pure diffusion. This can be shown by a von Neumann analysis of the central discretization of the diffusion problem, both in time and space. This scheme is also referred to as a Richardson scheme. The remaining forward-in-time scheme has a truncation error that is first-order in time. However time-steps are always very small.

4.1.2 Spatial discretization

The discrete collocation points are defined on a staggered grid, as displayed for a two dimensional case in figure 4.1. This grid system has been introduced by *Harlow and Welch* [1965]. *Peyret and Taylor* [1983] recommend the projection method to be used in combination with this grid configuration. The advantage of this grid arrangement is that spurious oscillations in the pressure, known as

"checkerboarding", do not occur. This is achieved due to the coupling of the velocity and pressure solutions at adjacent grid points using central differencing.

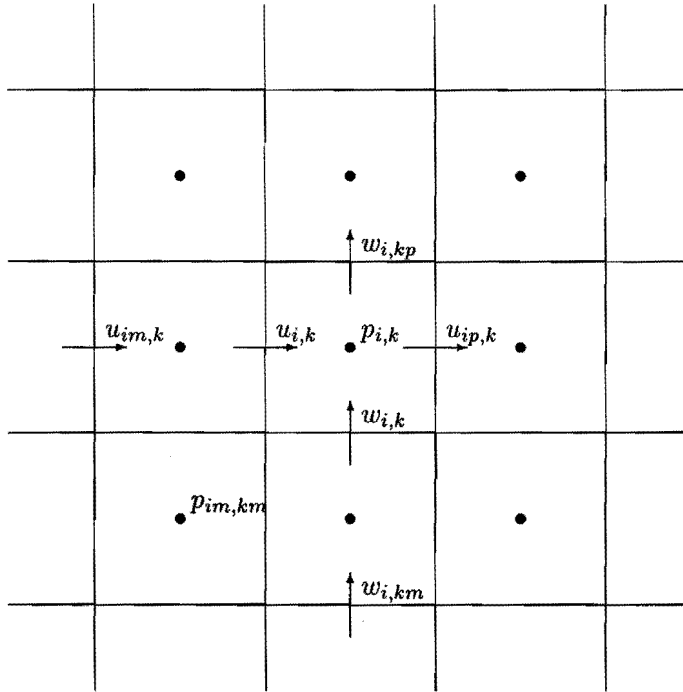


Figure 4.1: Staggered grid in two dimensions

Discretized scalar variables are defined at the centre of each cell and the discrete velocity components are defined at the cell faces. Vector quantities, like $u_{i,k}$, at a discrete point with index (i, k) are defined at the low index side of the scalar quantities, like $p_{i,k}$, as shown in the figure. In the discrete notations: $im = i - 1$, $ip = i + 1$.

For the spatial discretization a finite volume method is applied. The governing equations are integrated over a grid cell, yielding volume averaged equations. By discretization of the integral form of the conservation laws it can be ensured that the basic quantities mass, momentum and energy will remain conserved at the discrete level. Whenever possible, volume integrals are reduced to surface integrals using the divergence theorem. The resulting integrals are then approximated using a numerical integration rule (for details see *Press et al.* [1992]). The method is described extensively in *Pourquié and Eggels* [1991].

In the present work the discretization is equidistant and in Cartesian coordinates. The finite volumes are chosen centrally around the discrete points of the individual momentum components and scalars. The finite integration volume for imposing the conservation of mass is centred around the discrete pressure points.

Here the numerical integration rule used is the midpoint rule (which is second-order accurate). Whenever values are needed at points where they are not defined, second-order interpolation using neighbouring points is applied. The derivatives are also approximated with the same accuracy by central differences. Application of these techniques yields a numerical integration scheme, which is second-order accurate in space. As described in the previous subsection the scheme is also second-order accurate in time, except for the diffusion part, which is first-order.

Implementation of the outlined discretization strategy is straightforward, especially using an equidistant Cartesian mesh. For the discretization of the advection of momentum a scheme as proposed by *Piacsek and Williams* [1970] is used. They give a method in which errors in quadratic quantities, like kinetic energy or scalar variance, due to the existence of small divergences (machine accuracy) in the velocity field, cancel out. The scheme is described in detail by *Piacsek and Williams* [1970] for linear advection. It is not entirely straightforward for the nonlinear case, especially on a staggered grid. The strategy depends on the numerical method and the integration rule used. Therefore a derivation of the discretization for the present case is given in appendix B.

For the advection of scalars a central discretization is unstable for pure advection. Therefore, where needed, a second-order upwinding technique is used due to *van Leer* [1974] and *Leonard* [1991], as described in appendix C. In the appendix and in the next section the differences are exhibited. The main advantage of the method is the ability of having a stable and accurate advection using a relatively coarse discretization.

The remaining Poisson problem (4.9) is solved by a direct FFT-based solver, called CRAYFISHPAK (see *Schumann and Sweet* [1976]). Fourier transforms are used in the third and second spatial dimension, respectively. Then the tridiagonal systems for the first dimension are solved by Gauss elimination. The final solution is obtained by inverse Fourier transforms of the second and third dimension subsequently. The Fourier transforms are only fast if the vector length (the number of collocation points in the relevant directions) is a highly composite number, i.e. the product of powers of small primes.

4.1.3 Boundary conditions

Boundary conditions are implemented directly for quantities defined on the boundary. Second-order interpolation is used for all other quantities defined at positions outside the spatial boundaries of the problem. In this thesis either no-slip walls are used in combination with homogeneous Dirichlet or Neumann conditions for temperature, or periodic boundary conditions are applied. In the case of pre-

scribed boundary velocities b_i the conditions are taken as follows

$$u_i^* = b_i^{n+1} \quad \text{on } \Gamma; \quad (4.12)$$

$$u_i^{n+1} = b_i^{n+1} \quad \text{on } \Gamma. \quad (4.13)$$

Evaluating the discrete equivalence of (4.6) in boundary normal direction n yields a consistent boundary condition for the pressure,

$$\left. \frac{\delta p}{\delta n} \right|^{n+1} = 0 \quad \text{on } \Gamma. \quad (4.14)$$

However, one should note that the pressure should satisfy (4.3) and that condition (4.12) is purely artificial. According to *Marcus [1984]* and *Karniadakis et al. [1991]* the discrepancy may result in an erroneous numerical boundary layer. These aspects must be kept in mind when numerical results are interpreted.

Periodic boundary conditions are applied according to figure 4.2. Imposing $\phi(is) = \phi(if)$ and $\phi(if + 1) = \phi(is + 1)$, then results in an equal value of ϕ and its first derivative at both ends of the computational domain.

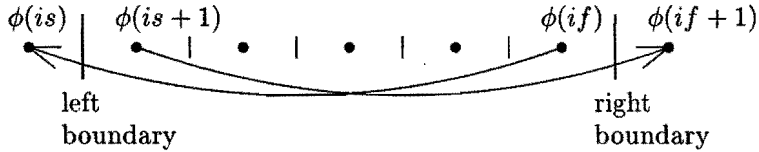


Figure 4.2: Implementation of periodic boundary conditions

4.2 Performance test

4.2.1 Test problem description

The numerical code was tested by comparison of solutions as obtained by *Desrayaud and Lauriat [1993]* for steady and unsteady confined buoyant two-dimensional plumes. These plumes are released from a discrete point source in the interior of the domain. The flow configuration is plotted in figure 4.3. Desrayaud and Lauriat solved the non-dimensional form of the governing equations for the two-dimensional case in vorticity-stream function formulation. The non-dimensionalisation was the same as in the present case, outlined in chapter 2.

The source term in the energy equation was described by

$$q' = \delta(x_s - x)\delta(z_s - z), \quad (4.15)$$

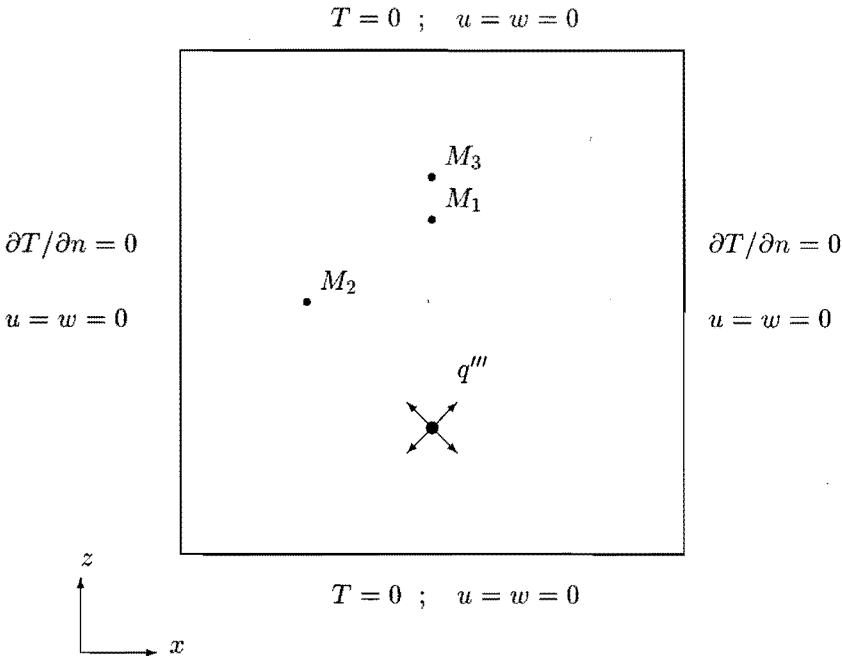


Figure 4.3: Flow domain and boundary conditions

where δ is the Dirac delta function and (x_s, z_s) is the source position, located in this case at $(\frac{1}{2}, \frac{1}{4})$, where the computational domain has the dimension $\Omega = (0, 1) \times (0, 1)$. In the discrete sense the Dirac function is approximated by one grid volume by imposing the condition that the integral equals unity.

The Prandtl number was taken to be $Pr = 0.71$. For the analysis of the flow extensive use was made of the values of several variables at three monitoring points $M_1 = (\frac{1}{2}, \frac{2}{3})$, $M_2 = (\frac{1}{4}, \frac{1}{2})$ and $M_3 = (\frac{1}{2}, \frac{3}{4})$ as depicted in figure 4.3. The indices of the variables and monitoring points correspond to each other. Also the streamfunction, and more specifically its maximum, is employed to monitor the flow.

For Rayleigh numbers lower than $Ra = 3.0 \cdot 10^7$, *Desrayaud and Lauriat* [1993] (called D&L hereafter) found that the system is attracted to a fixed point, representing steady motion. At slightly higher Ra numbers a purely periodic motion was observed. At Ra numbers that approach the critical Ra number from above, a transient is obtained, followed by a stationary flow. After some time this stationary flow starts to oscillate. It was noticed that the closer the Ra number is to the critical value, the longer is the time for attaining the asymptotic flow. This

phenomenon suggests that the onset of the periodic flow is due to the presence of a Hopf bifurcation point. Indeed, when the Ra number gets closer to the critical Ra number, the timespan comprising the transient and the stationary flow increases as $(Ra - Ra_c)^{-1}$. The amplitude of the oscillations was found to evolve like $(Ra - Ra_c)^{1/2}$, in accordance with the behaviour of a Hopf bifurcation. The flow was observed to undergo a supercritical Hopf bifurcation since no hysteresis effects were found. The behaviour of the amplitudes was used to determine accurately the critical point by linear extrapolation of the amplitudes at supercritical Ra numbers to zero oscillation amplitude. Thus, the critical Rayleigh number, Ra_c , was determined to be very close to $Ra = 3.0 \cdot 10^7$. However, since there is no comparison with other data, it must be remarked that the accuracy depends on the numerical method used. The steady solution together with the bifurcation will be subject of the present test.

For the sake of completeness here, the subsequent route to turbulent flow as found by D&L will be outlined briefly. At $Ra = 3.4 \cdot 10^7$ a second frequency was observed during the transient. At times greater than one this frequency vanished. The frequencies were found to be incommensurate and so the flow was classified as being quasi-periodic, turning to periodic at later times. At higher Ra numbers the flow becomes first periodic with two locked frequencies, and then intermittent. In the latter regime the length of the periodic windows between the chaotic bursts varied with $(Ra - Ra_c)^{-1/2}$.

4.2.2 Present calculations

In this section it will be checked if the transition to periodic flow can be predicted with the present method. Different schemes for the linear and non-linear advection will be used to investigate their influence on the solutions obtained. For the linear advection of temperature either a central second-order discretization is used, or the second-order upwinding of *van Leer* [1974] is employed. With respect to the discretization of the non-linear advection in the momentum equation all discretization methods as described in appendix B are used, i.e. a conservative and an advective scheme as well as the scheme of *Piacsek and Williams* [1970].

Besides the Finite Volume Method (FVM) also a Spectral Element Method (SEM), as developed by *Minev et al.* [1995a], has been applied as a third independent reference. With this method also the order of the approximations can be varied.

The SEM is, like the FVM, based on a splitting algorithm in order to perform a projection. All methods involved in this assessment, including that of D&L, suffer from inaccurate boundary conditions. In the method of D&L, boundary conditions for the wall vorticities were updated by evaluating the streamfunction at the previous level. The problems with the boundary conditions for the present FVM are outlined in the previous section. For each method, the inaccuracies are different. So in order to investigate the spectrum of effects accompanying

the incorrect prescription of boundary conditions, solutions as obtained from the different methods are compared. Also the order of the approximation is taken into account, employing the SEM. Simulations have been performed for cases just before and just beyond the first bifurcation to time dependent flow as assigned by D&L, i.e. at $Ra = 3.0 \cdot 10^7$ and increasing with steps of $0.1 \cdot 10^7$.

A typical size of the time-step as used in the present method is $\Delta t = 10^{-5}$ for a 65×65 grid. For the grid mentioned it was found that this time-step was sufficient in the sense of (4.11) for all forcing rates. The variation in the size of the time-steps with change in grid resolution was roughly determined by the advective criterion at the present Ra numbers. Employing an implicit time integration, D&L used a somewhat larger time-step of $\Delta t = 5 \cdot 10^{-5}$ at $Ra = 3.1 \cdot 10^7$. A dependence on spatial resolution was not mentioned. The time-steps used in the present SEM calculations are of size $\Delta t = 2.5 \cdot 10^{-5}$, each time using two intermediate convection steps.

Here the streamfunction is calculated from the vorticity by evaluating the Poisson equation given by

$$\frac{\partial^2 \psi}{\partial x_i \partial x_i} = -\omega. \quad (4.16)$$

The vorticity, having only one component $\omega = \partial v / \partial x - \partial u / \partial y$, is determined with the same second-order accurate approximations as outlined in the previous section. Then the Poisson equation is solved using the same direct solver as is used for evaluating the pressure, applying appropriate boundary conditions, in the present case $\psi = 0$ on all boundaries.

4.2.3 Stationary case

For the stationary case at $Ra = 3.0 \cdot 10^7$ results as obtained by D&L and present results are compared to each other. The Finite Volume Method as outlined in the previous part of this chapter is mainly used. Later on, also the Spectral Element Method is employed. It must be noted that time integrations for this case are performed for a time span $t = [0, 1]$ if not mentioned otherwise. At the final time, $t = 1$, a stationary solution is obtained. This does not mean that the solution stays steady for larger times.

The obtained stationary flow is depicted in figure 4.4. Qualitatively, in a stationary situation, these pictures are the same for each method, provided that the resolution is high enough. Results for central differencing and upwinding are given in table 4.1, together with the results as obtained by D&L. It was found that the upwinding scheme is two times as expensive as the central scheme is, increasing the overall computing time with about 15 %.

With respect to the discretization of the non-linear advection in the momentum equation it was found that the solution was identical for all employed discretization methods. For the overall numerical scheme it is expected that the computational efforts for these discretizations do not differ significantly.

grid	ψ_{\max}	u_2	w_2	w_3	T_3
33×33	71.37	110.4	-41.80	640.4	0.041
65×65	71.94	107.9	-42.15	675.5	0.044
129×129	72.42	108.3	-41.57	684.9	0.045

grid	ψ_{\max}	u_2	w_2	w_3	T_3
33×33	59.59	82.58	-27.21	710.3	0.044
65×65	68.78	97.78	-37.56	687.8	0.045
129×129	71.59	106.0	-40.41	687.5	0.045

grid	ψ_{\max}	u_2	w_2	w_3	T_3
33×33	66.50	123.8	-46.66	715.8	0.042
65×65	71.25	118.6	-45.25	697.8	0.044
129×129	72.31	112.8	-42.83	691.5	0.045

Table 4.1: Results for $Ra = 3.0 \cdot 10^7$ obtained by, top: Desrayaud and Lauriat, middle: present with central differences, bottom: present with second-order up-winding

In the case of the 33×33 grid, using the upwinding technique, the solution becomes oscillatory at about $t = 0.7$. Although the grid is very coarse, these oscillations correspond to the physically correct oscillations at slightly higher Ra numbers, and not to so-called grid oscillations. The simulation on the same grid with central differencing stays stable after the transient up to $t = 1.0$. However, this simulation shows for the steady state the formation of a wiggle in the temperature profile at $x = \frac{1}{2}$ in the neighbourhood of the top wall. Furthermore, just below the source a negative temperature arises with a value of -0.0067. This is not the case anymore at the 65×65 grid, although there is still a local minimum at the underside of the heat source. At the finest grid these phenomena are totally vanished.

No clear second-order convergence can be observed in both grid refinement series. One of the reasons may be the fact that the problem definition is not grid independent, the heat source occupying in every case one grid volume. Therefore, convergence could be improved by defining a heat source distribution as function of the coordinates, e.g. a Gaussian hill:

$$q' = \frac{1}{\pi\sigma^2} e^{-r^2/\sigma^2}, \quad (4.17)$$

in which r is the radial distance from the centre of the heat source and σ is a measure for the width of the source distribution. The width of the heat source, σ , was chosen in order to obtain comparable results with the former discrete heat

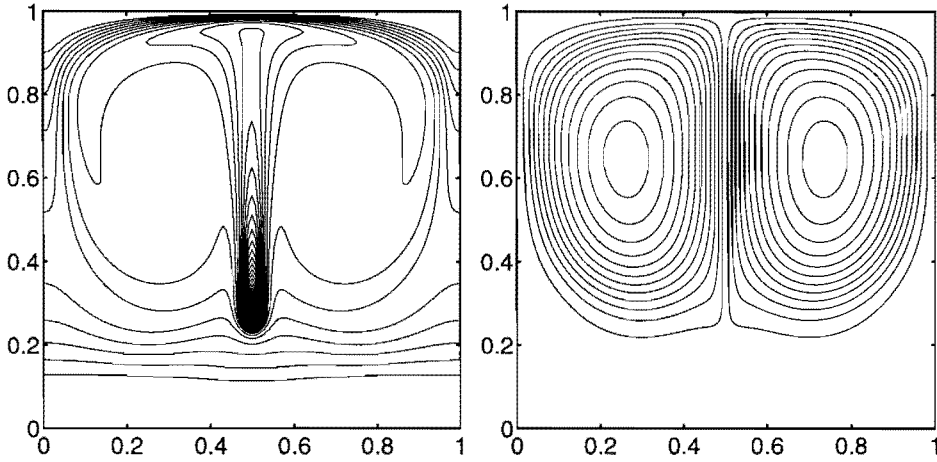


Figure 4.4: Results obtained from second-order upwinding on 129×129 grid, left temperatures (0.012:0.003:0.25), right streamlines (-69:6:69)

source in the limit to infinite resolution. Since it was found that the solution is converged to a great extent at a grid resolution of about hundred volumes in each dimension, σ was taken to be 0.01. For this case calculations were performed, both with the described FVM and the mentioned SEM-technique. In all SEM calculations a mesh of 8×8 elements was used, increasing the order of approximation per element. With the heat source distribution as employed by D&L it would practically be impossible to use a spectral method because of the non-smoothness of the heat source.

The results are given in table 4.2. In this comparison the FVM was applied using the second-order upwinding technique for advection of internal energy and

grid	ψ_{\max}	u_2	w_2	w_3	T_3	t_{cpu}
SEM 8×8 , order 4	-	87.76	-29.41	548.8	0.027	12700
SEM 8×8 , order 6	-	103.9	-39.74	674.8	0.043	35200
SEM 8×8 , order 8	-	108.8	-41.84	697.1	0.046	81500
FVM 33×33	79.46	139.3	-51.41	885.0	0.062	1100
FVM 65×65	72.42	119.5	-46.20	707.9	0.045	9000
FVM 129×129	72.58	112.2	-43.23	692.2	0.045	107400

Table 4.2: Results for $Ra = 3.0 \cdot 10^7$ with a Gaussian source of $\sigma = 10^{-2}$. Spectral Element Method (SEM) and Finite Volume Method (FVM) results. Computing times, t_{cpu} , are measured for a time integration of $t = [0, 1]$.

the scheme of *Piacsek and Williams* [1970] for the non-linear advection of momentum. At the 33×33 grid the flow becomes oscillatory at $t \approx 0.45$ and later on more frequencies appear. This is not surprising since integrating the Gaussian heat source at this grid yields a value of 1.66, decreasing to 1.03 and 1.00 on a 65×65 and 129×129 grid, respectively. Thus, at coarse grids, effectively the Ra number is increased by a false representation of the heat source. With these simulations a better convergence can be observed, which is thus not surprising. Due to the differences in the total heating rate, as caused by the poor representation of the source distribution, the simulations do not converge to a sufficient precision. This could be improved by a correction factor for the total heating rate or by using a source width that can be resolved on all grids. With the spectral method at the highest accuracy it was found that the flow bifurcates to periodic motion at $t \approx 2.0$. This does not mean that the SEM solution is inferior. This point will be discussed in the paragraph on unsteady plume motion hereafter.

Simulations as performed with the FVM at low spatial resolution seem to be advantageous compared to the SEM from the viewpoint of computational effort as measured by the CPU-times. Double spatial resolution in the FVM is accompanied by a double temporal resolution in order to assure numerical stability. For a two-dimensional problem this results in an eight-fold increase of CPU-time. The reason for the progressive increase when refining to the highest resolution is due to the fact that 129 is not highly composite, resulting in a relative large computational effort in solving the Poisson problem. In the SEM the time-steps were decreased linearly with the order of approximation. Therefore an increase in the CPU-time for subsequent simulations is expected with a factor $27/8$ and $64/27$. In the practical simulations the proportionality seems to be somewhat less. Thus, for the two dimensional case the two methods used are quite competing. Implementing subgrid-scale models is much easier in the FVM method.

A source width of $\sigma = 4 \cdot 10^{-2}$ can be resolved on all grids. For this case calculations have been performed of which the results are displayed in table 4.3. For most of the variables the convergence seems to be quadratic, except for w_2 . This is due to the non-linearity of the problem. The property of having quadratic convergence using a second-order accurate method is only guaranteed for linear problems at sufficient resolution.

4.2.4 Oscillating plumes

To examine the instationary behaviour of the plume and to check the computational method in this case, first a simulation was performed at a Rayleigh number $3.2 \cdot 10^7$ on a 65×65 grid. The computation was started from the solution on the same grid at $t = 1$ and $Ra = 3.0 \cdot 10^7$ using the method of *Piacsek and Williams* [1970]. The flow showed a bifurcation at $t \approx 2.0$ both for the central and upwind calculations. The fundamental frequency in both simulations is equal to 305.2

grid	ψ_{\max}	u_2	w_2	w_3	T_3
33 × 33	69.17	121.0	-49.83	706.8	0.040
65 × 65	72.80	112.3	-47.06	694.9	0.043
129 × 129	73.66	106.1	-44.32	688.9	0.044

Table 4.3: Results for $Ra = 3.0 \cdot 10^7$ with a Gaussian source of $\sigma = 4 \cdot 10^{-2}$

± 6.1 , where D&L give a value of 299.7, with a minimal accuracy of ± 16 (not explicitly given for every separate case). It can be concluded that the results are the same within the given accuracies.

Using the alternative discretization methods for the non-linear advection results in a similar behaviour. There is only a small time difference of maximal 0.03 in the instant at which the oscillation sets in. Due to this lag the phases differ, but the frequencies and amplitudes are the same.

In order to investigate the instationary behaviour of the plumes more thoroughly, the second-order upwinding technique of *van Leer* [1974] for the advection of temperature is used together with the method of *Piacsek and Williams* [1970] to discretize the non-linear advection in the momentum equation.

Since the fact that with the SEM an oscillating plume was found at $Ra = 3.0 \cdot 10^7$, one might wonder to what extent the bifurcation point depends on the numerical method and the resolution used. Comparing present results from the FVM and SEM with those of D&L might give some impression of the performance of the various methods. First, applying the above specified discretization method, the bifurcation point was determined at a resolution of 65×65 grid points. Prescribing different forcing rates, ranging from $Ra = 3.1 \cdot 10^7$ up to $Ra = 3.5 \cdot 10^7$ with step $0.1 \cdot 10^7$, the transient time together with the amplitudes a_{u_1} and a_{u_2} of u_1 and u_2 are determined. The transient time, t_{trans} , is defined as the length of the period from $t = 0$ up to the instant at which the heat flux through the top, q''_{top} , of the confinement reaches a minimum after the oscillation sets in. This instant is depicted in figure 4.5 for $Ra = 3.5 \cdot 10^7$. Also the fundamental frequency, f_{fund} , of the oscillations was determined and compared to those of D&L. These amplitudes, transition times and frequencies are given in table 4.4.

The frequencies of the oscillating plumes are the same within the given accuracies. The variation of the amplitudes with the forcing is depicted in figure 4.6. Using these data the bifurcation point is localized by extrapolating the data of the lowest two forcing rates to zero amplitude. Thus the bifurcation point is localized around $Ra = 2.8 \cdot 10^7$, somewhat lower than the value $Ra = 3.0 \cdot 10^7$ of D&L. Also the transient time at $Ra = 3.1 \cdot 10^7$ was found to be shorter than the value of D&L, being $t_{\text{trans}} \approx 5$. The amplitude of u_2 indicates a little difference in the bifurcation point compared to the other two tendencies. This may be due

Ra	t_{trans}	a_{u_1}	a_{u_2}	f_{fund}	$f_{\text{fund}} (\pm 16) \text{ D\&L}$
$3.1 \cdot 10^7$	2.19	43.8	13.7	301 ± 1.5	294
$3.2 \cdot 10^7$	1.65	50.4	15.6	305 ± 6.1	300
$3.3 \cdot 10^7$	1.33	56.1	17.0	311 ± 6.1	305
$3.4 \cdot 10^7$	1.11	60.9	18.2	317 ± 6.1	310
$3.5 \cdot 10^7$	0.98	65.2	19.1	320 ± 1.5	315

Table 4.4: Transition time, amplitudes and fundamental frequency at several forcing rates.

to convergence of this value, that may be insufficient. At the present 65×65 grid the second frequency does not appear yet at the highest two forcing rates.

At a higher resolution it was found that the transient time becomes a little smaller and the frequency somewhat higher. Also using the SEM with an 8×8 grid and an eight-order approximation at $Ra = 3.0 \cdot 10^7$ results in an oscillating plume with fundamental frequency 318.6 ± 1.2 after an elapsed transient time of magnitude $t \approx 2$.

All summarized results of present simulations indicate a lower bifurcation point compared to the value assigned to it by D&L, of $Ra = 3.0 \cdot 10^7$. Increasing the grid resolution seems to result in a value even somewhat below $Ra = 2.8 \cdot 10^7$.

4.2.5 Conclusions

On the basis of the above results a discretization is chosen for all subsequent simulations. Representation of the advection of scalars like temperature and subgrid kinetic energy will be performed with the second-order upwinding scheme of *van Leer* [1974], because of its ability to represent the pure advection of almost any profile with relatively good accuracy (see appendix C). Besides it gives physically more correct results in case the grid resolution is on the poor side, as found from the stationary calculations. This is obtained at the expense of an increased computational effort, for this single term, of a factor two compared to central discretization. This means that the overall increase per time-step is about 15 %.

For the advection of momentum the scheme of *Piacsek and Williams* [1970] is preferred. It gives results comparable to the conservative and advective second-order discretizations as outlined in appendix B, and may be slightly cheaper in computational effort.

The chosen schemes seem to be preferable from the interpretation of present results. Furthermore, very similar results are found comparing present calculations with those of D&L. Differences in any considered variable do not exceed a few percents, both in the stationary case and in the unsteady cases. For the

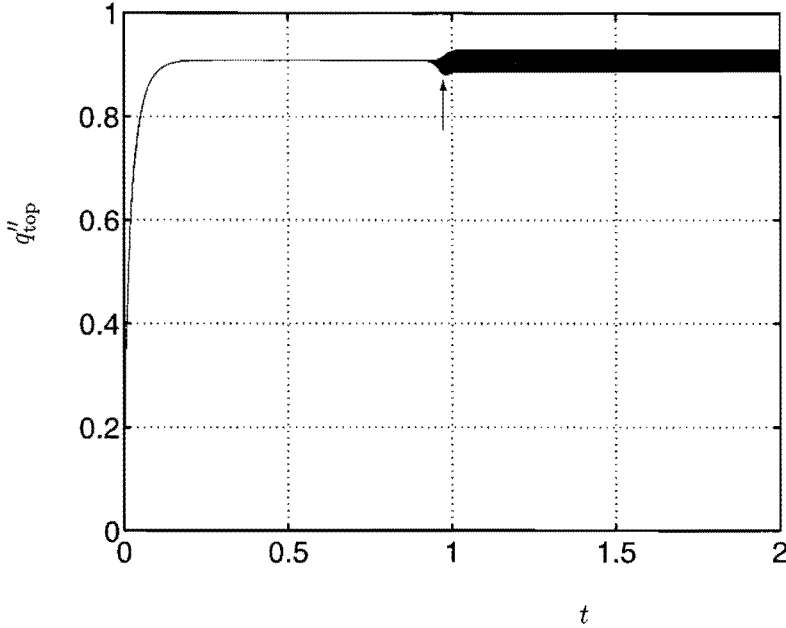


Figure 4.5: Definition of the transient time for $Ra = 3.5 \cdot 10^7$.

difference of the bifurcation point this margin holds as well.

A grid refinement study and the additional SEM calculation support that the bifurcation point is somewhat lower than the estimated value $Ra_c = 3.0 \cdot 10^7$ as obtained by D&L. The present estimation is $Ra_c \leq 2.8 \cdot 10^7$. Inaccuracy of boundary conditions seem to have a minor impact on the solutions for highly advective plume flows. Employing the present FVM, a fair accuracy is obtained at moderate grid resolution, and related to it, computational effort.

4.2.6 Epilogue

With respect to the discretization of the subgrid scale models to be used in the LESs there are no tests carried out involving flow problems. In the previous direct numerical simulations the diffusion is adequately represented. Otherwise the subtle balance between different terms would be disturbed and the bifurcation would be represented very poorly. The additional feature that comes into play within the application of eddy viscosity models is the spatial variation of the diffusion coefficient. This artefact should have no consequences with respect to the discretization used. Furthermore, test cases of well defined, method independent turbulent natural convection flows, are not known to exist. In cases involving additional discretization features, these will be documented where they occur.

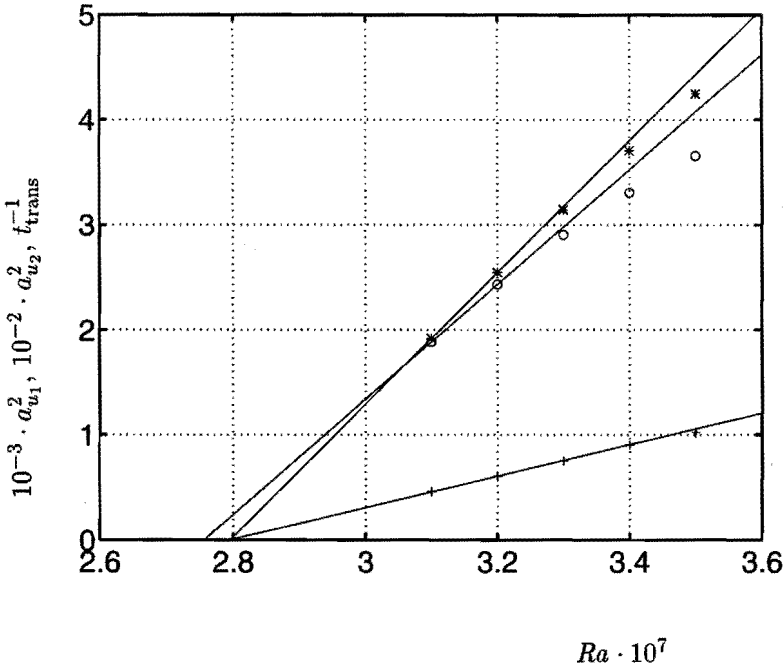


Figure 4.6: Squared amplitudes and inverted transient time as function of Ra . $10^{-3} \cdot a_{u_1}^2$: *, $10^{-2} \cdot a_{u_2}^2$: o, t_{trans}^{-1} : +

Further on in this thesis, flows to be considered are defined by much higher forcing rates. These flows will become three-dimensional and can not be compared in detail anymore. Firstly, because of the loss of correlation between identical situations, up to any finite precision. This is due to the highly chaotical character of the flow as discussed in chapter 2. Secondly because the considered flows exhibit a complicated structure in time as well as in space.

At high forcing rates a direct detailed comparison is not appropriate anymore. At the moment there are mainly two ways of dealing with this fact. First, as will be the case in this thesis, statistics will be compared. Mainly mean flow quantities and standard deviations will be used, but also spectra, quantifying the contributions of isolated spatial and temporal Fourier modes. On the other hand, in turbulence research, coherent structures are often compared. This originates from the philosophy that the flow organizes itself by creating typical persistent structures that appear very often at more or less random locations. This analysis will not be followed in the present study because first a sufficient matching in terms of statistics has to be satisfied.

Chapter 5

Laboratory measurements

5.1 Introduction

To validate the numerical results an experimental setup was designed. The objective is to realize a setup in which a well defined transitional plume flow can be analyzed in detail. In a physical experiment, the number, resolution and accuracy of data that can be sampled is considerably less than in a numerical simulation. Also it is not possible to specify boundary conditions very accurately. However, it is aimed to obtain results that are at least comparable to data that can be acquired with numerical models. Hence, on the one hand the flow configuration is chosen as to show the intended flow regime. On the other hand the configuration must possess the property of having a low sensitivity with respect to the boundary conditions that are not actively controlled.

In thermal convection problems the most interesting features are the temperature and velocity distributions, both spatially and temporally. Measuring these field data involves non-invasive methods, i.e. techniques in which the intrusion is kept at an acceptable low level. Extracting complete 3D data fields from experiments is hardly possible yet. Full 3D measurements of temperature fields may be obtained by tomographic methods. However this can only be achieved with high financial expenses. Measurement of 2D temperature fields can be done in several ways. As will be outlined in the next section, in the present study use is made of shadowgraphy as a qualitative tool. Another method regards the use of the reflectometric properties of liquid crystals, as function of the temperature. Liquid crystal thermography (LCT), as described by *Sillekens* [1995], was attempted. Yet, the spectral resolution is estimated to be too low to obtain reliable time dependent 2D field information. The qualitative field information is comparable to the shadowgraphic images.

Velocity field measurements are somewhat easier to perform. In fact it has a quite long tradition by means of, for example, using streak photography. In applying streak photography, particles or flakes are suspended in the fluid or, in

case of a free surface, are put on top of it. Adjustment of a proper shutter time with respect to the occurring velocities results in a streak image. From these images the $2D$ velocity components can be determined by measuring the streaks. Though, a priori knowledge of the direction must be added. In stationary flow the streak image constitutes a streamline plot. In the past, the streak length was measured manually. Nowadays, by digitizing and analyzing the images automatically, quantitative information can be acquired much faster. At the moment the first results of relative high resolution $3D$ velocity measurements appear in literature. For the time being, in reducing experimental and data processing complexity, $2D$ measurements are preferred. From $2D$ data, spatial derivatives and two-dimensional dynamics can still be obtained, a main advantage of field measurements. For an overview of image analysis techniques the reader is referred to *Adrian* [1991] and *Nieuwstadt* [1993].

In thermal convection the temperature and velocity fields are highly coupled. Because of this and the above mentioned facts, it is chosen to perform $2D$ velocity measurements, supported with local temperature measurements. The temperature measurements are performed with thermocouples and stored on file. Velocities are determined with particle tracking velocimetry (PTV). Additionally, shadowgraphy is used as a qualitative tool to adjust the heating rate to a value that causes the flow to show a spatial transition. The experimental techniques as exploited will be outlined in the last section of this chapter.

Before that, first the experimental setup is discussed. Basically it consists of a container filled with water. The water is subjected to a heat source present in the container, resulting in a plume. The induced flow that we aim for is of a quasi two-dimensional nature. Therefore the heat source consists of a prismatic element. The element releases a two-dimensional laminar plume, which converts in a much broader, turbulent three-dimensional flow downstream. The design of the setup is constrained by numerical and physical artefacts. An optimization for the design is needed. This and the adjustment of the forcing of the flow will also be discussed.

5.2 Experimental setup

5.2.1 Construction

A schematic drawing of the setup is given in figure 5.1. Following the arguments that will be outlined in the next subsection, the dimensions of the flow domain are taken to be $W \times H \times D = 0.3 \times 0.2 \times 0.2 \text{ m}$. In the domain an electrical heating element is mounted, which has the form of a strip of size $W \times H \times D = 0.002 \times 0.02 \times 0.2 \text{ m}$. It is positioned in the symmetry plane, its lower side at a height of 0.01 m . At the heat flux intended, the size of the element's surface is needed to keep the temperature differences in the fluid within a range of 5° C .

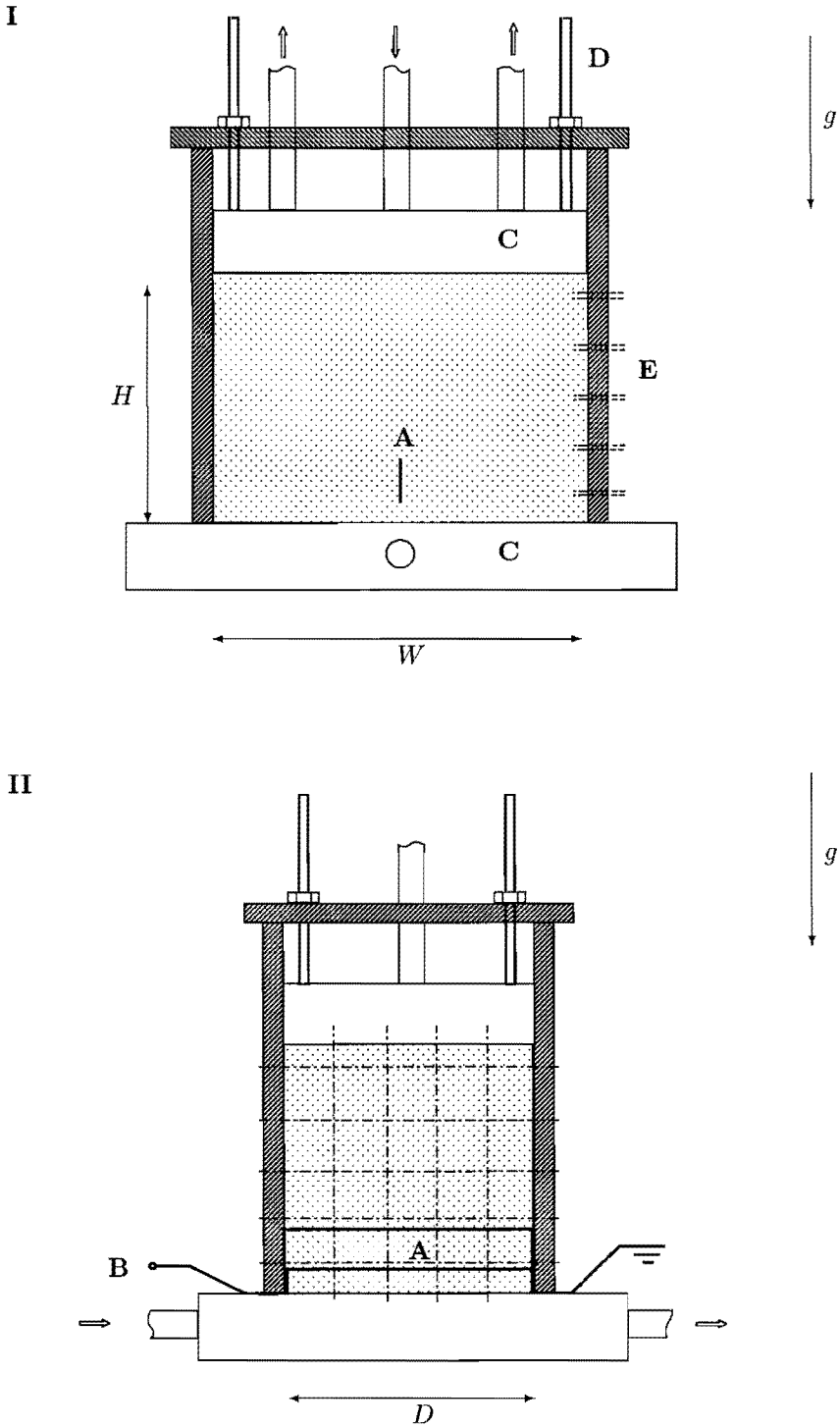


Figure 5.1: The experimental setup: I front view, II side view; A heating element, B power supply, C heat exchangers, D aspect ratio adjustment, E probe access matrix.

The vertical orientation of the heat source yields a laminar plane plume release at a well defined, fixed position. The heating element consists of a customer specified flexible *Kapton*[®] heater¹ with a resistance of 5 Ω . Two strips of copper are stuck to the sides to decrease the flexibility. The orientation of the resistant material in the flexible heating strip is in longitudinal direction. A direct current power supply is used with an adjustable range up to 50 V and 10 A. Using this configuration, Ra (as defined by 2.17) could be varied from zero to $4.6 \cdot 10^{11}$ at an ambient temperature of 20° C and to $1.0 \cdot 10^{12}$ at a temperature of 35° C. At the maximum heating rate the mentioned temperatures correspond to the start of the experiment and the equilibrium temperature, respectively. Due to this temperature increase Pr drops from 6.9 to 4.8. At the start the heating element has to warm up before it begins to emit the heat to the water. The time constant of this starting effect is $\tau_{el} = \rho c_p V / \alpha A$, attaining a value of about 3 s.

The experimental cavity is equipped with confining top and bottom heat exchangers. The heat exchangers are supplied by water from a tank by a centrifugal pump at a rate of about $1 \cdot 10^{-4} \text{ m}^3/\text{s}$. The height of the top heat exchanger is made adjustable and a small gap between the heat exchanger and the wall is maintained. In this way the heating causes no hydrostatic pressure effects. From the heat exchangers the water flows back to the tank. The temperature in the tank is controlled by a *Julabo P1* thermostatic heater in combination with a cooler. The volume of the tank is ca. 0.1 m^3 and the power of the heater is 1.6 kW. The cooler consists of a coiled copper tube, connected to the water grid, supplying water at a temperature of ca. 14° C and at a rate of $2 \cdot 10^{-4} \text{ m}^3/\text{s}$. Thus, the temperature in the heat exchanger circuits is kept constant. Under the experimental conditions there is no problem in attaining a constant temperature with an accuracy of 0.1° C.

The side walls of the confinement are made of 0.01 m thick glass. The thickness of the walls ensured a heat loss through the sides, relatively small compared to the controlled heat exchange through top and bottom walls. In case of the maximum heating rate of 500 W, in the statistical steady state, the heat losses through the side walls are estimated to be 2 %. This relative amount of heat loss may be assumed to be constant, also at lower heating rates.

With the use of glass the flow domain is optically accessible. This is required for the performance of shadowgraphy and PTV. At one side of the flow domain a matrix of probe access holes of inner diameter 0.003 m are made. These could be sealed, both in the presence of a probe and in the absence of it.

As a successor of previously utilized setups the presently used configuration is empirically optimized as to possess a relative high reproducibility of observed flow phenomena. Top and bottom heat exchangers offer the feature of adjusting a prescribed homogeneous temperature at the start. Furthermore, after establishment of a recirculating plume flow, top cooling provides a downflow centred

¹*Kapton* is a registered trademark of E.I. DuPont Company

around the rising plume. In previous experiments it is observed that employing an approximate adiabatic top may result very easily in asymmetrical bifurcated flow, due to uncontrollable heat losses. The present configuration creates a more symmetrical flow, at least statistically. The bottom heat exchanger enforces a stratification up to the recirculating convection region. The heat source is embedded in the stratified layer. Together with the vertical orientation of the source this results in a well defined vertical plume release.

5.2.2 Constraints

The dimensions of the configuration and the positioning of the heat source are constrained by a number of requirements. Since water is used, the acceptable temperature range that may be exploited, is limited. This is due to physical and numerical reasons, the latter being more severe. These aspects will be discussed next to elucidate the design and to provide a framework for the interpretation of the experimental results.

Physical limitations

For the heating, in principal a line source is intended to be used, having zero surface area. The consequence is that at constant heating rate, temperatures will increase with the decrease of the size of the heating element. The temperatures that will be observed depend on the heat flux density at the surface area of the heating element. Since we want to have a flow medium consisting of just one continuous phase, temperatures are limited to the range zero to about $60^{\circ} C$. The latter is due to the starting of desaeration of the water, leading to the formation and release of bubbles. On the other hand, in order to obtain a shadowgraphical image, the temperature differences in the field must be large enough.

In order to attain large enough Rayleigh numbers, Ra , under the restriction of a limited temperature difference, the size of the enclosure must be large enough. This decreases also the maximal occurring frequencies and wave numbers in the flow. This may be regarded as favourable with respect to the size of the experimental spatial and temporal sampling rates.

In earlier attempts (*van der Burgt* [1994]) a horizontally mounted element at the bottom of a container was used, which yielded turbulent flow straight from the source at lower Ra and thus at lower temperature differences. At values of Ra where the images of shadowgraphy became visible the horizontal strip acted already as a heated flat plate. Mushroom shaped thermals are released from nucleation points, being more or less randomly distributed over the strip. Besides the problem with the shadowgraphy, decreasing Ra in this case results in an increased time scale. It also gives difficulties with detecting temperature differences.

The aspect ratio of the domain prevents the plume from sticking to a side

wall as observed experimentally and reported by *Jaluria* [1985]. This was verified by calculations as performed by *Desrayaud and Lauriat* [1993] and *Minev et al.* [1995b]. Exploiting confining heat exchangers, besides a hydrodynamical quasi steady state also a thermal quasi steady state may be achieved. The word quasi means that this steady state holds only for time averaged quantities, with an averaging period taken sufficiently long. Especially the top heat exchanger decreases the time constant for saturation of the integrating thermal system. At the Ra numbers under consideration the advective time scale is imposed by the overall heat exchange coefficient α . This time scale is given by $\tau_a^T \sim \rho c_p H / \alpha$, and it is much shorter than the conductive time scale, $\tau_d^T \sim H^2 / \kappa$. An estimated overall heat exchange coefficient $\alpha = \mathcal{O}(10^3)$ results in a ratio of the time scales being $\lambda / \alpha H = \mathcal{O}(10^{-2})$. The time constant for the present configuration becomes $\tau_a^T = \mathcal{O}(10^3)$ s.

Numerical limitations

The results of the physical experiments to be performed are subjected to comparison with data provided by numerical simulations. Therefore it must be possible to simulate the flow with sufficient accuracy. This means that the experimental situation together with boundary conditions have to be similar to the physical model. In applying simulations of the Boussinesq approximated equations there are severe restrictions on the temperature differences in the flow field. According to *Gray and Giorgini* [1976] the temperatures may not exceed a certain limiting range. Within this range the maximal error for different terms in the Boussinesq approximated equations are smaller than 10 %. They determined the ranges due to non-constantness of the volumetric expansion coefficient, β , the dynamic viscosity, $\rho\nu$, and the conductivity, λ , to be $1.25^\circ C$, $3.7^\circ C$ and $59^\circ C$, respectively. Using simulations of the full equations and the Boussinesq approximated equations, *Heiss* [1987] and *Lankhorst* [1991] found differences in the velocity field of lower than 10 % for temperature ranges lower than $5^\circ C$. Of course, the range around a temperature of $4^\circ C$ is strictly forbidden due to the local maximal density of water at this value.

It must be remarked that with the prescription of a constant heat flux the temperature differences are constant, although the mean temperature rises. This leads to a quasi steady state for the hydrodynamical and thermal fluctuations, after a short transient. Also the mean value of the velocity will become steady in a relatively short time whereas the mean temperature increases up to a saturation value, determined by a balance of heat input and drain.

5.2.3 Flow regime adjustment

In order to find the transitional flow regime, shadowgraphy is used to adjust the heat flux by visual inspection of the resulting qualitative projection. The

image arises due to the differential refraction of light as a consequence of the density differences caused by varying temperature gradients. Gradually varying light intensities on a screen constitute the image. By putting a light source in line with the heat source and a semi transparent projection screen on the other side of the setup the flow may be visualized. In this way a proper heat flux can be adjusted. Having this heat flux, the transition is positioned at approximately half way the vertical extent of the flow domain.

With the aid of shadowgraphy it is observed that a transitional flow as obtained with the present configuration is highly intermittent. Two coherent phenomena can be discerned quite clearly. In a relatively large amount of time an oscillation is present in the thermal plume. The spatial start of this oscillation moves irregularly along the laminar plume. Also this structure ensemble sways and twists irregularly. At a few moments in time an alternating shedding of vortical dipolar structures can be observed. This was most profound in experiments with an adiabatic top wall, as performed by *van der Burgt* [1994]. In this case there is no buoyancy produced by a cooling top wall and a stable thermal stratification influences the flow field. A typical example of the latter phenomenon is given in figure 5.2. Both phenomena occur irregularly in time and space.

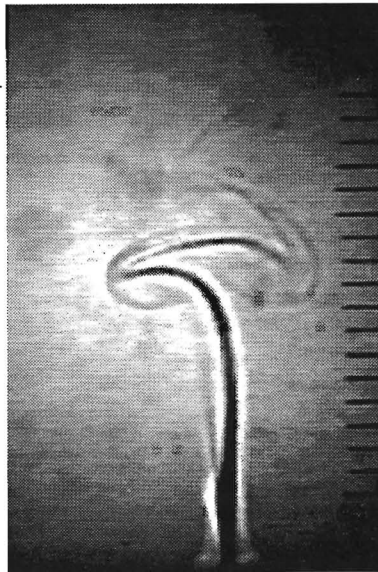


Figure 5.2: Typical vortex shedding transition phenomenon

5.3 Measurement techniques

5.3.1 Thermocouples

Principle and configuration

The working principle of thermocouples is the so-called Seebeck effect. It is the production of a small thermoelectric voltage difference at the interface of two dissimilar metals as function of the temperature. Therefore thermocouples consist of two dissimilar metal wires joined together at one end. Using a metal combination with a highly constant voltage to temperature ratio, temperatures can be measured accurately.

The thermocouples used are of type *Thermocoax* TKI05/25/D. These are K-type thermocouples, having a chromel-alumel junction with a sensitivity of $41 \mu V/^\circ C$. The actual thermocouple wires are covered with a sheath of inconel alloy 600, for mechanical and chemical protection. In between there is insulating material of mineral oxide. The outer diameter of the sheath is 0.5 mm . The hot junction is insulated from the sheath. The response time in still air as given by the manufacturer is 1.2 s . With this value the response time in water can be estimated by $\tau_{\text{water}} = \tau_{\text{air}} \kappa_{\text{air}} / \kappa_{\text{water}} \approx \mathcal{O}(10^{-2}) \text{ s}$, with κ the coefficient of thermal diffusion.

The thermoelectric signal is supplied to an A/D-converter as an interface to computer storage. The converter is of type *MINI-16* of Strawberry Tree Inc.. It has eight analog input channels with 16-bit resolution and an input range of 25 mV . These values in combination with K type thermocouples span a range of $625^\circ C$, with a resolution of $0.01^\circ C$. The converter is equipped with a cold junction compensation and linearization for several thermocouple types, and a timer for precision timing.

The data acquisition is performed by use of the software package *Quicklog PC* of Strawberry Tree Inc., which runs on a 40 Mhz 386 SX PC. In normal mode the sampling rate of logging to file is limited to about 10 Hz using 4 channels. The timesteps between subsequent logs, then, are not equally sized. In "fast mode" it is possible to acquire data at the full rated speed of the hardware. In this mode a block of data is read as a burst into memory. While it is reading data the computer is only dedicated to this single task. Now the sampling spaces are equal but the size of a burst is limited. In the configuration used the maximum burst size is 16000 data, i.e. temperature samples.

The chosen sample rate is 25 Hz , being the same as the maximal sample rate of the video frames used in the PTV. Moreover this frequency corresponds to time intervals of 4 times the response time, yielding an accuracy of $(1 - e^{-4})$ or 98 % for step responses. An estimate of the occurring physical frequencies is obtained by a preliminary measurement.

The thermocouples are supported by tubes with a diameter of 2 mm . The tubes lead the temperature gauges through the probe access holes and position

them at the correct location. At the end of the tubes the thermocouples are protruding out of it by a few centimeters. At this point there is a seal to avoid leakage. The invasiveness of the thermocouple and its support can best be expressed by its Reynolds number. Using the laminar boundary layer solution the maximum velocity at $Ra = 10^{12}$ is about 0.05 m/s . At the position where this occurs, using the diameter of the thermocouple, the perturbative Reynolds number is approximately 20. This may be considered small enough to prevent the occurrence of downstream von Kármán vortex shedding.

Preliminary measurement

Preliminary thermocouple measurements are performed to confirm the estimations as given in the previous section. Also additional information concerning frequencies and distributions may be obtained. Therefore a measurement was carried out at the maximum heat input, being 464 W . For convenience all values will be given here in full dimension. Scaling can only be performed when the thermal diffusivity is known. This quantity is a function of temperature. The present measurements can be used to obtain a suitable ambient temperature needed for the scaling.

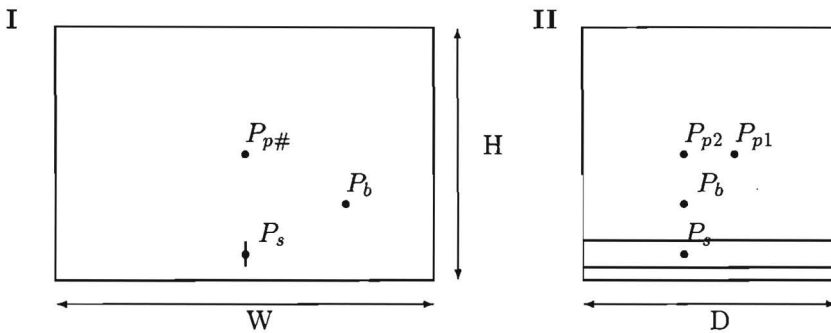


Figure 5.3: Positions of temperature gauges: I front view, II side view

At the maximum heat input, temperatures are measured at four locations in the flow. These locations are at the source, point P_s , at two positions in the middle of the plume 0.04 m apart in the direction of the heat source, P_{p1} and P_{p2} , and in the recirculating bulk, P_b , as depicted in figure 5.3. The coordinates of these points measured in centimeters from the left-bottom-front corner of the confinement are $P_s = (15, 8, 2)$, $P_{p1} = (15, 12, 10)$, $P_{p2} = (15, 8, 10)$ and $P_b = (23, 8, 6)$, respectively. Here, the heat exchangers are kept at a temperature of 20.2° C , whereas the ambient temperature has a value of 19.5° C .

In figure 5.4 the initial increase in temperature of the thermal element is depicted. The earlier mentioned time constant for reaching 63% of the total

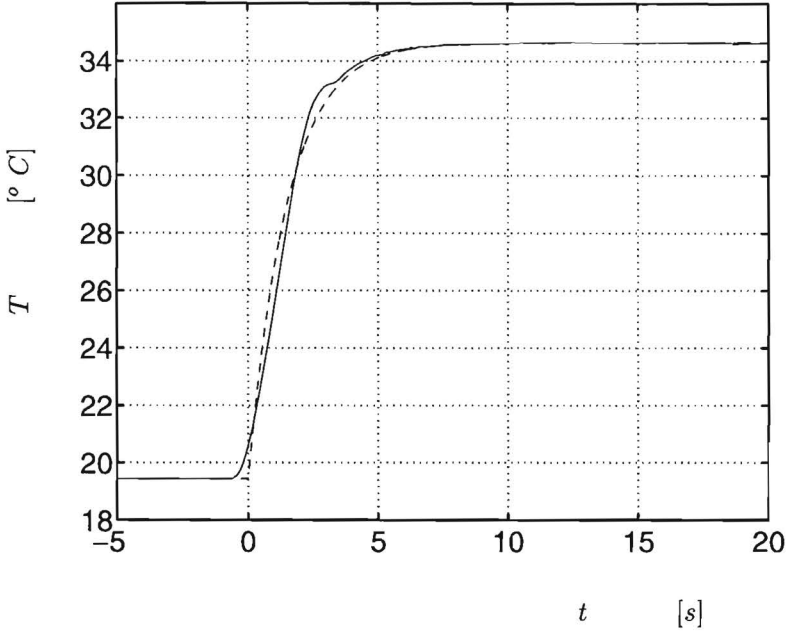


Figure 5.4: Measured and fitted starting behaviour of the heating element

temperature increase of 3 s seems to be an overestimation. This is due to the uncertainty in the heat transfer coefficient. The plot shows a fit with τ_{el} equal to 1.5 s. This starting effect has to be taken into account in the numerical simulations.

In figure 5.5 the temperatures in points P_{p1} and P_b are plotted as function of time. The temperatures in P_{p1} and P_{p2} have the same characteristics. Therefore in figure 5.5 only the temperature at P_{p1} is plotted. It can be observed that there is an integral heating of the system with respect to time, which is similar for both plotted points. The time constant τ_a^T of this heating effect is about 1600 s. At the end of the measurement, which is after approximately $3\tau_a^T$, a thermal equilibrium is reached. The amplitude of the temperature fluctuations in the bulk is much smaller than that in the plume, due to downstream mixing. The minimum temperature in the plume is at every time approximately equal to the instantaneous temperature in the bulk. This can be explained by the fact that there is entrainment in the plume. Fluid from the ambient, having bulk temperature, is entrained into the plume.

As mentioned already, the measured values in points P_{p1} and P_{p2} are similar. This similarity is most profound in statistical measures of the fluctuations. The distribution of the fluctuations is best expressed by the power spectral density and the probability density. For obtaining the latter the integral heating up of the

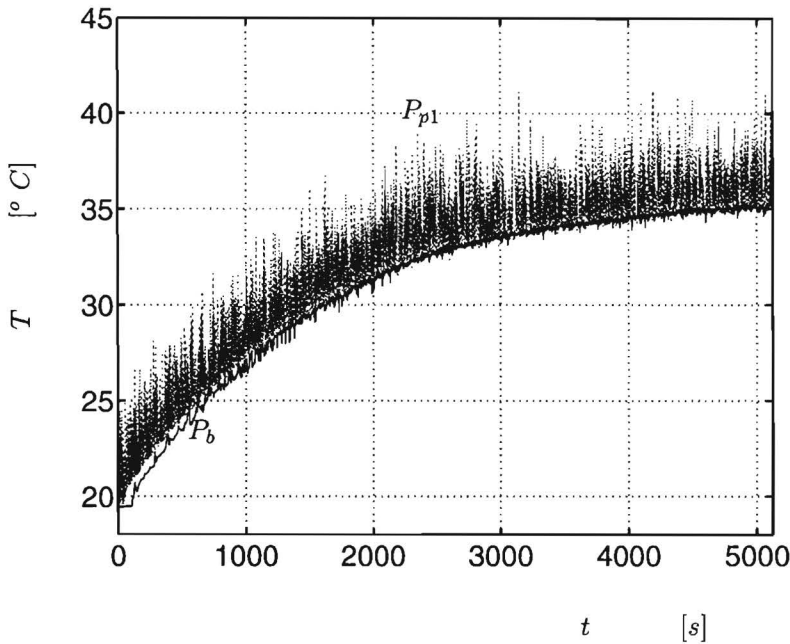


Figure 5.5: Temperature as function of time, dotted: P_{p1} , full line: P_b

system must be subtracted of the total signal. For this heating the function $T_{\text{int}} = T_0 + \Delta T \cdot (1 - \exp(-t/\tau))$ is taken, with $T_0 = 20^\circ \text{C}$, $\Delta T = 16^\circ \text{C}$ and $\tau = 1600 \text{ s}$. The obtained probability density is given in figure 5.6, whereas the power spectral density is depicted in figure 5.7. The probability density, or briefly distribution, possesses a large skewness, while for isotropic turbulence a symmetric profile is expected. Water of a certain minimal ambient temperature is entrained into the plume. Because of this the left tail falls off relatively quickly. The temperature distribution in the bulk is more Gaussian but due to the smaller fluctuations, and therefore the relative importance of long time scales, this distribution is less converged. The power spectral density shows at low frequencies a slow decay that increases up to higher frequencies. An energy containing range is visible up to a frequency of 1 Hz , whereas up to 5 Hz most energy is resolved. A more detailed comparison of the original signals is shown in figure 5.8. At the start there is a high correlation, indicating a two-dimensional flow field. After a short time the flow becomes three-dimensional and the correlation vanishes. The statistical quantities remain the same. The change in physical properties with increase in mean temperature and the accompanying variations in the Rayleigh and Prandtl numbers do not have a noticeable influence on the statistics.

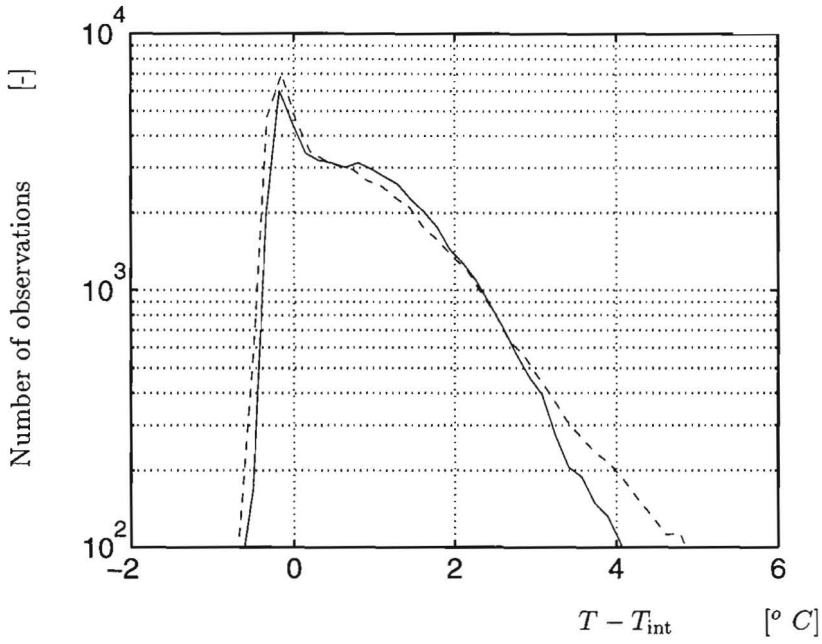


Figure 5.6: Temperature distribution, full line: P_{p1} , dashed: P_{p2}

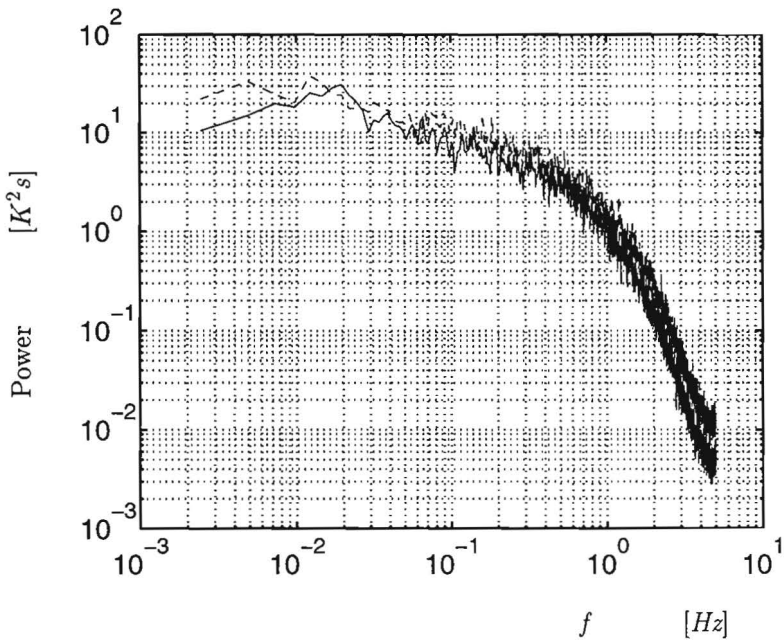


Figure 5.7: Spectral density of the temperature signal, full line: P_{p1} , dashed: P_{p2}

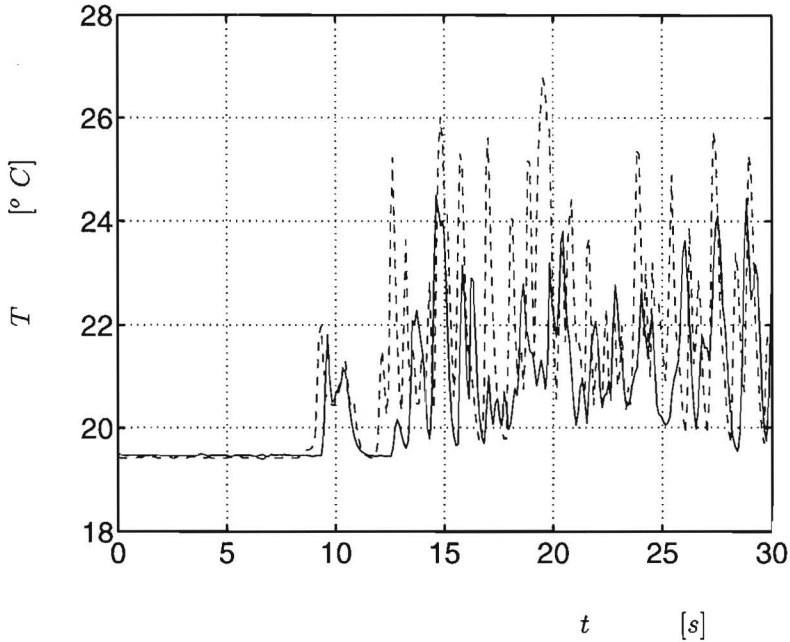


Figure 5.8: Temperature as function of time, full line: P_{p1} , dashed: P_{p2}

5.3.2 Particle tracking velocimetry

Optical arrangement

The flow is illuminated by intersection of the domain with a sheet of light, provided by two slide projectors, equipped with 250 W halogen light bulbs. Because of the obstruction of the light by the heating element and the intensity decrease due to the seeding and the diverging light beam, light sources at both sides of the setup are used. The light sheet is confined to approximately 5 mm thickness by a slit cut in matt black cardboard, covering the sides of the setup. Also the back of the setup is covered to eliminate the influence of indirect light. The entire configuration is placed in a dark room.

The flow is seeded using *Optimage NB3* particles with a typical size of 100 μm in a concentration of about 0.001 Vol.%. The particles are first wetted in a small amount of ethanol (± 0.1 Vol.%) to prevent them from adhering to the surface. After addition of the particle/ethanol mixture the top heat exchanger is positioned. The density of the particles is $\rho_p = 1000 \pm 20 \text{ kg/m}^3$ and they are polycrystalline in structure giving them a high scattering efficiency of light.

The image of the particles illuminated by the light sheet is recorded on Super-VHS tape using a 3 CCD Super-VHS camera, equipped with a zoom lens (VCR: *Panasonic AG-7350*, camera: *JVC KY-F30*). The resolution of the camera is

625 × 625 at 25 Hz for full frames, consisting of two interlaced fields of odd and even lines. The horizontal × vertical resolution of the VCR is > 400 × 625 lines.

Use is made of LEDs indicating reference points and the starting point of the experiment. Exploiting the reference points eliminates possible vibrations. At the beginning of an experiment a lighting LED marks exactly the starting moment. A grid is used defining world coordinates to map the recorded geometry to the physical geometry. The difference originates from optical deformations like the aberration of the camera lens. Before starting the experiment a recording is made of this grid in situ, for use in later processing.

Tracking algorithm

The actual tracking algorithm consists of three parts: (i) image acquisition and enhancement, (ii) particle detection and location and (iii) particle matching. These tasks are performed with the computer package *DigImage* as a basis (*Dalziel* [1993]). This package runs on a 486 DX PC and is able to control the VCR. The algorithm was developed with emphasis on simplicity and efficiency. The latter is needed to obtain large numbers of field files, which are necessary to describe turbulence statistics.

After recording an experiment a well defined audio pulse is added to the audio channel of the video tape. The audio pulse is used as a time correction signal. The correct frame is acquired using a *Data Translation DT-2862* arithmetic frame grabber, with a resolution of 512 × 512, 8 bit each. The VCR is controlled by the PC in order to perform image acquisition of the exact frame while the VCR is in "play" mode. The first video field to be grabbed is defined by the increasing intensity of a LED that defines the start of the experiment. After acquisition of the right frame a background image is subtracted to amplify the instantaneous character of the image. The background image is constructed by taking a long time average of the digitized video fields. Then a minmax filter is applied removing background variations with an extent larger than the maximum allowed particle size.

Next, the reference points are located and the differences with the reference coordinate system are calculated. If the error exceeds a preset limit a new attempt is made to acquire the image. The reference mapping is used to determine the world coordinates of the current image. This is performed by mapping a least squares bi-quadratic polynomial as obtained from the world coordinates.

Particles are located by making use of an intensity threshold above which a region is considered to be a particle. To determine the validity of the speckle being a particle, the shape, size and intensity characteristics of such a particle are checked against the allowable limits. The position of a valid particle is determined by taking the intensity centroid. Location in this way gives subpixel accuracy. Having particles extending at least three pixels in each direction, the location has an accuracy of better than 0.2 pixels.

The matching algorithm will be described very briefly, for details the reader is referred to *Dalziel* [1993]. The method is based on a transportation algorithm, a technique frequently used in operations research for determining optimal associations between two sets. The sets are two particle images P and Q at time levels t^n and t^{n+1} , respectively. Particles p_i are defined for $i = 1, M$ and q_j for $j = 1, N$. Associations are defined by $\alpha_{ij} = 1$ if particle p_i at t^n is considered the same as q_j at t^{n+1} . Otherwise α_{ij} is identical to zero. To define the optimal set of pairings a cost function c_{ij} for the association α_{ij} is defined, expressing the likelihood of the pairing. High c_{ij} means a low likelihood for the pairing. The basic idea is to minimize the object function ζ , constituting the summarized weighted association:

$$\zeta = \alpha_{ij}c_{ij} \quad (5.1)$$

The algorithm used to minimize ζ makes use of relational indices in order to maintain unique pairings, i.e. for each matrix index i and j separate there is exactly one α_{ij} that equals unity. This algorithm is given in appendix D.

To quantify the cost or likelihood of a matching, c_{ij} , a pricing policy has to be defined. It consists of assigning a minimal cost to associations that are closest to an expected pairing. The expectation is determined from an Euler forward advection of a particle in frame P over a time step $\delta t = t^{n+1} - t^n$. Then the cost is defined as the squared distance between an actual particle position q_j and the estimation:

$$c_{ij} = \|\mathbf{x}_i + \mathbf{u}_i\delta t - \mathbf{x}_j\|^2 \quad (5.2)$$

Here an estimation of the velocity \mathbf{u}_i is determined from an earlier matching.

Additional constraints are used acting as price premiums or discounts. These constraints are expressed by applying extra multiplication factors to the basic cost c_{ij} . The most important is the introduction of a factor expressing the uncertainty of the estimated velocity. This is most profound when dealing with an appearing particle, a particle that has not been matched before. In this case the velocity is estimated from the local neighbourhood. Also ellipticity, size and threshold level are used as additional criteria. The first two of these criteria express the possibility that we might have to do with two particles very near to each other in the image plane. The last one expresses the preference of particles that have to be matched, i.e. for identified particles that are more likely to be physical particles. The dependence of the algorithm on the last three criteria is only weak.

Data processing

The raw data obtained from the matching algorithm are processed with three objectives: enlarging accuracy, spurious vector removal and interpolation on a square lattice. The accuracy of the velocities as found by the matching algorithm is enlarged by averaging over subsequent frames.

Then, spurious vector removal is applied to the unstructured original data. Subsequently the filtered data are interpolated on a grid. These processes are described in the following. Typical results are given in figures 5.9, 5.10 and 5.11. They show results of the particle location algorithm, the averaging and spurious vector removal procedure, and the spline interpolation, respectively, as applied in the present study. It concerns an experiment with a heating rate of $35\text{ V} \times 6,3\text{ A} = 220.5\text{ W}$. The instantaneous data are sampled at frame 1950 which is recorded at $t = 78\text{ s}$ from the start. In figure 5.9 it can be observed that the particles found are not distributed uniformly over the domain. Especially in the vicinity of the lower and right walls less particles are found. This is due to light scattering at the right wall and shadows caused by the heat source.

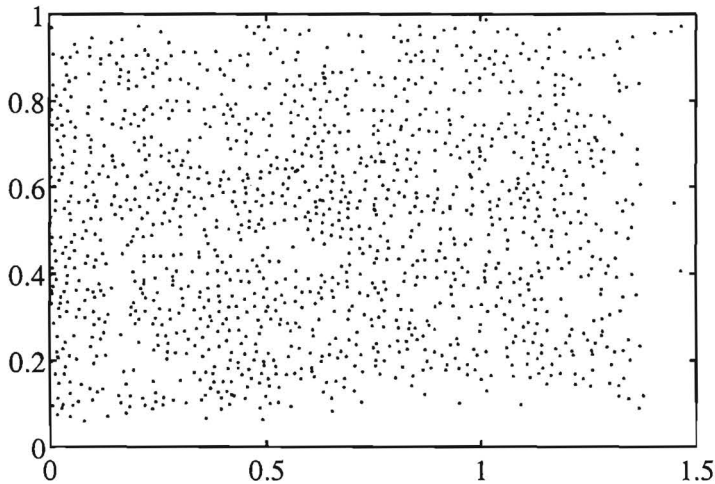


Figure 5.9: Particles found, frame 1950

The localization procedure to determine the position of the particles has some finite accuracy limited by the image resolution and the size of the particles. At low velocities this accuracy determines the velocity. Therefore the velocity of a particle obtained between subsequent matchings is averaged. In the present study the averaging procedure covers five matchings, as motivated in the next section. Hence, particles that can not be matched this number of times are eliminated.

The occurrence of unphysical or spurious vectors, as obtained from the particle tracking algorithm, is practically unavoidable. Due to an optimization between data yield and quality, an amount of stray vectors is always present. The matchings are simply unknown, and only some uncertainty may be reduced. As discussed this happens in the matching algorithm, but from visual inspection it seems that this is not quite enough. Therefore a filter is used based on a certain maximum allowable amount of variation within a searching area. The variation

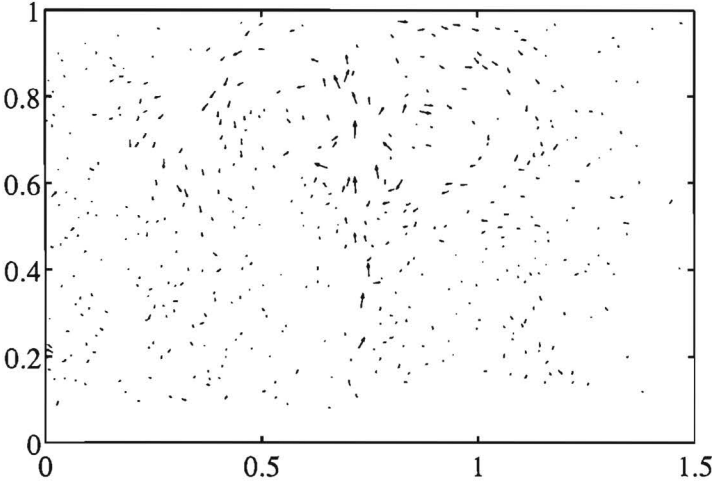


Figure 5.10: Final unstructured velocity field, frame 1950

criterion is chosen to be twice the standard deviation. More specifically, the following steps are taken. For a particle i all other particles are determined that lie within a certain distance r_f from particle i . Then the means (μ_u^i and μ_w^i) and the standard deviations (σ_u^i and σ_w^i) of the individual velocity components are determined over this set of particles, including particle i . Subsequently the length of the actual velocity deviation of particle i with respect to its neighbourhood is computed, according to

$$\sigma_{\text{test}}^i = \sqrt{(u^i - \mu_u^i)^2 + (w^i - \mu_w^i)^2}. \quad (5.3)$$

This is compared to the length of the standard deviation of the vector components,

$$\sigma^i = \sqrt{(\sigma_u^i)^2 + (\sigma_w^i)^2}. \quad (5.4)$$

If the actual deviation σ_{test}^i is larger than two times the standard deviation σ^i the vector is removed from the data field. For a Gaussian distributed field this means that 5 % of the data will be removed, even when there are no stray vectors. Experience turns out that the amount of stray vectors does not exceed 5 % so that two times the standard deviation is a proper choice. The radius of the area taken into account, r_f , is determined by the amount of data found in each area. A very small amount of data may lead to non-significant statistics. On the other hand we want to preserve the localness, so that the area may not be too large. A radius r_f of about 5 % of the characteristic domain size is found to give good results.

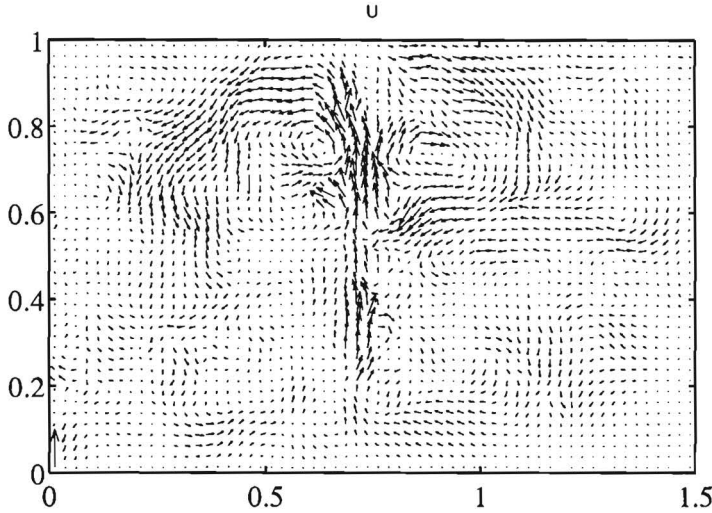


Figure 5.11: Grid interpolated velocity field, frame 1950

For the interpolation of the unstructured field data to a grid, an algorithm as used by *Nguyen Duc and Sommeria* [1988] is employed. The interpolating function for each velocity component is an analytical expression. The coefficients of it are calculated in order to minimize the second-order derivatives. It can be written for any velocity component u_i at point (x, z) :

$$u_i(x, z) = a + bx + cz + \sum_{i=1}^N d_i r_i^2 \ln r_i^2 \quad (5.5)$$

with

$$r_i = \sqrt{(x - x_i)^2 + (z - z_i)^2} \quad (5.6)$$

The coefficients a , b and c are obtained from a least-square linear fit. The remaining coefficients d_i are calculated by applying equation (5.5) to each particle, yielding a linear system of N equations with zeros on the main diagonal. The main interesting features of the interpolation are twofold. It does not show spurious oscillations like high-order polynomial interpolations do. Besides, the interpolation gives the exact measured value at the particle locations, because the coefficients d_i are defined in such a way.

Error estimates

The accuracy of the particle tracking algorithm is mainly determined by the accuracy of determining a particle position, the particle sedimentation velocity and the particle response to acceleration. The physical domain with an extent of

0.3 m is depicted on the image plane with an extent of 512 pixels, having about 1700 pixels/m. The typical accuracy of the localisation of a particle with a size of about 3 pixels in each direction is 0.1 pixel (*Dalziel* [1993]). This yields a position accuracy of $\sigma_x = 0.1/1700 = 6 \cdot 10^{-5}$ m. Having accurately spaced samples in time with interval $\delta t = 0.04$ s, thus, an accuracy for the velocity of $\sigma_u = 0.0015$ m/s is found. Using statistics, or a convolution of the velocity field over N_s samples in time, leads to a standard deviation of $\sigma_u^{N_s} = \sigma_u/\sqrt{N_s}$, making use of the central limit theorem. If the highest occurring frequency suffices $f_{\max} \leq 1/(2N_s\delta t)$ still a resolved velocity is obtained. Using $N_s = 5$ for averaging the determined instationary velocity field yields an accurate description of the flow (see fig. 5.7). In the present measurements about 1000 particles were found in each frame, of which 500 could be tracked over $N_s = 5$ frames. Thus the mean spatial resolution is determined by these 500 particles with a mean mutual distance of about 10^{-2} m. The velocities are interpolated to a finer grid, containing 63×42 equidistant gridpoints.

The sedimentation of the particles due to a slight density difference between particles and working fluid can be estimated by balancing the particles gravitational force with the Stokes drag. Since the particles are nearly spherical and the particle Reynolds numbers are lower than unity, this is a good guess. The estimated accuracy of the velocities σ_u due to the sedimentation speed u_{ps} then becomes:

$$u_{ps} = \frac{\rho_p - \rho}{\rho} \frac{g d_p^2}{18\nu} \quad (5.7)$$

This yields a value of $\mathcal{O}(10^{-4})$ m/s which is an order below the value due to location accuracy. The response of a particle to a sudden acceleration can be determined by balancing the Lagrangian instationary forces on the particle with the Stokes drag. This gives a first-order integrating response with a typical reaction time given by:

$$\tau_a = \frac{\rho_p d_p^2}{18\rho\nu} \quad (5.8)$$

which is as large as $\mathcal{O}(10^{-3})$ s, being considerably smaller than the temporal sample spacing.

Chapter 6

Results for water plumes: Experiment versus LES

6.1 Introduction

In this chapter subgrid-scale modelling is tested by comparison with experimentally obtained data and the results of numerical simulations. This procedure can be performed in two ways, generally referred to as "*a priori* testing" on the one hand and "*a posteriori*" testing on the other hand; a denotation as introduced by *Piomelli et al.* [1988].

A direct comparison of the experimental data with those obtained by a Large-Eddy simulation, using a particular subgrid scale model, is generally referred to as *a posteriori* testing. The term *a posteriori* testing is also used if the reference data are generated by direct numerical simulation (DNS). The process of *a posteriori* testing is the standard way to evaluate a model.

The other method, *a priori* testing, employs the reference data to pronounce directly upon the quality of a subgrid model. In this case the high resolution reference data are filtered spatially. Using the data at the two resolution levels, subgrid stresses are calculated. These stresses are then compared to the subgrid stresses determined with a model acting on the filtered data. Thus, the performance of several models can be evaluated, and suitable candidates can be discerned for actual large-eddy simulations. However, a good agreement between the real stresses and the stresses as obtained by using a model is not a guarantee for a successful LES. In an LES the SGS model affects the resulting resolved velocity and temperature field. The latter is taken as an input for evaluating the model. As a consequence a discrepancy between experimental data and LES data is likely to occur. The different sets of input data should converge with improvement of the model.

The *a priori* method, employed on the basis of DNS data, was pioneered by *Clark et al.* [1979] and *McMillan and Ferziger* [1979]. At present it has become

a widely used investigation tool. However, using DNS data restricts the test to relatively low, forcing rates, i.e. low Reynolds or, as in the present case, low Rayleigh numbers. One of the first extensive studies based on experimental data at relatively high Reynolds numbers was performed by *Liu et al.* [1994]. A drawback of the latter study, in comparison to the studies using DNS data, is the fact that only two-dimensional fields were used. Contrary to the flow conditions as investigated in the present study, it must be stressed that the majority of *a priori* testing so far has been performed on forced convection, in which there are at least two homogeneous directions.

In the present chapter both methods will be applied. Firstly, velocity fields will be subjected to two-dimensional *a priori* testing. Therefore buoyant production can not be evaluated. Then, simulations are performed and the obtained data will be compared to the experimental velocity fields. In this *a posteriori* testing, the temperatures at localized points are involved additionally. Before evaluating the performance of the different models first the obtained flow field will be considered and analyzed. Amongst a statistical description of the primitive variable field, the latter comprises a description of the obtained subgrid stresses and the interscale kinetic energy transfer over the typical filter width length scale.

In contrast to the rest of this thesis in this chapter all obtained quantities are presented in full dimension. In presenting the experimental data, scaling would result in a loss of information. This is due to non-Boussinesq effects together with the absence of a physical reference basis.

In the PTV experiments the spatial sample resolution is not enough to represent the dissipation range. Resolving this range would imply a sample spacing that is equal to, or even smaller than the Kolmogorov scale. This is not a drawback in the perspective of the present study. The purpose of this study involves the validation of LESs and the testing of SGMs. The objective of LES is to represent only the energy containing eddies with sufficient accuracy. This means that our direct interest is concerned with intermediate length scales, in which the energy just decreases as a function of the spatial wavenumber.

6.2 Results from particle tracking experiments

6.2.1 Experimental conditions

The experimentally investigated flow in this chapter was obtained using the setup discussed in chapter 5. The setup was filled with demineralized and de-aerated water. The temperature control in the heat exchangers supply tank was turned on, together with the flow through the heat exchangers. This situation was maintained for about two hours, spanning the time before the actual start of the experiment. This time span is needed to obtain a hydrodynamically stagnant and thermally homogeneous initial condition.

At the start of the experiment the temperature of the water in the setup was $19.5^\circ C$. The heat exchangers were kept at $19.5^\circ C$ and the ambient temperature in the laboratory was $19.9^\circ C$. The power supply is turned on at a heating rate of $\pm 1102.5 W/m$. The heating of the fluid has a delay of $1.5 s$ due to the internal heating of the element as discussed in chapter 5. Using the given heating rate, the dimensionless governing parameters are $Pr = 7.0$ and $Ra = 2.1 \cdot 10^{11}$, defined at a reference temperature of $20.0^\circ C$.

During the experiment the mean temperature in the setup will rise. Due to this effect the Ra -number will increase and Pr will drop. Therefore, the experimental results will be presented in full dimension. Later on in the comparison the results of numerical simulations will be scaled to full dimensions, using a suitable magnitude of the scaling quantities.

A vertical cross-section of the resulting flow was recorded on video-tape, and temperatures were measured at several locations. The experiment lasted for 600 seconds, assuring to have enough data in order to pass a transient of the flow field and to sample sufficient integral time scales to analyze the statistically stationary flow. Flow statistics as presented in the next sections are obtained from the video recordings in the time interval [80-600] s.

6.2.2 Mean flow

The recorded video tape was subjected to the tracking algorithm, resulting in unstructured vector fields. These vector fields were interpolated on a grid of size 63×42 , yielding a spatial grid width of $\Delta \approx 4.76 \cdot 10^{-3} m$. These steps are performed according to the method discussed in chapter 5. The final resolution in time was $5 Hz$. Then the statistics of the resulting structured fields are determined at the given spatial resolution. The number of fields on which the analysis thus is constituted amounts 2600 velocity fields. A single realization from which the statistics are built up was already given in figure 5.11. The two-dimensional plane in which the velocities are measured contains a horizontal and a vertical component that are indicated by u_1 and u_3 , respectively (see also figure 1.2).

A vector plot of the mean flow is given in figure 6.1. A nearly symmetrical flow pattern is established, consisting of a plume that drives a circulation pattern in the upper half of the setup. The magnitude of the mean flow can not be estimated easily, e.g. by using an entrainment assumption as outlined in section 2.4.4. Both the molecular and turbulent dissipation are very much influenced by the presence of the confining walls. The width of the plume suddenly increases as the bulk of recirculating fluid entrains it at half the setup height. The mean entraining flow is directed almost perpendicular to the plume. Below this level the entrainment is much smaller and the fluid does not flow horizontally towards the plume anymore. In this region the fluid is bent downwards before the attraction to the plume becomes large enough.

In fact the time mean flow clearly characterizes the spatial transition of the

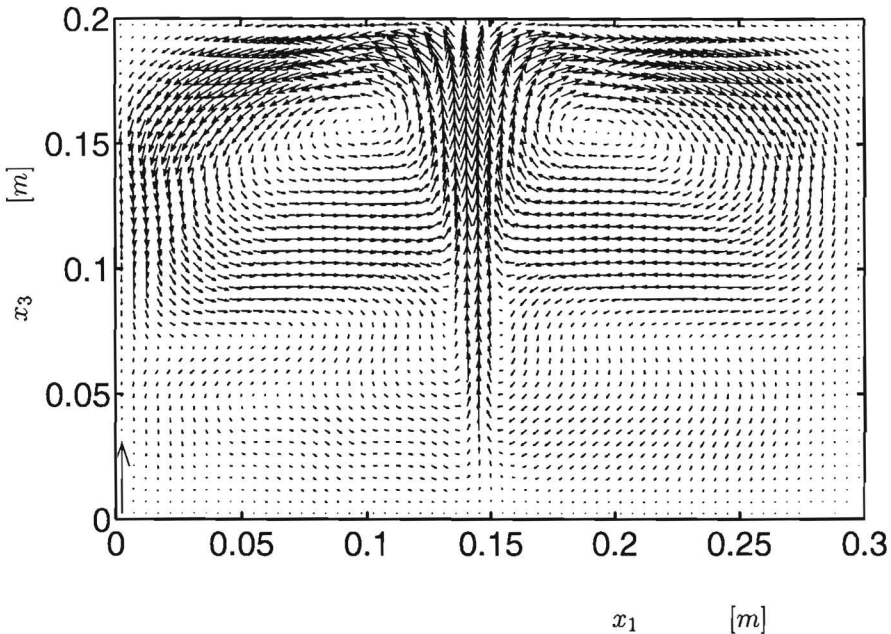


Figure 6.1: Mean flow velocity vectors at $x_2 = \frac{1}{2}D$ as obtained by PTV at $Ra = 2.1 \cdot 10^{11}$ and $Pr = 7.0$. Scaling: 0.01 m/s magnitude is displayed by the left-bottom vector.

flow. At the height where the entrainment increases at an appreciable rate, the flow may be defined as spatially transitional. It turns from laminar, below this location, to turbulent, above it. Though the fluctuations of the vertical velocity are large directly above the source, this does not indicate turbulence. A small oscillation of the laminar plume causes this behaviour. The oscillations are irregular although the plume is still laminar. A sample sequence of the temperature at P_{p1} (see figure 5.3) is given in figure 6.2. The irregular oscillations are nearly always present. They are mainly due to upstream influences and turbulence which is convected back to the source region. Arriving there this turbulence possesses a reduced but still noticeable kinetic energy.

The velocity in the lower plume part is low compared to results obtained from laminar boundary layer assumptions or turbulent entrainment assumptions as described in sections 2.4.1 and 2.4.4, respectively. The flow in this region can be described as an irregularly oscillating laminar plume flow. Therefore the time mean flow has a broader lateral distribution with a decreased maximum, as compared to a stationary laminar plume. On the other hand, the particle tracking velocimetry experiments exhibited a relatively low spatial resolution. Because of the relatively small particle density compared to the laminar plume

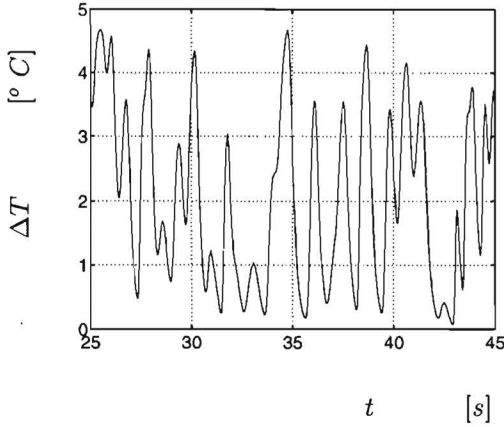


Figure 6.2: Temperature record at P_{p1} of an irregular oscillating plume.

velocity width, the plume flow in this region could not be captured accurately. Additionally, the present confined enclosure causes a recirculating large scale flow, which is in contrast to the assumptions made in the mentioned laminar and turbulent models of chapter 2.

The effect of the irregular oscillations of the laminar plume on the time mean profile can be estimated. From the lateral velocity u_1 at the centre line, the displacement of the laminar plume can be determined. A cumulative summation of this displacement indicates the plume position as function of time. It is found that at a height of 0.07 m , i.e. 0.05 m above the middle of the heat source, the plume oscillates in a lateral region bounded by approximately 0.02 m from the centre line. The standard deviation of the off-centre-line-position amounts 0.0115 m . Convoluting the laminar boundary layer profile with a Gaussian probability density function for the plume position, results in the estimation for the time mean velocity profile. For the probability density function the calculated standard deviation of the plume position is used. This results indeed in a lower vertical centre line velocity, compared to both steady laminar boundary layer profiles and the turbulent entrainment approximation. The result is given in figure 6.3. The vertical centre line velocity found by this procedure agrees much better with the results from the particle tracking velocimetry. The overall profile of the PTV is somewhat lower due to a background downwards oriented flow. The width of the plumes as obtained by the turbulent entrainment model, the laminar oscillating model and the PTV are comparable to each other. The width of the PTV result is somewhat smaller due to the presence of vortices at both sides of the plume. These vortices are only present in a relatively small amount of sample times.

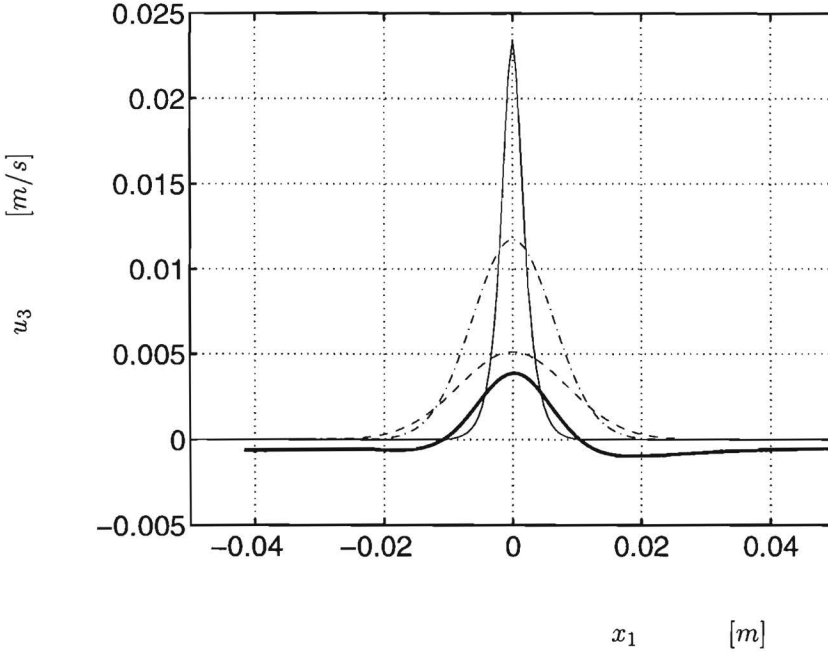


Figure 6.3: Mean flow u_3 profiles at the line $[x_1, 0.10, 0.07]$ m; thin full line: steady laminar boundary layer approximations, dash-dotted: integral turbulent entrainment approximations with $\alpha = 0.157$ and $\beta_T = 1.281$, dashed: oscillating laminar boundary layer plume, bold full line: PTV result.

6.2.3 Flow fluctuations

The convergence of the flow to a steady state is checked by inspection of the statistics of the velocity as function of time. The velocities were taken at the midpoint because of our interest in the transitional region. These statistics should approach a converged value, which is zero in case of the mean horizontal velocity component. The velocities in the middle, the mean and the standard deviation of it, as function of time, are displayed in figure 6.4, as well as their probability densities. It shows that at the end of the experiment the statistics are nearly constant.

It seems that there exists a tendency consisting of a long term decrease of the mean and standard deviation of the horizontal velocity. At the same time these statistics for the vertical component seem to increase slightly. The latter is mainly caused by the temperature dependent properties of the working fluid. The deviation of especially the horizontal mean component may be caused by an asymmetry of the setup, including an installation orientation which is not level. On the other hand, the difference of the mean horizontal velocity with its expected ideal value at the end of the experiment, relative to its standard

deviation is within 10 percents. This justifies a qualitative analysis, not ascribing too much significance to the numerical values obtained.

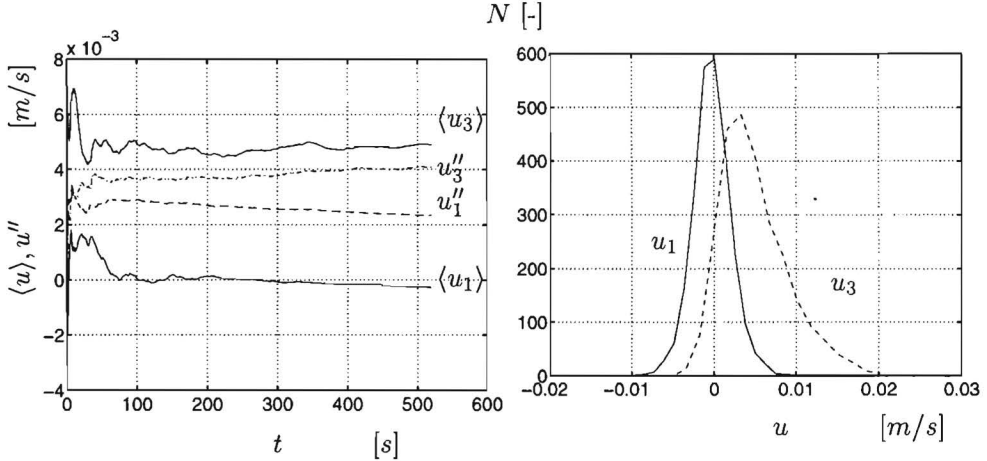


Figure 6.4: Evolution of the statistics of the velocity components at point $[0.15, 0.10, 0.10]$ m as function of time (left), and their distributions (right).

The probability densities behave according to expectations based on physical grounds. Having no net forcing in horizontal direction results in a symmetrical distribution with mean zero. It is Gaussian-like due to multiple interactions. The distribution of the vertical component is positioned for the major part at positive values and it is skewed. The forcing, resulting locally in instantaneous strong updraughts, is responsible for both effects.

The spatial distribution of the fluctuations of the velocity components in the plane under consideration gives some insight in the turbulent behaviour of the plume. A contour plot of the standard deviations of the velocities are displayed in figure 6.5. These fluctuations in time are denoted by a double prime: u_i'' , in contrast to time mean values that will be signified by angular brackets, e.g. $\langle u_i \rangle$. Due to lateral oscillations of the plume, the standard deviation of the vertical component u_3 is rather high already at small elevations from the heat source. Furthermore, its magnitude behaves like the mean vertical velocity. The fluctuations of the horizontal velocities are largest in the region where the lateral entrainment has a maximum.

By integrating the two-dimensional velocity divergence over discrete volumes of size 2Δ , an estimate can be obtained of the velocity differences $\Delta u_2(2\Delta)$ in source axial direction. The axial velocity difference is given by

$$\begin{aligned} \Delta u_2(2\Delta) = & (u_1(x_1 + \Delta, x_2, x_3) - u_1(x_1 - \Delta, x_2, x_3)) + \\ & (u_3(x_1, x_2, x_3 + \Delta) - u_3(x_1, x_2, x_3 - \Delta)). \end{aligned} \quad (6.1)$$

This provides a measure of the three-dimensionality of the flow. Again the mean

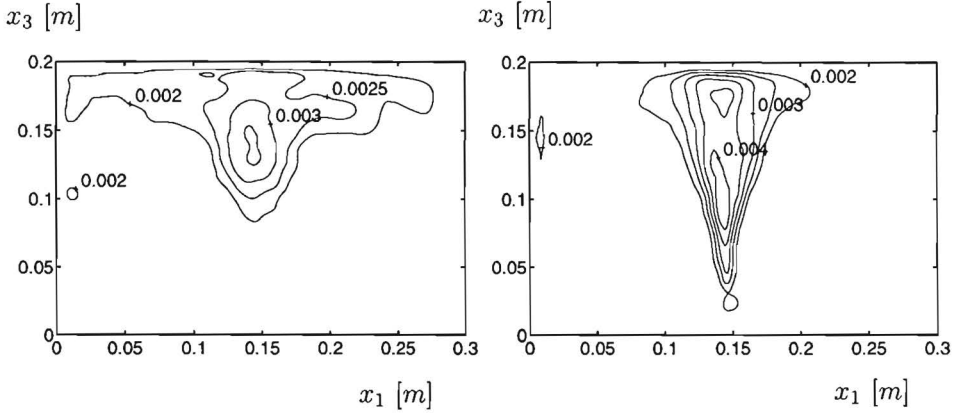


Figure 6.5: Spatial distribution of the standard deviation of velocity components at $x_2 = \frac{1}{2}D$. Left: u_1'' , right: u_3'' , contour levels in m/s.

value and the standard deviation are calculated and depicted in figure 6.6. The standard deviation of the axial velocity demonstrates evidently that the flow is three-dimensional. Also the frequency contents are similar to those in the other two directions.

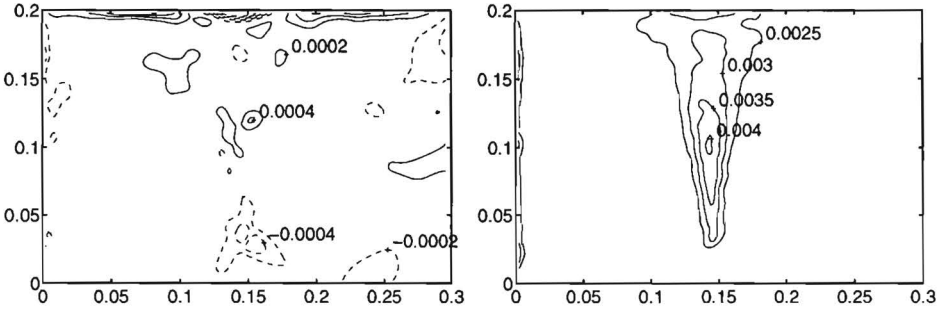


Figure 6.6: Spatial distribution of the axial velocity component at $x_2 = \frac{1}{2}D$. Left: $\langle \Delta u_2(2\Delta) \rangle$, right: $\Delta u_2''(2\Delta)$, contour levels in m/s.

From the velocity standard deviations the dissipation rate per unit mass can be estimated on the basis of an equilibrium range energy drain. Assuming a turbulent integral length scale l , it becomes: $\epsilon \approx u_3''^3/l$. Employing an integral length scale $l = H$, the dissipation rate in the core of the plume reaches a value of $\epsilon \approx 3.2 \cdot 10^{-7} \text{ m}^2/\text{s}^3$. With this value, the microscales of length due to Kolmogorov and Taylor can be estimated to be: $\eta = (\nu^3/\epsilon)^{1/4} \approx 1.3 \cdot 10^{-3} \text{ m}$ and $\lambda \approx u_3'' \sqrt{15\nu/\epsilon} \approx 2.7 \cdot 10^{-2} \text{ m}$, respectively. The spatial sample resolution of $\pm 10^{-2} \text{ m}$ (see chapter 5) therefore is not enough to represent the dissipation range. This under the hypothesis that a three dimensional equilibrium range would be present. However, the resolution is in accordance with the remarks as

stated in the introduction and it resolves the energy containing eddies.

6.2.4 Subgrid stresses

The instantaneous structured velocity fields are used in order to obtain the subgrid stresses, which were defined by

$$\tau_{ij} = \overline{u_i u_j} - \bar{u}_i \bar{u}_j \quad (6.2)$$

For this purpose a top-hat filter of size 2Δ is chosen, in order to be consistent with the mathematical formulation and numerical implementation in the actual Large-Eddy simulations. For the same reason an extended trapezoidal integration rule is used for the filter operations.

From the two-dimensional measurements only three of the six subgrid stress components can be determined: τ_{11} , τ_{13} and τ_{33} . The mean subgrid stresses and their standard deviations are depicted in figure 6.7.

The largest values of the subgrid stresses occur in the plume region, in which τ_{33} is particularly large. At the top wall high values of τ_{11} are present in the areas at which the plume spreads out to the left and to the right. Except for the top wall region these stress components do correlate fairly well with the temporal standard deviations of the corresponding velocity components. The cross-component of the subgrid stress τ_{13} possesses much smaller values than the other two, the difference being an order of magnitude. This is caused by cancelling out of positive and negative contributions. High values of τ_{33} correspond with high values associated to small boundary layers, i.e. in the plume region. In the same way the large value of τ_{11} in the transitional region can be explained by relatively small entraining regions.

The trace of the subgrid scale stresses constitutes a grid scale pressure, which is incorporated in the already existing pressure term, in an actual LES. Therefore, in the comparison with subgrid stress models later on, one should look at the deviatoric part of it. This is not possible since the measurement is only two-dimensional. In 6.7 the stress tensor is depicted with full trace. While this affects the τ_{11} and τ_{33} components, the value of τ_{13} will stay uncontaminated. Later on in the comparison with subgrid models an approximation is applied to obtain traceless experimental stresses.

Inspection of the standard deviations of the subgrid stresses shows that the fluctuations of all subgrid stresses are more equalized over the different components. They also have a more similar spatial distribution, except for the prominent fluctuations of τ_{11} at the top wall. It also shows that τ_{11} and τ_{33} remain positive most of the time, while τ_{13} more or less alternates around zero. On the other hand, the clear time mean τ_{13} behaviour suggests the existence of a coherent phenomenon. A real dissection into flow patterns would require a proper orthogonal decomposition.

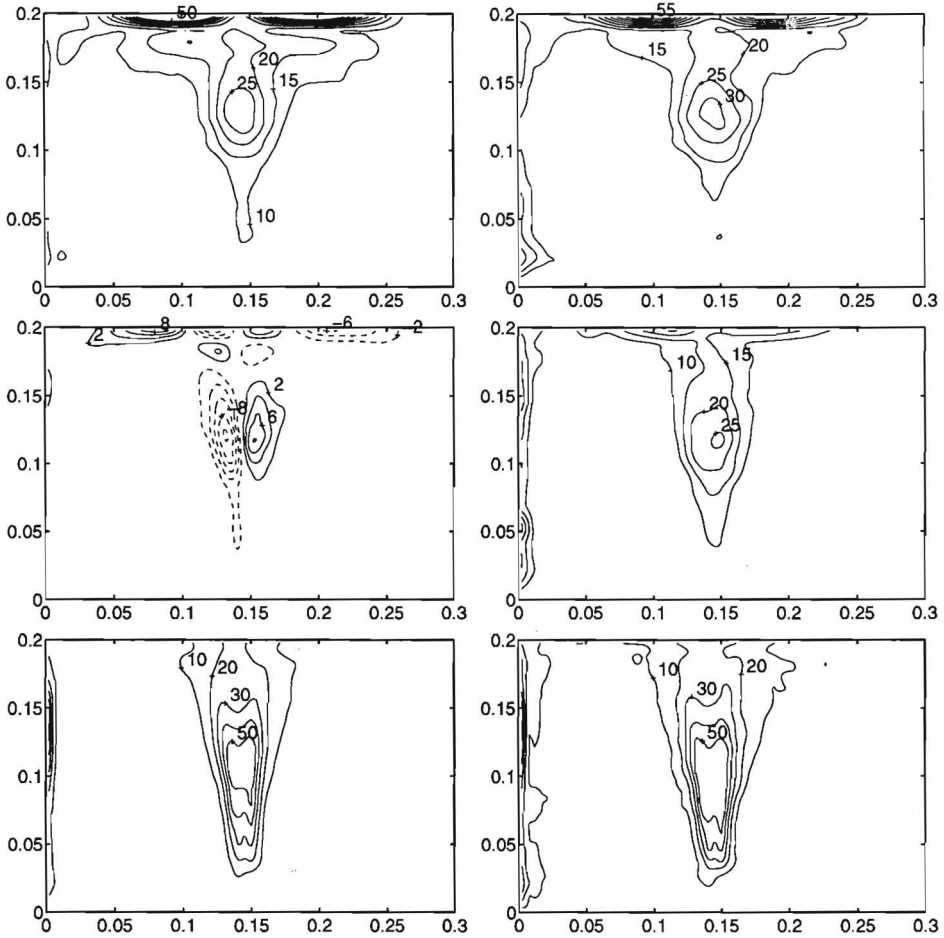


Figure 6.7: Subgrid stresses at $x_2 = D/2$, top to bottom: τ_{11} , τ_{13} and τ_{33} , Left: time mean stresses; right: standard deviations. Levels multiplied by 10^7 .

The large fluctuations at the left confining wall compared to those at the right wall may be caused by a set of physical and non-physical artefacts. The light sheet at the left wall was of a better quality compared to that at the right wall. Even with the use of local intensity equalization (after recording), this resulted in a larger number of particles detected at the left wall. This effect was already depicted in figure 5.9. In combination with instantaneously occurring large values of the second spatial derivatives near the wall this results in the large standard deviations of the subgrid stresses. Another reason might be the presence of reflection effects of particles at the confining glass surface. Occasionally a particle may be matched with its own reflection. However, the interest of the investigation is focussed on the plume region. In this area no spurious effects are observed.

6.2.5 Energy transfer

With the filtered velocity field the rate of strain tensor \bar{S}_{ij} can be calculated at the filtered level using a straightforward finite difference scheme. The rate of strain tensor, together with the subgrid scale stresses, define the interscale kinetic energy transfer as outlined in section 3.2.4. It can be written as function of the filter width:

$$\epsilon(2\Delta) = -\tau_{ij}\bar{S}_{ij} \quad (6.3)$$

In the present case the length scale separating resolved components from subgrid components is defined with the filter to be 2Δ . The energy transfer thus defined is from scales above 2Δ to scales below this value. If $\epsilon(2\Delta)$ is positively valued the kinetic energy is drained from the resolved scale to the subgrid scale. This is the case in the inertial subrange.

Again not all components involved in the contraction 6.3 are known. Here only contributions from the known components are taken into account. It is hardly possible to make some proper assumptions to estimate the unknown components of τ_{ij} and \bar{S}_{ij} . To make a just interpretation of the energy transfer possible such a blurring would be unwanted. Following *Liu et al.* [1994] the trace of the stress tensor is not subtracted here, i.e. the stresses as given in the previous section are used. In figure 6.8 the time mean kinetic energy transfer and its standard deviation are given. The mean kinetic energy transfer shows some regions with

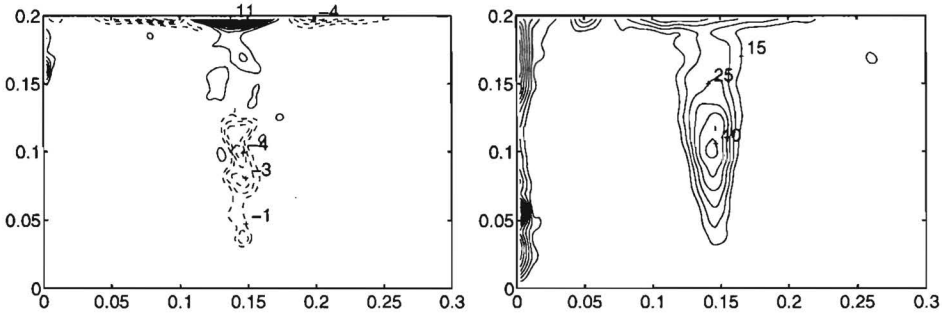


Figure 6.8: Kinetic energy transfer $\epsilon(2\Delta)$ at $x_2 = \frac{1}{2}D$, left: time mean, right: standard deviation. Levels multiplied by 10^7 .

positive and negative values. If the turbulence were purely dissipative, only positive values would occur. In the plume region and near the top wall there are areas of negative energy transfer. This means that kinetic energy is transferred from small scales to larger spatial scales. This phenomenon is called "backscatter". It is expected that the occurrence of backscatter disqualifies the effectivity of subgrid scale models that are based on a statistical equilibrium assumption.

The time mean backscatter here originates from the injection of kinetic energy at a scale that is smaller than 2Δ . It has to be kept in mind that because of

this a dissipative drain of kinetic energy might be present also below this 2Δ level. Though most of the kinetic energy is present in the lower wavenumbers and must therefore be transferred from the high wavenumbers downwards. This is also expected to happen at the Δ level to a smaller degree.

Besides the time mean backscatter in the lower part of the plume, instantaneous backscatter occurs in the total upflowing area. This is demonstrated by the standard deviation of the interscale kinetic energy transfer $\epsilon''(2\Delta)$. It shows that the instantaneous values are about ten times as large as the mean value. Thus backscatter and forward scatter are equally important phenomena in the plume region. Integrating the energy transfer and its standard deviation over the domain yields values of $1.0 \cdot 10^{-7} W/m$ and $3.5 \cdot 10^{-5} W/m$, respectively. The latter was evaluated over the region at the right from position $x = 0.043$. Therefore interscale kinetic energy transfer is much more important than the net kinetic energy drain. This is in agreement with results as found by analyzing forced convective flows resulting from direct numerical simulation, e.g. by *Piomelli et al.* [1991] and *Domaradzki et al.* [1993].

It can be concluded that backscatter is essential in the present problem at the 2Δ level, especially when most of the fluctuations are to be simulated. At the Δ level the influence might be strongly reduced. A subgrid scale model should therefore exhibit the ability for providing backscatter. At least a reduction in subgrid dissipation to zero in laminar, i.e. resolved regions, is an advantageous property. Therefore dynamic modelling is preferred beforehand. However, at $Pr > 1$, as in the case of water, the modelling of the subgrid fluxes may be more critical.

6.2.6 *A priori* testing

On the basis of the filtered velocity fields the subgrid stresses are calculated according to several models. Here the Smagorinsky model, the structure function model and the dynamic model will be taken into account. The objective of this analysis is to discern between the predictive qualities of the mentioned SGS models in a statistical sense. Thus a realization at some point in time may yield a low correlation between predicted and exact subgrid effects. In the present study this constitutes a tolerable degree of freedom inasmuch as most engineering flows are to be characterized with numerical methods long beyond any predictability horizon. The issue of predictability is addressed in more detail in chapter 7.

It must be kept in mind that the filtered velocity field is obtained with a top-hat filter of size 2Δ . In the test the deviatoric part of the "exact" subgrid stresses are compared to the model stresses. Since the normal subgrid stress in axial direction τ_{22} can not be determined in a straightforward way, the analysis will be kept two-dimensional. This yields for the "exact" deviatoric subgrid stresses

$$\tau_{ij}^d = \tau_{ij} - \frac{1}{2} \tau_{kk} \delta_{ij}. \quad (6.4)$$

This strategy yields a result identically equal to an application of the assumption $\tau_{22} = (\tau_{11} + \tau_{33})/2$. The two known normal stresses τ_{11} and τ_{33} thus become exactly the opposite of each other. The deviatoric stresses are given in appendix E, together with the deviatoric parts of L_{ij} , C_{ij} and R_{ij} that compose the total stress.

The intensities and the mean of the Reynolds stresses are relatively small compared to the Leonard and cross stresses, as can be observed in the appendix. Thus the fluctuations at the Δ level are much smaller than those at the 2Δ level. This is in accordance with a decreasing spectrum at larger wave numbers. However, for a three-dimensional equilibrium range, i.e. $E(k) \propto k^{-5/3}$, the expected difference in intensity amounts a factor $(\frac{1}{2})^{-5/3} = 3.2$. The observed difference, being a decade, would be in accordance with a spectrum with exponent $(^{10}\log(\frac{1}{2}))^{-1} = -3.3$ instead of $-5/3$. This suggests a two-dimensional turbulent inertial range around $k = \pi/2\Delta - \pi/\Delta$, according to *Kraichnan* [1967]. Such an inertial range has an exponent equal to -3 . Alternatively this behaviour could be due to the fact that this range of wavenumbers might lie in a dissipation range. On the basis of the estimation of the Kolmogorov microscale the latter hypothesis must be rejected. However, it is not yet very clear how the interpolation of the unstructured original data to a regular grid (with increased resolution on average) extends the spatial spectrum. It is this artefact that makes the above analysis a tentative exercise.

In the composition of the mean value of τ_{11} the influences of L_{11} and C_{11} are of equal and major importance. Since these components exhibit an almost equal standard deviation that is about twice as large as the standard deviation of the total stress, L_{11} and C_{11} must have a large negative correlation. For τ_{13} the influence of the Leonard term is particularly large in the top region, whereas the cross term is more profound in the lower plume region. According to the standard deviations here again a large negative correlation between Leonard stress and cross stress must be present. These negative correlations are also an attribute of two-dimensional motion as can be observed in a two-dimensional vortical flow field, e.g. given by $u_1 = \sin(2\pi kx_3)$, $u_3 = \sin(2\pi kx_1)$, which is also divergence free.

Subsequently, on the basis of the filtered velocity field the subgrid stresses are determined according to the subgrid scale models. The lack of information concerning the determination of the exact top-hat subgrid stresses also appears in the calculation of the magnitude of the resolved rate of deformation tensor $|\bar{S}|$. The value of this property serves as a scaling factor in the models for the predicted stresses. Again not all composing parts can be determined, because of the absence of information about the axial velocity u_2 . Accordingly the unknown cross components are neglected and the value of \bar{S}_{22} can be determined on the basis of zero divergence, i.e. $\bar{S}_{22} = -(\bar{S}_{11} + \bar{S}_{33})$. Later on, in the *a posteriori* analysis of the LES data, a similar approach will be followed. Then an additional quantification will be performed to estimate the influence of three-dimensional

effects.

The Smagorinsky model and the structure function model give similar results. The latter model only yields values approximately a factor two lower compared to the Smagorinsky model. The value of τ_{13} as determined by the Smagorinsky model is similar to the "exact" subgrid stress, except for the top wall region in which the predicted stress is opposite to the real stress. Qualitatively the fluctuation of τ_{13} and τ_{33} as predicted by the Smagorinsky model agrees fairly well with that obtained by gridscale information. In the plume region the time mean τ_{11} and τ_{33} components are in disagreement with the exact values. Employing the dynamic model yields better results for these components, though the agreement is still very poor. For τ_{13} the dynamic model predicts opposite values and the temporal fluctuations of all components are underestimated.

Contrary to the subgrid stresses, the interscale kinetic energy transfer as obtained by the dynamic model gives results that are very similar to the exact transfer rates. This energy transfer is depicted in figure 6.9, and has to be compared to figure 6.8. A good quantitative agreement for the mean interscale kinetic energy transfer is obtained if the dynamic procedure is applied, though the result near no-slip walls depends heavily on the implementation of the dynamic procedure. Boundary conditions for the filtering operations have to be applied. In the next subsections this issue is addressed in more detail. The standard deviation of the kinetic energy transfer is estimated to be half of the exact standard deviation. It seems that the effective resolution of subgrid stresses and gridscale strains differs somewhat, causing the distinction.

In evaluating \mathcal{L}_{ij} and M_{ij} the 2Δ hat filter has to be applied to several flow quantities. Therefore boundary conditions at the no-slip walls have to be met. Here it is assumed that all stresses and strains do not alter over the boundary. This is a logical consequence of the impermeable no-slip condition for the velocity components.

The dynamic parameter C is calculated at each point of the Δ grid. Afterwards it is filtered to the 2Δ grid. This is allowed since the parameter is defined on the basis of similarity between the 4Δ scale and the 2Δ scale. Therefore on the one hand a Δ resolution for C would not be representative. On the other hand, nearly singular values of C caused by an almost zero value of $M_{ij}M_{ij}$ are thus filtered out. Since the kernel of the filter exceeds the domain boundaries, a crucial aspect of the filtering operation here is the implementation of boundary conditions for C at the no-slip walls. Application of a homogeneous Neumann condition leads to the present results. One could also plead for a homogeneous Dirichlet condition since the flow is laminar at the wall. However, in an actual LES this is already obtained by setting the boundary condition for the eddy viscosity accordingly. A Dirichlet condition for C at the upper confinement causes the energy transfer to be limited too much.

The energy transfer determined with the Smagorinsky and the structure function model result in values four and two orders of magnitude lower, respectively,

than the dynamic model for both the time mean and fluctuating transfer rates. The spatial distribution of the energy transfer is equal for both models. They both reveal increased values at the top wall, being positive in this entire region. Relating the evaluation of the energy transfer, these models are inferior with respect to the dynamic model. Yet, in applying the dynamic model care must be taken in the application of appropriate boundary conditions at no-slip walls.

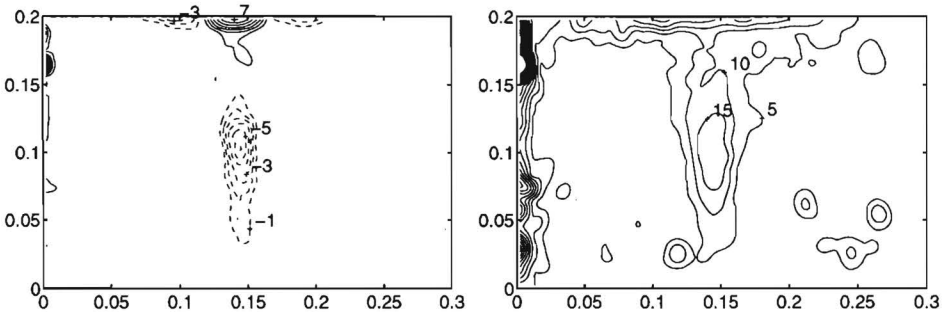


Figure 6.9: Kinetic energy transfer $\epsilon(2\Delta)$ at $x_2 = \frac{1}{2}D$ determined with the dynamic model, left: time mean, right: standard deviation. Levels multiplied by 10^7 .

Evaluating the dynamic model on the experimental data reveals a value for the dynamic constant C , and thus for the Smagorinsky constant C_s as function of space. The statistics of the dynamic constant are given in figure 6.10. Here again the backscatter is irrefutably present. In the plume region the dynamic constant has a minimal magnitude of -0.01 , corresponding with a negative Smagorinsky constant of magnitude 0.1. The maximal fluctuation of the dynamic constant corresponds to a fluctuating Smagorinsky constant with amplitude 0.16.

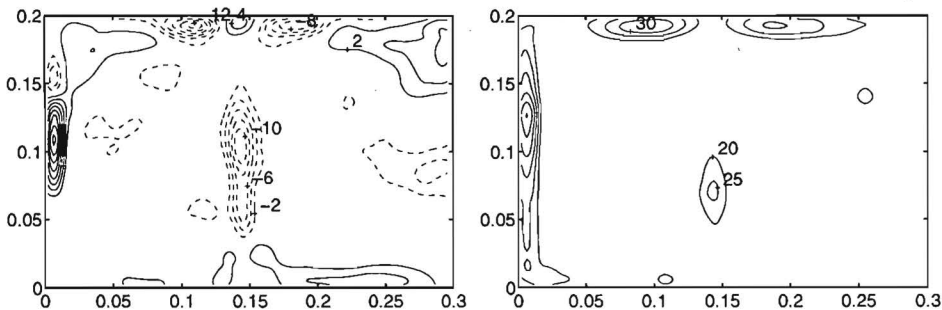


Figure 6.10: Value of the dynamic parameter C at $x_2 = \frac{1}{2}D$, left: time mean, right: standard deviation. Multiplication factor 10^3

Finally it has to be remarked that not the subgrid stress is responsible for the impact on the resolved field. In fact the divergence of the subgrid stress

$\partial\tau_{ij}/\partial x_j$ has to be considered as it appears in the governing equations. However, an accurate agreement between modelled and real subgrid scale stresses yields also a sufficient description of its divergence.

6.3 LES results: *a posteriori* testing

6.3.1 General remarks

In this section results of Large-Eddy simulations will be presented. As already expressed in the introduction, confrontation of actual simulations with reference data is the only ultimate method of validation. In the present study first a no-model simulation was performed on the large-eddy grid. In the next section results from this simulation are presented. Then by applying SGS models, improvements or deteriorations become apparent. Together with the experimental velocity and temperature data it is expected that conclusions can be drawn with a fair rigour.

The computational grid as employed in the simulations corresponds with the resolution of the physical particle tracking experiments. The grid size was taken $63 \times 42 \times 42$ in all computations. Also the temporal sample density could be taken identically the same as in the experimental case, without violating the stability criterion. A total of 15000 time steps were taken for each simulation. The velocity information at the vertical cross-section $x_2 = \frac{1}{2}D$ was analyzed in exactly the same way as the experimental data were treated. Thus, cross-sections were evaluated after the initial transient starting at sample number 2005, with a sample frequency of 1 out of 5.

The experimental heat flux, length scales and material properties correspond to values of $Ra = 2.1 \cdot 10^{11}$ and $Pr = 7$, material properties were taken constant at $20^\circ C$. The turbulent Prandtl number is taken equal to $Pr_t = 1/3$. The heat flux generated by the heat source is equally divided over the source-containing grid volumes. The flow resistance generated by the no-slip heating strip is neglected. In a no-model simulation a no-slip condition was compared to a free evolution of the velocity field at the source. No significant differences in the statistics of the velocity field were found.

Because of the symmetry of the problem a symmetrical solution always exists. However, this symmetrical solution is not stable at the Ra number under consideration. The development of the instability is governed by the initial perturbation and the machine accuracy of the computing facility. In general, applying no initial perturbation in an LES results in a flow persisting to be stable much too long. An additional circumstance is the physical initial non-homogeneity that may be low but is always present. Therefore a random temperature perturbation was applied over the entire domain. The limits of the dimensionless temperature perturbation were set to $\pm 5 \cdot 10^{-6}$, adding no net thermal energy. With the present heat flux this corresponds with the equivalence of a physical maximum temper-

ature perturbation of $\pm 0.01^\circ C$. Results from numerical experiments expressing the role of the initial perturbation are provided in chapter 7.

Calculations are performed on a Cray C98/4256 supercomputer, using a standard accuracy of 64 bits. On the specified resolution a time step takes approximately 0.23 CPU-seconds, excluding the evaluation of an SGS model.

6.3.2 Velocity information

Zero model results

The coarse grid numerical simulation, without using an SGS model, results in flow velocity statistics as depicted in figure 6.11. The mean flow shows a vertical velocity in the plume that is about three times as high as the velocity found in the experiment. The part of the flow domain occupied by the time mean recirculation is too large. The fluctuations of the velocity, however, as monitored in the midpoint of the depicted cross-section, is in better agreement with the experimental data. The time mean plume flow displays a linear spread with height, just as predicted by a turbulent entrainment assumption.

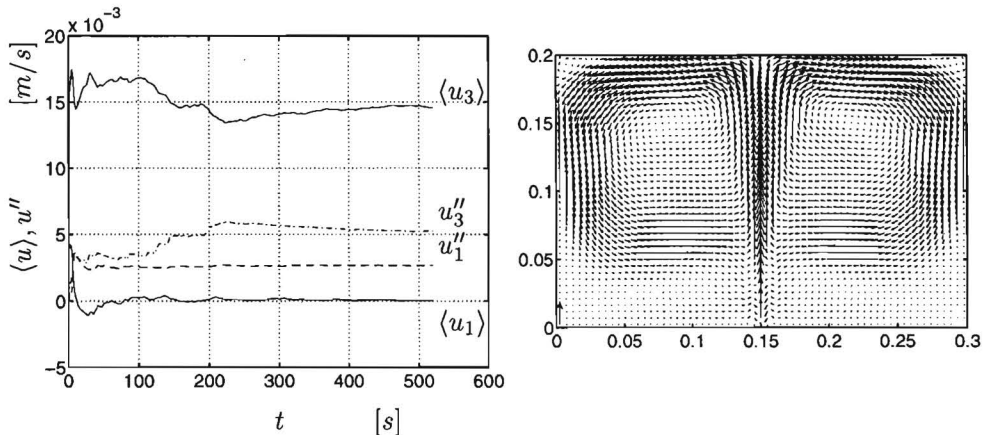


Figure 6.11: Results from the coarse grid simulation without model. Left: statistics as function of time at point $[0.15, 0.10, 0.10]$ m, right: time mean vector plot at $x_2 = \frac{1}{2}D$, scaling: 0.01 m/s magnitude is displayed by the left-bottom vector.

The observed behaviour is a consequence of the application of a coarse grid without accounting for additional dissipation. Therefore small scales cannot be represented. Thus numerical diffusion forces the conserved kinetic energy to appear in the larger scales, accompanied by smaller frequencies. In this way the kinetic energy of the mean flow is overestimated. Representation of the friction at the top and side walls is expected to be particularly insufficient. This results in a better conversion of potential to kinetic energy in the plume, which on its

term does not degrade fast enough and stays at large stationary scales. The large scale inertia forces cause the recirculation zone to be too large.

The mean and fluctuating kinetic energy drain, again over the 2Δ scale, amounts $3.2 \cdot 10^{-8}$ and $5.8 \cdot 10^{-7}$ W/m, respectively. The mean is a factor three lower than the experimentally observed amount, whereas the fluctuating component is 60 times lower. This supports the above explanation of the discrepancy. The spatial distribution of the statistics of the kinetic energy transfer, calculated from the two-dimensional velocity field at $x_2 = \frac{1}{2}D$, is depicted in figure 6.12. The distributions are similar to the exact transfer rates (see figure 6.8). The values are 5-20 times lower for the mean transfer rate and 30-60 times for the fluctuating component.

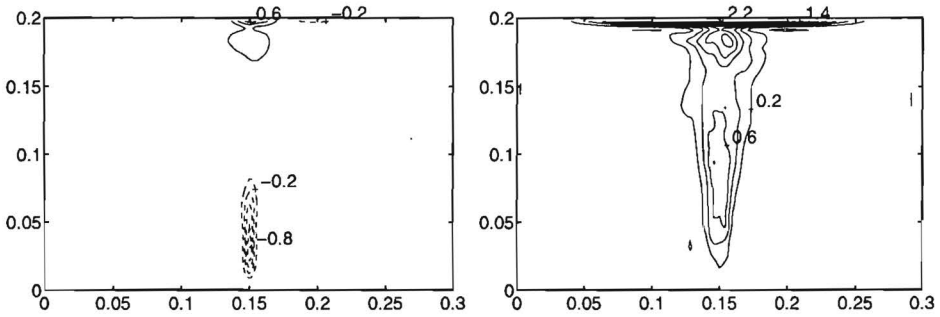


Figure 6.12: Kinetic energy transfer $\epsilon(2\Delta)$ from the two-dimensional velocity field at $x_2 = \frac{1}{2}D$, $\tau_{ij} = 0$ model, left: time mean, right: standard deviation. Levels multiplied by 10^7 .

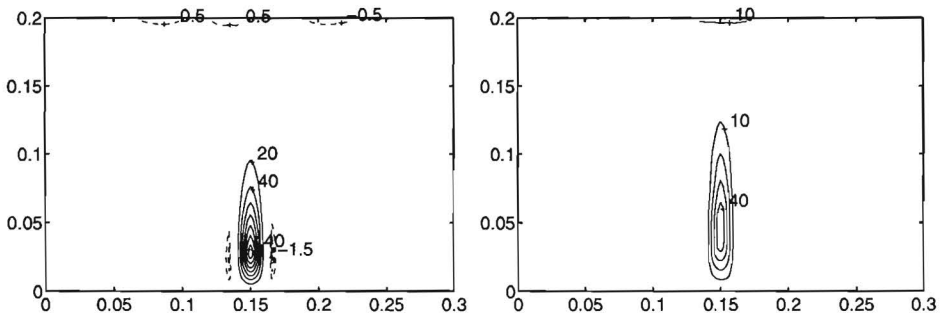


Figure 6.13: Buoyant production $g\beta\overline{u_3'T'}$ from the two-dimensional field at $x_2 = \frac{1}{2}D$, $\tau_{ij} = 0$ model, left: time mean, right: standard deviation. Levels multiplied by 10^7 .

The buoyant production $g\beta\overline{u_3'T'}$ seems to be of greater importance than the kinetic energy transfer. The mean and fluctuation of this quantity is depicted in figure 6.13. Near the source the maximum of the specific mean buoyant produc-

tion is approximately $1.4 \cdot 10^{-5} \text{ m}^2/\text{s}^3$ or $1.4 \cdot 10^{-2} \text{ W}/\text{m}^3$. For a local equilibrium of subgrid energy a high turbulent dissipation would be required in the source area. However, in the source area the flow is laminar. Therefore a local equilibrium model comprising buoyant production on a 2Δ grid would deteriorate the results. Taking into account the effect of transport of turbulent energy would give some improvement, though the energy would rise too fast due to an insufficient representation of both the velocity and temperature boundary layers.

Though they are neither large nor intense, there are negative mean buoyant production regions. In these regions a positive spatial fluctuation of temperature correlates with a negative fluctuation of vertical velocity and vice versa. At the sides of the plume this is due to a difference in boundary layer thicknesses of velocity and temperature. If they had an equal thickness instantaneously, the spatial fluctuations would have the same sign and their product would be positive everywhere. Near the cooled top wall, cold descending fingers, appearing when the upward velocity is low, may be advected back to the top. Relatively warm regions near the top wall are pushed downwards now and then. The mean buoyant production shows that the first event is a little more important, though the amplitude of both phenomena must be almost the same. This is demonstrated by the fluctuation of the buoyant production, which is a factor ten larger than the mean at this location.

Results from LES

Calculations were performed with the aid of several SGS models. First the standard Smagorinsky model was used. Results of this simulation are displayed in figures 6.14 and 6.15. The main difference with the $\tau_{ij} = 0$ model calculation is the decrease in plume velocity. This is an improvement. However, the midpoint vertical velocity is still two times as high as the experimentally found value. The fluctuations are again in good agreement with the experimentally obtained values. Again a large recirculating mean flow pattern establishes. Penetration of this recirculation to the lower left and right regions is even more profound and in less agreement with the experimental observed recirculation. Therefore the local eddy diffusivities must be tuned more specifically to the local dynamics.

The kinetic energy transfer is again similar to the exact value, only much too low, see figure 6.15. A comparison with the $\tau_{ij} = 0$ model simulation displays a decrease of this transfer.

Simulations with the structure function model, the buoyant Smagorinsky model and the Kolmogorov-Prandtl model yield only marginal modifications of the obtained flow. In the buoyant version of the Smagorinsky model the mean plume velocity increases somewhat. This may be explained by the negative mean temperature gradient with height, causing the turbulent viscosity to increase. However, for the upstream part of the plume, this temperature drop with height takes place in the laminar plume. Thus it is not creating turbulent subgrid fluc-

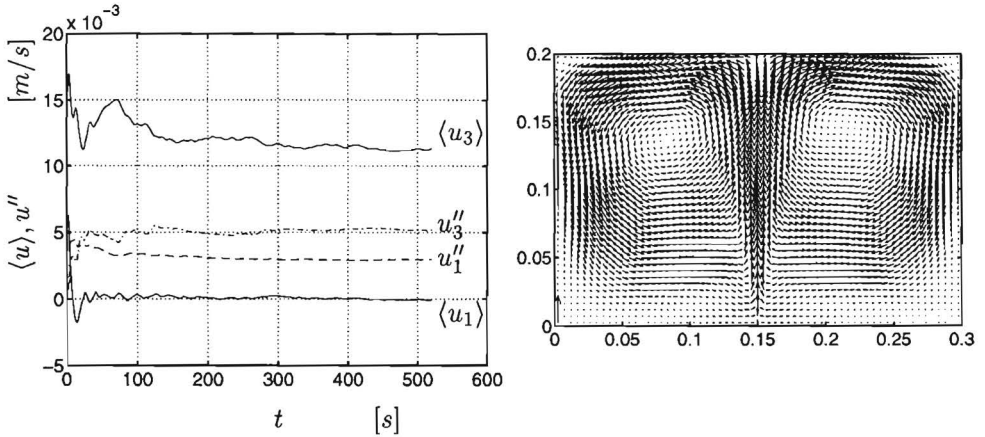


Figure 6.14: Results from the Smagorinsky model. Left: statistics as function of time at point $[0.15, 0.10, 0.10]$ m, right: time mean vector plot at $x_2 = \frac{1}{2}D$, scaling: 0.01 m/s magnitude is displayed by the left-bottom vector.

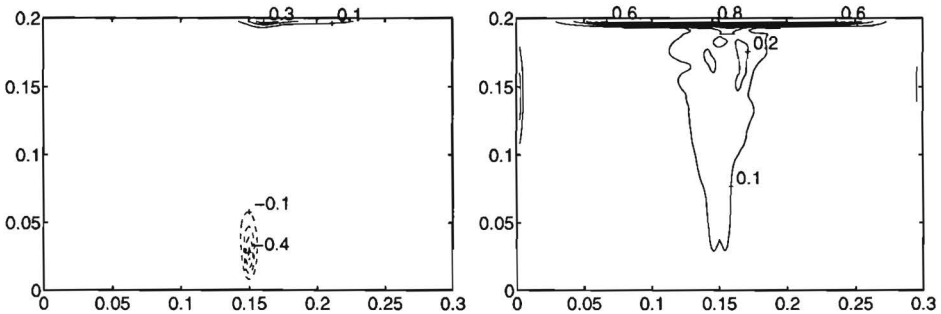


Figure 6.15: Kinetic energy transfer $\epsilon(2\Delta)$ at $x_2 = \frac{1}{2}D$, Smagorinsky model, left: time mean, right: standard deviation. Levels multiplied by 10^7 .

tuations as is assumed. Beyond the transition it does create subgrid fluctuations, but the model cannot discern between the two regions. The effect should not be taken into account when the negative gradient is monotonic and the profile is laterally confined. Both are characteristics of the laminar plume region.

Again, having an increased value of the eddy diffusivity, the viewpoint is subscribed that a higher eddy viscosity leads to less fluctuations and thus to a larger kinetic energy of the mean flow. The mean kinetic energy is determined by the conversion of potential energy to kinetic energy, which is determined by both eddy diffusivities. To reduce the uncertainty connected to this conversion would require the simulation of an uncoupled flow problem. It is recommended to study a comparable forced convection problem, like a confined box with a point source of momentum.

In a way, application of the dynamic model shows some improvement. This is obtained at the expense of a larger CPU-time, which is more than two times as large (0.53 CPU-seconds per time step) as needed for a Smagorinsky model. From a practical point of view the dynamic procedure could not be applied without additional restrictions. Allowing the dynamic parameter to attain large negative values would result in a total viscosity that is negative. As explained earlier in this thesis, this results in an unstable numerical scheme. Allowing a value of the total viscosity between zero and the molecular viscosity is an option. However, in executing this approach, it was found that the timesteps had to be decreased with at least a factor of two. Velocities were found to rise incidentally to very large values, causing a violation of the CFL stability criterion. Thus C was limited to zero for the present calculations. It must be realized that the potential improvements of the method are very much restricted by this approach, in which backscatter is not possible anymore.

Simulations with the present implementation of the dynamic model thus results in eddy diffusivities with a molecular value in the plume region. This causes the mean vertical velocities in the plume to rise to the $\tau_{ij} = 0$ model value, as is demonstrated by figure 6.16. Also the downward penetration of the recirculating flow is comparable to the $\tau_{ij} = 0$ model result.

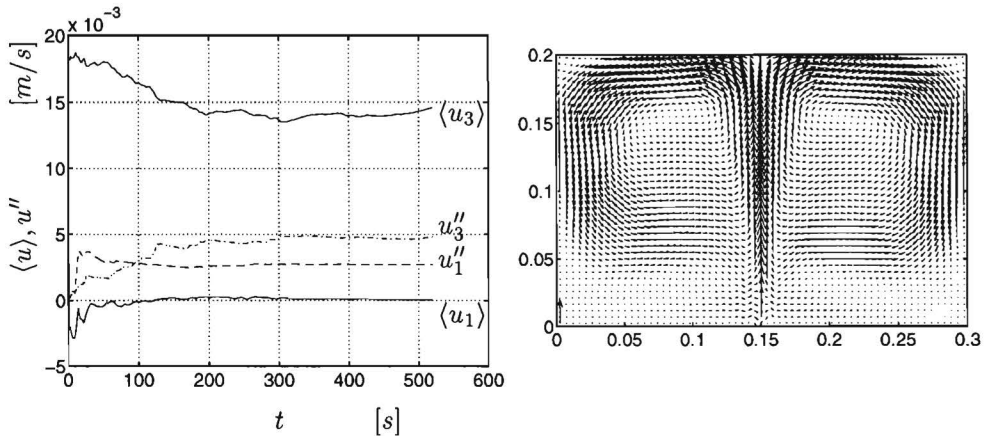


Figure 6.16: Results from the dynamic model. Left: statistics as function of time at point $[0.15, 0.10, 0.10]$ m, right: time mean vector plot at $x_2 = D/2$, scaling: 0.01 m/s magnitude is displayed by the left-bottom vector.

The kinetic energy transfer over the 2Δ scale is depicted in figure 6.17. Compared to the $\tau_{ij} = 0$ model simulation hardly an improvement is obtained. Still the values are much too low. With regard to this feature, other SGS models yielded values that are even worse. Here the positiveness of the dynamic parameter still damps the high wavenumber dynamics and so the kinetic energy transfer.

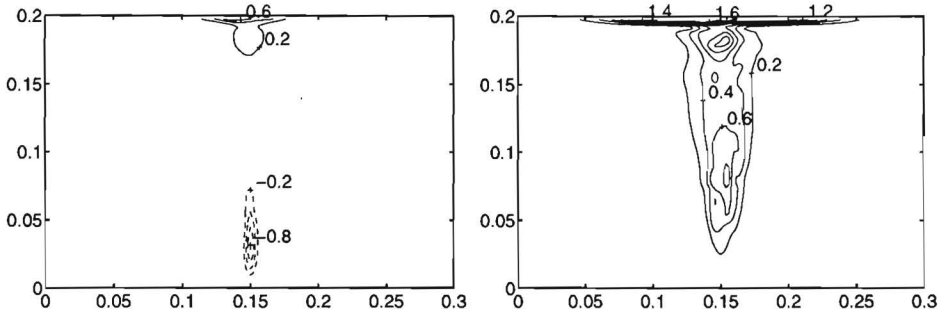


Figure 6.17: Kinetic energy transfer $\epsilon(2\Delta)$ obtained from a two-dimensional velocity field at $x_2 = D/2$, dynamic model, left: time mean, right: standard deviation. Levels multiplied by 10^7 .

Outside the plume region the eddy viscosity rises above the molecular value, as expected in a more homogeneous isotropic turbulent flow. This is depicted in figure 6.18. The mean value of the dynamic parameter attains a typical value of 0.1, corresponding with a rather high value of the Smagorinsky constant of about 0.3. The very high values in the lateral vicinity of the source corresponds with high curvatures of streamlines at the specified location. In a very short distance the flow changes from a lateral flow direction towards the source to an upward flow. This can also be observed in the vector plot, that even shows a wiggle in the velocity. Also at the walls, the value of C becomes very large. However, boundary conditions for the diffusivities are prescribed according to a laminar near wall behaviour. At the present grid resolution this might not be justified. The global qualitative picture of C -values is in agreement with the findings of the *a priori* results of the PTV experiment. Both results show a negative value in the plume core.

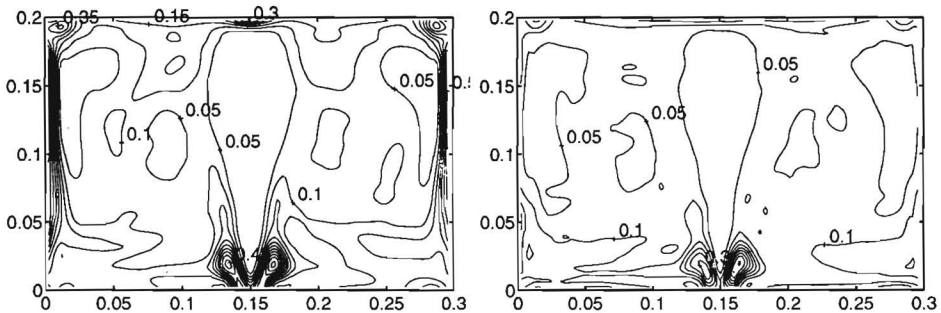


Figure 6.18: Dynamic parameter C at $x_2 = \frac{1}{2}D$, left: time mean, right: standard deviation.

In the dynamic calculation, a constant value of the turbulent Prandtl number

of $Pr_t = 1/3$ was used. The dynamic evaluation of Pr_t resulted in singular values of the eddy diffusivity of heat. This is due to the large number of zero crossings of Pr_t in the instantaneous fields. The zero crossings of C together with those of $P_j R_j$ resulted in a very spotty picture of Pr_t that, on its turn, frequently crosses the zero value. In retrospect the outlined evaluation of the combination C and Pr_t as proposed by Lilly [1992] is recognized to be inconsistent. It is a combined problem, expecting a coupled treatment. Such a treatment was suggested and successfully employed by Wong and Lilly [1994] for Rayleigh-Bénard convection.

6.3.3 The initially rising dipole

Here a closer look is given at the starting behaviour of the flow. It is presented on the basis of numerically obtained instantaneous temperature fields; a convenient tracer, since it is both the origin and the result of the flow. As a reference, a two-dimensional direct numerical simulation is performed. Convergence with grid refinement was checked, using grids of size 189×126 , 378×252 and 756×504 . It was found that the solution at 378×252 was converged with sufficient accuracy. Thus, a correct representation of the heat source is provided. At a lower resolution the penetration velocity of the dipole was too low. Due to the high Prandtl number the thermal boundary layer is thinner than the hydrodynamic boundary layer. With decreasing resolution the first incorrect representation arises in the temperature field. Numerical diffusion causes an artificial increase in thermal boundary layer width. Therefore the buoyant force and hence the velocities are underestimated.

The result after 16.8 seconds from the start is compared to results of LES. Therefore the original temperature field of the DNS is taken, as well as the spatially filtered field. The filter is specified by a top-hat convolution with a kernel of 6×6 , to obtain the correct filtered temperature field as defined in the LES at the present resolution. At the given time the results of LES were found to be still symmetrical, whereas the DNS already starts to diverge slightly from symmetry. This was also seen in the experimental setup. In order to make the instantaneous comparison possible, in the DNS no perturbation was applied. Thus the initial symmetry period was increased. Possible realizations of divergences from symmetry, connected to subgrid scale motion, is filtered out in the LES. It is assumed, however, that this will not significantly alter the analysis. Results of the DNS are given in figure 6.19.

In figure 6.20 results are given for the $\tau_{ij} = 0$ model and Smagorinsky model simulations, which are characteristic for the LESs. It is demonstrated that the rising speed of the initial dipole for the LESs is larger compared to the DNS. This is due to an underestimation of the flow friction on the coarse grid. Firstly this is the consequence of the insufficient representation of velocity gradients. Secondly it is due to the assumption of a real no-slip heat source in the DNS, contrary to a free volume heat source in the LES case. The $\tau_{ij} = 0$ model simulation can

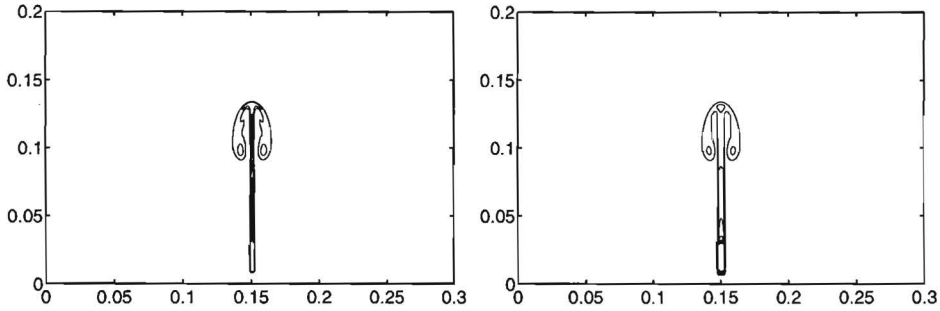


Figure 6.19: Temperature contours of starting dipole at $t = 16.8$ s obtained by DNS. Left: full resolution, representing T . Right: filtered DNS to LES grid resolution, representing \bar{T} . Contours starting at 21° C with increments of 1° C.

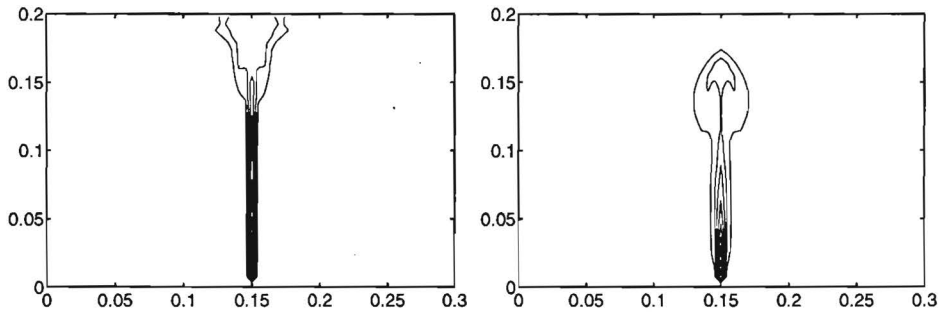


Figure 6.20: Temperature contours of starting dipole at $t = 16.8$ s. Left: $\tau_{ij} = 0$ model, right: Smagorinsky model. Contours starting at 20.5° C with increments of 0.5° C.

be appended in the above presented sequence of DNS results with decreasing resolution. At the present resolution also the hydrodynamic friction is largely underestimated, causing a high rising speed.

Accounting for subgrid dissipation employing a standard Smagorinsky model with a Kolmogorov constant of $C_k = 1.5$ is demonstrated to be insufficient. The prediction of backscatter in the centre of the plume seems to be in dissonance with this observation. Thus, particularly penetration fronts in a more or less stagnant ambient, like the present initial dipole, seem to be accompanied with an underpredicted subgrid friction. A slower penetration prediction might appear together with a backscatter at the centre of the plume, restoring the boundary layer thickness. The present observations of the rising speeds are in qualitative agreement with the time mean flow results in the previous sections, showing qualitatively similar differences between the upward velocities. At later times the unstable flow creates lateral velocity fluctuations that are much larger in the DNS, compared to the LES. This results in an additional decrease of upward

velocity in the DNS.

The increased diffusivity of temperature created by the filtering operator in the DNS is similar to the Smagorinsky model results. The latter is obtained on the account of the combination of the present wrong estimation of the eddy viscosity with the prescribed turbulent Prandtl number. Therefore it is hard to pronounce upon the correctness of Pr_t , though it is clear that larger values of the subgrid kinetic energy dissipation are required locally. On the one hand this may be achieved by employing larger values of the Smagorinsky constant, at least locally. On the other hand, an increase of Pr_t would yield a thinner thermal boundary layer, resulting in larger velocity gradients and thus a larger subgrid kinetic energy dissipation. It must be stated that Pr_t is not a property of the flow but mere a molecular parameter. Therefore, some kind of dynamic evaluation is still preferred.

6.3.4 Local temperatures: measurements versus LES

In the middle of the considered cross-section of the flow, temperature records were made as function of time. The application of thermocouples provided the exper-

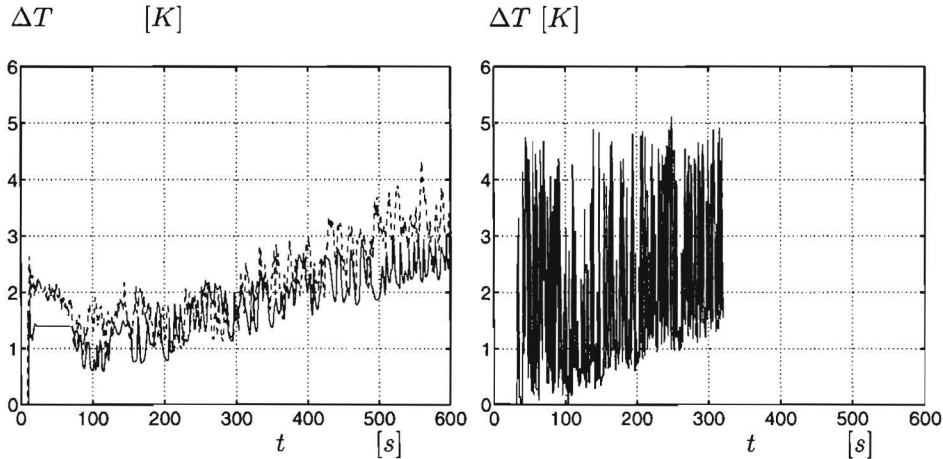


Figure 6.21: Temperature difference as function of time at point P_{p1} , left: LES, full line: Smagorinsky model, dashed line: $\tau_{ij} = 0$ model, right: measurement.

imental data. The temperature increase as obtained by the Smagorinsky model and the $\tau_{ij} = 0$ model are depicted in figure 6.21. Besides an integral increase in bulk temperature fluctuations are present. The increase in bulk temperature is a consequence of the initial discrepancy between the thermal energy supply by the source and the drain by the upper and lower conducting walls. In fact the drain appears to be negligible, considering a temperature rise of $2.625/600$ K/s connected to the heat input. As a consequence of the meandering motion of the

plume, fluctuations are present of about 1 K , which is in agreement with the maximum large scale temperature difference at this height.

At the right side of the figure a measurement is presented. A few records were made yielding similar data. The fluctuations are about 5 K . This is also in agreement with the laminar boundary layer solution and the $2D$ DNS, the latter presented in figure 6.19 in the previous section. The only difference is an irregular oscillation of the plume, causing a fluctuation instead of a constant temperature rise. For convenience the boundary layer solution as presented in chapter 2 for

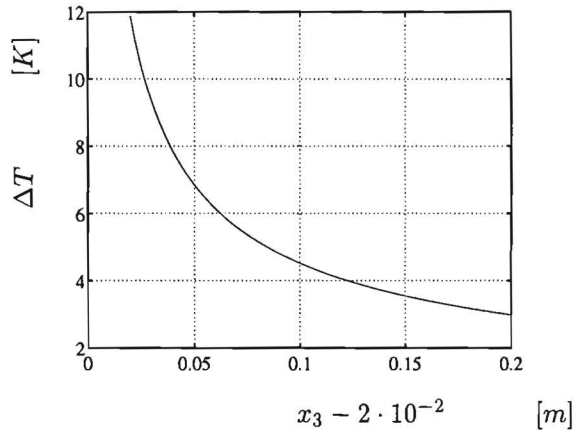


Figure 6.22: Temperature difference of laminar plume as function of height from virtual source origin.

the present set of (Ra, Pr) is given in figure 6.22. The temperature is given as function of height above the virtual origin, which must be defined in the actual situation facing the fact that boundary conditions are not identical. Temperature records are made at mid-depth, being 8 cm above the middle of the heat source. Taking this distance to the virtual origin, it can be observed that the laminar boundary layer temperature is approximately equal to 5 K .

To make a fair comparison with the temperature measurements possible, the obtained data from the physical experiment should be spatially filtered. Evidently this is not possible, though under the Taylor assumption of "frozen turbulence", the spatial filter may be substituted by a temporal filter. It was found that a temporal top-hat filter with a time span of 6 s yields results comparable to those of the LESs. Remarkable is that this filter length does not relate to any expected ratio of gridwidth and a characteristic transport velocity at the considered point. It must be remarked again that there is a poor representation of the thermal boundary layer relative to the hydrodynamic boundary layer. In figure 6.23 the filtered physical data are shown together with power spectra of the signals obtained by numerical and physical experiments.

High frequencies are poorly represented by the simulations. Only the very

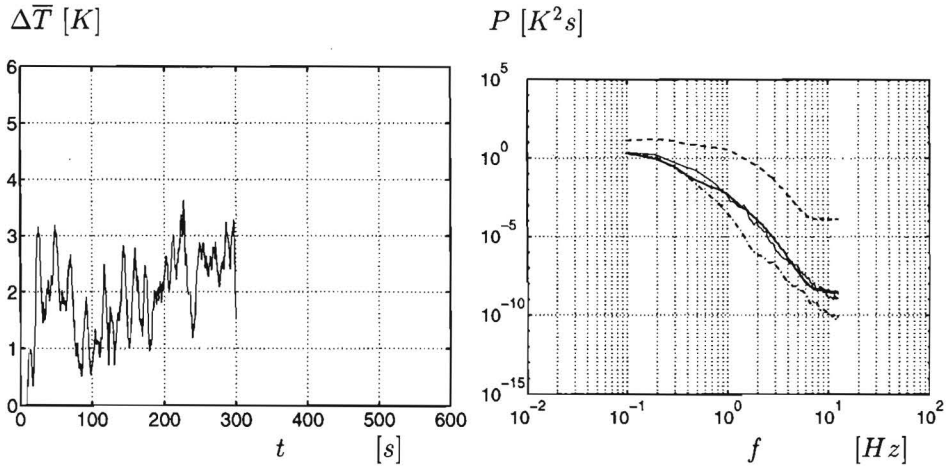


Figure 6.23: Statistics of temperature difference. Left: convoluted measurement, right: spectra; full bold line: mean spectrum of convoluted measurements, bold dashed: mean spectrum of original measurements, bold dash-dotted: spectrum obtained from Smagorinsky model, full thin line: spectrum obtained from $\tau_{ij} = 0$ model.

slow fluctuations are comparable to physically found values, regarding their spectral power density. This is in contrast to the spatial fluctuations in the initial rising dipole as described in the preceding section. Later on, as a transitional and turbulent region appears, spatial and temporal fluctuations are suppressed in the simulations even with zero eddy diffusivities. Thus a too large part of the fluctuating kinetic energy is supplied to only the largest scales of motion, connected to low frequencies.

6.4 Conclusions

The transitional flow regime of a water plume in a confined tank has been investigated experimentally and numerically. Experimental velocity data were obtained using PTV in a vertical cross-section. Furthermore, local thermocouple measurements were carried out. Effects of initial stratification as well as heat losses may be considered to be negligible. With the PTV the global mean motion and the global fluctuations are very well represented. However, near the plume origin only a very small amount of particles are responsible for the description of the flow. On the contrary, uncontrolled heat losses and initial inhomogeneities, like thermal stratification, hardly influenced the results. The results of the PTV revealed a three-dimensional transitional velocity field. Large scale time mean recirculation zones were found to be present confined to the upper half of the flow domain.

Employing the velocity fields from the experiment *a priori* tests were performed. Only the statistics of the subgrid stresses in each point of the vertical cross-section were taken into account. On the basis of filtered velocity fields, stresses were calculated with existing subgrid scale models. No sufficient similarity with the exact stresses was found. Only a fair representation was found for the interscale kinetic energy transfer over the scale of the filterwidth with the dynamic model.

Comparing actual simulations performed with several SGS models, yielded poor agreement with the PTV data. The plume velocity was overestimated and the penetration of the time mean recirculation zone in the lower part of the flow domain was too deep. This behaviour was found to be connected to the bad representation of high wavenumbers and frequencies. Especially the thermal boundary layer is insufficiently represented. Therefore most of the kinetic energy was captured by the mean flow. These findings were supported by the local temperature measurements.

Here, as in traditional large-eddy modelling, the treatment of the subgrid stresses has received very much attention. Thus, assuming a model for the subgrid stresses, the subgrid fluxes are related to them with the turbulent Prandtl number. This may be an appropriate approach for large scale turbulent convection flows. In the present configuration, however, it all starts with heat fluxes at a subgrid scale. This heat input is always represented at the grid scale. At this stage the simulation is not able to represent a laminar boundary layer anymore. Especially in the transitional and source region, grid refinement is recommended, thereby suppressing also the role of the subgrid model in these regions. An additional problem is the representation of the confining no-slip walls.

In the next chapter, a geometry is applied which has a heat source large enough to represent it at a fine DNS grid as well as on a coarse LES grid. In this way the above discussed problem will be avoided.

Chapter 7

Results for air plumes: DNS versus LES

7.1 Introduction

In this chapter results of a Direct Numerical Simulation (DNS) will be confronted with the results of Large-Eddy Simulations (LES). With the DNS as a reference basis a vast amount of data is provided with high spatial and temporal resolution. On a global level the mean field and standard deviations can be used for comparison. In order to interpret these data more local data can be used, both in space and time. The latter contains instantaneous field information as well as probability density functions and spectral distributions.

A huge amount of computer effort is needed to perform a DNS. Therefore redundancy must be avoided. With the present numerical method as described in chapter 4 the spatial and temporal sampling of the velocity and the temperature field are at the same rate. In order to produce data with high relevancy the characteristic wavenumbers of velocity and temperature fields are objected to be very close to each other. The differences in the distributions of spectral power with wavenumber depends largely on the Prandtl number. In order to perform an efficient DNS and to provide data with physical relevance, the Prandtl number is chosen to be $Pr = 0.71$. This corresponds to the value for air.

In contrast to plumes occurring in water, air plumes possess a more similar distribution of thermal and hydrodynamical quantities. As demonstrated in chapter 2, the boundary layer thicknesses are almost equal for a laminar plume in air. In water the velocity layer is about three times as thick as the thermal layer.

In a turbulent field with a Kolmogorov wavenumber k_η , the conductive wavenumber $k_{\eta T}$, which is connected to the largest wavenumber in the temperature field, depends on the Prandtl number. It is given by *Lesieur* [1990] to be $k_{\eta T} = Pr k_\eta$ for $Pr > 1$ and $k_{\eta T} = Pr^{3/4} k_\eta$ for $Pr < 1$. Thus at high Prandtl numbers

(water) a relatively warm or cold blob will be stretched and folded to larger wavenumbers. At low Pr numbers the diffusion of heat is more important.

The geometry as used in the DNS corresponds to the flow problem as defined by *Desrayaud and Lauriat* [1993] and was taken as a two-dimensional test problem in chapter 4. In the DNS a third direction parallel to the heat source is extended with an equal dimension. In this direction periodic boundary conditions are assumed. Thus in determining statistics, fluctuations in time as well as variations in this homogeneous direction can be used. If the flow statistics are known to be symmetrical with respect to the midplane $x_s = 0.5$ beforehand, an additional averaging may be carried out, weighing values at $x' = x_s - x$ with the mirrored values at $-x'$. In determining the flow statistics, the mentioned methods reduce the integration time and with it, the minimal computational effort needed.

The heat source distribution is defined by a Gaussian hill according to

$$q' = \frac{1}{\pi\sigma^2} e^{-r^2/\sigma^2}; \quad r = \sqrt{\left(x - \frac{1}{2}\right)^2 + \left(y - \frac{1}{4}\right)^2}, \quad (7.1)$$

with a suitably chosen width, σ . The latter concerns the accuracy with which the source can be represented and depends on the minimal gridsizes that are used. In the present thesis a width of $\sigma = 2.5 \cdot 10^{-2}$ was defined. With grid resolutions starting at 45×45 in the direction perpendicular to the source the given distribution can be represented with sufficient accuracy. This with respect to the discrete integral of the flux over the domain, which does not exceed a difference from 1 of 10^{-5} . In contrast to the situation in the preceding chapter the heat flux is instantly prescribed.

The forcing rate or Rayleigh number depends on the maximal allowable grid size as used in the DNS with respect to the random access storage of the computer. Computations were carried out on a Cray C98/4256 with a core memory of 256 Mwords. With a grid resolution of 195^3 about half of this storage capacity is used. On the basis of a two-dimensional convergence test it was found that a maximal forcing of $Ra = 10^{10}$ could be applied. This forcing rate is about three magnitudes above the value at which, apart from the initial transient, time dependent motion appears. As outlined in chapter 4 this first oscillation in the $2D$ plane starts at about $Ra = 3 \cdot 10^7$.

In this chapter first two-dimensional motion at $Ra = 10^{10}$ will be investigated with respect to convergence, predictability and two-dimensional dynamics. The aim of this study is to estimate the spatial and temporal resolution required for the $3D$ DNS, together with an appropriate initial perturbation. Furthermore, two-dimensional features will be uncovered, which will be compared to three-dimensional phenomena. Then the DNS will be discussed and results will be presented. The transient to three-dimensional motion will be considered as well as the quasi-stationary turbulence appearing thereafter. Finally, results of LES will be given and compared to the DNS. Since the results in the present chapter are

all numerically determined using the Boussinesq approximation, it is convenient to switch to dimensionless quantities again.

7.2 Results of two-dimensional simulations

7.2.1 Convergence of two-dimensional flow

The initial dipole

First the starting flow is investigated. The resulting temperature fields are plotted in figure 7.1 for $t = 1.2 \cdot 10^{-4}$ with an increased grid resolution. At this moment in time the dipolar structure is initiated and has risen to the upper half of the domain, heading for the top confinement. Grids involved, contained an amount of collocation points of 49^2 , 99^2 , 195^2 and 390^2 , respectively.

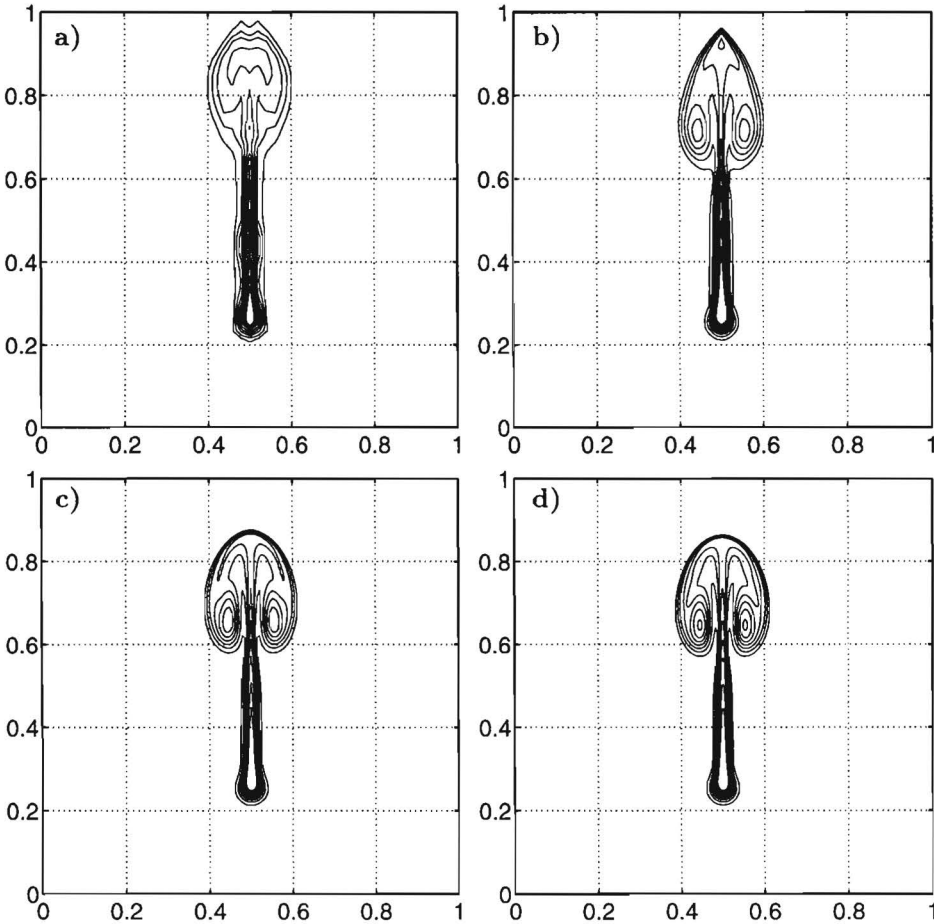


Figure 7.1: Temperature distributions at $t = 1.2 \cdot 10^{-4}$, $Ra = 10^{10}$, $Pr = 0.71$. Contour levels [$10^{-3} : 10^{-3} : 10^{-2}$]. Resolution: a) 49^2 ; b) 99^2 ; c) 195^2 ; d) 390^2 .

In the direction of increasing spatial resolutions the dipole is traveling with diminishing speed. The low resolution simulations are not able to capture the velocity gradients with sufficient accuracy. This results in an underestimation of Newtonian friction, allowing relatively large rising speeds. At very low resolution it is expected that numerical thermal diffusion becomes large, resulting in large structures of low temperature. This would lead to lower velocities. However, the latter phenomenon is not observed at the present resolutions.

At low resolution the spectral energy at wavenumbers connected to the grid size is not low enough to resolve the flow. This results in a wiggly shape of the temperature contours. Convergence of the position and smoothness of the dipolar structure with grid refinement is clearly present. An acceptable representation of the occurring physical phenomena is observed at the 195^2 grid.

The present $2D$ convergence in the initial phase of the plume flow under investigation is not a guarantee for the convergence in the three-dimensional turbulent case, although it is felt as to give a good indication about the resolution required. First there is the issue of unpredictability. Instantaneous realizations can not be compared anymore at later times due to the inevitable unpredictability as already mentioned briefly before in chapter 2. Therefore statistics have to be compared. In the next section these statistical results are presented. Also the dependence on the initial perturbation will be shown. To get an impression of the time dependent flow, temperature fields are given as function of time in appendix F. Second there is the three-dimensional dynamics of the flow. On the one hand it might be argued that vortex stretching will increase the energy containing wavenumber range at the high end. Since buoyant flows are more space filling this is not expected to have a large influence. On the other hand, at small scales, laminar entrainment will be present, steepening free boundary layers that will be convected over the entire domain. However, this convective abrasion is already present in the $2D$ case. This can be observed in the vicinity of the plume centre in the direction of each separate poles of the dipole. Here, by laminar entrainment of relatively cold fluid, each monopole grazes at the laminar plume, decreasing the thermal boundary layer thickness.

Laminar boundary layer flow

An additional check can be obtained by a comparison of the results from laminar boundary-layer theory with those of $2D$ simulation. This is again an instantaneous evaluation at a time where a more or less stationary and symmetrical laminar plume has developed in the initial phase of the flow. Since there are more approximations used in the laminar boundary-layer theory, the comparison might be regarded as a check for the validity of this theory. For instance, the forcing rate may be neither too large nor too small, because it concerns convective plumes that are not turbulent. However, a variation of the Rayleigh number will not be carried out here.

The results of the comparison are shown in figure 7.2. Here the value of ϕ as defined in equation (2.51) is calculated back from the values of T . Also the similarity variable η is calculated from the $2D$ 195^2 grid. In the figures the similarity variable for the $2D$ full Navier-Stokes simulation is taken at lines of constant height. Results of simulations are taken at time $t = 5 \cdot 10^{-4}$, see appendix F. A Gaussian source distribution is taken as well as a point source,

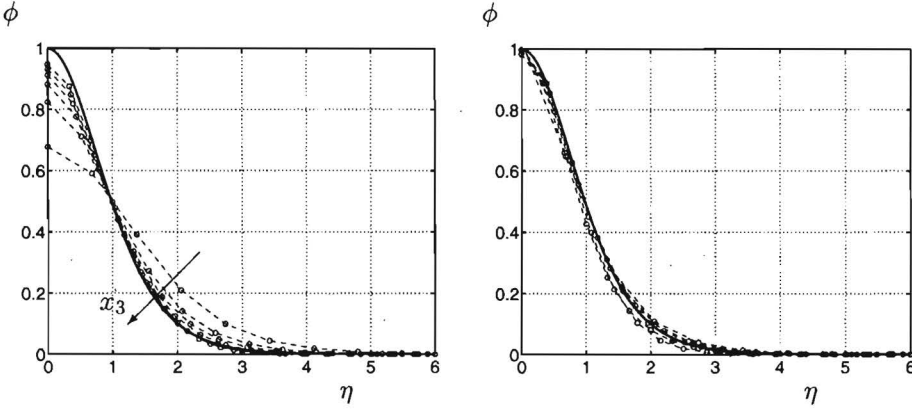


Figure 7.2: Temperature distributions $\phi(\eta)$ at $t = 5 \cdot 10^{-4}$ and heights $x_3 = 0.3513$ increasing with $\Delta x_3 = 0.1026$. Left: present Gaussian source. Right: point source containing a single grid cell. Circles indicate Navier-Stokes simulation grid points, the bold line indicates the boundary-layer theory result.

containing a single grid cell. It can be observed that the point source simulation matches almost exactly with the boundary layer results, which validates the code. In later analysis a Gaussian source distribution will be used. To investigate how much this influences the results it is also compared to the boundary layer profile. The temperature distribution from the Gaussian source shows some differences. Especially at low heights the Gaussian distribution results in a large deviation from boundary-layer theory. Downstream, the results are converging to each other, though they do not reach the value of $\phi = 1$ at the midplane. However, the latter is due to the differences in boundary conditions. In case of the distributed source, temperatures at low η are smaller than the point source prediction and larger at large η .

In both cases the derivative of the streamfunction f' matches accurately at small values of η , typically up to $\eta = 2$. At higher values of the similarity variable combined with high values of x_3 a non-vanishing value $f' \approx 0.1$ is present. This is a consequence of the top wall that produces a recirculation at the investigated moment in time.

In the present confined geometry the laminar boundary-layer theory provides data that are in accordance with the obtained Navier-Stokes flow. This in a

time interval starting with the collision of the initial dipole with the top wall and ending with the symmetry breaking instability. After this instability it still provides data for maximum occurring velocities and temperatures, though the exact location is not known. The boundary layer starts a meandering motion, occupying a very large lateral region in the $2D$ case (see appendix F). As will be shown later, this region is much less extended in the $3D$ case, especially at low elevations from the source.

7.2.2 The predictability horizon in $2D$ flow

So far the analysis of the flow concerned instantaneous symmetrical flow fields. The symmetry is a consequence of the symmetrical flow configuration, boundary conditions and initial conditions. The occurring phenomena in a hypothetical $2D$ flow are equal to those occurring in a slice of the $3D$ flow perpendicular to the homogeneous direction. However, at high Rayleigh numbers the flow is unstable and after some time a symmetry breaking bifurcation appears (a symmetrical solution still exists). Since this happens in the two-dimensional plane, the initial asymmetrical flow manifest itself equally in two and three dimensions. Within a specified flow medium the length of the symmetric period depends on the forcing of the flow and the initial perturbation. In a numerical simulation it depends also on spatial resolution, temporal resolution and machine accuracy. The flow medium and forcing are already specified as well as the computational grid. Stability of the numerical scheme specifies the temporal sampling rate, which is $\Delta t = 2.5 \cdot 10^{-7}$.

In order to perform an efficient $3D$ DNS, knowledge of the length of the symmetric transient is indispensable. On the one hand a large initial perturbation is preferred, resulting directly in three-dimensional motion. However, there will still remain a transient towards quasi-steadiness because the average kinetic energy has to be provided by the potential source. Another disadvantage is the disruption of natural occurring phenomena for some time interval that is not exactly known. A very small perturbation, on the other hand, results in a flow that is two-dimensional for a long time. It would be a waste to spend computer time connected to the $3D$ problem for a result that may have been calculated in two dimensions. Therefore a $2D$ study is carried out to investigate the consequences of the initial perturbations.

Initial temperature perturbations are added to the zero initial temperature field in order not to harm the incompressibility of the flow. For this purpose a standard random generator was used as e.g. given in *Press et al.* [1992]. Based on an initial so-called "seed" it realizes subsequent numbers for the temperature at each collocation point. These numbers are defined in a specified interval, centred around zero to add no net thermal energy to the flow field. Half the size of the interval is denoted as a_T , the intensity of the perturbation. The intensity was varied in steps from $a_T = 10^{-4}$ up to $a_T = 10^{-14}$. In each step the

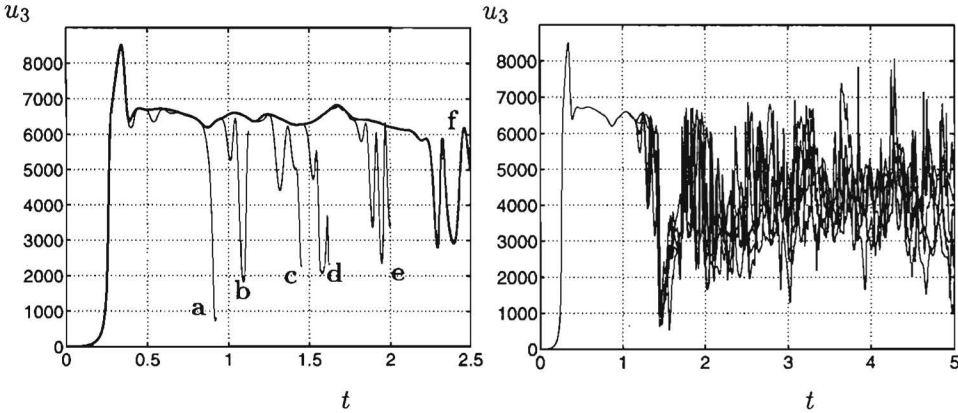


Figure 7.3: Vertical velocity as function of time ($\cdot 10^{-3}$) at position $(x_1, x_3) = (0.5, 0.7487)$. Left: influence of initial random perturbation on T with intensities $a_T = 10^{-4}$ (a), 10^{-6} (b), 10^{-8} (c), 10^{-10} (d), 10^{-12} (e) and for the bold line $a_T = 10^{-14}$ (f). Right: influence of the generator seed at $a_T = 10^{-8}$; using six different values.

intensity was decreased with two decades. The first value is about a decade below the undisturbed resulting temperatures, whereas the last value is approaching machine accuracy as given by $\epsilon \approx 10^{-15}$, for 64 bits floating point representations.

Results are given in figure 7.3. The bold line is the result of the simulation with the smallest perturbation intensity $a_T = 10^{-14}$. The first peak at $t \sim 0.3$ corresponds with the pass of the initial dipole, after which a decrease occurs due to the collision at the top wall (see appendix F). After this collision a rebound of the monopoles from the no-slip wall occurs, accompanied by the creation of vorticity of opposite sign. This is a physical effect that was also found experimentally by *van Heijst and Flór* [1989] and numerically by *Orlandi* [1990]. Thus it is not due to the approximation of the boundary conditions as discussed in section 4.1.3.

For this computation the symmetry is getting lost at approximately $t = 2.2 \cdot 10^{-3}$. At that moment the value of the vertical velocity decreases rapidly due to a transverse motion of the boundary layer. With the increase of the perturbation intensity this occurs earlier, and can be observed by the deviation from the bold line. The largest perturbation disrupts the flow already just after the dipole collision. As a second test, in the right graphic of figure 7.3, the initial seed was varied at constant intensity. It can be observed that all realizations start to diverge from each other at the same moment in time. Thus predictability is lost at the moment of symmetry breaking. Initially there is still some coherent dynamics that is lost after a while. Then, the oscillations start to fill up a velocity band.

In terms of predictability it is shown that with every subsequent decade of accuracy of the approximation of the zero initial field, the predictability horizon is shifted forward with approximately a same period, of about $2.5 \cdot 10^{-3}$.

In order to perform an efficient 3D DNS, without to much disruption a perturbation of $a_T = 10^{-8}$ was found to be appropriate.

7.2.3 Turbulence statistics of 2D flow

The transitional buoyant plumes under consideration originate from a two-dimensional flow. At higher elevations from the source a curling motion develops, embedded in a more or less two-dimensional recirculating flow. If the three-dimensional curling motions are of small spatial extent it should be possible to perform successfully simulations on 2D grids, either DNS or LES.

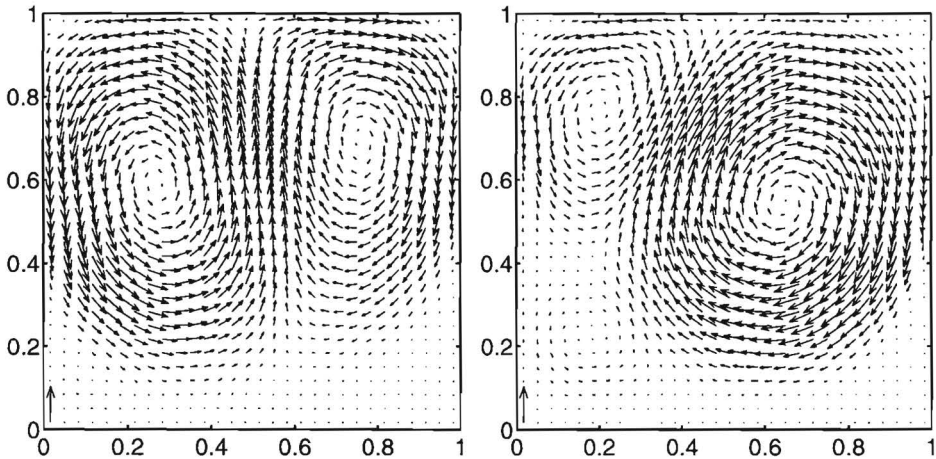


Figure 7.4: Vector plot of time mean velocity at $Ra = 10^{10}$, $Pr = 0.71$. Left: gridsize 49^2 , right: gridsize 195^2 . The lower left corner vector is of length 5000.

To investigate the 2D turbulent flow statistics were determined over the period $t = 0.005 - 0.01$. These flows were simulated without a subgrid-scale model on three grids, defined by 49^2 , 99^2 and 195^2 equidistant volumes at $Ra = 10^{10}$, $Pr = 0.71$. Results for the mean field are depicted in figure 7.4. Though the statistics may not have been fully converged, it can be observed that there is a large-scale flow bifurcation. Here the left-right symmetry of the flow problem may not be used for fast convergence of statistical data. At the finest grid the flow consists of a large circulating region occupying most of the flow domain. At the coarse grid this is not so profoundly present. Thus the energy drain connected to numerical diffusion at coarse grids results in a flow field which resembles more the 3D case (see figure 7.9). At the fine grid the injected kinetic energy is able to

follow the inverse energy cascade of *Kraichnan* [1967]. However, as will be shown with the 3D DNS in section 7.3, the coarse grid mean flow contains a much too large kinetic energy. Once fluctuations are created they are advected through the entire domain with a relatively small dissipation. Standard deviations of the velocity components are almost constant throughout the domain. Regions of decreased values of the fluctuations are only found near walls perpendicular to the fluctuating component in question. Thus extra dissipation must be provided as might be done with a subgrid-scale model in a LES. In the next section results of 2D LES will be discussed.

7.2.4 Results of 2D LES

As discussed in chapter 3, subgrid scale modelling is based on the equilibrium kinetic energy drain of 3D turbulence. Therefore a subgrid scale model provides the dissipation at the gridscale connected to this drain. If indeed a 3D equilibrium range exists just beyond the cut-off, which is fed by the gridscale kinetic energy injection, a standard model would yield results in agreement with the physical problem. This in analogy with the geophysical large-scale atmospheric circulation. Here we will again look at the start up behaviour and to the developed field.

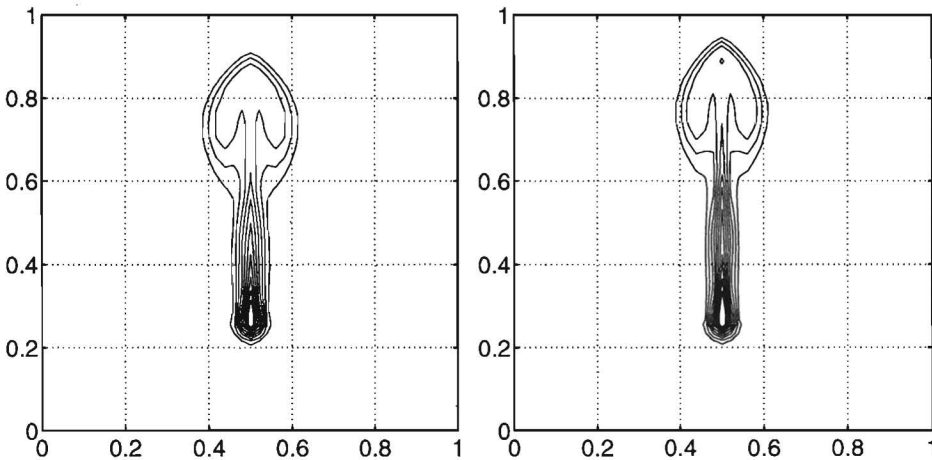


Figure 7.5: Temperature distributions at $t = 1.2 \cdot 10^{-4}$ with $Ra = 10^{10}$, $Pr = 0.71$, obtained with the Smagorinsky model at gridsize 49^2 . Contour levels $[10^{-3} : 10^{-3} : 10^{-2}]$. Left: $Pr_T = 1/3$; right $Pr_T = 1$.

In figure 7.5 it is demonstrated that for the starting flow, the incorporation of a Smagorinsky model yields an improved result with respect to the $\tau_{ij} = 0$ model simulation as given in figure 7.1. The travelling speed of the dipolar

structure is limited as a result of the increased friction. Furthermore the influence of the turbulent Prandtl number is shown. According to the position of the dipole it must be observed that a low turbulent Prandtl number like $Pr_T = 1/3$ is preferable in comparison with $Pr_T = 1$. Not only the additional flow friction reduces the dipole speed, also an increased eddy diffusivity, resulting in smaller buoyancy forces, is responsible for an improved matching with the 2D converged solution. On the other hand it is shown that the thermal boundary layer is more localized at the higher value of Pr_T . A combination of higher eddy diffusivities, together with an increased value of Pr_T eventually results in an optimal combination. Therefore the model input values C_s and Pr_T should be tuned to the flow. Without loss of generality this would be attained by a proper dynamic model, both for stresses as well as fluxes.

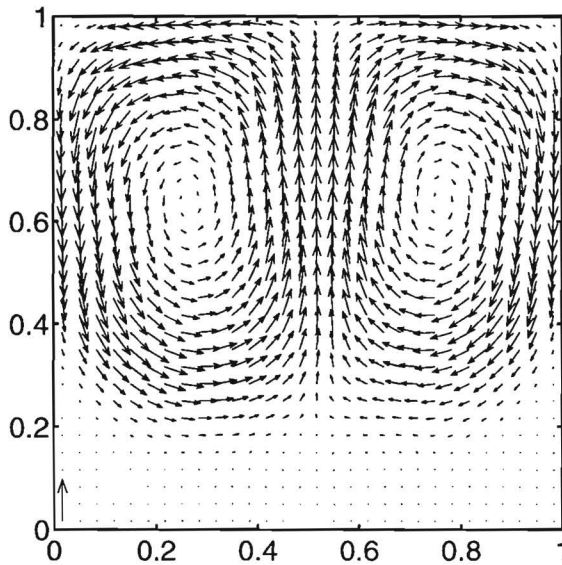


Figure 7.6: Vector plot of time mean velocity at gridsize 49^2 and $Ra = 10^{10}$, $Pr = 0.71$, obtained by the Smagorinsky model ($Pr_T = 1/3$). Lower left corner vector is of length 5000.

The time mean flow shows an increased symmetry. A more detailed examination shows that the mean velocities in the plume region are larger than those obtained with the $\tau_{ij} = 0$ model calculation of section 7.2.3. On the other hand the fluctuations over the entire flow domain exhibit a lower intensity. Thus more kinetic energy is supplied to the time mean flow and dissipated at the large scales by the model on the account of the instationary small-scale fluctuations. Both two-dimensionality and the incompressibility condition are responsible for the creation of large structures. In the three-dimensional case large stresses can be

absorbed by motion out of the present $2D$ plane, accompanied by the formation of smaller structures. The kinetic energy of these structures can be dissipated more efficiently by a subgrid model.

7.3 Results of direct numerical simulation

7.3.1 The transient

The initial symmetrical part of the transient in three dimensions is equal to its counterpart in two dimensions. From the moment of the symmetry breaking bifurcation the $3D$ simulation starts to be interesting. Though the start is two-dimensional, a $3D$ simulation is used also for this period, allowing axial modes to grow from their machine accuracy value right from the beginning.

The $3D$ DNS at $Ra = 10^{10}$, $Pr = 0.71$, consisted of 37,000 time steps, the first 13,000 of length $\Delta t = 2.5 \cdot 10^{-7}$, and the last 24,000 of length $\Delta t = 2.0 \cdot 10^{-7}$. The period simulated with the longer time steps up to $t = 0.00325$ corresponds with the transient, whereas the latter period up to $t = 0.00805$ deals with the quasi-stationary situation. The initial temperature perturbation intensity was $a_T = 10^{-8}$ and the flow becomes asymmetrical at about $t = 0.00125$ as is the case in the $2D$ situation, depicted in figure 7.3. The transient to $3D$ motion at about $t \sim 2.0$ is depicted in figure 7.7, in which the vertical and axial component of the velocity at location $(x_1, x_3) = (0.5, 0.75)$ are given as function of the axial coordinate y and time. Later on velocity data at this monitoring line will be used as a key element in the comparison between DNS and LES. The monitoring line is located at an elevation defined in the expected transitional region. Furthermore the vertical and axial velocity components at this line are expected to constitute a sensitive pair of flow tracers. This in the sense that the vertical component originates as a result of the potential to kinetic energy conversion, whereas the axial components appears as a result of downstream instabilities.

It is demonstrated that $3D$ motion initially manifests itself as a $2D$ flow that changes in planes along the axial direction. At this stage hardly no axial velocity or velocity fluctuations are present. As the velocity distributions in the $x_1 - x_3$ planes at various x_2 get more out of phase the third velocity component starts to grow from its initial zero value. Note the difference in intensity scales for the vertical and axial velocity component. From the given data it can not be observed whether the changes in the homogeneous direction are due to a meandering of the boundary layer ($3D$) or to a change in profile height in this direction ($2D$ symmetrical in each slice). Three dimensional visualisation revealed that the boundary layer is still almost two-dimensional. Downstream vortices are shed in which isothermal surfaces bulge somewhat, resulting in lumps of slightly increased temperature. These lumps of higher temperature are the cause of the development of vortices with a rotation axis lying in the $x - z$ plane. In this way axial velocities start to grow and due to interactions the flow becomes turbulent,

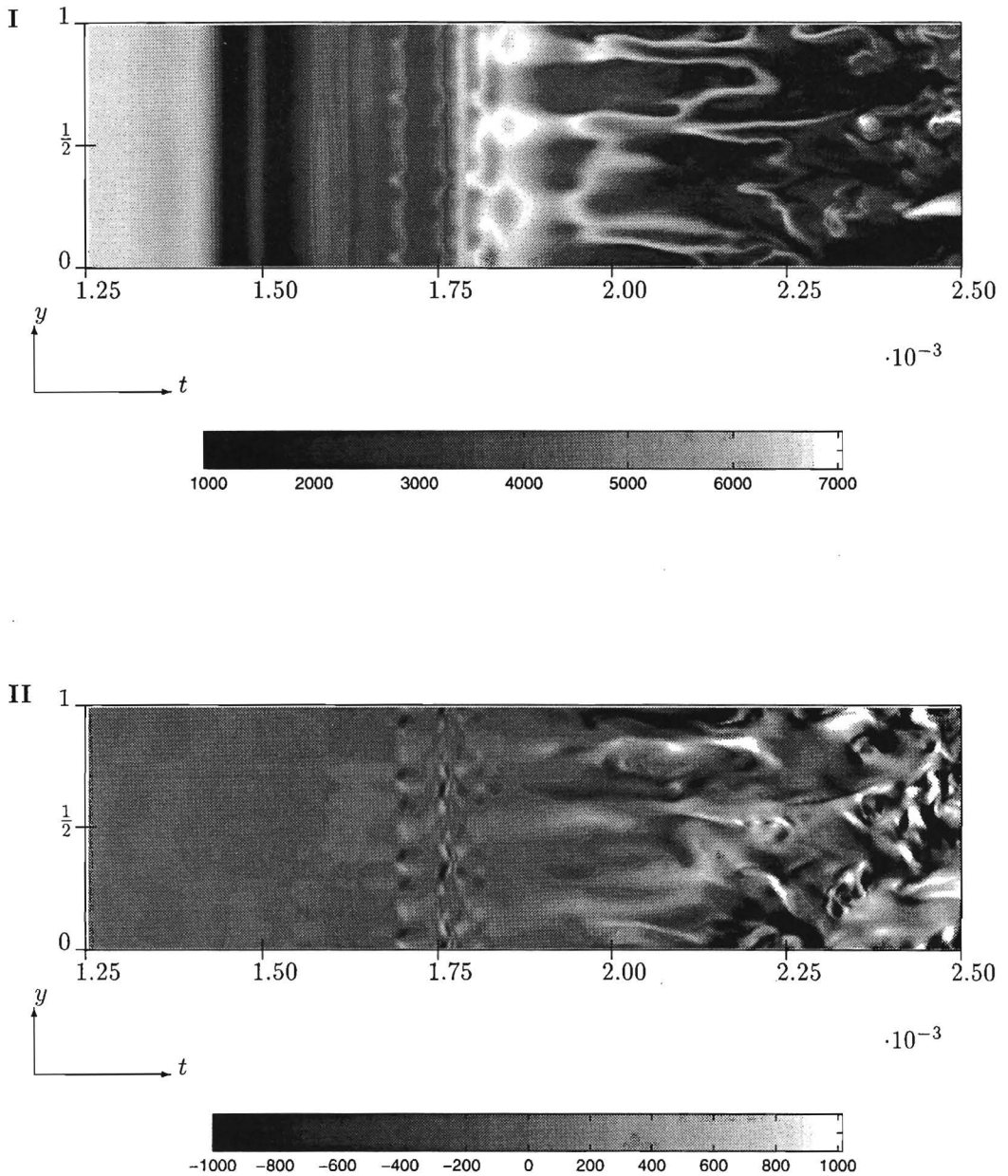


Figure 7.7: Vertical velocity I and axial velocity II as function of axial coordinate and time at $x_1 = 0.5, x_3 = 0.75$. Evolution in simulated time interval $1.25 \cdot 10^{-3} < t < 2.5 \cdot 10^{-3}$.

especially in the downstream region. A time series of temperature contour plots in a cross-section are given in appendix G. The sequence is comparable to that given for the 2D case in appendix F, and the differences of 2D and 3D dynamics can be clearly observed.

Figure 7.8 shows an instantaneous sample (of the appendices) of the temperature distribution as observed in the 2D and 3D cases. In the 2D case large structures are present that bend and fold. The main flow occupies almost the entire domain, because the kinetic energy is captured in the 2D plane. The entire plume oscillates heavily. In the 3D case the plume shows a laminar vertical structure at small elevations from the source. Downstream it becomes turbulent and due to 3D motion smaller structures are created effectively. Kinetic energy is drained to smaller scales and there is no large recirculating flow. This is why a rather stable thermocline develops at the source height.

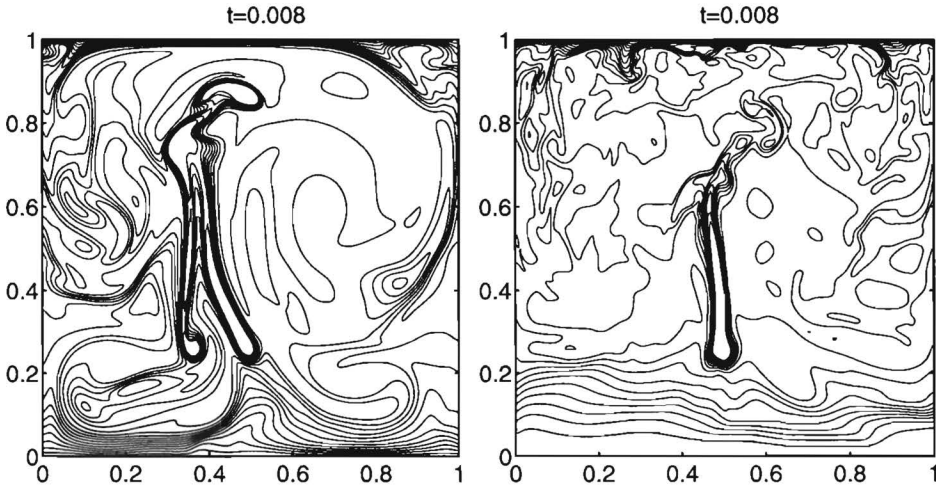


Figure 7.8: Instantaneous temperature distributions in the 2D case (left) and 3D case (right). Contour values (0.0005:0.0005:0.01).

7.3.2 Flow statistics

The statistics of the flow were determined on the basis of 24 full resolution field files, equally spaced over the time interval $t = 0.00325 - 0.00805$. Averaging was performed over the homogeneous direction and over the specified samples (24 fields times 195 collocation points). A vector plot of the time mean flow is depicted in figure 7.9. The statistically steady flow is characterized by a convergence towards a symmetrical flow, with respect to the midplane x_s . Employment of the symmetry condition seems to be justified in determining the statistics of the flow. Here this condition is not used in order to give an impression of the

slow convergence that must be connected to the presence of quite dominant large scales. Statistics, as obtained from records containing data written over a homogeneous line every five time steps, show a good convergence. Thus it can be concluded that the time integration was long enough. The poor convergence of statistics for full $x_1 - x_3$ planes is due to the relatively small number of fields involved in the evaluation.

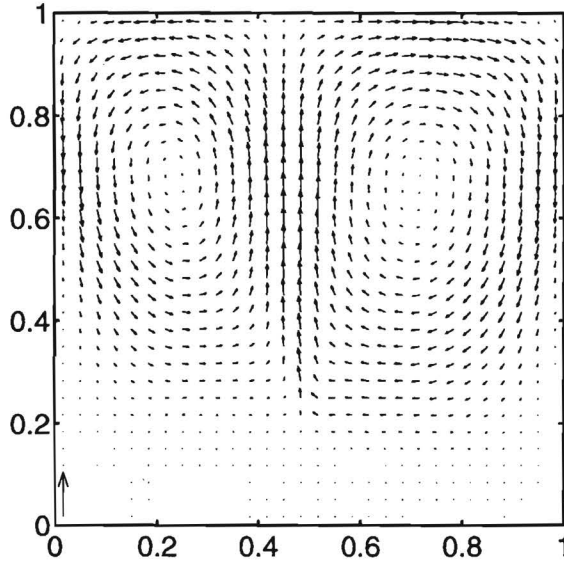


Figure 7.9: Vector plot of time mean velocity at $Ra = 10^{10}$, $Pr = 0.71$. Lower left corner vector is of length 5000.

As shown in figure 7.9 a time mean circulation appears starting from a height corresponding with the source position and filling the upper part of the box. Penetration into the region below the source is almost ruled out and a stagnant layer emerges. Right from the source there is a nearly linear spreading of the vertical flow profile up to the vortex cores in the centre of the recirculation zones. In this region the entrainment varies only slowly. Downstream the entraining region the flow collides with the top confinement and spreads to the upper left and right corner, following them without separation from the wall. Then an almost vertical downflow precedes the backflow to the source position, which occupies the wall region at heights $x_3 = 0.4 - 0.6$. A turbulent flow profile as predicted by an entrainment assumption for unconfined plumes, as given in 2.4.4, is not found in any region of the plume. The recirculation causes the vertical velocity to cross the x -axis linearly in the entraining region. The maximum centre line velocity found has a value just exceeding 2000, whereas the entrainment assumption predicts a constant value of nearly 2800. Thus the bounded flow domain together with

transitional phenomena alters the flow severely, compared to the free turbulent plume.

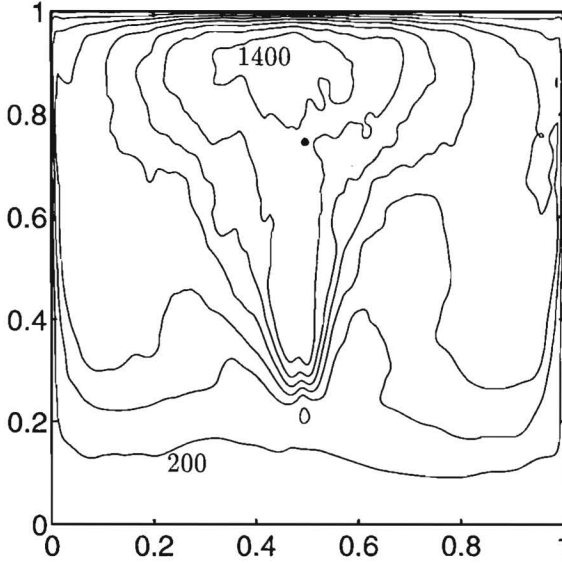


Figure 7.10: Contour plot of the standard deviation of the vertical velocity. Contours starting at 200 and increasing with 200. The dot denotes the monitoring line.

In the 3D plume, in contrast to the resulting velocity statistics as occurring in the 2D plume, all fluctuations of the velocity culminate in the centre of the box near the top wall. Contour plots of these fluctuations are presented in figures 7.10 and 7.11. Especially the standard deviation of the vertical and axial components show large values in this region, of which the latter exhibits a particularly large increase in a thin layer near the top confinement. From these figures and from the evolution of the temperature field (appendices F and G) it can be concluded that the flow is essentially three-dimensional.

In table 7.1 the mean values and standard deviations of the vertical and axial velocity components at the monitoring line are listed. To make a fair comparison with the results from the LESs as described in the next section, the spatial filtering operation is necessary in case of the present DNS result. The LESs will be performed on a 45^3 grid, whereas the DNS grid is defined by 195^3 collocation points. Thus the ratio of grid resolutions as employed by the DNS and LESs has a value of $4\frac{1}{3}$, which is not an integer. In order to obtain a minimum estimate for the grid-filtered fluctuations a convolution filter of size 5Δ is used. This results in values of $\bar{u}_3'' = 1282$, and $\bar{u}_2'' = 727$, whereas the full resolution fluctuations are given by $u_3'' = 1328$ and $u_2'' = 746$, respectively. The time mean components are not affected by the filtering operation.

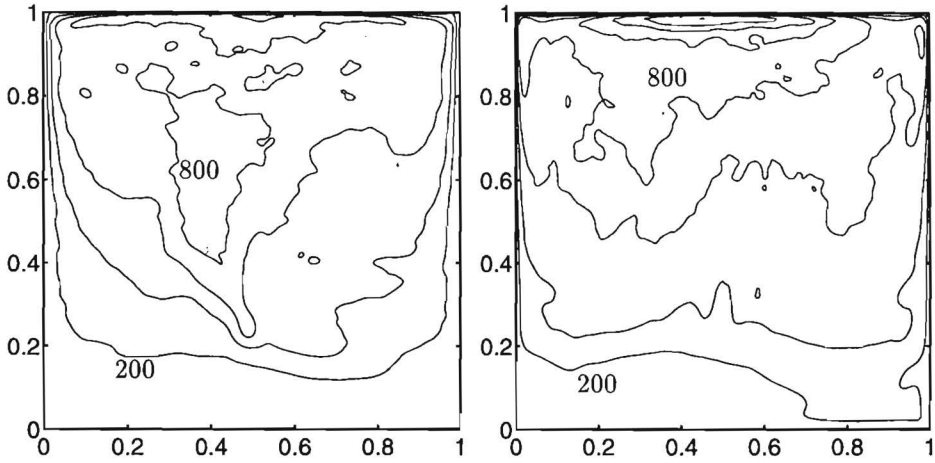


Figure 7.11: Contour plot of the standard deviation of the horizontal velocity (left) and axial velocity (right). Contours starting at 200 and increasing with 200

not affected by the filtering operation.

The time mean axial velocity component shows a value that slowly converges to zero. However, a small deviation is left and can be interpreted as an estimator for the convergence, using the assumption that it should go to zero. Relative to the standard deviation it is within 3 %, which is considered to be sufficient. Recognizing that for a 2D forcing the Rayleigh number is relatively low to obtain isotropy, the fluctuations of the observed components do not differ that much. Furthermore it can be observed that the intensity of the mean flow and the fluctuation are within the same order of magnitude, as expected in purely natural convection flows.

From the recorded axial velocity at the monitoring line, spectral and probability density distributions are given in figure 7.12. The frequency axis for the temporal spectrum is scaled with the mean vertical component of the velocity. This is what constitutes Taylor's frozen turbulence hypothesis.

The spectrum shows a gradually increasing decay rate at larger wavenumbers. Its shape is the result of several simultaneous phenomena. It starts with the buoyant source that is defined to possess a relatively small spatial dimension. This source is responsible for the injection of kinetic energy into the modes of relatively high wave numbers. In the transitional region the plume bends and folds. On average these structures constitute a rising motion with an increased width. This motion is responsible for the large-scale recirculation as observed in the time mean flow. Also large-scale fluctuating motions are present that gradually lose their kinetic energy to the benefit of smaller scales. Furthermore there is the redistribution of kinetic energy in the transitional bending and folding

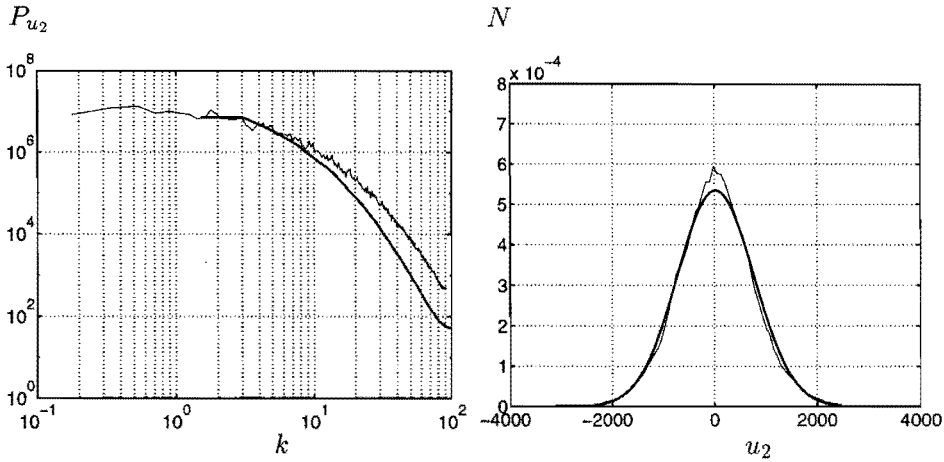


Figure 7.12: Statistics of the axial velocity at the line $(x_1, x_3) = (0.5, 0.7487)$. Left: spectral density, bold line: spatial, thin line: temporal (frequencies divided by $\langle u_3 \rangle$); right: normalized distribution, thin line: result from simulation, bold line: Gaussian with same mean and standard deviation.

process itself, probably both upscale and downscale. Thus the spectrum cannot be explained by any simplified assumptions.

The fact that the temporal and spatial spectrum correspond very well with each other at low wavenumbers supports the validity of Taylor's hypothesis, though it seems that at high frequencies a larger convection velocity is needed to extend its vigour. This corresponds with small scale structures having a relatively large convection speed. The reason for this is not very clear and may be of a physical or a numerical nature.

The probability density distribution shows an almost Gaussian behaviour, as generally found in a multiple interaction process. Again in the comparison with LES results, filtered values should be used. However, since the distribution is Gaussian, its shape for the filtered velocity is given by the values in table 7.1. As far as the spectra are concerned, up to the Nyquist wave number of the LESs there is almost no difference due to the filtering operation. At this wave number, $k = 22.5$, the intensity decrease in the spectrum as a result of the filtering operation is only about 19 %¹. At higher wave numbers it decreases up to 100 % at $k = 90$.

¹Application of a top hat filter with a width $\Delta = 1/45$ in the Fourier domain, G , results in an amplification of the spectrum with a factor

$$G^2 = \left(\frac{\sin(\pi k \Delta / 2)}{(\pi k \Delta / 2)} \right)^2 \quad (7.2)$$

	$\langle \bar{u}_3 \rangle$	\bar{u}_3''	$\langle \bar{u}_2 \rangle$	\bar{u}_2''
DNS	1824	1282	22	727
Zero model	2353	1292	-10	761
Smagorinsky model	2069	1293	19	676
Smagorinsky model $Pr_t = 1/2$	1993	1302	10	682
Structure function model	1912	1353	65	703
Buoyant Smagorinsky model	2375	1255	-17	621
Kolmogorov Prandtl model	2114	1274	13	699
Dynamic model	2324	1283	-25	775

Table 7.1: Flow statistics at $(x_1, x_3) = (0.5, 0.7487)$ produced by DNS and several LESs.

7.4 Large-Eddy simulations

Employing several subgrid scale models, large-eddy simulations have been performed at a relatively low resolution of 45^3 collocation points. Quantities as presented in the previous section, concerning the DNS, are compared with present LES results. Model constants used in the LESs and prescribed explicitly are all given by a Kolmogorov constant $C_k = 1.5$. The LES simulations consisted of 40,000 time steps of length $\Delta t = 5 \cdot 10^{-7}$. The last 20,000 time steps were used to calculate the statistics in the time interval $t = 0.01 - 0.02$. Statistics of axial and vertical velocity at the monitoring line are again given in table 7.1.

It was found that the differences of the statistics at the monitoring line represent a tendency that can be found in the entire flow field for each simulation. The distribution of the statistical quantities over the $x - z$ plane is for all simulations similar to the distribution as found for the DNS. Due to the longer integration time the distribution of observed values of the axial velocity is closer to a Gaussian distribution compared to the DNS case. As expected, the fields are more symmetrical than the obtained DNS field is. An example is the time mean vector plot for the simulation with the Smagorinsky model at $Pr_t = 1/3$ as given in figure 7.13. A global comparison of the structure of the mean flow with the DNS shows a good agreement.

In general it is observed that quantities that deviate at the monitoring point in the given plane, show a tendency in the same direction over the entire domain. Thus table 7.1 gives a good qualitative impression of the performance of several subgrid scale models. Here a better agreement of all LES calculations with the reference basis (the DNS) is obtained, compared to the results for plumes in water as presented in the previous chapter. However, the differences with the reference basis for each model are similar.

With respect to the mean flow, as is indicated by the value of $\langle \bar{u}_3 \rangle$, a better

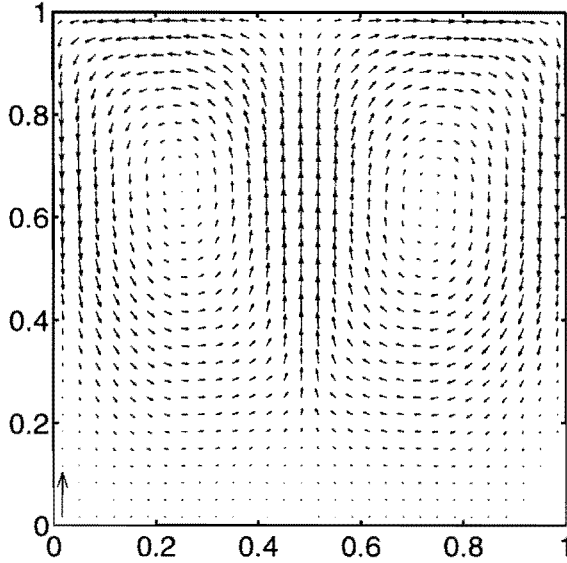


Figure 7.13: Vector plot of time mean velocity at $Ra = 10^{10}$, $Pr = 0.71$, obtained with Smagorinsky model, $Pr_t = 1/3$. Lower left corner vector is of length 5000.

agreement is obtained with the more simple models, like the Smagorinsky model and particularly the structure function model. With the latter model the difference with the DNS is within 5 %. Furthermore, an improvement is obtained if the turbulent Prandtl number is increased. The $\tau_{ij} = 0$ model situation as well as the buoyant Smagorinsky model and the dynamic model result in an overestimated mean flow, up to 30 % for the buoyant Smagorinsky model. Here the dynamic model yields again minimal values for the dynamic parameter in the plume region. Therefore it results in a similar $\tau_{ij} = 0$ model behaviour, with almost no additional turbulent dissipation. The buoyant Smagorinsky model, on the other hand, yields an increased eddy viscosity due to the unstable local stratification in the plume. Thus a laminarizing effect leads to reduced fluctuations and subsequently to an enlarged mean kinetic energy. By putting the stratification effect in a non-equilibrium description like the Kolmogorov-Prandtl model, an improvement is obtained. Using this model there is less net influence of the stratification term. In the downstream region, where the lateral plume oscillations are large and partial plume roll-up is present, produced subgrid kinetic energy is effectively redistributed. Together with local instantaneous unstably stratified situations this reduces the eddy viscosity.

Except for the buoyant Smagorinsky model, the differences in the fluctuations are not so large. Besides its performance for the mean flow the structure function model results in the largest deviation for the fluctuation of the vertical velocity

of about 5 %. However, it shows from the mean value of the axial velocity that convergence to zero is not yet attained that close. The fluctuations in axial velocity differ with maximal 7 %. This amount is reached at the upper side by the dynamic model and is caused by aliasing effects. At the other side, the same difference resulting in smaller fluctuations of axial velocity is obtained with the standard Smagorinsky model. The difference is made in allowing gridscale fluctuations on the one hand and dissipating them rigorously on the other. It must be stated that the explanations for the observed differences are quite tentative and should be investigated more thoroughly.

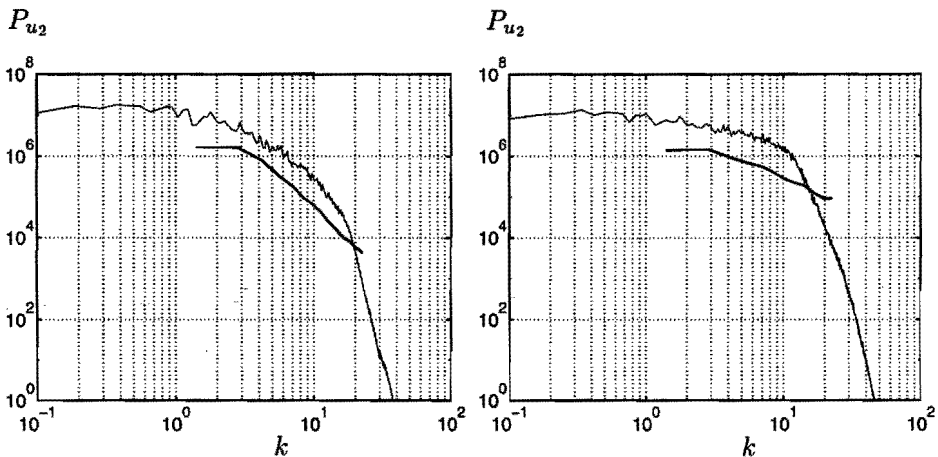


Figure 7.14: Spectral densities of the axial velocity at the line $(x_1, x_3) = (0.5, 0.7487)$. Bold line: spatial, thin line: temporal (frequencies divided by u_3). Left: result obtained with Smagorinsky model, right: results of dynamic model.

The resulting difference in gridscale energy is depicted by the spectra as given in figure 7.14. A relatively large gridscale energy is observed in the results of the dynamic model. Large wave numbers possess a too small amount of kinetic energy in both situations. The latter is again due to the injection of kinetic energy at small spatial scales. A downward energy transport to small wave numbers is not accounted for at a proper rate. Either a dissipative model or inaccurate numerical presentation of the associated modes and the prohibition of backscatter are responsible for this behaviour. The temporal spectra are in better agreement with the DNS results (fig. 7.12), although they show a similar behaviour as for the spatial scales. Here small frequencies are present with the correct intensity, whereas high frequencies fall off relatively fast. These high frequencies are connected to small spatial scales that are very much affected by the models and numerical representation. The larger amount of fluctuations present in the temporal spectra compared to the spatial spectra may be regarded as a return to a

more $2D$ organized flow, which still describes a chaotic meandering motion.

7.5 Conclusions

Buoyant air flow in a confined geometry was investigated using DNS and LES. In order to study the required grid resolution, the behaviour of the initial transient and the loss of stability, first $2D$ simulations were performed. By investigating the convergence it was found that for the $2D$ case at $Ra = 10^{10}$ and $Pr = 0.71$ a grid resolution of 195^2 grid points was sufficient to adequately simulate the flow. Furthermore, for a flow originating from a point source and just after the collision with the top confinement, laminar boundary layer solutions were found to match the present full Navier-Stokes solutions very well. By defining a larger source region, solutions at small elevations are more diffused, though downstream they tend to the same profile.

By increasing the intensity of initial perturbations in the flow, stability was found to be lost at an earlier stage. Thus a suitable intensity was found for the $3D$ DNS. Statistics of the $2D$ turbulent flow showed a large-scale circulating pattern which is not symmetric. Large fluctuations are created in this background flow, which were convected with a low dissipation rate. Performing a $2D$ LES resulted in a flow more similar to the $3D$ flow that was expected to emerge. Here the time mean flow was already symmetrical.

The $3D$ DNS yielded a $2D$ flow for the initial transient. Shortly after the symmetry breaking bifurcation subsequent axial planes started to give a gradually changing solution with the axial coordinate. These were the first $3D$ effects appearing in the flow. In this stage the divergence of the axial velocity from its initial zero value was still negligible relative to fluctuations of the vertical velocity with the axial coordinate. From this stage on these axial velocities started to grow up to their steady state statistics.

The time mean turbulent flow, emerging after the described transient, showed a tendency towards a symmetrical flow. It was found that all fluctuations culminate near the top wall, in the centre of the box. Particularly the fluctuations in the axial direction showed a relatively sharp increase just below the top confinement. Spectral statistics of the axial velocity component at the line $(x_1, x_3) = (0.5, 0.7487)$ were found to fall off fast with increasing wavenumbers and frequencies. At this line Taylor's hypothesis was found to be valid at low frequencies. Since kinetic energy is injected at relatively small scales a complex redistributing process is found to be present.

Globally, most LESs resulted in a solution, similar to the DNS. Especially the relatively simple equilibrium models showed a good agreement. The Smagorinsky model as extended with the buoyant production term resulted in a distortion of the similarity with the DNS. Application of the Kolmogorov-Prandtl model restored a large part of this disagreement.

In using these models, a tuning of the model constants seems to exhibit a potential of yielding even better results. Therefore dynamic modelling is considered to be advantageous. Yet, application of the dynamic procedure to the turbulent stresses did not result in a satisfactory agreement. In the plume region the dynamic parameter was estimated to be negative most of the time. In keeping the numerics stable a lower bound of zero had to be applied. Thus backscatter, an important phenomenon in the plume region, was directly prohibited. This gave rise to results almost identically equal to a $\tau_{ij} = 0$ model simulation. Here, in applying the dynamic procedure the representation of the smallest scales of motion by the numerics may be of crucial importance.

Chapter 8

Concluding discussion and final remarks

In this thesis transitional plume flows in confined geometries are analyzed and predicted. The objective was to gain insight into the transitional behaviour and to reduce the computational effort needed in numerical simulations by means of a suitable Large-Eddy Simulation. Therefore a proper SubGrid Model (SGM) has to be defined, that parameterizes the subgrid stresses and subgrid heat fluxes sufficiently well.

Most analyses on subgrid scale modelling and practical realizations of LESs as documented in the literature are concerned with forced flows. Most frequently these flows exhibit a relatively large turbulent dissipation rate. Here we are concerned with plume flows that are buoyancy induced and originate from discrete sources. Then a spatial transition from laminar to turbulent flow is accompanied by relatively low (buoyant) forcing rates. Therefore the integral turbulent dissipation is small. Furthermore the resulting flow is very non-homogeneous, a feature that additionally has its reflections on the degree of local isotropy.

Literature survey revealed boundary-layer type equations describing free plumes originating from a line heat source. These similarity equations are solved numerically. In the fully turbulent case, approximations can be made about the time mean profile shape and the entrainment rate. This results directly in a solution for the turbulent time mean profiles. In a confinement, however, both solutions have only a minor practical significance. Recirculation effects, wall resistance and the establishment of a stratification often affect the flow in a decisive way. On the other hand, these solutions are indispensable in serving as first guidelines in estimating the magnitudes of relevant properties, also for the purpose of numerical simulation.

Subsequently the confined plume configuration was analyzed using the full Navier-Stokes and energy equations. The equations were numerically solved using a Finite Volume Method (FVM). The method, as well as particular discretization

schemes and the numerical code were validated for a two-dimensional air plume, confined in a cavity. This configuration was also utilized by *Desrayaud and Lauriat* [1993] to describe routes to chaotic convection using numerical simulation. This research was used as a reference basis, together with additional numerical experiments using a Spectral Element Method (SEM). The comparison yielded quantitatively similar results, e.g. the maximum difference of the estimated critical Rayleigh number was within 7 %. Here both methods (FVM and SEM) revealed a value at the lower side of this region.

A basis of validation with respect to the flow phenomena subjected to LES was created by means of experimental data and a Direct Numerical Simulation (DNS). Experimental data were gathered in a plume flow induced by a heating element surrounded by water at a forcing of $Ra = 2.1 \cdot 10^{11}$. Measurements were carried out in a two-dimensional cross-section by means of Particle Tracking Velocimetry (PTV). The resulting data were sampled on an equidistant grid with spacing Δ using an interpolation method. They can be summarized as follows:

- A converged representation of the flow statistics was obtained.
- The transitional region, defined by a sudden broadening of the mean flow, was located in the centre of the flow domain.
- Above the transition two recirculation regions filled the upper half of the domain.
- A low correlation of time mean SGM stresses with exact stresses was found.
- In the transitional region, backscatter and forward scatter of kinetic energy are of equal importance.
- A qualitative good representation of the exact interscale kinetic energy transfer was obtained with the dynamic model applied to filtered data.

Subsequently numerical simulations were performed with several SGMs. This resulted in a common behaviour defined by:

- A description of the heat source with sufficient resolution is essential.
- An overestimation of the velocity in the plume region.
- An exaggeration of the penetration of the recirculating mean motion in the lower part of the flow domain.

One of the reasons for this observed behaviour was the insufficient representation of the buoyant source and the thermal boundary layer, that could not be restored by the modelling. This results in a much too stable boundary layer with a decreased buoyancy force, together partially responsible for the observed net effects. Additionally, the inability to represent backscatter led to the observed

discrepancy. Application of the dynamic model could not improve these results due to the restriction on the backscatter as given by numerical stability of the present FVM.

As a second source of reference, a DNS was performed for air at $Ra = 10^{10}$. In this situation a heat source was defined that could be represented accurately at the DNS grid of 195^3 , as well as on the much coarser LES grid of 45^3 . The 3D DNS revealed that:

- A symmetrical time mean recirculation covered the domain above the heat source.
- The flow was essentially three-dimensional, especially near the top wall.
- No clear turbulent inertial range was present.

Application of LES to the air plume yielded much better results than the LESs for the water plumes did. The main observations are:

- An additional kinetic energy drain by an SGM has to be incorporated.
- The Smagorinsky model and the structure function model performed fairly well.
- There is not enough statistics present in the subgrid scales to allow a statistical description.

Here again because of numerical reasons, backscatter could not be allowed, resulting in a similar performance of the zero model (coarse grid DNS) and the dynamic model situation.

Summarizing, it can be stated that numerical prediction of the behaviour of transitional plumes originating from small buoyancy sources by means of LES is a very delicate affair. Globally this is due to three major causes. First, especially at high Prandtl numbers, care must be taken to resolve the thermal boundary layer as well as the hydrodynamical boundary layer. Second, enough subgrid scales must be present to allow a statistical description of the flow. However, if a scale similarity is present a dynamical model could be used. This model has also the potential to represent backscatter.

Backscatter is very hard to handle. In the literature several ways of dealing with instantaneous localized backscatter are provided. A number of methods are summarized by *Moin and Jimenéz* [1993] and a recent contribution is given by *Meneveau et al.* [1996]. In global dissipative flows, first all kinds of averaging operations were introduced to filter it out. Then, in dealing with larger more persistent areas of backscatter, dynamic Kolmogorov-Prandtl closures were used. Application of such kind of closure allows backscatter, decreasing the subgrid kinetic energy down to zero. At this value it is limited in a natural way.

In a transitional plane plume flow a large coherent and persistent area of backscatter is present. The above mentioned methods cannot deal with this properly.

References

- R.J. Adrian. Particle-imaging techniques for experimental fluid mechanics. *Annu. Rev. Fluid Mech.*, 23:261–304, 1991.
- M. Antonopoulos-Domis. Large-eddy simulation of a passive scalar in isotropic turbulence. *J. Fluid Mech.*, 104:55–79, 1981.
- R. Asselin. Frequency filter for time integrations. *Monthly Weather Rev.*, 100:487–490, 1972.
- Hao Bai-Lin. *Chaos*. World Scientific Publishing Co Pte Ltd., 1984.
- J. Bardina, J.H. Ferziger, and W.C. Reynolds. Improved turbulence models based on LES of homogeneous incompressible turbulent flows. Technical Report TF-19, Stanford University, Department of Mechanical Engineering, 1984.
- G.K. Batchelor. *The Theory of Homogeneous Turbulence*. Cambridge University Press, 1953.
- G.K. Batchelor. *An Introduction to Fluid Dynamics*. Cambridge University Press, 1967.
- R.G. Bill Jr. and B. Gebhart. The transition of plane plumes. *Int. J. Mass Heat Transfer*, 18:513–526, 1975.
- J. Boussinesq. *Théorie analytique de la chaleur, vol. 2*. Gauthier-Villars, Paris, 1903.
- R.A. Clark, J.H. Ferziger, and W.C. Reynolds. Evaluation of subgrid-scale models using an accurately simulated turbulent flow. *J. Fluid Mech.*, 91(1):1–16, 1979.
- S.B. Dalziel. Decay of rotating turbulence: some particle tracking experiments. In F.T.M. Nieuwstadt, editor, *Flow Visualisation and Image Analysis*. Kluwer Academic Publishers, 1993.
- P.A. Davies and M.J. Valente Neves, editors. *Recent Research Advances in the Fluid Mechanics of Turbulent Jets and Plumes*. Kluwer Academic Publishers, 1994.
- J.W. Deardorff. A numerical study of three-dimensional turbulent channel flow at large Reynolds numbers. *J. Fluid Mech.*, 41:453–480, 1970.
- J.W. Deardorff. Strato-cumulus-capped mixed layers derived from a three dimensional model. *Boundary-layer Meteor.*, 18:495–527, 1980.
- G. Desrayaud and G. Lauriat. Unsteady confined buoyant plumes. *J. Fluid Mech.*, 252:617–646, 1993.
- J.A. Domaradzki, W. Liu, and M. E. Brachet. An analysis of subgrid-scale interactions in numerically simulated isotropic turbulence. *Phys. Fluids A*, 5:1747, 1993.
- J.A. Domaradzki, W. Liu, C. Härtel, and L. Kleiser. Energy transfer in numerically simulated wall bounded turbulent flows. *Phys. Fluids A*, 7:1583–1599, 1994.
- F. Ducros, P. Comte, and M. Lesieur. Large-eddy simulation of a spatially weakly-compressible boundary layer over an adiabatic flat plate. In *Symposium on Turbulence, Heat and Mass Transfer*, Lisbon, Portugal, August 1994.
- T.M. Eidson. Numerical simulation of the turbulent Rayleigh-Bénard problem using subgrid modelling. *J. Fluid Mech.*, 158:245–268, 1985.
- M.J. Feigenbaum. Quantitative universality for a class of nonlinear transformations. *J. Stat. Phys.*, 19:25–52, 1978.
- U. Frisch. *Turbulence: the Legacy of A.N. Kolmogorov*. Cambridge University Press, 1995.
- B. Gebhart, L. Pera, and A.W. Schorr. Steady laminar natural convection plumes above a horizontal line heat source. *Int. J. Heat Mass Transfer*, 13:161–171, 1970.
- B. Gebhart, Y. Jaluria, R.L. Mahajan, and B. Sammakia. *Buoyancy Induced Flows and Transport*. Hemisphere Publishing Corporation, 1988.

- M. Germano. Averaging invariance of the turbulent equations and similar subgrid scale modeling. Technical Report Manuscript 116, CTR, Stanford, California, 1990.
- M. Germano. Turbulence: the filtering approach. *J. Fluid Mech.*, 238:325–336, 1992.
- M. Germano, U. Piomelli, P. Moin, and W.H. Cabot. A dynamical subgrid-scale eddy viscosity model. *Phys. Fluids A*, 3(7):1760–1765, 1991.
- S. Ghosal, T.S. Lund, P. Moin, and K. Akselvoll. A dynamic localization model for large-eddy simulation of turbulent flows. *J. Fluid Mech.*, 286:229–256, 1995.
- J.P. Gollub and S.V. Benson. Many routes to turbulent convection. *J. Fluid Mech.*, 100(3):449–470, 1980.
- D.D. Gray and A. Giorgini. The validity of the Boussinesq approximation for liquids and gases. *Int. J. Heat Mass Transf.*, 19:545–551, 1976.
- P.M. Gresho. On the theory of semi-implicit projection methods for viscous incompressible flow and its implementation via a finite element method that also introduces a nearly consistent mass matrix. part 1: Theory. *Int. J. Num. Meth. Fluids*, 11:587–620, 1990.
- G. Grötzbach and U. Schumann. Direct numerical simulation of turbulent velocity, pressure and temperature fields in channel flows. In *Turbulent Shear-flows, Vol. I*, pages 370–385. Springer-Verlag, 1979.
- F.H. Harlow and J.E. Welch. Numerical calculation of time-dependent viscous incompressible flow of fluid with free surface. *Phys. Fluids*, 8(12):2182–2189, 1965.
- A. Heiss. *Numerische und experimentelle Untersuchungen der laminaren und turbulenten Konvektion in einem geschlossenen Behälter*. PhD thesis, Technischen Universität München, 1987.
- R.A.W.M. Henkes. *Natural-convection Boundary Layers*. PhD thesis, Delft University of Technology, the Netherlands, 1990.
- E. Hopf. Abzweigung einer periodischen Lösung von einer stationären Lösung eines Differentialsystems. *Ber. Math.-Phys. Kl. Sächs. Akad. Leipzig*, 94:1–22, 1942.
- Y. Jaluria. Thermal plumes. In S. Kakaç, W. Aung, and R. Viskanta, editors, *Natural Convection; Fundamentals and Applications*, pages 51–74. Hemisphere Publishing Corporation, 1985.
- G.E. Karniadakis, M. Israeli, and S.A. Orszag. High-order splitting methods for the incompressible Navier-Stokes equations. *J. Comp. Phys.*, 97:414–443, 1991.
- A.N. Kolmogorov. Local structure of turbulence in an incompressible viscous fluid at very large Reynolds numbers. *Dokl. Akad. Nauk SSSR*, 30:4:299–303, 1941. Also in: *Proc. R. Soc. Lond. A* (1991) 434, 9–13.
- P. de Korte, J.G.M. Eggels, and F.T.M. Nieuwstadt. The influence of the initial conditions on freely decaying isotropic turbulence. Delft Progr. Rep. 15:103–122, Delft University of Technology, the Netherlands, 1991–1992.
- N.E. Kotsovinos. *A Study of the Entrainment and Turbulence in a Plane Buoyant Jet*. PhD thesis, Calif. Inst. Techn., 1975.
- N.E. Kotsovinos and E.J. List. Plane turbulent buoyant jets. Part I: Integral properties. *J. Fluid Mech.*, 81:25–44, 1977.
- R.H. Kraichnan. Inertial ranges in two-dimensional turbulence. *Phys. Fluids*, 10:1417–1423, 1967.
- R.H. Kraichnan. Eddy viscosity in two and three dimensions. *J. Atmos. Sci.*, 33:1521–1536, 1976.
- D. Kwak, W.C. Reynolds, and J.H. Ferziger. 3-D time dependent computation of turbulent flows. Technical Report TF-5, Stanford University, Dept. Mech. Eng., 1975.

- L.D. Landau. On the problem of turbulence. *Akad. Nauk. Doklady*, 44:339, 1944.
- A.M. Lankhorst. *Laminar and Turbulent Natural Convection in Cavities; Numerical Modeling and Experimental Validation*. PhD thesis, Delft University of Technology, the Netherlands, 1991.
- A. Leonard. Energy cascade in large-eddy simulations of turbulent fluid flows. *Adv. in Geophys.*, A18:237–248, 1974.
- B.P. Leonard. The ULTIMATE conservative difference scheme applied to unsteady one-dimensional advection. *Comput. Methods Appl. Mech. Engrg.*, 88:17–74, 1991.
- M. Lesieur. *Turbulence in Fluids*. Kluwer, 1990.
- J. Lighthill. The recently recognized failure of predictability in Newtonian dynamics. *Proc. R. Soc. Lond.*, A 13:35–50, 1986.
- D.K. Lilly. The representation of small-scale turbulence in numerical simulation experiments. In *Proc. of the IBM Scientific Computer Symposium on Environmental Sciences*, pages 195–210, 1967. IBM Form No. 320-1951.
- D.K. Lilly. A proposed modification of the Germano subgrid-scale closure method. *Phys. Fluids A*, 4(3):633–635, 1992.
- E.J. List. Turbulent jets and plumes. *Ann. Rev. Fluid Mech.*, 14:189–212, 1982.
- S. Liu, C. Meneveau, and J. Katz. On the properties of similarity subgrid-scale models as deduced from measurements in a turbulent jet. *J. Fluid Mech.*, 275:83–119, 1994.
- E.N. Lorenz. Deterministic nonperiodic flow. *J. Atmos. Sci.*, 20:130–141, 1963.
- P.S. Marcus. Simulation of Taylor-Couette flow. Part I. Numerical methods and comparison with experiment. *J. Fluid Mech.*, 146:45–64, 1984.
- O.J. McMillan and J.H. Ferziger. Direct testing of subgrid-scale models. *AIAA J.*, 17(12):1340–1346, 1979.
- C. Meneveau, T.S. Lund, and W.H. Cabot. A Lagrangian dynamic subgrid-scale model of turbulence. *J. Fluid Mech.*, 319:353–385, 1996.
- O. Métais and M. Lesieur. Spectral large-eddy simulation of isotropic and stably stratified turbulence. *J. Fluid Mech.*, 239:157–194, 1992.
- J. Miles. Strange attractors in fluid dynamics. *Adv. in Appl. Mech.*, 24:189–213, 1984.
- P.D. Mineev, F.N. van de Vosse, L.J.P. Timmermans, and A.A. van Steenhoven. A second order splitting algorithm for thermally-driven flow problems. *Int. J. Num. Meth. Heat Fluid Flow*, 6(2):51–60, 1995a.
- P.D. Mineev, F.N. van de Vosse, and A.A. van Steenhoven. Transient natural convection in a 2-d enclosure with a heat source at the bottom. *J. Theor. Appl. Mech.*, Year XXV(4):94–108, 1995b. Sofia 1994-95.
- C.H. Moeng. A large eddy simulation model for the study of planetary boundary layer turbulence. *J. Atmos. Sci.*, 41:2052–2062, 1984.
- P. Moin and J. Jimenez. Large eddy simulation of complex turbulent flows. In *AIAA 24th Fluid Dynamics Conference, Orlando, July 1993*. AIAA-93-3099.
- J.M. Nguyen Duc and J. Sommeria. Experimental characterization of steady two-dimensional vortex couples. *J. Fluid Mech.*, 192:175–192, 1988.
- F.T.M. Nieuwstadt. Direct and large-eddy simulation of free convection. In *Proc. 9th Internat. Heat Transfer Conf., Jerusalem 19-24 August 1990*, pages 37–47. Amer. Soc. Mech. Eng., New York, 1990.
- F.T.M. Nieuwstadt, editor. *Flow Visualisation and Image Analysis*. Kluwer Academic Publishers, 1993.
- A. Oberbeck. Über die Wärmeleitung der Flüssigkeiten bei Berücksichtigung der Strömungen infolge von Temperaturdifferenzen. *Annalen der Physik und Chemie*,

- 7:271–292, 1879.
- A.M. Obukhov. On the distribution of energy in the spectrum of turbulent flow. *Dokl. Akad. Nauk SSSR*, 32:19, 1941. Also in: *Izv. Akad. Nauk SSSR Sev. Geogr. 1. Geofiz.* 5, 453.
- P. Orlandi. Vortex dipole rebound from a wall. *Phys. Fluids A*, 2(8):1429–1436, 1990.
- J.M. Ottino. *The Kinematics of Mixing : Stretching, Chaos, and Transport*. Cambridge University Press, 1990.
- L. Pera and B. Gebhart. On the stability of laminar plumes: some numerical solutions and experiments. *Int. J. Heat Mass Transfer*, 14:975–984, 1971.
- R. Peyret and T.D. Taylor. *Computational Methods in Fluid Flow*. Springer Series in Computational Physics. Springer-Verlag, 1983.
- S.A. Piacsek and G.P. Williams. Conservation properties of convection difference schemes. *J. Comp. Phys.*, 6:392–405, 1970.
- U. Piomelli and J. Liu. Large-eddy simulation of rotating channel flows using a localized dynamic model. *Phys. Fluids*, 7(4):839–848, 1995.
- U. Piomelli, P. Moin, and J.H. Ferziger. Model consistency in large eddy simulation of turbulent channel flows. *Phys. Fluids*, 31(7):1884–1891, 1988.
- U. Piomelli, H. Cabot, P. Moin, and S. Lee. Subgrid-scale backscatter in turbulent and transitional flows. *Phys. Fluids A*, 3(7):1766–1771, 1991.
- H. Poincaré. *Les Méthodes Nouvelles de la Mécanique Céleste*. Gauthier-Villars, Paris, 1892.
- Y. Pomeau and P. Manneville. Intermittent transition to turbulence in dissipative dynamical systems. *Comm. in Math. Phys.*, 74:189–197, 1980.
- M.J.B.M. Pourquié. *Large-eddy Simulation of a Turbulent Jet*. PhD thesis, Delft University of Technology, the Netherlands, 1994.
- M.J.B.M. Pourquié and J.G.M. Eggels. Discretization report. Technical report, Delft University of Technology, the Netherlands, 1991.
- W.H. Press, W.T. Vetterling, S.A. Teukolsky, and B.P. Flannery. *Numerical Recipes in FORTRAN. The Art of Scientific Computing. Second Edition*. Cambridge University Press, 1992.
- Lord Rayleigh. On convection currents in a horizontal layer of fluid when the higher temperature is on the under side. *Phil. Mag.*, 32:529–546, 1916.
- O. Reynolds. An experimental investigation of the circumstances which determine whether the motion of water shall be direct or sinuous, and the law of resistance in parallel channels. *Phil. Trans. R. Soc.*, 174:935–982, 1883.
- L.F. Richardson. *Weather Prediction by Numerical Process*. Cambridge University Press, 1922.
- W. Rodi. *Turbulent Buoyant Jets and Plumes*. Pergamon Press Ltd., 1982.
- R.S. Rogallo and P. Moin. Numerical simulation of turbulent flows. *Ann. Rev. Fluid Mech.*, 16:99–137, 1984.
- H. Rouse, C.S. Yih, and H.W. Humphreys. Gravitational convection from a boundary source. *Tellus*, 4:201–210, 1952.
- D. Ruelle and F. Takens. On the nature of turbulence. *Commun. math. Phys.*, 20:167–192, 1971.
- H. Schmidt and U. Schumann. Coherent structure of the convective boundary layer derived from large eddy simulation. *J. Fluid Mech.*, 200:511–562, 1989.
- U. Schumann. Subgrid scale model for finite difference simulations of turbulent flows in plane channels and annuli. *J. Comp. Phys.*, 18:376–404, 1975.

- U. Schumann and R. Sweet. A direct method for the solution of Poisson's equation with Neumann boundary conditions on a staggered grid of arbitrary size. *J. Comp. Phys.*, 20:171–182, 1976.
- J.J.M. Sillekens. *Laminar Mixed Convection in Ducts*. PhD thesis, Eindhoven University of Technology, 1995.
- A. Silveira Neto, D. Grand, O. Métais, and M. Lesieur. Large-eddy simulation of the turbulent flow in the downstream region of a backward-facing step. *Phys. Rev. Letters*, 66(18):2320–2323, 1991.
- J. Smagorinsky. General circulation experiments with the primitive equations. *Mon. Weather Rev.*, 91(3):99–165, 1963.
- C.G. Speziale. Galilean invariance of subgrid scale stress models in the large eddy simulation of turbulence. *J. Fluid Mech.*, 155:55–62, 1985.
- C.G. Speziale. Analytical methods for the development of Reynolds-stress closures in turbulence. *Annu. Rev. Fluid Mech.*, 23:107–157, 1991.
- G.I. Taylor. Statistical theory of turbulence. part I. *Proc. Roy. Soc., A*, CLI:421–444, 1935.
- D.J. Tritton. *Physical Fluid Dynamics*. Oxford Science Publications, 1988.
- J.S. Turner. *Buoyancy Effects in Fluids*. Cambridge University Press, 1973.
- J.S. Turner. Turbulent entrainment: the development of the entrainment assumption, and its application to geophysical flows. *J. Fluid Mech.*, 173:431–471, 1986.
- T.C.G. van der Burgt. Experimental analysis of a transitional plume. Master's thesis, Eindhoven University of Technology, the Netherlands, 1994. WOC-WET 94.015.
- G.J.F. van Heijst and J.B. Flór. Laboratory experiments on dipole structures in a stratified fluid. In J.C.J. Nihoul and B.M. Jouart, editors, *Mesoscale/Synoptic Coherent Structures in Geophysical Turbulence*, pages 591–608. Elsevier, Amsterdam, 1989.
- B. van Leer. Towards the ultimate conservative difference scheme. II Monotonicity and conservation combined in a second-order scheme. *J. Comput. Phys.*, 14:361–370, 1974.
- P.R. Voke. Low-Reynolds-number subgrid-scale models. Technical Report ME-FD/94.26, The University of Surrey, 1994.
- A.W. Vreman. *Direct and Large-Eddy Simulation of the Compressible Turbulent Mixing Layer*. PhD thesis, University of Twente, the Netherlands, 1995.
- B. Vreman, B. Geurts, and H. Kuerten. On the formulation of the dynamic mixed subgrid-scale model. *Phys. Fluids A*, 6(12):4057–4059, 1994.
- V.C. Wong and D.K. Lilly. A comparison of two dynamic subgrid closure methods for turbulent thermal convection. *Phys. Fluids*, 6(2):1016–1023, 1994.
- A.M. Yaglom. Comment on the papers on turbulence. In V.M. Tikhomirov, editor, *Selected Works of A.N. Kolmogorov, Volume I: Mathematics and Mechanics*, pages 488–503. Kluwer Academic Publishers, 1985.
- Y. Zang, R.L. Street, and J.R. Koseff. A dynamic mixed subgrid-scale model and its application to turbulent recirculating flows. *Phys. Fluids A*, 5(12):3186–3196, 1993.

Appendix A

Convergence of similarity solutions

Convergence of the numerically determined solutions of the similarity equations 2.45 is checked by investigation of the variables I as defined by 2.49, $f'(0)$ and $f(\infty)$ when refining the grid size, n_η . In the standard case the calculation domain was given by $\eta = [0, \eta_{\max}]$, with $\eta_{\max} = 10$. When found necessary, i.e. at large Pr number, the calculation domain was extended up to $\eta_{\max} = 15$. The value of $f(\infty)$ was approximated by the value at $f(\eta_{\max})$. Results are given in tables A.1 to A.4. All calculations were found to be converged up to satisfying accuracy at the largest grid sizes.

η_{\max}	n_η	I	$f'(0)$	$f(\eta_{\max})$
10	25	0.97672	0.65111	0.76488
10	50	1.00474	0.65866	0.77676
10	100	1.01180	0.65998	0.77979
10	200	1.01362	0.66032	0.78086

Table A.1: Convergence results for $Pr = 0.71$.

η_{\max}	n_η	I	$f'(0)$	$f(\eta_{\max})$
10	25	0.98657	0.61956	0.81102
10	50	1.01345	0.62492	0.82273
10	100	1.02033	0.62614	0.82576
10	200	1.02210	0.62646	0.82682

Table A.2: Convergence results for $Pr = 1.0$.

η_{\max}	n_{η}	I	$f'(0)$	$f(\eta_{\max})$
10	25	0.97785	0.46884	1.22500
10	50	1.00037	0.47220	1.23670
10	100	1.00624	0.47307	1.23974
15	200	1.00802	0.47375	1.25889

Table A.3: Convergence results for $Pr = 5.0$.

η_{\max}	n_{η}	I	$f'(0)$	$f(\eta_{\max})$
10	25	0.96202	0.43854	1.33167
10	50	0.98314	0.44133	1.34362
10	100	0.98872	0.44215	1.34682
15	200	0.99225	0.44400	1.39820
20	200	0.99167	0.44404	1.40713

Table A.4: Convergence results for $Pr = 7.0$.

Appendix B

Discretization of non-linear advection

The standard method of discretizing the non-linear term in the momentum equations in a finite volume method is by using the conservative form. In applying the conservative or flux form, all terms can be partially integrated and subsequently a midpoint rule is applied. In a two-dimensional situation this becomes for the advection in x -direction

$$\frac{1}{\Omega} \iint_{\Omega} \left\{ \frac{\partial uu}{\partial x} + \frac{\partial uw}{\partial z} \right\} d\Omega. \quad (\text{B.1})$$

Partial integration in the direction of the derivative and using the midpoint rule for the other direction yields

$$\begin{aligned} \frac{1}{\Omega} \iint_{\Omega} \frac{\partial uu}{\partial x} d\Omega &= \frac{1}{dx dz} \iint_{z x} \frac{\partial uu}{\partial x} dx dz = \frac{1}{dx dz} \int_z uu \Big|_{x-\frac{1}{2}dx}^{x+\frac{1}{2}dx} dz \\ &\approx \frac{1}{4dx} \left\{ \left(u(i, k) + u(ip, k) \right)^2 - \left(u(im, k) + u(i, k) \right)^2 \right\} \end{aligned} \quad (\text{B.2})$$

and

$$\begin{aligned} \frac{1}{\Omega} \iint_{\Omega} \frac{\partial uw}{\partial z} d\Omega &= \frac{1}{dx dz} \iint_{x z} \frac{\partial uw}{\partial z} dz dx = \frac{1}{dx dz} \int_x uw \Big|_{z-\frac{1}{2}dz}^{z+\frac{1}{2}dz} dx \\ &\approx \frac{1}{4dx} \left\{ \left(u(i, k) + u(i, kp) \right) \left(w(i, kp) + w(im, kp) \right) - \right. \\ &\quad \left. \left(u(i, k) + u(i, km) \right) \left(w(i, k) + w(im, k) \right) \right\}. \end{aligned} \quad (\text{B.3})$$

The total advection in x -direction is obtained by summing both contributions. However according to *Piacsek and Williams* [1970] this method does not conserve

quadratic quantities absolutely, i.e., algebraically. The conservative form is not fully adequate for prediction methods that involve a process in which the continuity is not identically zero. In the present case the value of the divergence depends on the accuracy to which the Poisson equation for the pressure is solved, which is the machine accuracy. The fact that the divergence does not vanish exactly gives a contribution to the integral of quadratic quantities, in this case kinetic energy. Therefore *Piacsek and Williams* [1970] call this method a *conditionally conserving* form.

Another form in which the non-linear term can be discretized is the advective form

$$\frac{1}{\Omega} \iint_{\Omega} \left\{ u \frac{\partial u}{\partial x} + w \frac{\partial u}{\partial z} \right\} d\Omega, \quad (\text{B.4})$$

which has no contribution of the divergence. It can be discretized by using a trapezoidal rule in the direction of the derivatives and using again a midpoint rule for the other direction, resulting in

$$\begin{aligned} \frac{1}{\Omega} \iint_{\Omega} u \frac{\partial u}{\partial x} d\Omega &= \frac{1}{dx dz} \iint_{z x} u \frac{\partial u}{\partial x} dx dz \\ &\approx \frac{1}{dx dz} \int_z \left\{ \frac{1}{2} u \frac{\partial u}{\partial x} \Big|_{x + \frac{1}{2} dx} + \frac{1}{2} u \frac{\partial u}{\partial x} \Big|_{x - \frac{1}{2} dx} \right\} dx dz \\ &\approx \frac{1}{4 dx} \left\{ \left(u(ip, k) + u(i, k) \right) \left(u(ip, k) - u(i, k) \right) + \right. \\ &\quad \left. \left(u(i, k) + u(im, k) \right) \left(u(i, k) - u(im, k) \right) \right\} \\ &= \frac{1}{4 dx} \left\{ u(ip, k)^2 - u(im, k)^2 \right\} \end{aligned} \quad (\text{B.5})$$

and

$$\begin{aligned} \frac{1}{\Omega} \iint_{\Omega} w \frac{\partial u}{\partial z} d\Omega &= \frac{1}{dx dz} \iint_{x z} w \frac{\partial u}{\partial z} dz dx \\ &\approx \frac{1}{dx dz} \int_x \left\{ \frac{1}{2} w \frac{\partial u}{\partial z} \Big|_{z + \frac{1}{2} dz} + \frac{1}{2} w \frac{\partial u}{\partial z} \Big|_{z - \frac{1}{2} dz} \right\} dx dz \\ &\approx \frac{1}{4 dx} \left\{ \left(w(i, kp) + w(im, kp) \right) \left(u(i, kp) - u(i, k) \right) + \right. \\ &\quad \left. \left(w(i, k) + w(im, k) \right) \left(u(i, k) - u(i, km) \right) \right\}. \end{aligned} \quad (\text{B.6})$$

According to *Piacsek and Williams* [1970] this form produces a contribution to the integral kinetic energy proportional to the divergence and of opposite magnitude to the conserving or flux form discretization. Averaging the two forms yields a

vanishing contribution in the variance equation of the non-vanishing divergence. In this way an *absolutely conserving* form is obtained, i.e. a form with algebraic conservation independent of the accuracy of the solution. This form becomes

$$\frac{1}{4dx} \left\{ u(ip, k) \left(u(ip, k) + u(i, k) \right) - u(im, k) \left(u(im, k) + u(i, k) \right) \right\} + \frac{1}{4dz} \left\{ u(i, kp) \left(w(im, kp) + w(i, kp) \right) - u(i, km) \left(w(im, k) + w(i, k) \right) \right\}. \quad (\text{B.7})$$

Furthermore, it follows that the latter form is also preferable because it is more economical to compute compared to the two other forms.

Appendix C

The "ULTIMATE"-van Leer scheme

Simple linear advection schemes do have some drawbacks. The second-order central scheme is unconditionally unstable for pure advection, resulting in wiggles in the presence of weak diffusion, and the first-order upwind scheme is very diffusive. In order to overcome the problems associated with these linear advection schemes, van Leer's second scheme was used (*van Leer* [1974]), with a modified criterion for switching to first-order upwind as proposed by *Leonard* [1991]. The modification does not influence the results, it only minimizes the computational costs, as will be shown.

The starting point of van Leer's second scheme is the advection of a scalar c

$$\frac{\partial}{\partial x_j} u_j c = -\frac{\partial c}{\partial t}. \quad (\text{C.1})$$

This may be discretized forward in time to yield a semi-discrete equation

$$\frac{\partial}{\partial x_j} u_j c = -\frac{c^{n+1} - c^n}{\Delta t}. \quad (\text{C.2})$$

For convenience the one-dimensional equivalent will be taken, and the subscript j will be dropped. Application of the derivations to a multidimensional system is straightforward. First this equation is written in the Lax-Wendroff form by using a Taylor expansion of $c = c(t)$,

$$c^{n+1} = c^n + \frac{\partial c}{\partial t} \Delta t \Big|_n + \frac{1}{2} \frac{\partial^2 c}{\partial t^2} \Delta t^2 \Big|_n + \mathcal{O}(\Delta t^3) \quad (\text{C.3})$$

so that the advection equation becomes

$$\frac{\partial}{\partial x} u c = -\frac{\partial c}{\partial t} - \frac{1}{2} \frac{\partial^2 c}{\partial t^2} \Delta t. \quad (\text{C.4})$$

The right-hand side is taken at time-step n , and the higher order terms are dropped. At constant advection velocity u we have according to (C.1), $\partial c/\partial t = -u\partial c/\partial x$ and $\partial^2 c/\partial t^2 = u^2\partial^2 c/\partial x^2$, so that

$$\frac{\partial}{\partial x}uc = u\frac{\partial c}{\partial x} - \frac{1}{2}u^2\frac{\partial^2 c}{\partial x^2}\Delta t. \quad (\text{C.5})$$

Applying a finite volume procedure to the former equation yields

$$\begin{aligned} \int_{x-\frac{1}{2}dx}^{x+\frac{1}{2}dx} \frac{\partial}{\partial x}ucdx &= \int_{x-\frac{1}{2}dx}^{x+\frac{1}{2}dx} \left(u\frac{\partial c}{\partial x} - \frac{1}{2}u^2\frac{\partial^2 c}{\partial x^2}\Delta t \right) dx \\ &= uc \Big|_{x-\frac{1}{2}dx}^{x+\frac{1}{2}dx} - \frac{1}{2}u^2\frac{\partial c}{\partial x}\Delta t \Big|_{x-\frac{1}{2}dx}^{x+\frac{1}{2}dx}. \end{aligned} \quad (\text{C.6})$$

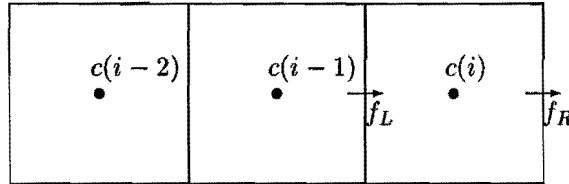


Figure C.1: Staggered grid in one dimension

In flux form the Lax-Wendroff scheme may now be written as

$$\int_{x-\frac{1}{2}dx}^{x+\frac{1}{2}dx} \frac{\partial}{\partial x}ucdx = f_R - f_L, \quad (\text{C.7})$$

with the fluxes as given in figure C.1 $f_R(i) = f_L(i+1)$ and

$$f_L = \underbrace{uc(i-1)}_{\text{upwind}} + \underbrace{\frac{1}{2}u \left(1 - u\frac{\Delta t}{\Delta x} \right) (c(i) - c(i-1))}_{\text{higher-order}}. \quad (\text{C.8})$$

The regularity of the solution can be represented by a monoticity monitor θ

$$\theta = \frac{c(i-1) - c(i-2)}{c(i) - c(i-1)}, \quad (\text{C.9})$$

that equals unity in linear parts and negative when there is a local extremum. The higher order part of the flux is limited by multiplication with a limiter function $L(\theta)$ due to van Leer,

$$L(\theta) = \frac{|\theta| + \theta}{1 + \theta}, \quad (\text{C.10})$$

giving

$$L(\theta) = \begin{cases} 0 & \text{if } \theta < 0; \\ 2 \frac{c(i-1) - c(i-2)}{c(i) - c(i-2)} & \text{if } \theta > 0 \end{cases} \quad (\text{C.11})$$

The flux can be written as the product of the advection velocity and some interpolated value of the scalar with the use of the limiter defined as

$$c^{\text{int}} = c(i-1) + \frac{1}{2} \left(1 - u \frac{\Delta t}{\Delta x} \right) (c(i) - c(i-1)) L(\theta). \quad (\text{C.12})$$

The final scheme becomes

$$c^{\text{int}} = \begin{cases} c(i-1) & \text{if } \theta < 0; \\ c(i-1) + \left(1 - u \frac{\Delta t}{\Delta x} \right) \frac{(c(i) - c(i-1))(c(i-1) - c(i-2))}{c(i) - c(i-2)} & \text{if } \theta > 0 \end{cases} \quad (\text{C.13})$$

Using this scheme may cause problems since θ and c^{int} may become singular in equivalued parts. Therefore we use the "ULTIMATE" strategy as proposed by *Leonard* [1991]. In this strategy the absolute curvature and slope are computed according to

$$\text{ACURV} = |c(i-2) - 2c(i-1) + c(i)| \quad \text{ADEL} = |c(i-2) - c(i)|. \quad (\text{C.14})$$

Now the higher order part in (C.13) is only taken into account whenever $\text{ACURV} \geq \text{ADEL}$. In linear parts the method switches to first-order upwinding, which has no truncation error in such region. Therefore singularity problems are avoided and the scheme is a little cheaper in computational cost, not evaluating a higher order part where first-order has no truncation error. The acronym "ULTIMATE" stands for the use of a universal limiter (UL) for transient interpolation modelling (TIM) of the advective transport equations (ATE).

Some common advection schemes are compared with the present scheme in figure C.2. Here a test is used as proposed by *Leonard* [1991], consisting of a step, a sine squared and a semi-ellipse. For details see *Leonard* [1991]. Figure C.2 shows the absolute supremacy of the present "ULTIMATE"-van Leer scheme.

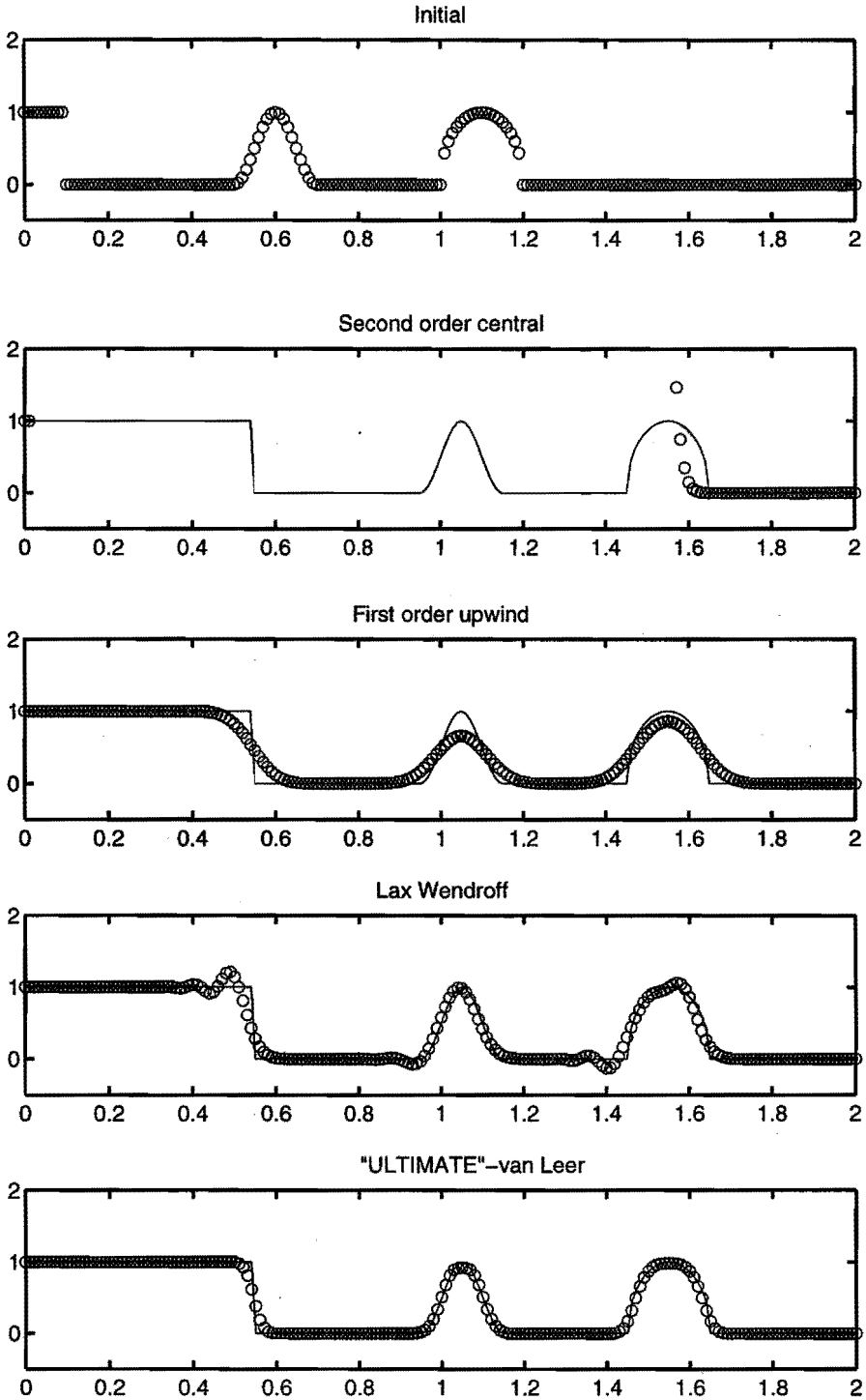


Figure C.2: Results of several advection schemes at Courant number $\sigma = 0.5$

Appendix D

PTV cost minimization algorithm

In the particle tracking algorithm, used in the present study, the finding of the optimal set of matchings is obtained by minimizing the function ζ as defined by

$$\zeta = \alpha_{ij}c_{ij}. \quad (\text{D.1})$$

The association is determined by the binary valued quantity α_{ij} , being equal to 1 for true associations. The likelihood of the pairing is given by a so-called cost function c_{ij} . Therefore the function ζ expresses a summarized weighted association or integral cost.

Reducing ζ is achieved by making use of the relational index $I(j)$ which has the value i , for which $\alpha_{ij} = 1$. Similarly an index $J(i)$ with value j , for which $\alpha_{ij} = 1$ can be defined. Both are needed because of the existence of particles in image P that are not appearing in Q and vice versa. The change in the overall cost can now be calculated for each $\alpha_{kl} = 0$ becoming 1. To keep the pairings unequivocal for every i there is exactly one α_{ij} that equals unity. This holds also for every j . This means that by putting a zero α_{kl} to unity that both $\alpha_{I(l)l}$ and $\alpha_{kJ(k)}$ must become zero. Sequentially this implies that also $\alpha_{I(l)J(k)}$ has to be

assigned to one, having

$$\left(\begin{array}{ccccccc} \alpha_{11} & \alpha_{12} & \dots & & & \dots & \alpha_{1M} \\ \alpha_{21} & \alpha_{22} & \dots & & & \dots & \alpha_{2M} \\ \vdots & \vdots & \ddots & & & & \vdots \\ & & & \alpha_{I(l)l} = \lambda^0 & \dots & \alpha_{kl} = \emptyset^1 & \\ & & & \vdots & & \vdots & \\ & & & \alpha_{I(l)J(k)} = \emptyset^1 & \dots & \alpha_{kJ(k)} = \lambda^0 & \\ & & & & & & \\ \vdots & \vdots & & & & \ddots & \vdots \\ \alpha_{N1} & \alpha_{N2} & \dots & & & \dots & \alpha_{NM} \end{array} \right) \quad (\text{D.2})$$

This interchange results in a change in cost. The change in overall cost is due to the costs associated with the change in the mentioned four α_{ij} values. The alteration is denoted by the reduced cost rc_{kl}

$$rc_{kl} = (c_{kl} + c_{I(l)J(k)}) - (c_{I(l)l} + c_{kJ(k)}). \quad (\text{D.3})$$

The pair kl which yields the most negative value of rc_{kl} will be allowed to enter the set of pairings along with pair $I(l)J(k)$. This process is repeated until no association has a negative value of rc_{kl} anymore. The definition of ζ ensures that this solution has the minimum value of the objective function and corresponds to the optimal set of associations.

Appendix E

Experimental stresses and *a priori* test

In this appendix the detailed results of the *a priori* test are given. The "exact" deviatoric stresses are depicted in figure E.1. The decomposition of the total stress in Reynolds, cross and Leonard stresses is given in figures E.2, E.3 and E.4. Furthermore *a priori* predictions of the time mean stresses and their standard deviations are calculated based on subgrid scale models. In figures E.5, and E.6 results are given for the Smagorinsky model and the dynamic model, respectively. These models are used while employing top-hat filtered data.

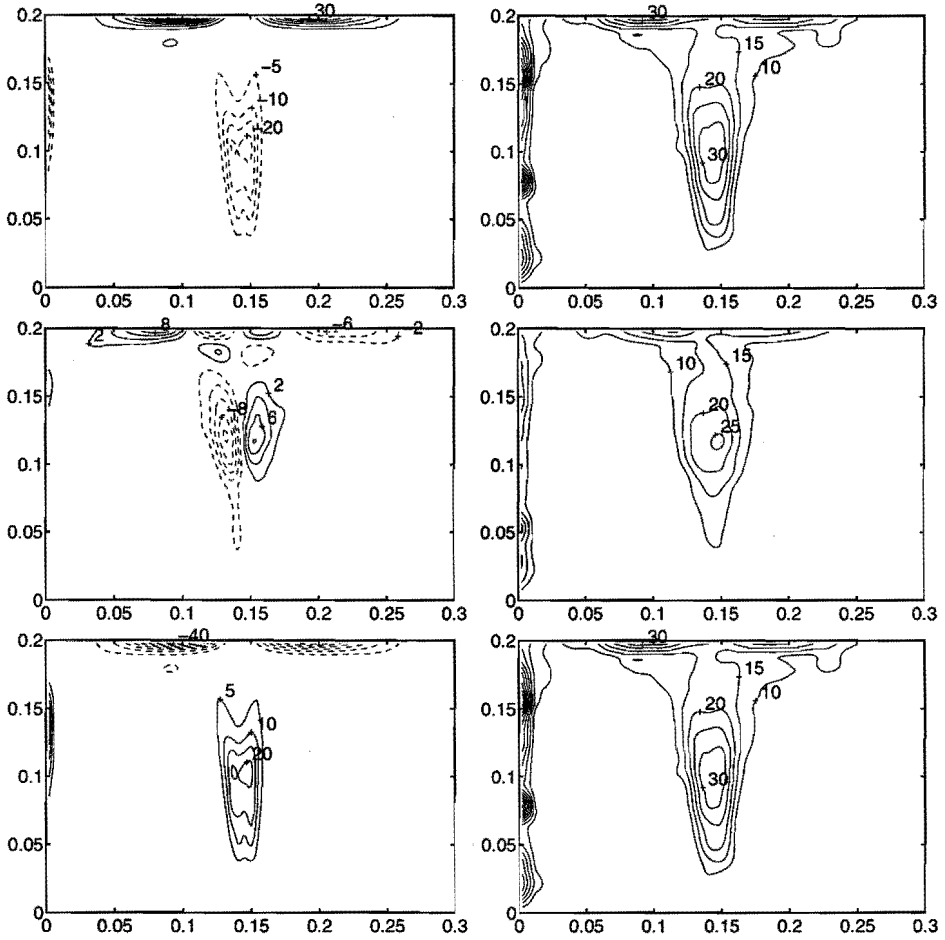


Figure E.1: Subgrid stresses, deviatoric parts, top to bottom: τ_{11} , τ_{13} and τ_{33} , Left: time mean stresses; right: standard deviations. Levels multiplied by 10^7 .

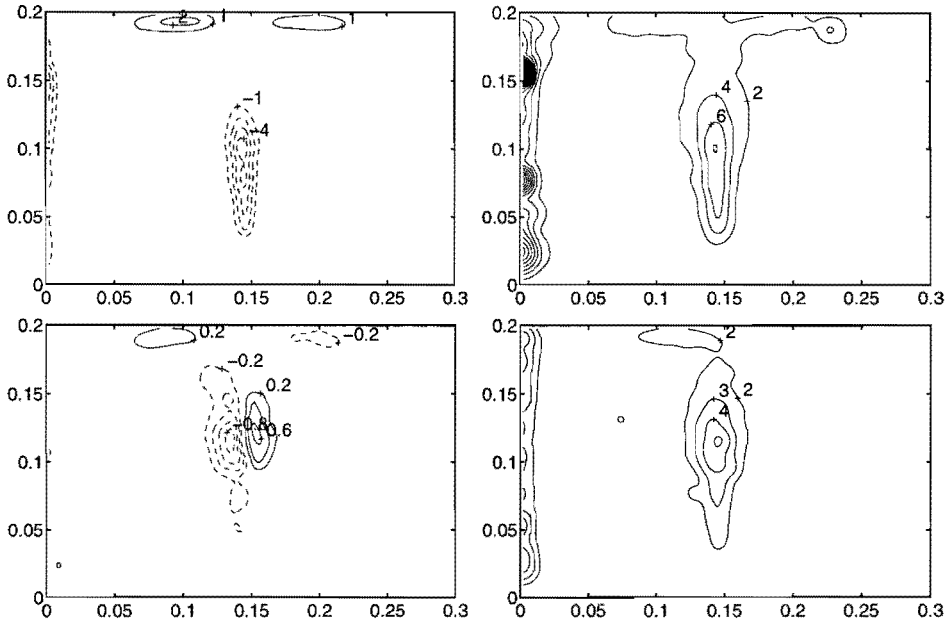


Figure E.2: Subgrid Reynolds stresses, deviatoric parts, top to bottom: R_{11} , R_{13} , Left: time mean stresses; right: standard deviations. Levels multiplied by 10^7 .

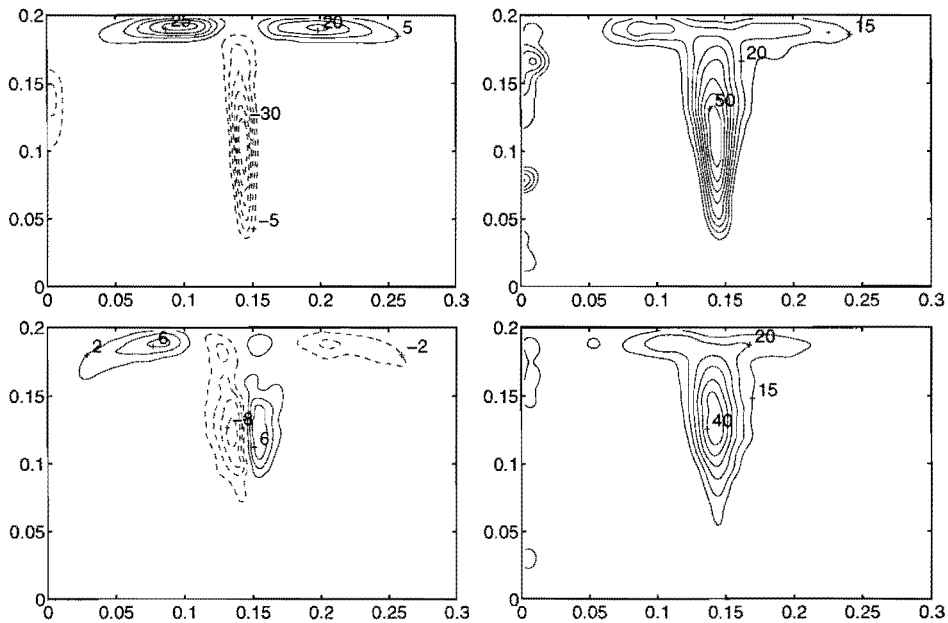


Figure E.3: Subgrid cross stresses, deviatoric parts, top to bottom: C_{11} , C_{13} , Left: time mean stresses; right: standard deviations. Levels multiplied by 10^7 .

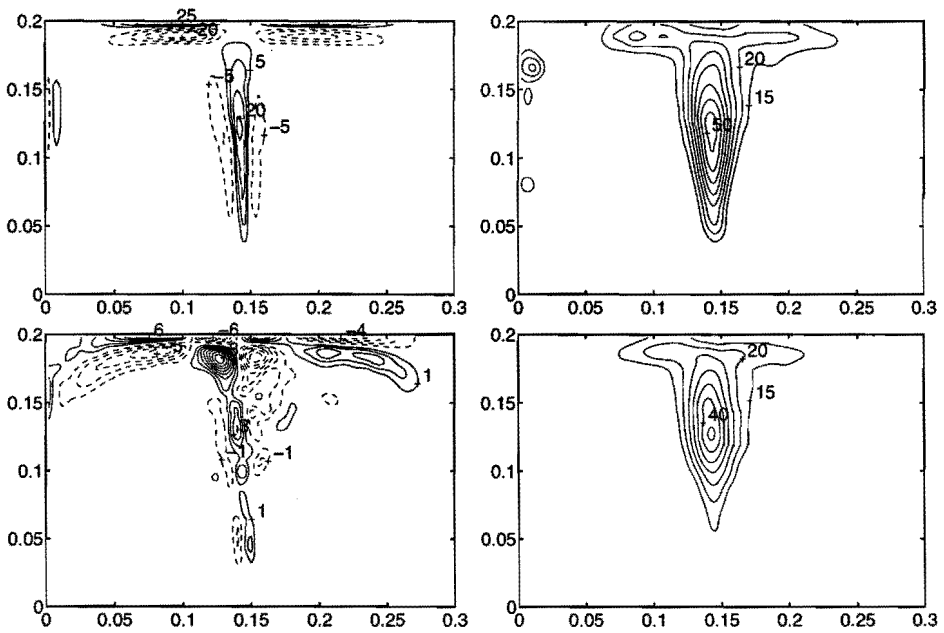


Figure E.4: Leonard stresses, deviatoric parts, top to bottom: L_{11} , L_{13} , Left: time mean stresses; right: standard deviations. Levels multiplied by 10^7 .

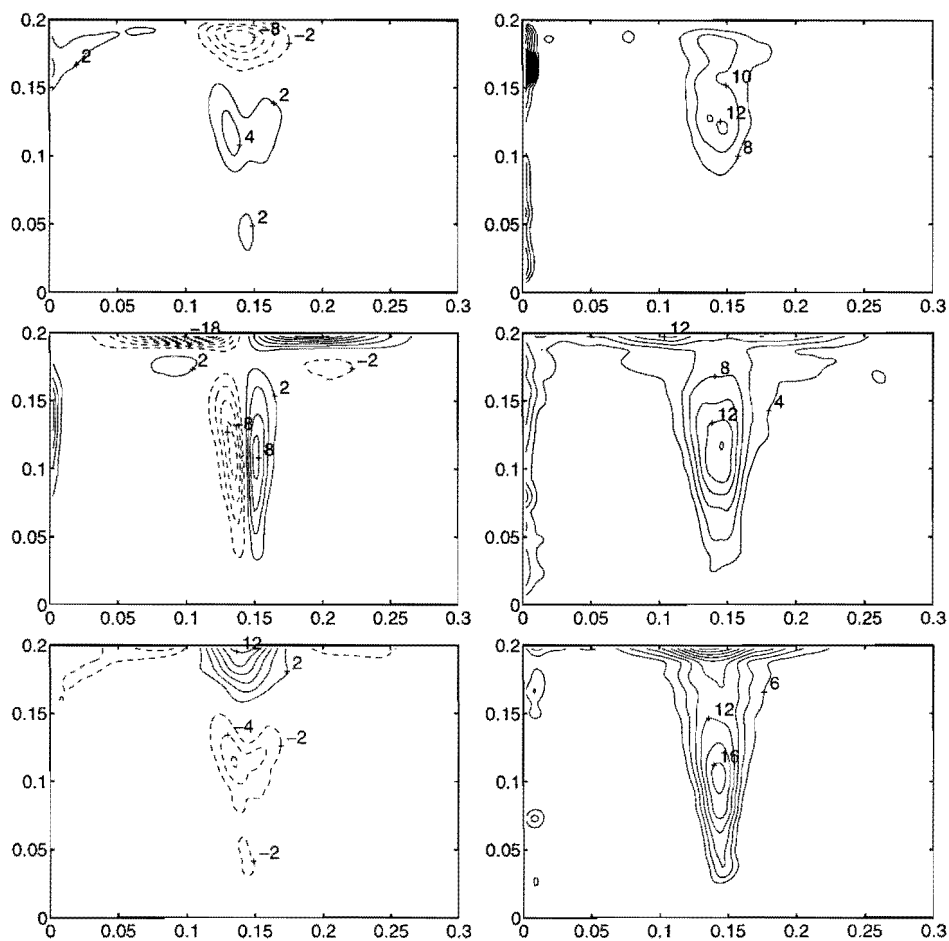


Figure E.5: Subgrid stresses, based on the Smagorinsky model, top to bottom: τ_{11} , τ_{13} and τ_{33} . Left: time mean stresses; right: standard deviations. Levels multiplied by 10^7 .

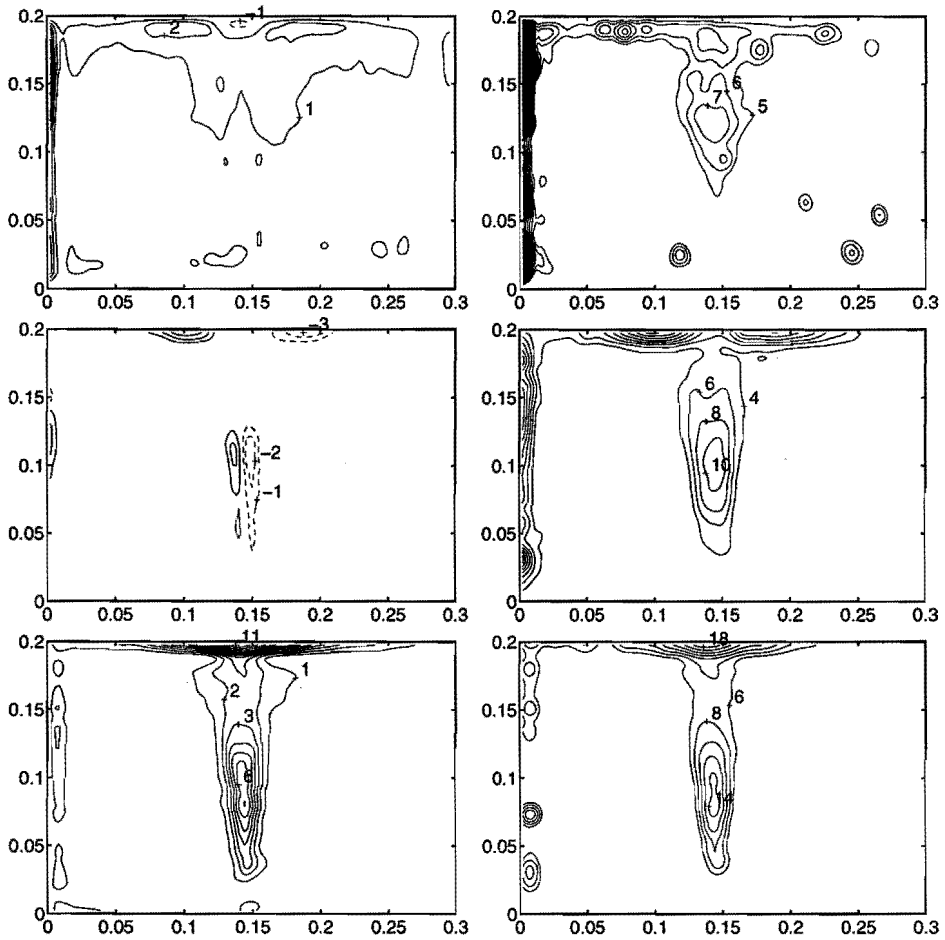
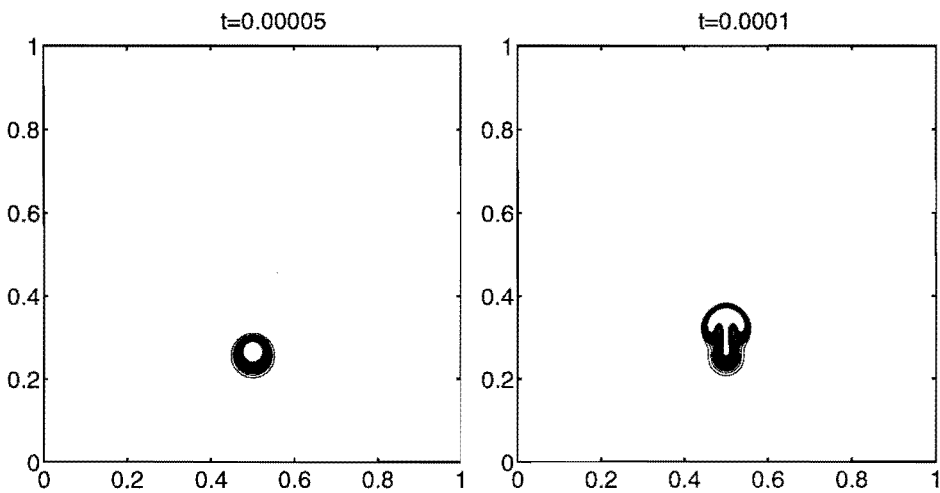


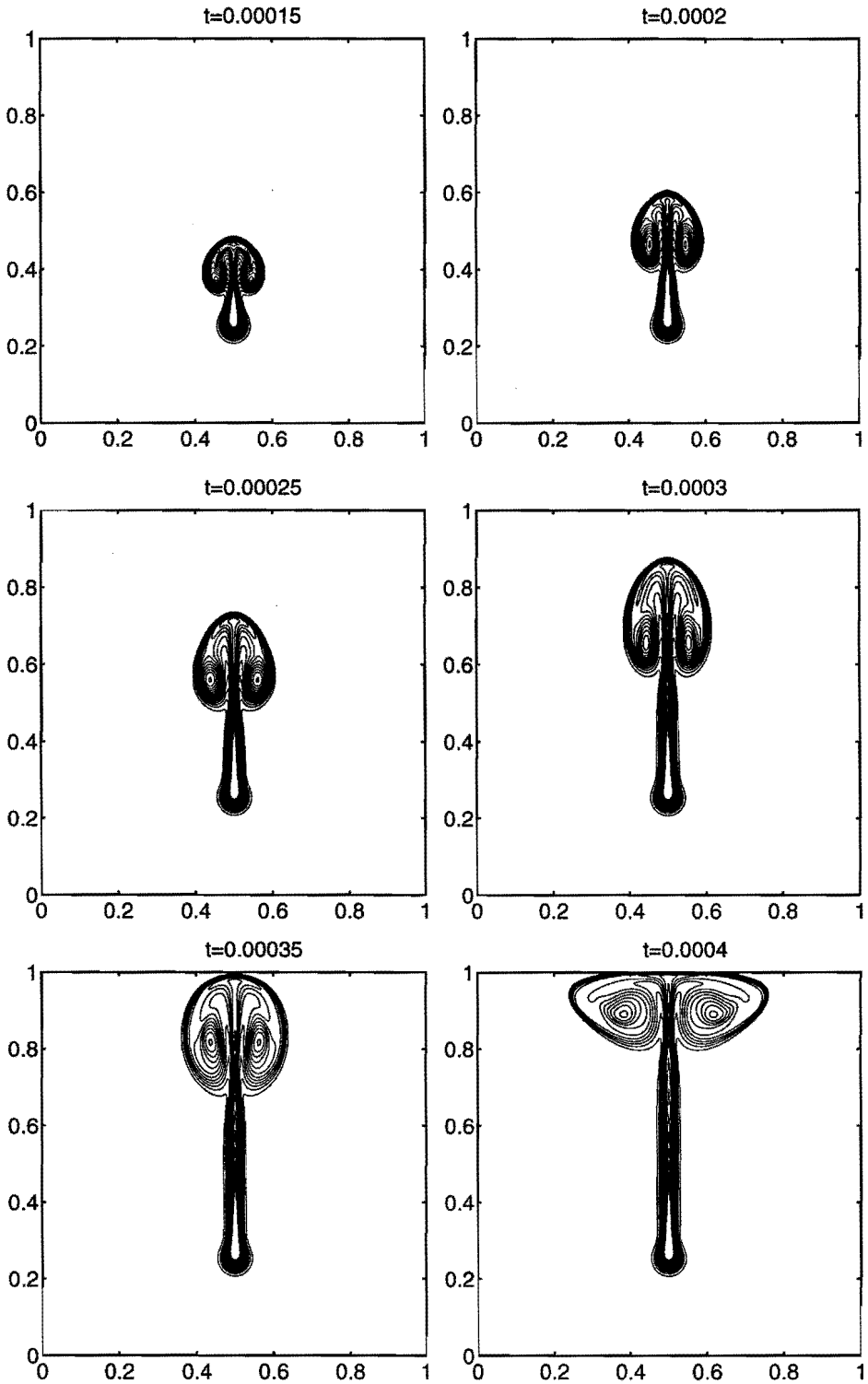
Figure E.6: Subgrid stresses, based on the dynamic model (DM), top to bottom: τ_{11} , τ_{13} and τ_{33} , Left: time mean stresses; right: standard deviations. Levels multiplied by 10^7 .

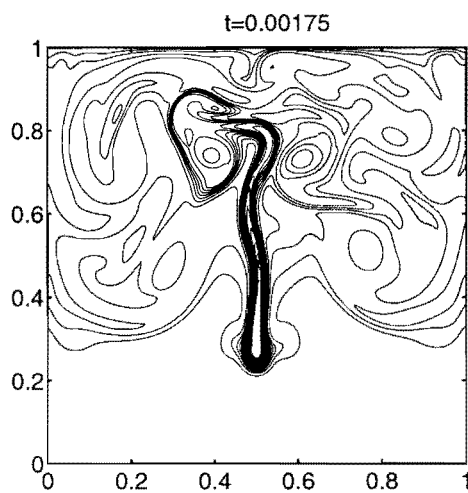
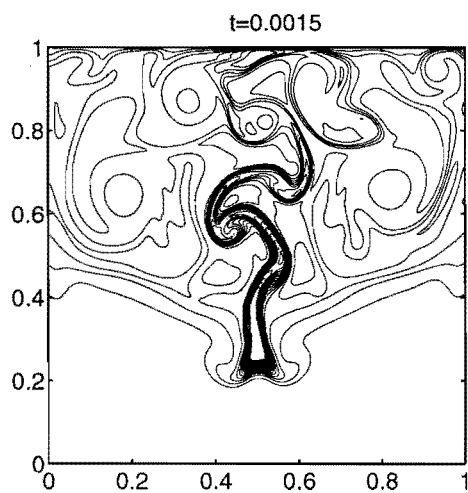
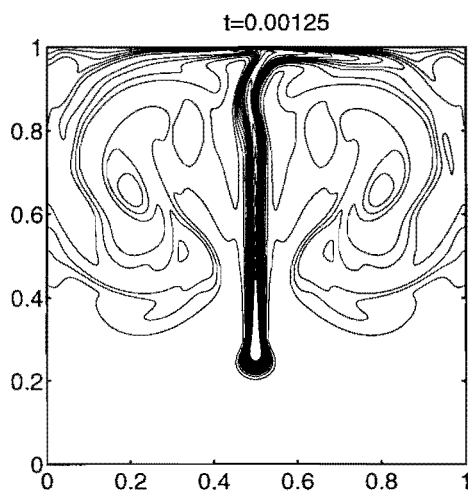
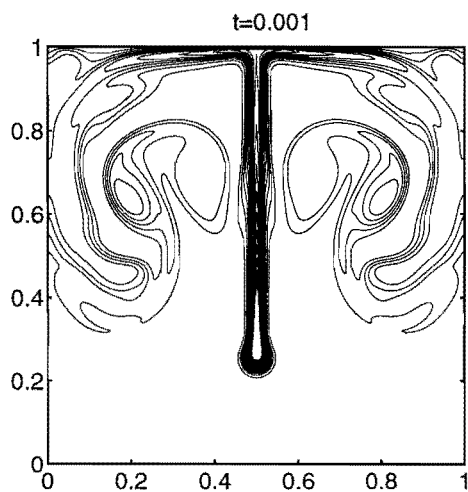
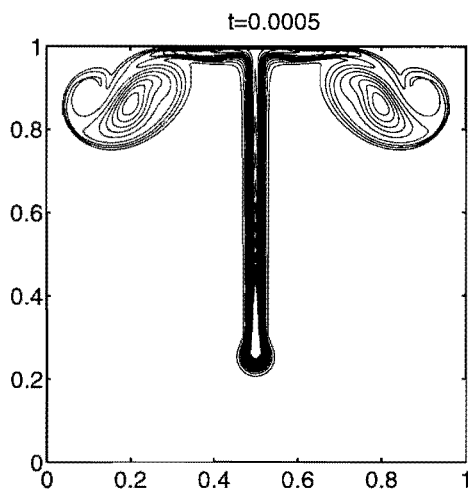
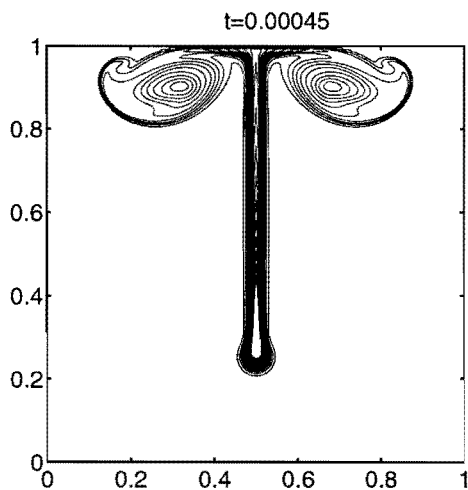
Appendix F

Development of a 2D plume in air

In this appendix the temperature field of a 2D plume is given as function of time. The dimensionless parameters are $Ra = 10^{10}$ and $Pr = 0.71$. The flow domain, boundary conditions and heat source distribution are specified in the introduction of chapter 7. The flow was simulated on a 195^2 grid. An initial perturbation of intensity $a_T = 10^{-8}$ is applied. Snapshots are given at a number of times, indicated at the top of each picture. Contour levels are given by $[5 \cdot 10^{-4}; 5 \cdot 10^{-4}; 10^{-2}]$.







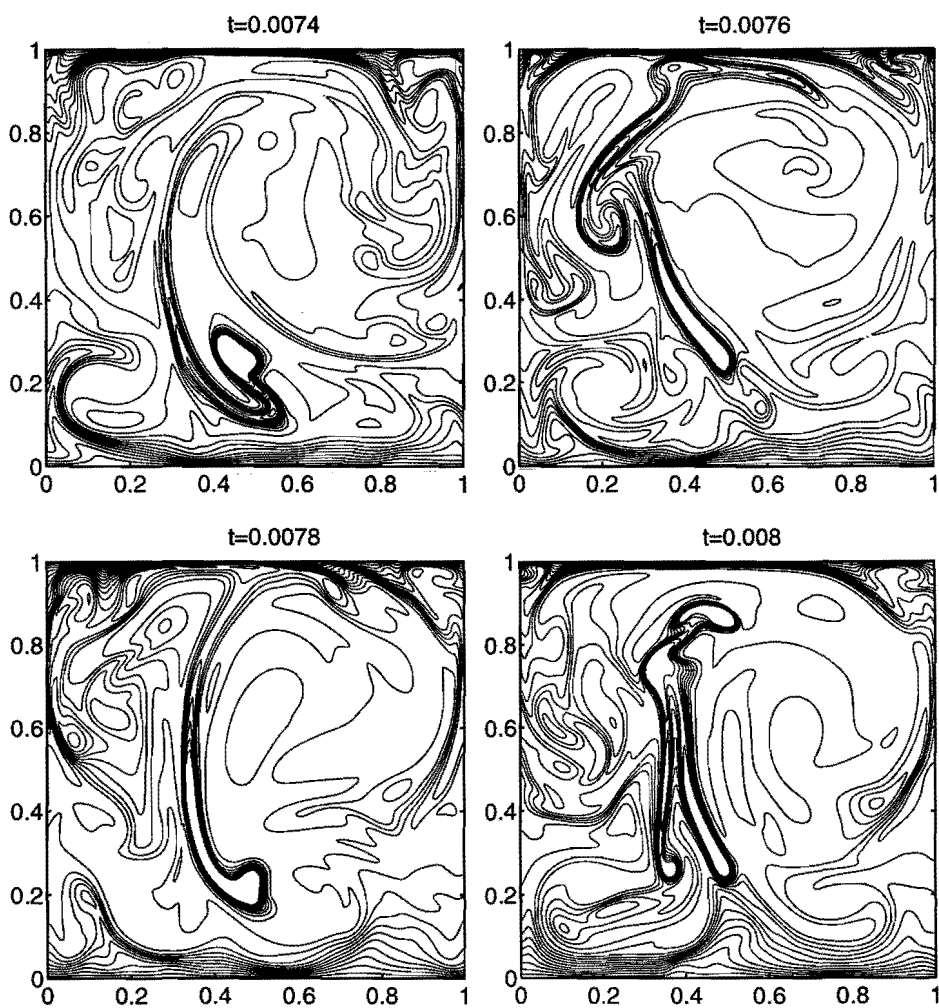
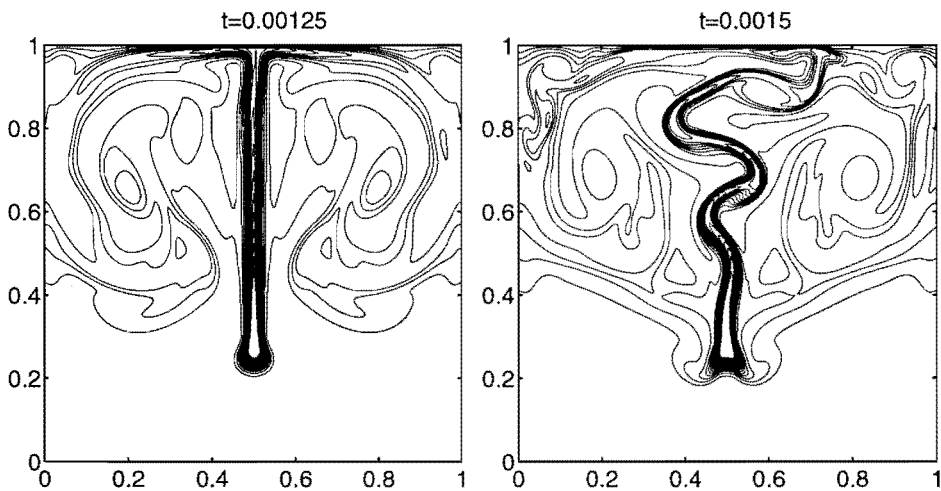


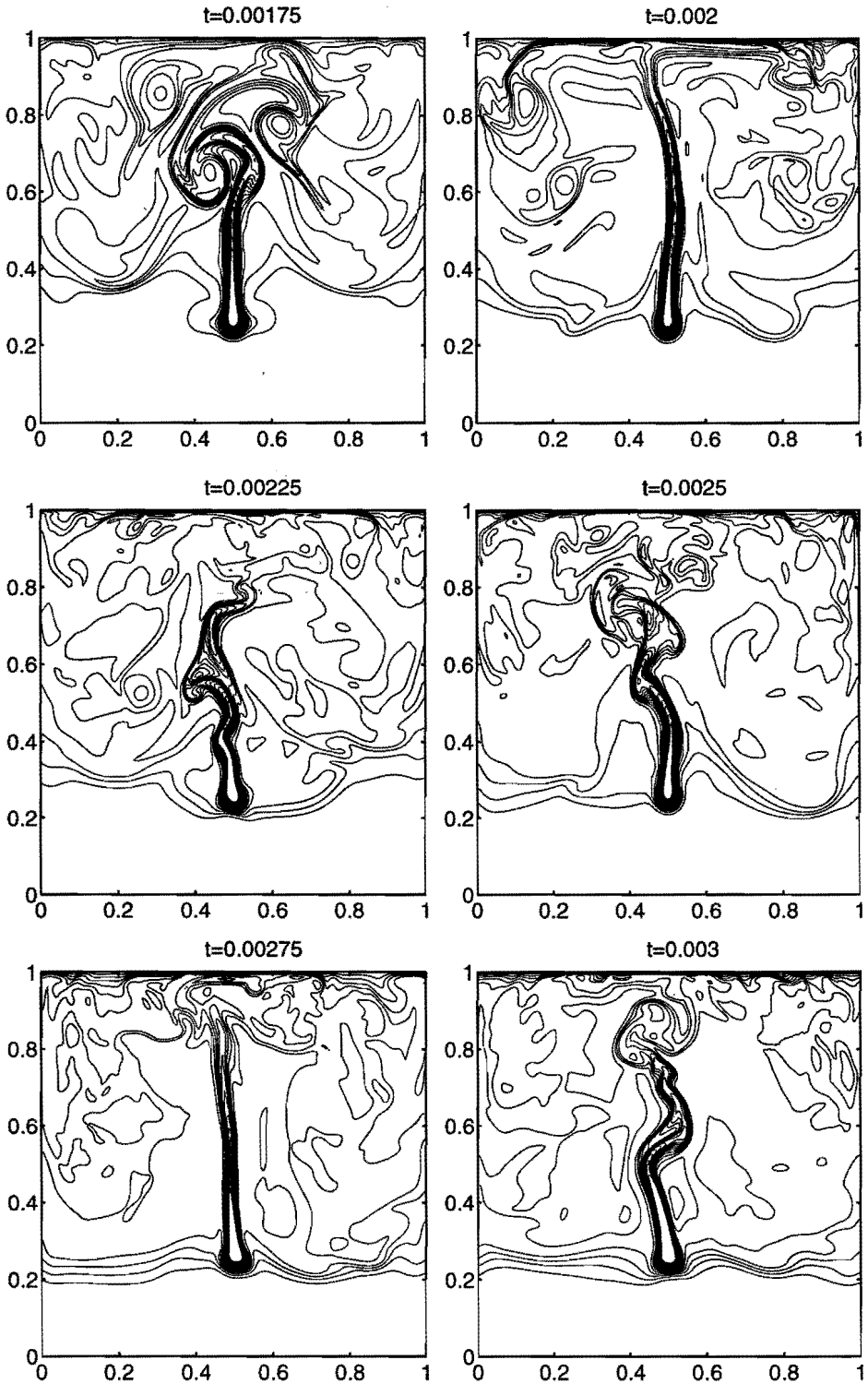
Figure F.1: Evolution of the temperature field in the 2D case, values (0.0005:0.0005:0.01)

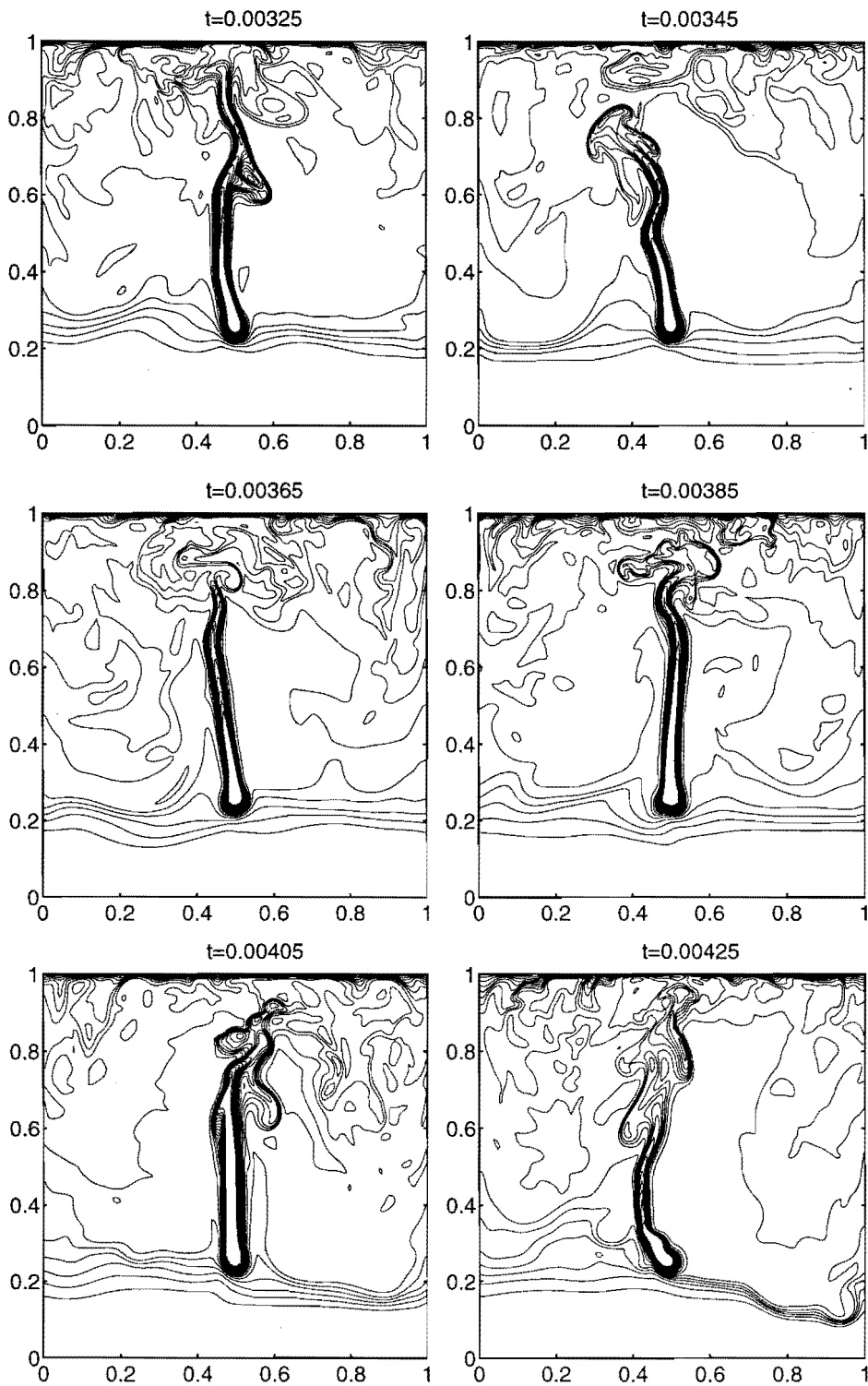
Appendix G

Development of a 3D plume in air

In this appendix the temperature field of a 3D plume is given as function of time. The dimensionless parameters are $Ra = 10^{10}$ and $Pr = 0.71$. The flow domain, boundary conditions and heat source distribution are specified in the introduction of chapter 7. The flow was simulated on a 195^3 grid. An initial perturbation of intensity $a_T = 10^{-8}$ is applied. Snapshots of cross-sections at the discrete position $j = 100$ are given at a number of times, indicated at the top of each picture. The evolution of the flow field up to the first picture in this appendix is equal to the two-dimensional starting flow, and is depicted in appendix F. Contour levels are given by $[5 \cdot 10^{-4}; 5 \cdot 10^{-4}; 10^{-2}]$.







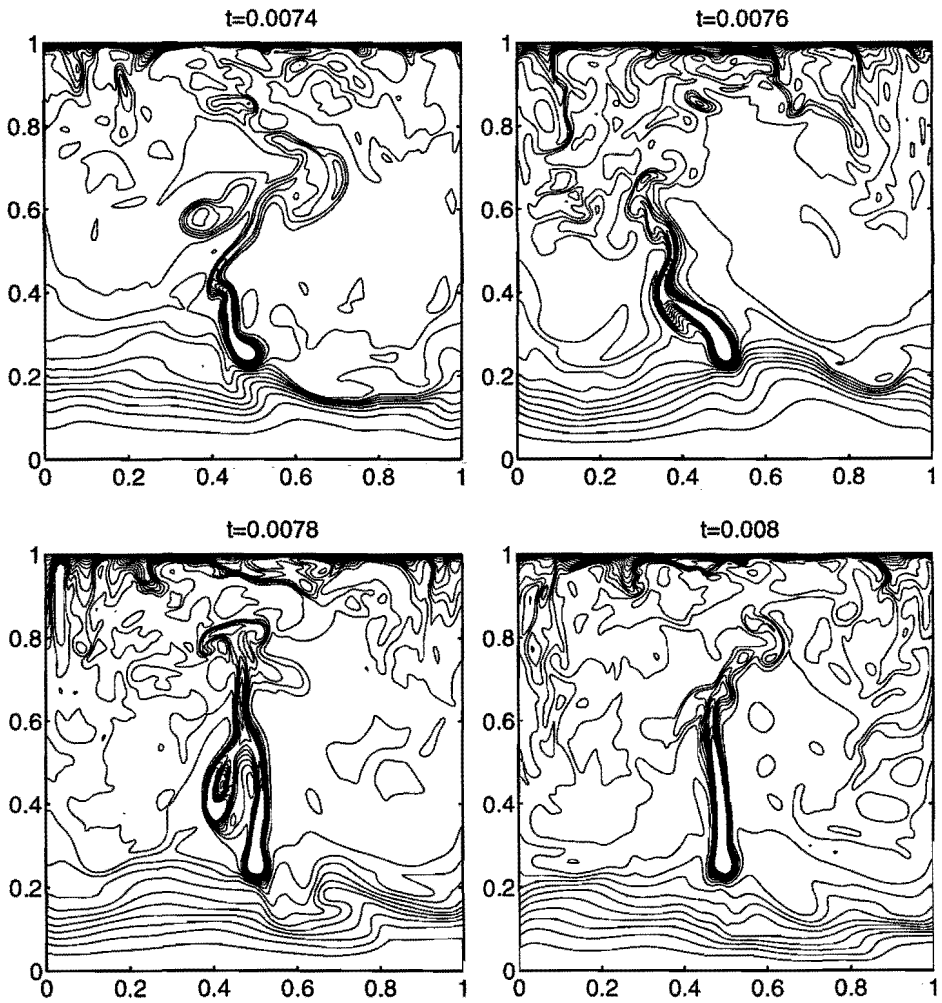


Figure G.1: Evolution of the temperature field in the 2D case, values (0.0005:0.0005:0.01)

Frequently used nomenclature

Although most quantities are treated sometimes as being dimensionless, the physical dimension is given between square brackets.

Symbols

A	area	$[m^2]$
B	buoyancy flux	$[m^3 s^{-3}]$
c_p	heat capacity at constant pressure	$[m^2 s^3 K^{-1}]$
C_k, C_s, C	Kolmogorov, Smagorinsky, dynamic constant	$[-]$
e	kinetic energy	$[m^2 s^{-2}]$
E	spectral kinetic energy density	$[m^3 s^{-2}]$
f	frequency	$[s^{-1}]$
f	similarity streamfunction	$[m^2 s^{-1}]$
F_2	structure function	$[m^2 s^{-2}]$
g	gravitational acceleration	$[m s^{-2}]$
h	subgrid flux	$[m K s^{-1}]$
H, W, D	domain height, width, depth	$[m]$
k	wavenumber	$[m^{-1}]$
K_h	eddy diffusivity	$[m^2 s^{-1}]$
K_m	eddy viscosity	$[m^2 s^{-1}]$
n	time step	$[-]$
p	pressure	$[kg m^{-1} s^{-2}]$
Pr	Prandtl number (after Ludwig Prandtl (1875-1953))	$[-]$
q'	heat flux per unit length	$[kg s^{-2}]$
q''	heat flux per unit area	$[kg m^{-1} s^{-2}]$
q'''	heat flux per unit volume	$[kg m^{-2} s^{-2}]$
r	radius	$[m]$
Ra	Rayleigh number (after John W. Strutt, Lord Rayleigh (1842-1919))	$[-]$
Re	Reynolds number (after Osborne Reynolds (1842-1912))	$[-]$
S	strain	$[s^{-1}]$
t	time	$[s]$
T	temperature	$[K; ^\circ C]$
u, v, w	velocity components	$[m s^{-1}]$
u_i	velocity components in direction i	$[m s^{-1}]$
V	volume	$[m^3]$
x, y, z	coordinates	$[m]$
x_i	coordinates in direction i	$[m]$

Greek symbols

α	entrainment rate	$[-]$
α	heat transfer coefficient	$[kg\ m^2\ s^{-3}\ K^{-1}]$
β	coefficient of thermal expansion	$[K^{-1}]$
β_T	width coefficient of turbulent temperature profile	$[-]$
δ	Kronecker delta	
Δ	grid spacing, difference	$[m]$
ϵ	kinetic energy transfer	$[m^2\ s^{-3}]$
η	Kolmogorov length scale	$[m]$
η	similarity coordinate	$[m]$
ϕ	similarity temperature	$[K]$
κ	thermal diffusivity	$[m^2\ s^{-1}]$
λ	thermal conductivity	$[kg\ m\ s^{-3}\ K^{-1}]$
λ	Taylor microscale	$[m]$
μ	mean	
ν	kinematic viscosity	$[m^2\ s^{-1}]$
ω	vorticity	$[s^{-1}]$
ψ	streamfunction	$[m^2\ s^{-1}]$
ρ	density	$[kg\ m^{-3}]$
σ	standard deviation	
τ	subgrid stress	$[m^2\ s^{-2}]$
τ	time constant	$[s]$

Notations

f^*	dimensionless quantity
\bar{f}	spatially filtered value
f'	spatially fluctuating value
$\langle f \rangle$	time averaged value
f''	temporal standard deviation

Abbreviations

DNS	direct numerical simulation
FDM	finite difference method
FVM	finite volume method
LES	large-eddy simulation
PTV	particle tracking velocimetry
SEM	spectral element method
SGM	subgrid scale model
SGS	subgrid scale

Summary

The present research is concerned with thermal plumes induced by prismatic heat sources and displaying a spatial laminar to turbulent transition. The plume of a cigarette is a striking example of such a flow, showing the transition clearly. In boilers, plumes affect the storage of heat in such a way that they decrease the storage efficiency. Heat advected from computer chips by plume flows ensure subcritical chip temperatures. Thus thermal plume flows are responsible for the performance of several devices. Therefore we want to predict these kind of flows.

Generally, the length scales involved range from very small in the free buoyant boundary layer to very large in recirculating patterns. To solve such flows entirely, by numerical approximation on a computer, would require vast amounts of computer storage, as well as CPU-time. Therefore the research focusses on the feasibility of the application of so-called "Large-Eddy Simulation" (LES). This is a technique in which the largest scales of motion are explicitly calculated. The effect of the smallest eddies on the larger structures is modelled. Several models are yet available. Mostly they are based on the theory of homogeneous isotropic turbulence. The accompanying energy drain can then be modelled with an eddy diffusivity.

In order to come to a fair assessment, experimental as well as numerical sources of reference data are employed. In an experimental setup the objected plume flow was established in water and subjected to "Particle Tracking Velocimetry" (PTV). The vigour of the flow as expressed by the Rayleigh number was $Ra = 2.1 \cdot 10^{11}$. For air a "Direct Numerical Simulation" (DNS) was performed at a lower Rayleigh number of $Ra = 10^{10}$.

The PTV yielded qualitatively good spatial information of the flow. It showed a recirculating region in the upper half of the flow domain starting with the transitional region. The DNS was carried out successfully yielding a resolved flow field, spatially as well as temporally. Furthermore the simulation period was sufficient to obtain converged statistics.

The PTV data revealed that in the transitional region the interscale kinetic energy transfer downscale and upscale are of equal importance. As a consequence equilibrium models are unable to display the physical correct effect of the small scales of motion. A scale similarity concept as employed by the dynamic model shows the ability to permit upscale energy transfer. However, this is limited by numerical stability. In the present case therefore it is hard to apply LES with sufficient accuracy. A good representation of the source is essential. In case of the DNS air flow, the agreement with LES was much better. Here less scales with an extent smaller than the grid width were present and so the model had only a weak influence. Furthermore it was found that relative cheap models performed best.

Samenvatting

Het huidige onderzoek betreft thermische pluimen veroorzaakt door lijnvormig warmtebronnen en met een ruimtelijke laminair-naar-turbulent overgang. Een sigarettenpluim is een goed voorbeeld van zo'n stroming waarbij de overgang goed te zien is. In boilers zorgen pluimen voor een daling van de kwaliteit van de warmte-opslag. In computers daarentegen zorgen pluimen voor de benodigde afvoer van warmte van de chips. Pluimen zijn dus verantwoordelijk voor de prestaties van verschillende apparaten. Daarom willen we het belangrijk dit soort stromingen te kunnen voorspellen.

In het algemeen reiken de lengteschalen van zeer klein in dunne grenslagen tot zeer groot in recirculatie gebieden. Het oplossen van zulke stromingen, met numerieke benaderingen op een computer, zou een zeer grote hoeveelheid aan data opslag en CPU-tijd vergen. Daarom richt het onderzoek zich op het aanwenden van zogenaamde "Large-Eddy Simulation" (LES). Dit is een techniek waar de grootste schalen van beweging expliciet berekend worden. Het effect van de kleinste wervels op de grotere structuren wordt gemodelleerd. Verschillende modellen zijn reeds voorhanden. De meeste modellen zijn gebaseerd op de theorie van homogene isotrope turbulentie. De hieraan gekoppelde energie afvoer kan dan gemodelleerd worden met een eddy-diffusiviteit.

Om een eerlijke vergelijking mogelijk te maken is gebruik gemaakt van zowel experimentele als numerieke referentiedata. In een experimentele opstelling is een pluim gecreëerd in water, waarbij "Particle Tracking Velocimetry" (PTV) is uitgevoerd. De thermische forcering uitgedrukt met behulp van het Rayleigh getal was $Ra = 2.1 \cdot 10^{11}$. Voor lucht is een "Directe Numerieke Simulatie" (DNS) uitgevoerd bij een lagere forcering van $Ra = 10^{10}$.

De PTV gaf kwalitatief goede ruimtelijke informatie van de stroming. In de bovenste helft van het stromingsdomein ontstaat een recirculatie zone, startend vanaf het overgangsgebied. De DNS is met succes uitgevoerd en het resultaat was een opgelost stromingsveld, zowel ruimtelijk als in de tijd. De simulatieduur was zodanig dat geconvergeerde statistieken zijn verkregen.

De PTV data toonde dat in het overgangsgebied de kinetische energieoverdracht van grote naar kleine schalen even belangrijk is als andersom. Het gevolg is dat evenwichtsmodellen niet in staat zijn het correcte fysische gedrag van de kleine schalen te verdisconteren. Een gelijkvormigheidsconcept zoals gebruikt wordt in het dynamische model laat echter wel de mogelijkheid zien van energieoverdracht van kleine naar grote schalen. Dit is echter beperkt op grond van numerieke stabiliteit. In het huidige geval is het daarom zeer moeilijk om een LES te gebruiken met voldoende nauwkeurigheid. Een goede representatie van de bron is essentieel. In het geval van de DNS luchtstroming is de overeenkomst met LES veel beter. Hier zijn minder schalen aanwezig die kleiner zijn dan het numerieke grid, zodat het model geringe invloed uitoefende. Relatief goedkope modellen presteerden hier het beste.

Nawoord

"Het leed is geleden de horizon schijnt wanneer de doden dronken zijn en Pierlala verdwijnt". In de afgelopen jaren is getracht een fysisch relevant proefschrift te schrijven, binnen randvoorwaarden van esthetica en perfectionisme. De mens en zijn zoektocht zijn onontkoppelbaar. In het begin met de neus op de monochrome terminals, kritisch de groene getallen controlerend die in schier oneindige rijen over het scherm rolden. Later met "fancy graphics", hetgeen een wereld opende maar daarnaast ook zeer veel vragen opriep. Er is veel geleerd. Gedeeltelijk ook door mij. Dit is niet alleen mijn eigen verdienste geweest. Hierbij wil ik een groot aantal mensen bedanken die een belangrijke factor waren in de realisatie van dit proefschrift. Dit zowel op een directe als indirecte manier.

Op de eerste plaats ben ik de directe begeleiding, Anton van Steenhoven en Camilo Rindt, veel dank verschuldigd. Beider constante ondersteuning en vertrouwen hebben voor een belangrijk deel geleid tot de verwezenlijking van het resultaat. De tweede promotor Prof. Frans Nieuwstadt had een grote bijdrage door zijn niet aflatende enthousiasme en nuttige suggesties. De overige leden van de kerncommissie, Prof. van Heijst en Prof. Mattheij, wil ik bedanken voor hun bruikbare opmerkingen en correcties.

Bij deze wil ik ook de afstudeerders en stagiaire bedanken die hun steentje hebben bijgedragen, in chronologische volgorde: Hugo Sparidans, Johan Kwast, Dorrit van der Burgt, Eddy van Doorn, Peter Hempenius, Gerdewan Jacobs en Erik (the half-a-bee) Hermens.

De technische en administratieve ondersteuning van Frits van Veghel, Rian Tielemans, Ad van Huygevoort, Lambert van der Schoot, Peter Ewalts, Ion Barosan en Frans Kuypers droegen bij tot een prettige samenwerking.

Jos Sillekens, Jacob van Berkel, Peter Minev, Gert van der Plas, JanKees Hogendoorn, Douwe de Vries en Rob Schook zijn een constante bron geweest van meer of minder fruitvolle en ook sappige discussies.

Verder wil ik mijn moeder, de rest van de familie en m'n vrienden bedanken voor de steun en de relativatie.

Curriculum vitae

- May 19th 1965 Born in Mill, The Netherlands.
- 1977–1983 Pre-university Education (VWO),
Merletcollege, Cuijk.
- 1983–1987 Mechanical Engineering,
Technical College (HTS) Arnhem.
- 1985–1992 Experienced labourer 1st degree,
PTT Post Mill.
- 1987–1991 Study Mechanical Engineering at the
Eindhoven University of Technology.
Graduated within the
Energy Technology Division,
Department of Mechanical Engineering.
Carried out in the
Aero-acoustics Division,
Fluid Dynamics Laboratory
of the Physics Department.
Graduated with honours.
- 1991–1996 Ph.D. research within the
Energy Technology Division,
Department of Mechanical Engineering,
Eindhoven University of Technology.
- 1996– Post-doc position within the
J.M. Burgers centre for fluid dynamics.

Stellingen

behorende bij het proefschrift van Rob Bastiaans:

Large-Eddy Simulation of Confined Transitional Plumes

I In het transitiegebied van een door een lijnbron geïnduceerde thermische pluim is de zogenaamde "backscatter", kinetische energie-overdracht van kleine naar grote ruimtelijke schalen, net zo belangrijk als "forward scatter".

Dit proefschrift.

II De turbulentiegraad van numeriek gesimuleerde turbulentie kan goed gekarakteriseerd worden door de verhouding tussen de grootte van de datavelden voor en na compressie.

III Kennis van de stromingsleer stoelt voornamelijk op het feit dat de belangrijkste fluïda, te weten lucht en water, optisch toegankelijk zijn.

IV Bij de behandeling van de CO_2 -problematiek in documentaires worden ten onrechte H_2O pluimen getoond.

V Festingers theorie, betreffende de cognitieve dissonantie vermijding, voorspelt dat personen deze theorie verwerpen.

L. Festinger [1957],
A Theory of Cognitive Dissonance,
Stanford University Press.

VI Iets wat geen bewuste risico's met lelijkheid neemt kan niet mooi zijn.

Alain de Botton [1993],
Essays in Love.

VII Duidelijke taal kan vaak alleen gebruikt worden met zware concessies aan de werkelijkheid.

VIII Onwetendheid is des wetenschappers libido.

IX Kinderen die "ik ben vies" op auto's schrijven hebben gelijk.

X Het fileprobleem kan opgelost worden door een verbod op deelname.

XI Het door P. de C. veelvuldig gebezigde "sapperdeflap" duidt op een handelswijze die meestal niet met voorbedachte rade was.

XII Een onmogelijkheid is geen onmogelijkheid.